J. Astrophys. Astr. (2009) **30,** 1–36

The Fate of Dwarf Galaxies in Clusters and the Origin of Intracluster Stars

Paramita Barai*, William Brito & Hugo Martel
Département de physique, de génie physique et d'optique, Université Laval, Québec City, Québec, G1K 7P4, Canada.
**e-mail: paramita.barai.1@ulaval.ca*

Received 2008 March 4; accepted 2009 March 13

Abstract. The main goal of this paper is to compare the relative importance of destruction by tides *vs.* destruction by mergers, in order to assess if tidal destruction of galaxies in clusters is a viable scenario for explaining the origin of intracluster stars. We have designed a simple algorithm for simulating the evolution of isolated clusters. The distribution of galaxies in the cluster is evolved using a direct gravitational N-body algorithm combined with a subgrid treatment of physical processes such as mergers, tidal disruption, and galaxy harassment. Using this algorithm, we have performed a total of 148 simulations. Our main results are:

- destruction of dwarf galaxies by mergers dominates over destruction by tides, and
- the destruction of galaxies by tides is sufficient to explain the observed intracluster light in clusters.

Key words. Cosmology—galaxies: clusters, dwarfs, interactions—methods: numerical.

1. Introduction

Dwarf galaxies (DGs) are defined as low-mass (10^7–10^9 $M_\odot$) galaxies having an absolute magnitude fainter than $M_B \sim -16$ mag, or $M_V \sim -18$ mag (Grebel 2001), have low surface brightness and low metallicity. They are the most numerous galaxies occurring in the Universe. A majority of galaxies in the local group are DGs (Mateo 1998). DGs have been seen in observations of nearby galaxy clusters, Coma (Thompson & Gregory 1993; Bernstein *et al.* 1995), Virgo (Sandage *et al.* 1985; Lee *et al.* 2003), Fornax (Bothun *et al.* 1991; Drinkwater *et al.* 2003), Centaurus (Mieske *et al.* 2007), and several galaxy groups (Karachentseva *et al.* 1985; Côté *et al.* 1997; Cellone & Buzzoni 2005).

The diffuse intracluster light (ICL) observed in clusters of galaxies is produced by stars, usually of low surface brightness, located outside individual galaxies but within the cluster and associated with the cluster potential. The first mention of IC light was made by Zwicky (1951). Since then, several observations have detected diffuse ICL in many galaxy cluster systems (Arnaboldi 2004; Gonzalez *et al.* 2005; Mihos *et al.* 2005;

Krick *et al.* 2006). The idea of IC globular clusters was proposed by West *et al.* (1995). Later on, distinct IC stars were observed (Arnaboldi *et al.* 2003; Gal-Yam *et al.* 2003; Gerhard *et al.* 2005), including globular clusters, red giant stars, and SN Ia. The origin and evolution of the IC stars and diffuse ICL are not well constrained at present.

The most popular formation mechanism of IC population is stripping of stars from cluster galaxies by gravitational tides, fast encounters between galaxies, and tidal interactions between colliding and merging galaxies (Miller 1983; Gregg & West 1998). From observations and cosmological simulations, at $z = 0$ at least 10–20% of all stars in a cluster are unbound to any one galaxy (e.g., Aguerri *et al.* 2005). The fraction of stars in ICL increases with mass of the clusters, and increases with density of environment: from loose groups ($< 2\%$, Castro-Rodriguez *et al.* 2003), to Virgo-like (10%, Feldmeier *et al.* 2004b; Zibetti *et al.* 2005) and rich clusters ($\sim$20% or higher, Tyson & Fischer 1995; Feldmeier *et al.* 2004a; Krick & Bernstein 2007). In the cores of dense and rich clusters (like Coma) the local ICL fraction can be as high as 50% (Bernstein *et al.* 1995).

In numerical studies of ICL production in clusters, there is always a trade-off between having good resolution or good statistics. Napolitano *et al.* (2003); Willman *et al.* (2004); Sommer-Larsen *et al.* (2005), and Rudick *et al.* (2006) simulate either one cluster or a few clusters, so even though their simulations have high resolution, they have poor statistics, in the sense that the cluster(s) they are simulating might not be representative of the whole cluster population. On the other extreme, Murante *et al.* (2004) simulate a very large cosmological volume, containing a statistically significant sample of clusters. Such large simulations, however, cannot resolve the scale of dwarf galaxies. Our goal is to have it both ways: achieving good statistics while resolving the processes responsible for destroying dwarf galaxies. This is achieved by combining large-scale cosmological simulations with a semi-analytical treatment of mergers and tidal disruption.

The main objective of our present work is to determine if DGs in clusters are more prone to destruction by tides or to destruction by mergers. This determination is then used to predict the contribution of DGs to the origin of IC stars. The DGs in a cluster can be tidally disrupted (by the field of a more massive galaxy or by the background halo) or the DGs can be destroyed when they merge with another galaxy. The impact of these two destruction mechanisms on the ICL is radically different. In the case of tidal disruption, the process contributes to IC stars in the cluster. In the case of merger, the DG is absorbed by a more massive galaxy, and there is essentially no contribution to the IC stars.

We perform numerical simulations of isolated clusters of galaxies, in order to examine which method of dwarf galaxy destruction is dominant, and how the process depends on environmental factors. We identify six possible outcomes for our simulated galaxies:

(1) the galaxy merges with another galaxy,
(2) the galaxy is destroyed by the tidal field of a larger galaxy but the fragments accrete onto that larger galaxy,
(3) the galaxy is destroyed by tides and the fragments are dispersed in the intracluster medium (ICM), contributing to the intracluster light,
(4) the galaxy is destroyed by the tidal field of the background halo,

(5) the galaxy survives to the present, and
(6) the galaxy is ejected from the cluster.

We designed a simple algorithm to follow the evolution of galaxies in an isolated cluster. The gravitational interaction between galaxies is calculated by a direct N-body algorithm. The other physical mechanisms governing the possible outcomes (mergers, tidal disruption, accretion, etc.) of the simulated galaxies are treated as 'subgrid physics', and are incorporated in the algorithm using a semi-analytical method. In the present work, we use this algorithm to simulate the evolution of isolated galaxy clusters, i.e., we assume that the cluster has already formed with its constituent galaxies in place, and it is neither accreting nor merging, except in section 4.7 where we consider accretion.

The remainder of this paper is organized as follows: In section 2, we outline the numerical model for our galaxy clusters. The methodology of our simulations is described in section 3. The results are presented in section 4. We discuss the implications of our main goals in section 5, and give our conclusions in section 6.

2. The numerical method

2.1 *The basic PP algorithm*

We treat the system as an isolated cluster consisting of N galaxies of mass m_i, radius s_i, and internal energy U_i, orbiting inside a background halo of uncollapsed dark matter and gas. We assume that the halo is spherically symmetric, and its radial density profile $\rho_{\rm halo}(r)$ does not evolve with time (hence, we are neglecting infall motion that would result from cooling flows). Furthermore, we assume that the halo is stationary: it does not respond to the forces exerted on it by the galaxies, and therefore its center remains fixed at a point that we take to be the origin. In section 4.7, we relax the assumption of an isolated cluster, and consider mass growth of the cluster with time, which can happen due to accretion.

We represent each galaxy by *one single particle* of mass m_i. The 'radius' s_i of the galaxy and its 'internal energy' U_i are internal variables that only enter in the treatment of the subgrid physics described in section 2.4. Our motivation for using this approach is the following: To simulate the destruction of dwarf galaxies by tides, it would seem more appropriate to simulate each galaxy using many particles. Supposing, however, that it takes at least 100 particles to properly resolve a dwarf galaxy experiencing tidal destruction, as the galaxies in our simulations cover three orders of magnitude in mass, the most massive ones would be represented by 100,000 particles. Even though the dwarf galaxies are much more numerous than the massive ones, the total number of particles would be above one million. This raises the following issues:

- With the use of tree codes, an $N = 10^6$-particle simulation is not considered prohibitive anymore. However, (1) our model has several free parameters, so we have a full parameter-space to study, and (2) one single cluster is not statistically significant, so for each combination of parameters we need to perform several simulations. For this paper, we performed 148 simulations. Doing 148 million-particle simulations would start to be computationally expensive.
- We could use unequal-mass particles, so that the most massive galaxies would not be represented by large number of particles. This is usually not a good idea.

N-body simulations with particles having widely different masses are known to suffer from all sorts of instability problems, which often require special algorithms to deal with. The approach we are considering here is more practical.

- In this paper, we consider isolated clusters. In a forthcoming paper (Brito *et al.* 2008), we will present simulations of a cosmological volume containing at least 100 clusters. The number of particles would then reach 100 million, and we would still need to explore the parameter space. This would be computationally very expensive. We will solve this problem using single-particle galaxies combined with a treatment of subgrid physics. The simulations presented in this paper can be seen as a test-bed for this approach.

The relatively small number of particles in our simulations (typically less than 1000) enable us to use a direct, particle–particle (PP) algorithm, which is the simplest of all N-body algorithms. We took a standard PP code, which evolves a system of N gravitationally interacting particles using a second-order Runge–Kutta algorithm. We modified the original algorithm to include the interaction with the background halo, and we added several modules to deal with the subgrid physics. In this modified algorithm, the number of particles N can vary, as they merge, are destroyed by tides, or escape the cluster.

2.2 *Gravitational interactions*

The acceleration of particle i (or galaxy i) is given by

$$\mathbf{a}_i = -G \sum_{j \neq i} \frac{m_j(\mathbf{r}_i - \mathbf{r}_j)}{\left(|\mathbf{r}_i - \mathbf{r}_j|^2 + \epsilon^2\right)^{3/2}} - \frac{G M_{\rm halo}(r_i)\mathbf{r}_i}{(r_i^2 + \epsilon^2)^{3/2}}\,, \tag{1}$$

where $\mathbf{r}_i$ and $\mathbf{r}_j$ are the positions of particles i and j, respectively, m_j is the mass of particle j, $M_{\rm halo}(r_i)$ is the mass of the background halo inside $r = r_i$, G is the gravitational constant, and ϵ is the softening length. This assumes that the background cluster halo is spherically symmetric and centered at the origin. In our PP algorithm, this expression is evaluated directly, by summing over all particles $j \neq i$. The softening length ϵ is chosen to be smaller than the initial radius of the smallest galaxies (see section 3.2 for the determination of the initial radius). Our results are not sensitive to the value of ϵ, as long as it is smaller than the radii of the smallest galaxies.

We evolve the system forward in time using a second-order Runge–Kutta algorithm. The timestep Δt is calculated using:

$$\Delta t = \min_i (\Delta t)_i\,, \qquad (\Delta t)_i = \min\left[\frac{\epsilon}{|\mathbf{v}_i|}, \left(\frac{\epsilon}{|\mathbf{a}_i|}\right)^{1/2}\right], \tag{2}$$

where $\mathbf{v}_i$ is the velocity of particle i, and we take the smallest value of $(\Delta t)_i$ to be the timestep Δt.

2.3 *The cluster halo density profile*

We consider two different types of density profile of the background halo of a cluster, $\rho_{\rm halo}(r)$: the β profile, and the NFW profile.

In the first case, we assume that the dark matter in the background halo follows a similar density distribution as the observed intracluster gas. A single β-model (isothermal) density profile is used for the gas (e.g., King 1962; Cavaliere & Fusco-Femiano 1976; Makino *et al.* 1998),

$$\rho_{\rm gas}(r) = \rho_0 \left[1 + \left(\frac{r}{r_c}\right)^2\right]^{-3\beta/2}, \tag{3}$$

where ρ_0 is the central density and r_c is the core radius. The values of ρ_0, r_c and β are taken from Piffaretti & Kaastra (2006), which give the gas density parameters for 16 nearby clusters. The halo density is then obtained by scaling the gas density with the universal ratio of matter (dark + baryonic) to baryons, $\rho_{\rm halo} = \rho_{\rm DM} + \rho_{\rm gas} = \rho_{\rm gas}\Omega_M/\Omega_b$, where Ω_M and Ω_b are the present matter (baryons + dark matter) density parameter and baryon density parameter, respectively. This assumes that the cluster baryon mass fraction follows the cosmic value of Ω_b/Ω_M, which is expected to be generally true (e.g., White *et al.* 1993; Ettori 2003), although precise estimations of cluster baryon content have shown deviations from the universal value (Gonzalez *et al.* 2007, and references therein).

In the second case, we consider that the distribution of gas and dark matter in the background halo both follow analytical models of the dark matter density having a functional form:

$$\rho_{\rm DM}(r) = \frac{\rho_s}{(r/r_s)(1 + r/r_s)^2} \tag{4}$$

(Navarro *et al.* 1997). Here, ρ_s is a scaling density and r_s is a scale length. The NFW profile is often parametrized in terms of a concentration parameter c. The parameters ρ_s and r_s are then given by:

$$\begin{aligned}\rho_s &= \frac{200c^3\rho_{\rm crit}(z)}{3[\ln(1+c) - c/(1+c)]} \\ &= \frac{25H^2(z)c^3}{\pi G[\ln(1+c) - c/(1+c)]},\end{aligned} \tag{5}$$

$$r_s = \frac{r_{200}}{c}, \tag{6}$$

where $\rho_{\rm crit}(z) = 3H^2(z)/8\pi G$ is the critical density at formation redshift z, and r_{200}, the virial radius, is the radius of a sphere whose mean density is $200\rho_{\rm crit}$ (200 times the critical density of the Universe at the epoch of formation). After scaling, the halo density profile is $\rho_{\rm halo} = \rho_{\rm DM}\Omega_M/(\Omega_M - \Omega_b)$.

Once we have chosen a particular density profile, the density is integrated to get the background cluster halo mass as:

$$M_{\rm halo}(r) = \int_0^r 4\pi x^2 \rho_{\rm halo}(x)dx. \tag{7}$$

This is the mass that enters in the last term of equation (1). Since the density profiles we consider do not have an outer edge where $\rho_{\rm halo} = 0$, we truncate the cluster background

halo at a maximum halo radius $R_{\rm halo}^{\rm max} = 5$ Mpc. Equation (7) is then solved numerically, to build an interpolation table for r in the range $\left[0,\ R_{\rm halo}^{\rm max}\right]$ that is then used by the code.

2.4 *The subgrid physics*

As mentioned in section 1, there can be six possible physical outcomes for our simulated cluster galaxies. In the following subsections, we describe the associated subgrid physics for each mechanism we use in our simulations. The possible outcomes are:

- the galaxy merges with another galaxy (section 2.4.1),
- the galaxy is destroyed by the tidal field of a larger galaxy but the fragments accrete onto that larger galaxy (section 2.4.4),
- the galaxy is destroyed by tides of a larger galaxy and the fragments are dispersed in the intracluster medium (section 2.4.3),
- the galaxy is destroyed by the tidal field of the background halo (section 2.4.3),
- the galaxy survives to the present (i.e., it is not destroyed by any process), and
- the galaxy is ejected from the cluster (section 2.4.5).

We describe our approach of simulating galaxy harassment in section 2.4.2.

2.4.1 *Encounter: Merger*

We simulate a pair of galaxies colliding (or synonymously, having an encounter) and the further consequences (e.g., merging) in the following way. An encounter is accounted for when two galaxies i and j, of radii s_i and s_j, overlap such that the center of the galaxy j is inside the galaxy i. Numerically the criterion is $r_{ij} < s_i$, where $r_{ij} = |\mathbf{r}_i - \mathbf{r}_j|$ is the distance between the centers of the galaxies. If $\mathbf{v}_i$ and $\mathbf{v}_j$ are the velocities of galaxies i and j, the center of mass velocity of the pair is $\mathbf{v}_{\rm cm} = (m_i\mathbf{v}_i + m_j\mathbf{v}_j)/(m_i + m_j)$. The kinetic energy in the center-of-mass rest frame is:

$$K_{ij} = \frac{1}{2}m_i|\mathbf{v}_i - \mathbf{v}_{\rm cm}|^2 + \frac{1}{2}m_j|\mathbf{v}_j - \mathbf{v}_{\rm cm}|^2. \tag{8}$$

The gravitational potential energy of the pair is:

$$W_{ij} = -\frac{Gm_im_j}{r_{ij}}. \tag{9}$$

Even though we are treating each galaxy as a single particle, in reality a galaxy is a gravitationally bound system with an internal kinetic energy and a potential energy, and these energies must be included in the total energy of the interacting pair of galaxies. Considering a galaxy as a bound virialized system its internal energy is:

$$U_i = U_{\rm potential} + U_{\rm kinetic} = \frac{U_{\rm potential}}{2} = -\frac{\zeta Gm_i^2}{2s_i}, \tag{10}$$

where ζ is a geometrical factor which depends on the mass distribution in the galaxies. Throughout this paper, we assume $\zeta = 1$ (see Appendix).

We then compute the total energy of the galaxy pair (in the center of mass frame) as:

$$E_{ij} = K_{ij} + W_{ij} + U_i + U_j. \tag{11}$$

If $E_{ij} \leq 0$, i.e., the system is bound, we then allow the galaxies to merge to form a single galaxy of mass $m_{\rm merge} = m_i + m_j$. To compute its radius, we assume that energy is conserved, hence the total energy E_{ij} in the center-of-mass rest frame is all converted into the internal energy of the merger remnant. Its radius is then computed from equation (10),

$$s_{\rm merged} = -\frac{\zeta G m_{\rm merge}^2}{2U_{\rm merge}} = \frac{\zeta G(m_i + m_j)^2}{2|E_{ij}|}\,. \tag{12}$$

The position and velocity of this merged object are set to those of the center-of-mass values of the galaxy pair before merger, in order to conserve momentum.

2.4.2 *Encounter: Galaxy harassment*

In a high-speed encounter the two interacting galaxies come into contact for a brief amount of time. The galaxies might survive a merger or tidal disruption, but the encounter adds some internal energy into them, making them less bound. We refer to this process as *Galaxy Harassment*. This process has been originally suggested as a possible explanation for the origin of the morphology–density relation in clusters (Moore *et al.* 1996). We incorporate galaxy harassment in our algorithm by increasing the radius (or the internal energy) of a galaxy when it experiences a non-merger encounter. This enlargement makes a galaxy more prone to tidal disruption at the next encounter.

In equation (11), if $E_{ij} > 0$, i.e., the system is not bound, then the galaxies in our simulation do not merge in the collision. Rather a part of the kinetic energy of the galaxies is converted into internal energy, making the collision inelastic. We assume that an equal amount of energy is transfered to each galaxy. Denoting the energy transfered as ΔE, the kinetic energy of the pair decreases by ΔE, while the internal energy of each galaxy increases by $\Delta E/2$. We assume:

$$\frac{\Delta E}{2} = \eta \min(|U_i|, |U_j|)\,, \tag{13}$$

where η is an energy transfer efficiency whose value is taken as $\eta = 0.2$. The internal energies of the two galaxies after the encounter are $U_i^{\rm after} = U_i^{\rm before} + \Delta E/2$ and $U_j^{\rm after} = U_j^{\rm before} + \Delta E/2$, respectively. By choosing $\eta < 1$, we are ensuring that the internal energy of each galaxy remains negative, that is, the transfer of energy does not unbind the galaxies. We recalculate the velocities $\mathbf{v}_i$ and $\mathbf{v}_j$ after collision while conserving momentum, assuming that only the magnitudes of velocity change, the directions remaining the same. We recalculate the size of each galaxy in the pair using equation (12),

$$s_i^{\rm after} = \frac{\zeta G m_i^2}{2|U_i^{\rm after}|}\,, \qquad s_j^{\rm after} = \frac{\zeta G m_j^2}{2|U_j^{\rm after}|}. \tag{14}$$

While allowing a size increase of the galaxies according to equations (12) and (14), we also considered a size cut-off. We assumed that the galaxies could grow only up to a maximum size given by the size of the largest galaxy at the beginning of the simulation.

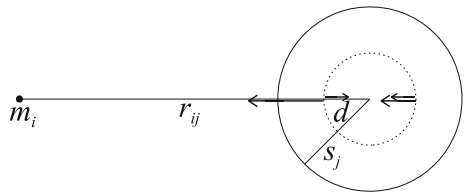

Figure 1. Calculation of the effects of tides caused by a galaxy of mass m_i on a galaxy of mass m_j and radius s_j. The two largest arrows show the gravitational accelerations caused by galaxy i; the two smallest arrows show the accelerations caused by galaxy j. See section 2.4.3 for details.

2.4.3 *Tidal disruption: Intracluster stars*

We consider two possible sources of external gravitation for the tidal disruption of a galaxy j: another galaxy i, or the background cluster halo. The tidal force on a galaxy due to the gravitational field of the external source is meaningful only if the galaxy lies entirely on one side of the external source, when the tides are directed radially outwards tending to tear apart the galaxy. Our calculation of the tidal field caused by a galaxy i of mass m_i is illustrated in Fig. 1. The galaxies i and j are separated by a distance r_{ij}. We calculate the resultant fields between two diametrically opposite points inside galaxy j, located at a radial distance $d \leq s_j$ along the line joining the centers of the two galaxies. The two small and two large arrows in Fig. 1 indicate the gravitational field (or acceleration) at the opposite points caused by galaxy j (self-gravity) and by galaxy i (external source of gravitation), respectively. The magnitude of the tidal field is given by the difference between the gravitational field caused by galaxy i at the two opposite points,[1]

$$a_{\rm tide}^{\rm galaxy} = \frac{Gm_i}{(r_{ij}-d)^2} - \frac{Gm_i}{(r_{ij}+d)^2}. \tag{15}$$

The gravitational field caused by galaxy j (two small arrows in Fig. 1) is directed radially inwards and acts opposite to the tides, tending to keep the galactic mass inside radius d intact. The difference between that self-gravitational field at the two opposite points is:

$$a_{\rm grav} = \frac{2Gm_j(d)}{d^2}, \tag{16}$$

where $m_j(d)$ is the mass of galaxy j inside radius d. When $a_{\rm tide}^{\rm galaxy} = a_{\rm grav}$, then the tides will exceed self-gravity at radii larger than d, while self-gravity will exceed the tides at smaller radii. Thus the layers of galactic mass located between radii d and s_j would become unbound, while the ones located inside radius d would remain bound. Hence, the galaxy would be partly disrupted. In our code, we simplify things by using an 'all-or-nothing' approach. A galaxy is either totally disrupted, or not disrupted at all. We consider that a galaxy is disrupted if half of its mass or more becomes unbound. If we assume an isothermal sphere density profile (as in Appendix), then the half-mass

[1]This reduces to the well-known form $a_{\rm tide}^{\rm galaxy} \propto d/r_{ij}^3$ in the limit $d \ll r_{ij}$, but we do not make this approximation here.

radius is given by $d = s_j/2$. This is the value of d we use in equations (15) and (16). The criterion of tidal destruction then becomes $a_{\rm tide}^{\rm galaxy}(d) \geq a_{\rm grav}(d)$, with $d = s_j/2$.

We also consider tidal disruption by the background cluster halo, but only if $r_j > s_j$ (that is, the galaxy does not overlap with the center of the halo). The magnitude of tidal field due to the cluster halo is:

$$a_{\rm tide}^{\rm halo} = \frac{GM_{\rm halo}(r_j - d)}{(r_j - d)^2} - \frac{GM_{\rm halo}(r_j + d)}{(r_j + d)^2}\,, \tag{17}$$

where $M_{\rm halo}(r)$ is given by equation (7). If $a_{\rm tide}^{\rm halo}(d) \geq a_{\rm grav}(d)$, with $d = s_j/2$, galaxy j is tidally destroyed by the gravitational field of the halo.

When galaxy j is considered to have been tidally destroyed by another galaxy i, the fragments of the disrupted galaxy might accrete onto galaxy i (section 2.4.4), or they might be dispersed into the ICM when $E_{ij} > 0$ (E_{ij} being the total energy of the galaxy pair given by equation 11). For tidal destruction by the cluster halo the disrupted fragments are always dispersed into the ICM. In both cases, the destroyed galaxy is removed from the list of existing particles. The code keeps track of the amount of mass added to the ICM (in the form of IC stars) by tidal disruption. This quantity is initialized to zero at the beginning of the simulation, and every time a galaxy is tidally destroyed with its fragment dispersed, the mass of that galaxy is added up to the total mass added to the ICM.

2.4.4 *Tidal disruption: Accretion*

We consider a possibility of accretion of the fragments of a tidally disrupted galaxy onto the galaxy causing the tides. This happens for the case of tidal disruption due to galaxies only (if the disruption is caused by the background cluster halo, the fragments are always dispersed as IC stars). This situation occurs when the conditions $a_{\rm tide}^{\rm galaxy} > a_{\rm grav}$ and $E_{ij} \leq 0$ are both satisfied (see section 2.4.3). The tidally disrupted galaxy accretes onto the more massive galaxy. The mass of the bigger galaxy increases from m_i to $m_i + m_j$. Thus a tidal disruption followed by accretion is similar to a merger (section 2.4.1), but these events are counted separately.

2.4.5 *Ejection*

When a galaxy ventures at distances larger than the cluster halo truncation radius $R_{\rm halo}^{\rm max}$ (see section 2.3), we consider that this galaxy has escaped from the cluster, and we remove it from the list. If we kept that galaxy, it might eventually return to the cluster. But in reality the universe contains many clusters, and a galaxy that moves sufficiently far away from one cluster will eventually feel the gravitational influence of other clusters, something that our algorithm, which simulates an isolated cluster, does not take into account. As we shall see, the ejection of galaxies from a cluster is quite uncommon in our simulations.

3. The simulations

3.1 *Cosmological model*

We consider a ΛCDM model with the present matter density parameter, $\Omega_M = 0.241$, baryon density parameter, $\Omega_b = 0.0416$, cosmological constant, $\Omega_\Lambda = 0.759$, Hubble

constant, $H_0 = 73.2\,\mathrm{km\,s^{-1}Mpc^{-1}}$ ($h = 0.732$), primordial tilt, $n_s = 0.958$, and CMB temperature, $T_{\mathrm{CMB}} = 2.725\,\mathrm{K}$, consistent with the results of *WMAP3* (Spergel *et al.* 2007). Even though the simulations presented in this paper are not 'cosmological' (we simulate isolated, virialized clusters), the particular choice of cosmological model enters the picture twice: in the determination of the radii of galaxies (see next section), and in the calculation of the elapsed time between the initial and final redshifts of the simulation.

In each simulation a cluster is evolved from $z = 1$ to the present ($z = 0$). We assume that the cluster will not experience any major merger during this period, and that, therefore, it is a good approximation to treat it as isolated. For our ΛCDM model, this represents a total evolutionary time of 7.63 Gyr.

3.2 *Initial conditions*

To set the initial conditions of our simulations, we need to determine the initial mass m, radius s, position $\mathbf{r}$, and velocity $\mathbf{v}$ of each galaxy. To determine the mass, we first assume that the luminosities of galaxies are distributed according to the Schechter luminosity function (Schechter 1976),

$$\phi(L)dL = \phi^* \left(\frac{L}{L^*}\right)^{\alpha} e^{-L/L^*} \frac{dL}{L^*}\,. \tag{18}$$

Here we use $L^* = 3.097 \times 10^{10}\,\mathrm{L_\odot}$ (corresponding to absolute magnitude $M^*_{b_J} = -20.07$), and $\alpha = -1.28$, which is appropriate for galaxies located in clusters (De Propris *et al.* 2003). This luminosity function spans over $-22.5 < M_{b_J} < -15$. While it might be reasonable to assume fixed values of L^* and α, the value of ϕ^* most likely varies amongst clusters. So we normalize equation (18) by imposing that, in each cluster, there are N_0 galaxies with luminosities $L > L_0$. We use $N_0 = 25$, and $L_0 = 0.2L^*$ (corresponding to $M_b = -19$) (Lewis *et al.* 2002). We select the luminosities using a Monte Carlo rejection method. We then assume a constant mass-to-light ratio $\Upsilon = 193\,\mathrm{h\ M_\odot/L_\odot} = 73$ (Brainerd & Specian 2003), and convert the luminosities to masses. The Schechter function spans up to a maximum mass $M_{\mathrm{max}} = 220 \times 10^{11}\mathrm{M_\odot}$. To generate the dwarf galaxies, the same Schechter function is extrapolated up to a minimum mass $M_{\mathrm{min}} = 1 \times 10^{9}\mathrm{M_\odot}$.

We take the radius s of each galaxy to be equal to the virial radius r_{200} (radius containing matter with 200 times the mean density of the Universe at the epoch of galaxy formation) corresponding to the galaxy mass $m = M_{200}$ using:

$$M_{200} = \frac{800\pi}{3} r_{200}^3 \bar{\rho} (1 + z_{\mathrm{coll}})^3. \tag{19}$$

Here, $\bar{\rho} = \rho_{\mathrm{crit}}\Omega_M = 3H_0^2\Omega_M/8\pi G$ is the mean matter density in the present universe, and z_{coll} is the redshift of collapse when the galaxy formed. To obtain z_{coll}, we use a simple spherical collapse model. First, by filtering the power spectrum for our ΛCDM model, we calculate the standard deviation $\sigma(m)$ of the linear density contrast $\delta = (\rho - \bar{\rho})/\bar{\rho}$ at the mass scale m. The distribution of the values of δ is then given by a Gaussian,

$$\mathcal{P}(\delta) \propto \exp\left(-\frac{\delta^2}{2\sigma^2}\right). \tag{20}$$

We pick randomly a present density contrast $\delta_0 = \delta(z = 0)$ from this distribution, using a Monte Carlo rejection method, and solve the following equation to get the collapse redshift $z_{\rm coll}$,

$$\Delta_c = \delta_0 \frac{\delta_+(z_{\rm coll})}{\delta_+(0)}\,, \tag{21}$$

where $\delta_+(z)$ is the linear growing mode (for $\Lambda \neq 0$ models, see, e.g., Martel 1991). Here, $\Delta_c = 3(12\pi)^{2/3}/20 = 1.686$ is the overdensity predicted by linear theory at recollapse. In the Monte Carlo method, we ensure that the galaxy collapse redshift is higher than $z = 1$, the redshift at which the cluster is considered to have been assembled (section 3.1), i.e., $z_{\rm coll} > 1$. We solve this equation numerically for $z_{\rm coll}$, and substitute the solution in equation (19), which we then solve to get the radius $s = r_{200}$.

To determine the locations of galaxies inside a cluster, we assume that their distribution is isotropic (in a statistical sense). We can therefore choose the spherical coordinates (θ, ϕ) of each galaxy randomly, using $\phi = 2\pi X_\phi$, and $\cos\theta = 2X_\theta - 1$, where X_ϕ and X_θ are random numbers drawn from a uniform deviate between 0 and 1. We still need to determine the radial co-ordinate r. Using the CNOC cluster survey, Carlberg *et al.* (1997) showed that the radial mass density $\rho(r)$ of matter and the radial number density $\nu(r)$ of galaxies are roughly proportional to each other, where both $\rho(r)$ and $\nu(r)$ are approximated by NFW profiles. Girardi *et al.* (1998) found that the halo mass follows the galaxy distribution in clusters, using a β-model for the halo/galaxy volume density profile. We assume that this proportionality holds for all clusters, and we generalize it to all the density profiles we use. Thus, the assumed background halo mass density profile (equations 3 and 4) gives us $\nu(r)$. We can then select the initial distances r from the cluster center using again a Monte Carlo rejection method. Since the masses and locations of the galaxies have been determined separately, we need to pair them, i.e., for each selected location, to decide which galaxy goes there. We do expect the most massive galaxies to reside near the center of the cluster. However, low-mass galaxies are not all located at large radii, and some of them might be located in the central region of the cluster as well. Indeed, if the galaxies in the central region were all massive, it would be impossible to reproduce the desired number density profile $\nu(r)$ and not have the galaxies overlap.

To prevent any overlap, we locate the galaxies as follows: We first position the most massive galaxy at the center of the cluster. Then we locate the next seven most massive galaxies between radii R_0 and $2R_0$, where R_0 is three times the radius of the most massive galaxy. We then locate the next 19 most massive galaxies between radii $2R_0$ and $3R_0$. Finally, the remaining galaxies are located randomly between radii 0 and $3R_0$. During the process we check that the galaxies do not overlap, by ensuring that the distance between the edges of two galaxies is greater than the radius of the larger galaxy, i.e., $r_{ij} - s_i - s_j > \max(s_i, s_j)$. In the process of locating a galaxy, if this criterion is not satisfied, we simply reject that location and generate a new one.

After assigning the masses, radii, and positions of all the galaxies, we determine the velocity of each galaxy. We consider the velocity a galaxy would have if it were in a perfect circular orbit at radius r,

$$v_{\rm circ}(r) = \left[\frac{G}{r}\left(M_{\rm halo}(r) + \sum_{j,\, r_j < r} m_j\right)\right]^{1/2}\,, \tag{22}$$

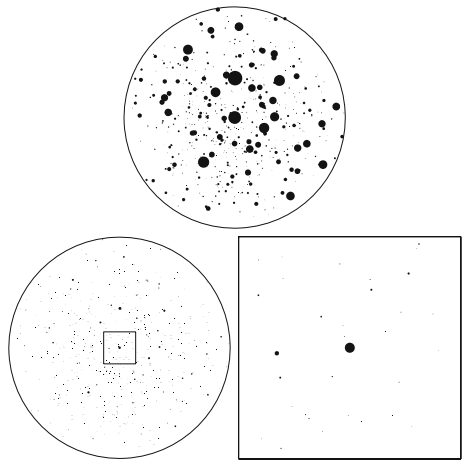

Figure 2. Initial conditions for run A12. Top panel: initial conditions at $z = 1$. The solid circles indicate the virial radii of galaxies. The large circle is the maximum distance $r = 3R_0 = 2.08$ Mpc from the cluster center. Lower left panel: same as top panel, with symbols rescaled to optical diameter of real galaxies. Bottom right panel: enlargement of the central $(0.6\,\mathrm{Mpc})^2$ (box on lower-left panel).

where the sum only includes galaxies inside radius r. The norm of the velocity is chosen by giving a random 10% deviation to the circular velocity, i.e., $v = v_{\mathrm{circ}}(1 + 0.1X_v)$, where X_v is a random number between -1 and 1. For the direction of the velocity, we follow a similar random angle generation technique as we did for the positions of galaxies.

Figure 2 illustrates the initial conditions for one of our simulations (run A12). The top panel shows the cluster at $z = 1$. The large circle represents the maximum distance $3R_0$ within which the galaxies are located initially. Each dot represents a galaxy, with the most massive one located in the center. Even though massive galaxies tend to be larger, there is no direct correspondence between the masses and radii because of the dependence on z_{coll} in equation (19), whose determination involves a Monte Carlo method.

Visually, this looks quite different from the optical pictures of actual clusters like Virgo. This is because each dot has a radius s equal to the virial radius r_{200}, that can exceed the optical radius by an order of magnitude. In the bottom left panel of Fig. 2, we show the same cluster, with all the dots rescaled in size so that the angular diameter of the central galaxy is equal to $8.3'$ at a distance of 16.8 Mpc, which is the observed optical diameter of M87. The bottom right panel shows a zoom-in of the central cluster region. It looks qualitatively similar to pictures of the central region of Virgo.

4. Results

We started by performing 10 series of simulations, for a total of 148 simulations. Table 1 summarizes the characteristics of each series. The first 2 columns show the series name and the number of runs, respectively. The slope of the Schechter luminosity function at $z = 1$ (used to generate the initial conditions) is listed in column 3. Columns 4 to 8 give the characteristics and relevant parameter values of the background cluster halo

Table 1. Series of simulations.

Series (col. 1)	Runs (col. 2)	$\alpha_{\rm start}$ (col. 3)	Profile (col. 4)	β (col. 5)	ρ_0, ρ_s [g cm^{-3}] (col. 6)
A	16	-1.28	β-Virgo	0.33	8.14×10^{-26}
B	17	-1.28	β-Virgo	0.33	8.14×10^{-26}
C	17	-1.36	β-Virgo	0.33	8.14×10^{-26}
D	16	-1.36	β-Virgo	0.33	8.14×10^{-26}
E	16	-1.36	β-Perseus	0.53	7.27×10^{-26}
F	16	-1.36	β-Perseus	0.53	7.27×10^{-26}
G	10	-1.28	NFW	···	2.35×10^{-25}
H	14	-1.31	NFW	···	2.35×10^{-25}
I	10	-1.31	NFW	···	2.35×10^{-25}
J	16	-1.36	β-Perseus	0.53	7.27×10^{-26}

	c (col. 7)	r_c, r_s [kpc] (col. 8)	cD (col. 9)	Harassment (col. 10)	Cluster-growth (col. 11)
A	···	3	×	×	×
B	···	3	×	√	×
C	···	3	×	√	×
D	···	3	√	√	×
E	···	28	×	√	×
F	···	28	√	√	×
G	5	200	×	√	×
H	5	200	×	√	×
I	5	200	√	√	×
J	···	28	×	√	√

profile. Columns 9 and 10 indicate respectively whether a cD galaxy was included in the cluster simulation, and whether galaxy harassment was included as part of the subgrid physics. Column 11 shows if we included cluster mass growth of the simulated cluster.

4.1 *Series A: Initial simulations*

We performed an initial series of 16 simulations, using for the background halo a β-profile with $\beta = 0.33$, a core radius $r_c = 3\,$kpc, and a central density $\rho_0 = 8.14 \times 10^{-26}\,$g cm^{-3}, which is appropriate for a cluster like Virgo (Piffaretti & Kaastra 2006). For this series, we did not include galaxy harassment. Our results are shown in Table 2. It shows the run number (column 1), and at the beginning of the run, the total mass $M_{\rm total}$ in galaxies, in units of $10^{11}\,{\rm M}_\odot$ (column 2), the number of galaxies $N_{\rm total}$ (column 3), and the Schechter luminosity function (equation 18) exponent $\alpha_{\rm start}$ (column 12). This exponent was obtained by performing a numerical fit to the distribution of galaxy masses. Because the masses were determined from a Monte

Table 2. Simulations for series A.

Run	$M_{\rm total}$ [10^{11}M$_\odot$]	$N_{\rm total}$	$N_{\rm merge}$	$N^{\rm gal}_{\rm tides}$	$N_{\rm accr}$	$N^{\rm halo}_{\rm tides}$	$N_{\rm eject}$	$f_{\rm surv}$	f_M	$f_{\rm ICS}$	$\alpha_{\rm start}$	$\alpha_{\rm end}$
A1	855.0	440	137	54	6	0	1	0.550	0.225	0.235	−1.26	−1.23
A2	862.0	702	343	182	24	0	1	0.217	0.490	0.522	−1.28	−1.12
A3	1100.4	480	126	43	7	0	0	0.633	0.136	0.161	−1.28	−1.24
A4	831.0	530	165	67	11	0	0	0.542	0.148	0.161	−1.26	−1.15
A5	980.4	459	175	58	8	0	1	0.473	0.128	0.144	−1.25	−1.18
A6	967.8	640	230	74	5	0	0	0.517	0.157	0.182	−1.29	−1.23
A7	720.0	579	263	114	7	0	0	0.337	0.359	0.384	−1.28	−1.20
A8	757.8	435	200	66	51	0	1	0.269	0.320	0.346	−1.27	−1.26
A9	925.6	514	223	83	12	0	1	0.379	0.245	0.273	−1.28	−1.17
A10	858.9	525	204	54	8	0	0	0.493	0.257	0.260	−1.31	−1.24
A11	880.2	547	224	68	9	0	1	0.448	0.257	0.278	−1.33	−1.25
A12	826.1	548	255	72	15	0	1	0.374	0.225	0.249	−1.29	−1.18
A13	1041.5	431	166	51	6	0	0	0.483	0.275	0.282	−1.27	−1.25
A14	957.3	486	174	52	4	0	0	0.527	0.261	0.265	−1.29	−1.22
A15	860.5	520	160	64	15	0	1	0.538	0.260	0.260	−1.26	−1.18
A16	858.0	483	255	72	8	0	0	0.306	0.323	0.337	−1.28	−1.19

Carlo rejection method, the exponent can differ from the intended value $\alpha = -1.28$ in equation (18) and listed in Table 1, but the deviations are small. Averaging over all runs, we get $\alpha_{\rm start} = -1.280 \pm 0.020$.

Columns 4–8 in Table 2 show the number of galaxies $N_{\rm merge}$ destroyed by mergers, the number of galaxies $N_{\rm tides}^{\rm gal}$ destroyed by tides caused by a massive galaxy, with the fragments dispersed in the ICM, the number of galaxies $N_{\rm accr}$ destroyed by tides caused by a massive galaxy, with the fragments being accreted onto that galaxy, the number of galaxies $N_{\rm tides}^{\rm halo}$ destroyed by the tidal field of the background halo, and the number of galaxies $N_{\rm eject}$ ejected from the cluster, respectively. Column 9 shows the fraction by numbers of galaxies $f_{\rm surv}$ that survive to the present.

We did not find a single occurrence of a galaxy destroyed by tides from the background halo, and the number of galaxies ejected is either 0 or 1. There are large variations in the other numbers from one run to the next, but some trends are apparent. Typically, 50% to 60% of the galaxies are destroyed. Run A2 is an extreme case, with 78% of the galaxies being destroyed. The destruction of galaxies by mergers dominates over the destruction by tides, by more than a factor of 2 except for run A7. If we treat the cases of tidal disruption followed by accretion as being mergers, then mergers dominate even more over tidal disruption. When galaxies are destroyed by tides, the dispersion of fragments into the ICM always dominates over the accretion of fragments onto the massive galaxy, but the ratio varies widely, from 114:7 in run A7 to 66:51 in run A8.

We evaluate the mass fraction $f_{\rm M}$ of galaxies contributing to the intracluster stars,

$$f_{\rm M} = \frac{M_{\rm tides}^{\rm gal} + M_{\rm tides}^{\rm halo}}{M_{\rm total} - M_{\rm eject}}\,, \tag{23}$$

where the letter M refers to the mass in galaxies, rather than their number. The galactic mass contribution to the ICM consists of galaxies destroyed by tides of another more massive galaxy, and by tides of the background halo (though there are no such cases in this series). Column 10 of Table 2 lists the values of $f_{\rm M}$.

We use a mass-dependent mass-to-light ratio of the galaxies having the form (ΛCDM cosmological simulations of Yang *et al.* 2003)

$$\left\langle \frac{M}{L} \right\rangle (M) = \frac{1}{2} \left(\frac{M}{L} \right)_0 \left[\left(\frac{M}{M_1} \right)^{-\gamma_1} + \left(\frac{M}{M_1} \right)^{\gamma_2} \right]. \tag{24}$$

The values of the free parameters are taken as $M_1 = 10^{11.27} h^{-1}{\rm M}_\odot$, $(M/L)_0 = 134\, h{\rm M}_\odot/{\rm L}_\odot$, $\gamma_1 = 0.77$, $\gamma_2 = 0.32$, which are for the best-fitting model of Yang *et al.* (2003) for concordance cosmology. The galaxy masses are converted to luminosities using the mass-to-light ratio. We then calculate the fraction $f_{\rm ICS}$ of the total luminosity of the cluster that comes from intracluster stars,

$$f_{\rm ICS} = \frac{L_{\rm tides}^{\rm gal} + L_{\rm tides}^{\rm halo}}{L_{\rm total} - L_{\rm eject}}\,. \tag{25}$$

The values of $f_{\rm ICS}$ are listed in column 11 of Table 2. Again, there are large variations. In particular, the fraction is very large for run A2, and very small for run A5. Averaging over all runs, we get $f_{\rm ICS} = 0.271 \pm 0.095$. Even though, in most cases about half the

number of galaxies are destroyed, they tend to be low-mass galaxies, which explains why $f_{\rm ICS} < 1 - f_{\rm surv}$, for all the runs.

The galaxies being destroyed by mergers and tides, or escaping are mostly low-mass galaxies. This leads to a flattening of the galaxy mass distribution function. We computed the best numerical fit to the Schechter luminosity function exponent α (equation 18) for the surviving galaxies at the end of the simulations. This is listed as $\alpha_{\rm end}$ in column 13 of Table 2. Averaging over all runs, we get $\alpha_{\rm end} = -1.206 \pm 0.040$.

4.2 *Series B: Turning on harassment*

We modified the algorithm to include the effect of galaxy harassment (see section 2.4.2), and rerun the calculations of series A with the same initial conditions. We also added one more run, B17. The results are shown in Table 3, which follows the same format as Table 2. Comparing with series A, the number of galaxies destroyed by mergers is very similar, but the number of galaxies destroyed by tides tends to be significantly higher. For instance, it goes from 67 to 94 for runs A4–B4, and from 64 to 86 for runs A15–B15. This is because, when a galaxy is subjected to harassment, its binding energy is reduced, and it becomes more prone to experience tidal disruption later. But the number of tidal disruptions followed by accretion does not change significantly. Hence, the additional, tidally-disrupted galaxies almost all contribute to the intracluster stars. The values of $f_{\rm ICS}$ are therefore increased relative to series A. The mean value is $f_{\rm ICS} = 0.288 \pm 0.082$.

This is not significantly larger than for series A. The additional galaxies destroyed are mostly low-mass galaxies. We also recalculated the best-fit Schechter exponent α for the surviving galaxies at $z = 0$. The mean value for the runs in this series is $\alpha_{\rm end} = -1.207 \pm 0.048$.

Figure 3 shows the total galaxy counts in mass bins, obtained by combining all the runs in series B, along with the fitting curves to a Schechter distribution function (equation 18). The best fit Schechter exponent for the initial galaxy distribution (the upper curve at $z = 1$) is $\alpha = -1.28$, and for the final surviving galaxy distribution (the lower curve at $z = 0$) is $\alpha = -1.20$. These values of α were obtained by performing the numerical Schechter function fits on the combined set of galaxies taken from all the 17 runs in this series, which amounts to 8770 initial galaxies at $z = 1$ and 3614 surviving galaxies at $z = 0$.

Clearly from Fig. 3, the fit at $z = 0$ (lower curve) is excellent. This shows that, in our simulations, a Schechter mass (luminosity) distribution function at $z = 1$ remains a Schechter distribution all the way to $z = 0$, though half of the galaxies are destroyed. Only the slope α changes with time.

4.3 *Series C: Steeping up the mass distribution function*

In the simulations of series A and B, the Schechter exponent α evolves from $\alpha \simeq -1.28$ at $z = 1$ to $\alpha \simeq -1.21$ at $z = 0$. Analyzing the combined set of galaxies of all the 17 runs in series B, we obtained the best fit Schechter exponent for the surviving galaxy distribution at $z = 0$ as $\alpha = -1.20$. This is a problem, since the value of $\alpha = -1.28$ is based on observations of nearby clusters (De Propris *et al.* 2003), and should be valid for clusters of galaxies at $z = 0$, whereas we used the same $\alpha = -1.28$ to start our simulations at $z = 1$, and it flattened to $\alpha = -1.20$ at $z = 0$. Ryan *et al.* (2007)

Table 3. Simulations for series B.

Run	$M_{\rm total}$ $[10^{11}{\rm M}_{\odot}]$	$N_{\rm total}$	$N_{\rm merge}$	$N_{\rm tides}^{\rm gal}$	$N_{\rm accr}$	$N_{\rm tides}^{\rm halo}$	$N_{\rm eject}$	$f_{\rm surv}$	f_M	$f_{\rm ICS}$	$\alpha_{\rm start}$	$\alpha_{\rm end}$
B1	855.0	440	134	62	6	0	1	0.539	0.237	0.248	−1.26	−1.24
B2	862.0	702	337	210	25	0	1	0.184	0.454	0.486	−1.28	−1.11
B3	1100.4	480	126	48	7	0	0	0.623	0.139	0.162	−1.28	−1.24
B4	831.0	530	159	94	12	0	0	0.500	0.184	0.202	−1.26	−1.15
B5	980.4	459	171	78	7	0	1	0.440	0.154	0.175	−1.25	−1.21
B6	967.8	640	226	85	6	0	0	0.505	0.173	0.199	−1.29	−1.23
B7	720.0	579	249	134	9	0	0	0.323	0.364	0.386	−1.28	−1.20
B8	757.8	435	172	79	62	0	1	0.278	0.271	0.293	−1.27	−1.27
B9	925.6	514	223	100	12	0	1	0.346	0.270	0.298	−1.28	−1.19
B10	858.9	525	206	68	7	0	0	0.465	0.298	0.311	−1.31	−1.25
B11	880.2	547	233	85	9	0	1	0.400	0.280	0.301	−1.33	−1.27
B12	826.1	548	241	92	19	0	1	0.356	0.240	0.265	−1.29	−1.20
B13	1041.5	431	160	58	4	0	0	0.485	0.269	0.274	−1.27	−1.26
B14	957.3	486	173	59	5	0	0	0.512	0.274	0.279	−1.29	−1.22
B15	860.5	520	155	86	17	0	1	0.502	0.277	0.278	−1.26	−1.19
B16	858.0	483	264	90	6	0	0	0.255	0.354	0.374	−1.28	−1.16
B17	792.6	451	178	83	16	0	1	0.384	0.346	0.359	−1.24	−1.13

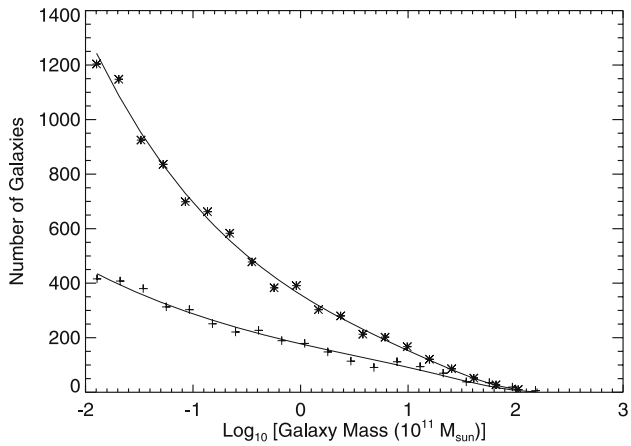

Figure 3. Mass distribution function for galaxies in series B, obtained by adding the numbers for all runs. Results are plotted for initial 8770 galaxies at $z = 1$ (asterisks) and surviving 3614 galaxies at $z = 0$ (plus signs). The curves show the best fit of a Schechter distribution function (equation 18), with $\alpha = -1.28$ at $z = 1$ (upper curve), and $\alpha = -1.20$ at $z = 0$ (lower curve).

recently determined the luminosity function of a large sample of galaxies at $z \simeq 1$, and concluded that there is a steepening of the faint-end slope with redshift, which is expected in the hierarchical formation scenario of galaxies. They obtained a value of the faint-end slope $\alpha = -1.32 \pm 0.07$ at $z = 1$.

In our simulations we take into account this flattening of the luminosity function over time as explained. The results of series A and B suggest that $|\alpha|$ decreases by ~ 0.08 between $z = 1$ and $z = 0$. Using this as a guide, we performed a new series of simulations, series C, using $\alpha_{\rm start} = -1.36$, with the hope that this value will evolve toward something close to $\alpha = -1.28$ at $z = 0$. The results are shown in Table 4. The average values of α are $\alpha_{\rm start} = -1.357 \pm 0.021$ and $\alpha_{\rm end} = -1.272 \pm 0.050$.

A plot analogous to Fig. 3 showed that at $z = 0$, a Schechter distribution function is still a good approximation to the mass distribution. The value of $\alpha_{\rm end}$ is close enough to our target value of -1.28. So from now on, in all subsequent series with the β model halo density profile, we will use an initial α of -1.36, as shown in Table 1. This value is well inside the range obtained by Ryan *et al.* (2007).

Using a steeper galaxy distribution while still requiring that the clusters contain 25 galaxies with $L > 0.2L_*$ (initial conditions in section 3.2) results in the initial number of galaxies being larger by a factor of about 2 (column 3 of Table 4). But the numbers of galaxies destroyed by mergers and tides are also higher relative to series B. As a result the trends are similar. In particular, mergers still dominate over tides by more than a factor of 2.

The run C1 has a larger number of galaxies ejected from the cluster. This is because the most massive galaxy, located at the center of the cluster, was particularly large. Its radius was $s = 385$ kpc, compared to $s < 300$ kpc for the other runs. This increased the value of R_0 (see section 3.2) used for setting up the initial conditions. As a result, more galaxies were located at larger radii, where they are more likely to escape. The mean value of $f_{\rm ICS}$ for this series is $f_{\rm ICS} = 0.302 \pm 0.088$.

Table 4. Simulations for series C.

Run	$M_{\rm total}$ $[10^{11}{\rm M}_\odot]$	$N_{\rm total}$	$N_{\rm merge}$	$N_{\rm tides}^{\rm gal}$	$N_{\rm accr}$	$N_{\rm tides}^{\rm halo}$	$N_{\rm eject}$	$f_{\rm surv}$	f_M	$f_{\rm ICS}$	$\alpha_{\rm start}$	$\alpha_{\rm end}$
C1	1144.3	948	322	123	13	0	7	0.509	0.162	0.179	−1.34	−1.27
C2	1009.9	936	283	138	19	0	1	0.529	0.195	0.218	−1.38	−1.30
C3	914.2	603	316	97	13	0	0	0.294	0.265	0.297	−1.35	−1.24
C4	970.5	635	162	86	11	0	1	0.591	0.216	0.227	−1.32	−1.28
C5	935.9	672	250	101	7	0	1	0.466	0.158	0.175	−1.33	−1.25
C6	948.2	1136	502	268	6	0	0	0.317	0.318	0.337	−1.35	−1.21
C7	926.4	884	276	155	10	0	1	0.500	0.258	0.270	−1.35	−1.28
C8	818.4	696	347	142	62	0	1	0.207	0.423	0.443	−1.35	−1.26
C9	875.9	903	421	255	44	0	1	0.202	0.405	0.416	−1.34	−1.19
C10	1110.5	785	286	100	20	0	1	0.482	0.168	0.190	−1.39	−1.39
C11	864.2	809	338	139	18	0	1	0.387	0.386	0.405	−1.40	−1.36
C12	1053.2	978	395	212	29	0	0	0.350	0.294	0.303	−1.36	−1.29
C13	1151.7	790	344	127	24	0	1	0.372	0.262	0.282	−1.37	−1.29
C14	876.8	684	335	133	23	0	1	0.281	0.320	0.341	−1.37	−1.21
C15	788.0	769	240	140	27	0	0	0.471	0.243	0.263	−1.35	−1.26
C16	905.1	578	284	80	24	0	1	0.327	0.430	0.434	−1.36	−1.29
C17	889.2	822	325	169	13	0	0	0.383	0.323	0.347	−1.36	−1.25

4.4 *Series D: Adding a cD galaxy*

A cD (*central dominant*) galaxy is a very bright supergiant elliptical galaxy with an extended envelope (or a *diffuse* halo) found at the center of a cluster (Schombert 1988). Several galaxy clusters have been found to have cD galaxies at their centers (e.g., Quintana & Lawrie 1982; Oegerle & Hill 2001; Jordan *et al.* 2004). We performed some simulations by incorporating a cD galaxy in the clusters. Being the brightest and most massive cluster galaxy, the mass of a cD is larger than the prediction of the normal Schechter distribution function (equation 18). So we introduced the cD galaxy manually at our simulated cluster center. We adopted a luminosity of $L_{\rm cD} = 10L^*$, which is a canonical value for a cD. Using a constant mass to light ratio ($\Upsilon = 193\,{\rm h}\,{\rm M}_\odot/{\rm L}_\odot$, section 3.2), this corresponds to a cD galaxy mass of $M_{\rm cD} = 437.6 \times 10^{11}{\rm M}_\odot$. When we wanted a cD galaxy present in the simulation we changed the mass of the cluster central galaxy (see sectoin 3.2) to the cD mass, $M_{\rm cD}$. This allowed us to keep the appropriate initial galaxy distribution for a cluster while incorporating a cD galaxy at rest, located at the center.

We performed simulations by adding a cD galaxy to our Virgo-like cluster, and called it series D. The results are listed in Table 5, from which certain trends are clear after incorporating a cD galaxy in the simulation. The total galaxy mass increases since a massive cD galaxy is being added. More prominent than in the previous series A, B, and C, here galaxy mergers outnumber tides by factors $\sim$ 2–3, which go as high as 4 in run D12.

A striking new feature in cases incorporating a cD galaxy is the increase in the number of accretions after tidal disruption by a galaxy, fully 1/4 of the galaxies being acreted in run D5. Since in these accretions, the smaller galaxy is tidally destroyed and is absorbed (or merged) by the massive galaxy (section 2.4.4), it appears, in our simulated clusters, that in the presence of a cD galaxy the number of effective mergers is very high.

The luminosity fraction imparted to ICS has decreased in all the runs, with a value as low as 0.085 in run D6. To explain such a result, we note that the most massive central galaxy (cD or otherwise) in our simulated cluster is never destroyed because of its large mass. In an encounter, it is normally the lower-mass galaxy that gets destroyed. Also the initial conditions of the most massive galaxy (at rest at the center, see section 3.2) make it less likely to be destroyed by the tidal field of the halo. If the central galaxy is a cD, a large mass fraction (as high as 38% in run D11) is locked into it, which can never contribute to the ICS. So a smaller mass fraction is available to be transferred to the ICS, which eventually leads to a decrease in $f_{\rm ICS}$. The mean value of $f_{\rm ICS}$ for series D is $f_{\rm ICS} = 0.161 \pm 0.047$.

4.5 *Series E & F: Other β profiles*

In the next two series of runs, we consider a different background halo. We use a β-profile with $\beta = 0.53$, a core radius $r_c = 28\,{\rm kpc}$ and a central density $\rho_0 = 7.27 \times 10^{-26}\,{\rm g\,cm^{-3}}$, which is appropriate for a cluster like Perseus (Piffaretti & Kaastra 2006). Series E and F do not include, and include a cD galaxy, respectively (hence series E should be compared with series C, and series F with series D).

The results for series E are shown in Table 6. The most notable feature is that some galaxies are destroyed by the tidal field of the background halo, something

Table 5. Simulations for series D.

Run	$M_{\rm total}$ [10^{11}M$_\odot$]	$N_{\rm total}$	$N_{\rm merge}$	$N_{\rm tides}^{\rm gal}$	$N_{\rm accr}$	$N_{\rm tides}^{\rm halo}$	$N_{\rm eject}$	$f_{\rm surv}$	f_M	$f_{\rm ICS}$	$\alpha_{\rm start}$	$\alpha_{\rm end}$
D1	1394.6	1023	345	165	83	0	0	0.420	0.127	0.160	−1.38	−1.33
D2	1374.4	866	330	97	37	0	1	0.463	0.085	0.113	−1.38	−1.33
D3	1431.1	906	257	199	187	0	0	0.290	0.125	0.156	−1.39	−1.32
D4	1163.2	754	211	152	120	0	0	0.359	0.117	0.156	−1.33	−1.26
D5	1239.5	788	283	167	197	0	0	0.179	0.167	0.213	−1.33	−1.21
D6	1158.8	527	131	59	53	0	1	0.537	0.065	0.085	−1.34	−1.30
D7	1300.7	663	236	85	73	0	1	0.404	0.151	0.204	−1.37	−1.31
D8	1298.4	773	296	113	116	0	0	0.321	0.120	0.159	−1.36	−1.33
D9	1299.5	652	256	95	63	0	1	0.364	0.141	0.186	−1.39	−1.33
D10	1169.4	589	193	76	67	0	1	0.428	0.106	0.143	−1.37	−1.32
D11	1145.8	741	282	143	79	0	1	0.318	0.124	0.157	−1.38	−1.25
D12	1227.5	732	235	57	22	0	9	0.559	0.075	0.099	−1.39	−1.35
D13	1334.2	952	330	166	70	0	0	0.406	0.151	0.199	−1.35	−1.31
D14	1286.0	844	283	184	115	0	1	0.309	0.203	0.266	−1.34	−1.24
D15	1470.8	888	298	115	56	0	0	0.472	0.140	0.173	−1.36	−1.33
D16	1454.4	966	288	170	125	0	0	0.396	0.086	0.109	−1.34	−1.30

Table 6. Simulations for series E.

Run	$M_{\rm total}$ [10^{11}M$_\odot$]	$N_{\rm total}$	$N_{\rm merge}$	$N_{\rm tides}^{\rm gal}$	$N_{\rm accr}$	$N_{\rm tides}^{\rm halo}$	$N_{\rm eject}$	$f_{\rm surv}$	f_M	$f_{\rm ICS}$	$\alpha_{\rm start}$	$\alpha_{\rm end}$
E1	1065.4	1023	406	159	24	8	1	0.415	0.297	0.313	−1.38	−1.31
E2	1034.0	866	326	104	7	6	2	0.486	0.168	0.192	−1.38	−1.31
E3	1051.3	906	405	213	19	14	0	0.282	0.446	0.464	−1.38	−1.27
E4	799.4	754	250	177	35	7	0	0.378	0.391	0.424	−1.34	−1.25
E5	868.7	788	394	201	42	12	0	0.176	0.492	0.521	−1.32	−1.22
E6	795.8	527	154	67	7	6	1	0.554	0.303	0.314	−1.34	−1.29
E7	947.7	663	276	97	9	3	1	0.418	0.376	0.398	−1.37	−1.31
E8	941.0	773	395	121	11	8	0	0.307	0.348	0.381	−1.37	−1.28
E9	934.5	652	263	109	10	6	1	0.403	0.325	0.350	−1.39	−1.34
E10	807.5	589	210	98	11	5	1	0.325	0.448	0.343	−1.38	−1.35
E11	760.7	741	349	142	9	8	1	0.313	0.283	0.314	−1.48	−1.23
E12	946.4	732	227	57	4	2	28	0.566	0.149	0.178	−1.39	−1.35
E13	953.4	952	344	180	14	11	0	0.423	0.349	0.377	−1.35	−1.29
E14	950.5	844	325	197	23	6	1	0.346	0.395	0.435	−1.33	−1.29
E15	1145.5	888	320	118	13	5	0	0.486	0.339	0.342	−1.36	−1.29
E16	1125.4	966	439	146	10	10	1	0.373	0.393	0.422	−1.34	−1.26

that never happened with Virgo-like clusters. In order to explain such a behavior we note that tidal disruption by the cluster halo generally occurs with galaxies at a distance $r < 1$ Mpc from the cluster center. Our simulated Perseus-like cluster halo mass profile rises more steeply than the Virgo-like cluster up to $\sim$1.7 Mpc, making Perseus more massive in the inner regions. So a galaxy at a smaller distance, precisely at $r < 1.7$ Mpc, from the cluster center feels a larger tidal field from a more massive halo, and is more prone to be disrupted in the Perseus-like cluster.

The numbers of other galaxy outcomes are comparable for Perseus-like and Virgo-like clusters, with mergers dominating over tides. The mean $f_{\rm ICS}$ for series E is $f_{\rm ICS} = 0.360 \pm 0.090$. This $f_{\rm ICS}$ is somewhat larger than the Virgo-like cluster mean (series C). This can be attributed to the non-zero tidal disruption by the cluster halo, resulting here in a finite contribution to the ICS luminosity fraction.

Table 7 shows the results for series F, i.e., simulations of a Perseus-like cluster with a cD galaxy at the center. Here few galaxies are destroyed by the tidal field of the cluster halo, yet the number is smaller than in series E. It appears, then that the presence of a cD galaxy reduces the number of tidal disruptions by the background halo, since galaxies that would be destroyed by the tidal field of the central parts of the halo are being destroyed by the cD galaxy instead.

Comparing the results for series D and series F (Virgo-like and Perseus-like clusters with a cD galaxy,) the numbers – merger, galaxy-tide and accretion are similar. Series F continues the trend of increased accretions when a cD galaxy is introduced. Also series F has a smaller fraction of luminosity going to ICS. The mean $f_{\rm ICS}$ for series F is $f_{\rm ICS} = 0.166 \pm 0.041$. This $f_{\rm ICS}$ is very similar to that of the relevant Virgo-like cluster mean (series D). This implies that in the presence of a cD galaxy, the ICS luminosity fraction is not so sensitive to the parameters of the β-model density profile.

4.6 *Series G, H & I: NFW profile*

We now consider a background halo described by a NFW profile (see section 2.3, equation 4), with a scale radius $r_s = 200$ kpc, and a concentration parameter $c = 5$. These values are adopted from observational studies of galaxy clusters (Arabadjis *et al.* 2002; Pratt & Arnaud 2005; Maughan *et al.* 2007) where the authors found the best fitting NFW model parameters for cluster mass profiles.

We do not necessarily expect the flattening of the Schechter mass function to be the same for the NFW profile halo and the β-profile halo. So at first we performed a series with $\alpha = -1.28$ (see Table 1), and called it series G. The results are listed in Table 8.

To contrast an NFW-model cluster with a β-model cluster, series G should be compared with series B, since these are with $\alpha = -1.28$, include galaxy harassment, and no cD galaxy. The most striking feature is the large number of galaxies destroyed by the tidal field of the NFW cluster halo. This halo tidal disruption was nil (in the Virgo-like cluster) to a handful (in the Perseus-like cluster) for the β-model background halo. With the NFW profile, the number of halo tides is comparable to the galaxy tides, even exceeding the latter in runs G5 and G6.

The reason for such a behavior is that the NFW halo mass profile rises much more steeply than the β-model mass profile of a Virgo-like cluster up to a distance $r \sim 1.9$ Mpc. So the NFW halo is significantly more massive (by factors as high as 4–5) than the β-model halo at distances $r < 1$ Mpc, where halo tides are dominant

Table 7. Simulations for series F.

Run	$M_{\rm total}$ [10^{11}M$_\odot$]	$N_{\rm total}$	$N_{\rm merge}$	$N^{\rm gal}_{\rm tides}$	$N_{\rm accr}$	$N^{\rm halo}_{\rm tides}$	$N_{\rm eject}$	$f_{\rm surv}$	f_M	$f_{\rm ICS}$	$\alpha_{\rm start}$	$\alpha_{\rm end}$
F1	1394.6	1023	386	153	88	4	1	0.382	0.138	0.174	−1.38	−1.28
F2	1374.4	866	304	96	47	1	2	0.480	0.106	0.136	−1.38	−1.33
F3	1431.1	906	277	183	196	1	0	0.275	0.144	0.185	−1.39	−1.25
F4	1163.2	754	211	180	109	0	0	0.337	0.126	0.165	−1.33	−1.27
F5	1239.5	788	288	166	199	0	0	0.171	0.158	0.202	−1.33	−1.21
F6	1158.8	527	141	60	55	1	1	0.510	0.092	0.115	−1.34	−1.29
F7	1300.7	663	253	81	70	1	1	0.388	0.113	0.155	−1.37	−1.28
F8	1298.4	773	295	124	108	2	0	0.316	0.134	0.173	−1.36	−1.29
F9	1299.5	652	226	93	61	2	1	0.413	0.153	0.202	−1.39	−1.38
F10	1169.4	589	182	83	72	0	1	0.426	0.133	0.178	−1.37	−1.33
F11	1145.8	741	269	148	76	1	1	0.332	0.154	0.201	−1.38	−1.29
F12	1227.5	732	194	58	26	0	31	0.578	0.067	0.090	−1.39	−1.36
F13	1334.1	952	322	175	85	1	0	0.388	0.121	0.154	−1.35	−1.29
F14	1286.0	844	272	180	107	0	1	0.336	0.197	0.259	−1.34	−1.30
F15	1470.8	888	306	103	54	1	0	0.478	0.108	0.134	−1.36	−1.31
F16	1454.4	966	314	155	135	2	1	0.372	0.097	0.126	−1.34	−1.29

Table 8. Simulations for series G.

Run (col. 1)	$M_{\rm total}$ [10^{11}M$_\odot$] (col. 2)	$N_{\rm total}$ (col. 3)	$N_{\rm merge}$ (col. 4)	$N_{\rm tides}^{\rm gal}$ (col. 5)	$N_{\rm accr}$ (col. 6)	$N_{\rm tides}^{\rm halo}$ (col. 7)
G1	721.9	372	72	55	6	47
G2	1034.3	637	129	80	4	63
G3	821.1	530	127	89	5	73
G4	992.3	457	113	61	9	44
G5	899.7	618	94	56	7	64
G6	947.1	452	95	31	2	34
G7	865.2	542	170	91	7	77
G8	1011.6	725	169	101	7	71
G9	1100.6	726	214	144	17	103
G10	1174.4	619	190	76	2	57
	$N_{\rm eject}$ (col. 8)	$f_{\rm surv}$ (col. 9)	f_M (col. 10)	$f_{\rm ICS}$ (col. 11)	$\alpha_{\rm start}$ (col. 12)	$\alpha_{\rm end}$ (col. 13)
G1	1	0.513	0.486	0.498	−1.27	−1.26
G2	7	0.556	0.405	0.406	−1.29	−1.26
G3	1	0.443	0.587	0.589	−1.31	−1.29
G4	1	0.501	0.211	0.229	−1.28	−1.26
G5	8	0.629	0.443	0.443	−1.29	−1.28
G6	17	0.604	0.263	0.288	−1.31	−1.32
G7	1	0.362	0.543	0.555	−1.31	−1.25
G8	1	0.519	0.502	0.510	−1.24	−1.20
G9	1	0.340	0.467	0.501	−1.27	−1.23
G10	6	0.465	0.458	0.454	−1.28	−1.23

(as discussed in section 4.5). Consequently galaxies near the cluster center experience a larger tidal field and are more likely to be tidally disrupted.

This larger number of halo tides alters several results in our simulated NFW model cluster as compared to the β-model. The mergers exceed the galaxy tides, usually by factors 1.3–1.8 (except runs G6 and G10, where the factors are 3 and 2.5). But when tides by galaxy and cluster halo are added together, they become comparable to or even exceed the number of mergers. The accretions are always small in number, and when added to mergers do not have much effect on the above.

The mean $f_{\rm ICS}$ for series G is $f_{\rm ICS} = 0.447 \pm 0.113$. This is significantly larger than the ICS luminosity fraction obtained with the β-model clusters. The reason is again the numerous halo tides. Some massive galaxies are being destroyed by the tidal field of the NFW halo, when they come near the cluster center, and this is contributing a large mass (and luminosity) fraction to the ICS. In this series G, we obtained the average values of α as $\alpha_{\rm start} = -1.285 \pm 0.022$ and $\alpha_{\rm end} = -1.258 \pm 0.034$.

Also combining the set of galaxies of all the 10 runs in series G, we obtained the best fit Schechter exponent for the surviving galaxy distribution at $z = 0$ as $\alpha = -1.25$. Analogous to our approach for the β-model in section 4.3, we note that $|\alpha|$ decreases by $\sim$0.03 between $z = 1$ and $z = 0$. So we performed a new series of simulations,

series H, using $\alpha_{\rm start} = -1.31$, expecting that this will evolve to $\alpha \sim -1.28$ at $z = 0$. This series includes galaxy harassment but no cD galaxy. The results for series H are shown in Table 9.

Series H continues the trends of series G pertaining to a NFW profile. There are a large number of halo tides that dominate the mass fraction, and result in a high value of $f_{\rm ICS}$. The combined numbers of tidal disruptions (by galaxy and halo) are comparable to or exceed the numbers of mergers. The mean $f_{\rm ICS}$ for series H is $f_{\rm ICS} = 0.491 \pm 0.132$. In this series H, we obtained the average values of α as $\alpha_{\rm start} = -1.310 \pm 0.020$ and $\alpha_{\rm end} = -1.288 \pm 0.036$.

We then performed a series of simulations by putting a cD galaxy at the center of the NFW cluster halo, and called it series I. The results are shown in Table 10. Here, the numbers of tides by the cluster halo and by other galaxies are comparable; when added the total occurrence of tides compares to or exceeds that of mergers. Comparing series H and series I (NFW-type clusters respectively without and with a cD galaxy,) there are more accretions when a cD galaxy is introduced (similar to series D and F). The trend seen before with the Perseus-like clusters (between series E and F), that the number of tidal disruptions by the background halo reduces in the presence of a cD galaxy, is almost absent in the NFW-type clusters. Galaxies approaching the cluster center get destroyed by the tidal field of the halo before the cD galaxy can have any effect.

The galactic luminosity fractions dispersed into the ICM are neither too high, nor too low. We suspect this is the combined effect of putting a cD galaxy in an NFW type cluster. There is a tendency of the ICS luminosity fraction to be high in an NFW model cluster, and a cD galaxy tends to reduce the luminosity fraction imparted to the ICM. These two opposing trends cause the $f_{\rm ICS}$ values to be moderate in series I. Here the mean $f_{\rm ICS}$ is $f_{\rm ICS} = 0.381 \pm 0.059$.

4.7 *Series J: Cluster mass growth*

We performed a series of simulation in which we consider mass growth of the background cluster halo with time by accretion. The mass growth rate is adopted from the N-body simulations of Wechsler *et al.* (2002), where the functional fit to the mass accretion histories of dark matter halos is given by

$$M(z) = M_0 e^{-\kappa z}. \tag{26}$$

Here, $M(z)$ is the halo mass at $z > 0$, M_0 is the final halo mass at $z = 0$, and κ is a constant depending on halo mass. Figure 4 of Wechsler *et al.* (2002) plots the average mass accretion histories, from which we read $M(z = 1)/M_0 \sim 0.75$ for massive halos ($M_0 > 3 \times 10^{13} {\rm h}^{-1} {\rm M}_\odot$). Hence we consider that there has been 33% growth of halo mass from $z = 1$ to $z = 0$, the evolution time in our simulations (section 3.1).

We assume that the density profile of the cluster halo remains the same. We calculate the initial halo mass at $z = 1$ using a β-profile with $\beta = 0.53$, a core radius $r_c = 28$ kpc and a central density $\rho_0 = 7.27 \times 10^{-26}$ g cm^{-3}, which is appropriate for the Perseus cluster (section 4.5). This halo is then allowed to evolve up to $z = 0$ according to the mass growth rate in equation (26). We use, for each run, exactly the same initial conditions as in series E.

The results for series J are shown in Table 11. Comparing series E and series J (Perseus type clusters respectively without and with cluster growth), there are more

Table 9. Simulations for series H.

Run	$M_{\rm total}$ $[10^{11}{\rm M}_\odot]$	$N_{\rm total}$	$N_{\rm merge}$	$N_{\rm tides}^{\rm gal}$	$N_{\rm accr}$	$N_{\rm tides}^{\rm halo}$	$N_{\rm eject}$	$f_{\rm surv}$	f_M	$f_{\rm ICS}$	$\alpha_{\rm start}$	$\alpha_{\rm end}$
H1	894.3	755	171	152	5	122	0	0.404	0.620	0.656	−1.33	−1.33
H2	866.2	556	195	68	5	92	1	0.351	0.563	0.596	−1.28	−1.24
H3	955.0	621	161	84	2	67	1	0.493	0.396	0.394	−1.33	−1.35
H4	758.6	588	153	113	7	109	1	0.349	0.702	0.724	−1.30	−1.30
H5	1103.6	997	197	132	5	68	22	0.575	0.375	0.407	−1.30	−1.26
H6	1008.7	774	266	162	10	148	0	0.243	0.682	0.704	−1.29	−1.24
H7	1027.4	639	101	40	4	47	28	0.656	0.316	0.342	−1.32	−1.30
H8	833.8	601	126	75	5	70	7	0.529	0.496	0.498	−1.29	−1.28
H9	740.3	494	109	53	9	54	4	0.536	0.398	0.417	−1.30	−1.28
H10	952.9	744	159	96	13	92	1	0.515	0.451	0.474	−1.35	−1.32
H11	779.4	519	113	54	9	59	2	0.543	0.375	0.391	−1.31	−1.25
H12	993.6	741	163	86	3	57	10	0.570	0.306	0.320	−1.33	−1.29
H13	931.8	534	131	60	5	62	2	0.513	0.412	0.423	−1.31	−1.33
H14	1012.8	748	202	117	8	95	1	0.434	0.508	0.534	−1.30	−1.26

Table 10. Simulations for series I.

Run (col. 1)	$M_{\rm total}$ $[10^{11}{\rm M}_{\odot}]$ (col. 2)	$N_{\rm total}$ (col. 3)	$N_{\rm merge}$ (col. 4)	$N_{\rm tides}^{\rm gal}$ (col. 5)	$N_{\rm accr}$ (col. 6)	$N_{\rm tides}^{\rm halo}$ (col. 7)
I1	1189.1	495	114	53	26	75
I2	1255.5	705	183	100	16	87
I3	1189.9	643	152	127	35	119
I4	1153.5	548	108	78	8	66
I5	1309.4	821	228	139	19	87
I6	1330.8	596	105	56	2	54
I7	1315.8	775	215	126	37	105
I8	1188.1	691	118	91	12	71
I9	1236.6	574	103	73	12	56
I10	1093.4	634	96	96	8	64

	$N_{\rm eject}$ (col. 8)	$f_{\rm surv}$ (col. 9)	f_M (col. 10)	$f_{\rm ICS}$ (col. 11)	$\alpha_{\rm start}$ (col. 12)	$\alpha_{\rm end}$ (col. 13)
I1	1	0.457	0.322	0.399	−1.34	−1.31
I2	0	0.452	0.326	0.423	−1.34	−1.32
I3	0	0.327	0.391	0.494	−1.29	−1.31
I4	1	0.524	0.255	0.335	−1.32	−1.30
I5	1	0.423	0.341	0.445	−1.33	−1.31
I6	9	0.621	0.265	0.334	−1.31	−1.30
I7	0	0.377	0.299	0.372	−1.33	−1.31
I8	1	0.576	0.248	0.305	−1.36	−1.35
I9	1	0.573	0.295	0.344	−1.32	−1.30
I10	1	0.582	0.274	0.359	−1.31	−1.29

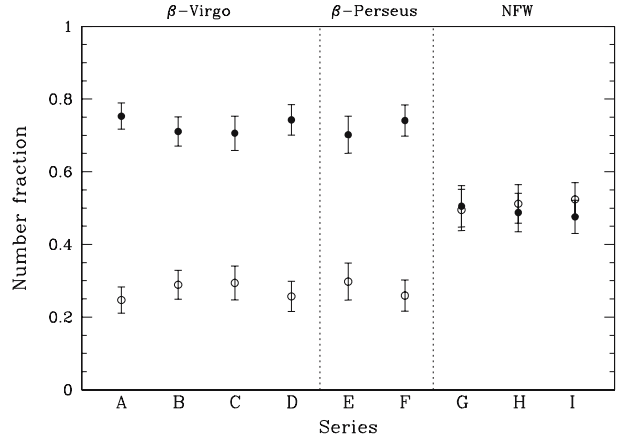

Figure 4. Fractional number of galaxies destroyed by mergers, $f_{\rm destroyed}^{\rm mergers}$ (filled circles), and by tides, $f_{\rm destroyed}^{\rm tides}$ (open circles), averaged over all runs within each series of Table 1. Error bars show the standard deviation.

Table 11. Simulations for series J.

Run	$M_{\rm total}$ $[10^{11}{\rm M}_\odot]$	$N_{\rm total}$	$N_{\rm merge}$	$N_{\rm tides}^{\rm gal}$	$N_{\rm accr}$	$N_{\rm tides}^{\rm halo}$	$N_{\rm eject}$	$f_{\rm surv}$	f_M	$f_{\rm ICS}$	$\alpha_{\rm start}$	$\alpha_{\rm end}$
J1	1065.4	1023	462	194	24	9	1	0.326	0.308	0.324	−1.38	−1.25
J2	1034.0	866	350	114	10	10	1	0.440	0.316	0.342	−1.38	−1.34
J3	1051.3	906	430	233	22	16	0	0.226	0.474	0.496	−1.38	−1.25
J4	799.4	754	263	193	29	12	0	0.341	0.508	0.523	−1.34	−1.25
J5	868.7	788	402	220	43	13	0	0.140	0.570	0.598	−1.32	−1.24
J6	795.8	527	167	81	10	13	1	0.484	0.404	0.425	−1.34	−1.28
J7	947.7	663	278	119	10	4	1	0.379	0.451	0.473	−1.37	−1.31
J8	941.0	773	412	132	9	8	0	0.274	0.400	0.436	−1.37	−1.26
J9	934.5	652	303	105	10	8	1	0.345	0.374	0.404	−1.39	−1.29
J10	807.5	589	239	100	13	4	1	0.394	0.355	0.379	−1.38	−1.32
J11	760.7	741	362	157	7	10	1	0.275	0.416	0.445	−1.38	−1.24
J12	946.4	732	274	55	4	6	9	0.525	0.233	0.275	−1.39	−1.34
J13	953.4	952	389	201	14	15	0	0.350	0.388	0.422	−1.35	−1.26
J14	950.5	844	329	227	27	8	1	0.299	0.462	0.493	−1.33	−1.28
J15	1145.5	888	366	142	17	7	0	0.401	0.340	0.345	−1.36	−1.28
J16	1125.4	966	459	161	12	13	1	0.331	0.476	0.478	−1.34	−1.27

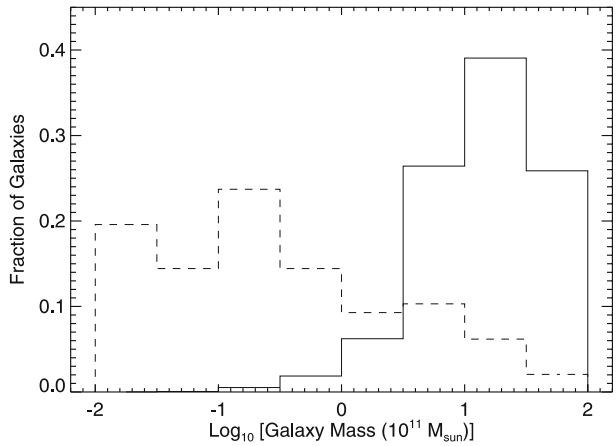

Figure 5. Mass histogram of number fraction (*dashed line*) and luminosity fraction (*solid line*) of galaxies contributing to the ICL in run C3.

galaxy interactions in the growing cluster, which cause the survival fraction to decrease. In series J, the numbers of mergers and galaxy tidal disruptions increase by factors up to 1.2. The numbers of accretions, halo tides, and ejections remain almost same or increase slightly.

There is an increase in the ICS luminosity fraction in the growing cluster, because of the larger number of tidal disruptions. The mean $f_{\rm ICS}$ in series J is $f_{\rm ICS} = 0.429 \pm 0.083$. This is somewhat higher than the mean value in series E.

5. Discussion

5.1 *Mergers and tides*

To quantify the relative importance of destruction by tides and by mergers, we calculated, for each run, the following fractional numbers:

$$f_{\rm destroyed}^{\rm mergers} = \frac{N_{\rm merge} + N_{\rm accr}}{N_{\rm destroyed}}, \tag{27}$$

$$f_{\rm destroyed}^{\rm tides} = \frac{N_{\rm tides}^{\rm gal} + N_{\rm tides}^{\rm halo}}{N_{\rm destroyed}}, \tag{28}$$

where $N_{\rm destroyed} = N_{\rm merge} + N_{\rm tides}^{\rm gal} + N_{\rm accr} + N_{\rm tides}^{\rm halo}$. We then averaged the fractions over all the runs in each series of the simulations. The results for the set of series in Table 1 are shown in Fig. 4. The destruction by mergers clearly dominates over destruction by tides for the β model, while they are of comparable importance for the NFW model.

In order to investigate the mass distribution of the galaxies contributing to the ICL in our simulations, we plotted the mass histograms of the number fractions and the luminosity fractions of such galaxies in run C3, as shown in Fig. 5. These fractions are with respect to all the galaxies ending up in the ICM in this run. While most of

the galaxies destroyed by tides are dwarfs, the destruction of few galaxies of mass $M > 10^{11}\mathrm{M}_{\odot}$ provides more than 60% of the intracluster light.

We can show that, contrary to popular belief, the destruction of DGs alone cannot explain the observed ICL. We calculated the total light fraction of all the galaxies (destroyed or not) with $M < 10^{11}\mathrm{M}_{\odot}$ in our simulated cluster of run C3. This would be the fraction of intracluster light if all DGs, and only DGs, were destroyed. We get the luminosity fraction of DGs as 0.034, which is smaller than the most observed ICL fraction values. To obtain larger values, compatible with observations, either (1) clusters must contain dwarfs many times more than a Schechter distribution would predict, (2) dwarfs galaxies have a much lower M/L ratio than we assumed, or (3) some intermediate-mass or massive galaxies are destroyed.

The last argument is the most plausable, and it is supported by our simulations: some intermediate-mass or massive galaxies are getting destroyed by the tidal field of the most massive galaxy. Note that in this high mass range we are in the exponential tail of the Schechter distribution. The mass ratios between the most massive galaxy and the high-mass ones destroyed are factors of about 3 to 5, so destruction by tides is viable.

5.2 *Intracluster stars*

There have been several observational measurements of the light fraction contained in the ICS with respect to the total light in a cluster. We collected some values of the ICS fraction from the literature, and list them in Table 12. In Fig. 6 we show the ICS luminosity fraction we obtained in our simulations, plotted as horizontal lines showing the average f_{ICS} from the runs in series A–J (Table 1, section 4). For comparison, the observed f_{ICS} values (from Table 12) are shown by the symbols and error bars. We can clearly see that the ICS luminosity fraction in clusters from observations fall well within our simulation predictions. A few clusters have too small f_{ICS}, which are probably galaxy groups and low-mass clusters.

Our simulation results indicate that the tidal destruction of galaxies (by other galaxies and by the cluster halo) in clusters can sufficiently explain the observed fraction of ICL. Also our results (in section 4) imply that for each cluster halo density profile, namely, β and NFW models, f_{ICS} increases with the mass of the cluster halo. This is consistent with the studies finding that more massive clusters have a larger fraction of ICL than the less massive ones (Lin & Mohr 2004; Murante *et al.* 2004).

5.3 *Limitations of the method*

The strengths and weaknesses of the methodology used in this work both reside in our somehow original approach of using one single particle to represent each galaxy, combined with a subgrid treatment of galaxy mergers, tidal disruption, and galaxy harassment.

On the positive side, this approach has enabled us to perform a very large number of simulations (148 total), covering a fairly large parameter space, while obtaining statistically significant results. Doing this many simulations without resorting to subgrid physics would have been computationally prohibitive. In implementing the subgrid physics, we have attempted to make the most reasonable choices possible.

Table 12. Observed values of the intracluster light fraction.

Index	Cluster	$f_{\rm ICS}$ (%)	$\Delta f_{\rm ICS}$ (%)	Reference
1.	Coma	50	–	Bernstein *et al.* (1995)
2.	Abell 1689	30	–	Tyson & Fischer (1995)
3.	Abell 1651	<5	–	Gonzalez *et al.* (2000)
4.	M96 (Leo) group	<1.6	–	Castro-Rodriguez *et al.* (2003)
5.	HCG 90	45	5	White *et al.* (2003)
6.	Virgo	15.8	8	Feldmeier *et al.* (2004b)
7.	A801	16	4.7	Feldmeier *et al.* (2004a)
8.	A1234	17	4.4	Feldmeier *et al.* (2004a)
9.	A1553	21	16	Feldmeier *et al.* (2004a)
10.	A1914	28	16	Feldmeier *et al.* (2004a)
11.	93 clusters	50	10	Lin & Mohr (2004)
12.	683 clusters	10.9	5.0	Zibetti *et al.* (2005)
13.	A4059	22	12	Krick & Bernstein (2007)[a]
14.	A3880	14	6	Krick & Bernstein (2007)
15.	A2734	19	6	Krick & Bernstein (2007)
16.	A2556	6	5	Krick & Bernstein (2007)
17.	A4010	21	8	Krick & Bernstein (2007)
18.	A3888	13	5	Krick & Bernstein (2007)
19.	A3984	10	6	Krick & Bernstein (2007)
20.	A141	10	4	Krick & Bernstein (2007)
21.	AC 114	11	2	Krick & Bernstein (2007)
22.	AC 118	14	5	Krick & Bernstein (2007)

[a]Krick & Bernstein (2007) measured these $f_{\rm ICS}$ values in the r band.

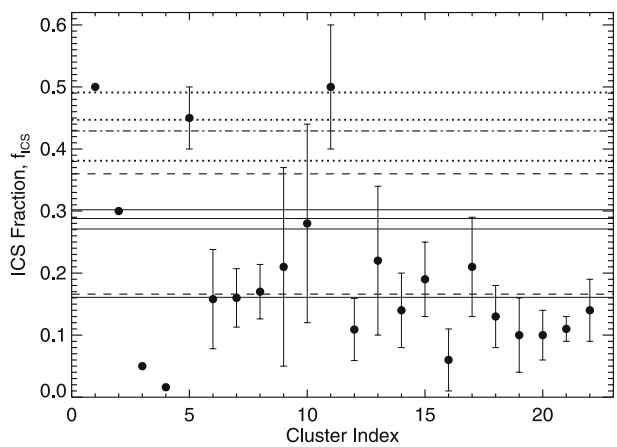

Figure 6. Fraction $f_{\rm ICS}$ of intracluster stars. The horizontal lines show the average $f_{\rm ICS}$ values in our simulations, from the runs of the series in Table 1 (section 4), with *solid line*: Virgo-like cluster (series A–D), *dashed line*: Perseus-like cluster (series E–F), *dotted line*: NFW model cluster (series G–I), *dot-dashed line*: Perseus-like growing cluster (series J). The symbols and error bars show actual measurements, as tabulated in Table 12.

One free parameter is the geometric factor in equation (10), but for reasonable density profiles, the values of that factor do not appear to vary much. The assumption that a galaxy is considered 'tidally disrupted' if 50% of its mass becomes unbound is also the most reasonable one we could make. Our technique for generating the initial conditions is based on four key assumptions:

(1) the galaxy distributions are isotropic,
(2) the galaxy number density profile $\nu(r)$ follows the density profile $\rho_{\rm halo}(r)$ of the background cluster halo,
(3) the mass is segregated in the cluster, with the most massive galaxies being located in the center, and
(4) the cluster is in equilibrium (except for series J).

So even though our prescription for generating the initial conditions contains many tunable parameters, we believe that the underlying approach is sound.

On the negative side, two particular aspects of the methodology can be considered weak. First, the treatment of galaxy harassment is highly speculative. We have assumed that some amount of orbital kinetic energy ΔE is dissipated into internal energy during an encounter between two galaxies, that this amount is related to the initial internal energies of the galaxies, and that the energy dissipated is distributed equally between the two galaxies. The dissipation of energy and its consequences during a real galactic encounter are certainly much more complex. The implemented subgrid model could thus, potentially, be refined.

Another important limitation of our approach is that it deals with isolated clusters in equilibrium (except for series J). In the real universe, clusters constantly experience mergers and accretion. We justify our approach by the fact that most clusters will experience, at some epoch, a *major merger*, during which most of the final mass of the cluster is assembled. From that point, if we can neglect the addition of mass by minor mergers and accretion, the cluster can be treated as isolated. Of course, such scenario cannot describe all clusters. In a forthcoming paper (Brito *et al.* 2008), we will present a study of cluster formation and evolution inside a cosmological volume containing many clusters. This will be achieved by implementing the subgrid approach described in this paper into a cosmological N-body algorithm.

6. Summary and conclusion

We have designed a simple model for the evolution of galaxies in an isolated cluster, in order to compare the destruction of dwarf galaxies by mergers *vs.* tidal disruptions, and to predict the contribution of DGs to the origin of intracluster stars. Our algorithm combines a direct N-body computation of gravitational interactions, along with a subgrid treatment of the other physical processes (merger, tidal disruption, accretion, etc.) of the galaxies. Using this algorithm, we have performed a total of 148 numerical simulations of galaxy clusters, examining the fate of DGs. Our results and conclusions are as follows:

- The destruction of dwarf galaxies by mergers dominates over destruction by tides, in most of our simulation runs with all the models (β-Virgo, β-Perseus, NFW) of cluster halo density.

- The destruction of galaxies by the tidal field of other galaxies and by the cluster halo imparts a significant amount of galactic mass into the ICM. This is sufficient to account for the observed fraction of intracluster light in galaxy clusters. In our simulations, the average ICS luminosity fraction, $f_{\rm ICS}$, has a range 16–49%. We see a clear trend of increase of $f_{\rm ICS}$ with the mass of the cluster halo. All these are well consistent with observations and other numerical studies.
- In the NFW model simulated clusters, there are a large number of tidal disruptions of galaxies caused by the gravitational potential of the cluster halo, and this component dominates the mass fraction. We note that it has been our assumption that the cluster halo is stationary, and does not evolve in response to the forces exerted on it by the galaxies (section 2.1). Such an assumption is probably a poor one with the NFW model clusters. We point out that this could imply a possible solution to the cusp crisis of cluster dark matter halos. The central cuspy region of the cluster dark matter halo could have inelastic encounters with the member galaxies, which could inject energy into the halo and erase the cusp.
- In our simulations, the presence of a cD galaxy increases occurrences of accretion, decreases tidal disruptions by the cluster halo, and reduces the ICS luminosity fraction. This is opposite to the trend seen from observations that $f_{\rm ICS}$ is higher in the presence of a cD.
- The vast majority of galaxies destroyed by tides are dwarfs. However, a few high-mass ($M > 10^{11}{\rm M}_{\odot}$) galaxies are also destroyed, and these can provide a substantial fraction of the ICL. Furthermore, the destruction of such high mass galaxies is required, since the dwarfs alone do not contain enough stars to account for the observed ICL, even if they were all destroyed.

Acknowledgements

This work benefited from stimulating discussions with L. Edwards and C. Robert. We thank John Kormendy for useful correspondence. All calculations were performed at the Laboratoire d'astrophysique numérique, Université Laval. We thank the Canada Research Chair Program and NSERC for support.

Appendix

The internal energy of galaxies

Since we represent galaxies as individual particles, we cannot directly compute their internal energy. We therefore need an estimate that can then be used in equation (10). We write the potential energy of a galaxy of mass M and radius R as:

$$W = -\frac{\zeta G M^2}{R}, \tag{29}$$

where ζ is the *geometric factor*, which depends on the shape and density distribution of the galaxy. For a uniform-density sphere, $\zeta = 3/5$. In our simplified model, we treat galaxies as spheres, but we should certainly not assume a uniform density. Instead, any galaxy will be centrally concentrated. The value of ζ will depend on the assumed density profile, but we do not expect that dependence to be very strong if we stick with

reasonable profiles. So we consider the simplest case of an isothermal sphere with a cut-off radius R. The density and mass inside r are given by:

$$\rho(r) = \frac{M}{4\pi R r^2}, \tag{30}$$

$$m(r) = \frac{Mr}{R}, \tag{31}$$

where $M \equiv m(R)$ is the total mass. The gravitational field is given by:

$$\mathbf{g} = -\nabla\phi = -\frac{Gm(r)}{r^2}\hat{r} = -\frac{GM}{rR}\hat{r}. \tag{32}$$

We integrate this expression, with the boundary condition $\phi(R) = -GM/R$, to get the gravitational potential,

$$\phi = \frac{GM}{R}\left(\ln\frac{r}{R} - 1\right). \tag{33}$$

The potential energy is given by:

$$\begin{aligned} W &= \frac{1}{2}\iiint \phi(r)\rho(r)d^3r \\ &= \frac{GM^2}{2R^2}\int_0^R \left(\ln\frac{r}{R} - 1\right)dr \\ &= -\frac{GM^2}{R}. \end{aligned} \tag{34}$$

Hence, $\zeta = 1$ for an isothermal sphere. Interestingly, this is not much different from the value of 3/5 for a uniform sphere. This supports our claim that the sensitivity of ζ on the density profile is weak. For the kinetic energy, we assume that the galaxies are virialized. Hence, $K = -W/2$, and therefore the internal energy is given by:

$$U = K + W = -\frac{GM^2}{2R}. \tag{35}$$

References

Aguerri, J. A. L. *et al.* 2005, *AJ*, **129**, 2585.
Arabadjis, J. S., Bautz, M. W., Garmire, G. P. 2002, *ApJ*, **572**, 66.
Arnaboldi, M. *et al.* 2003, *AJ*, **125**, 514.
Arnaboldi, M. 2004, *IAUS*, **217**, 54.
Bernstein, G. M., Nichol, R. C., Tyson, J. A., Ulmer, M. P., Wittman, D. 1995, *AJ*, **110**, 1507.
Bothun, G. D. *et al.* 1991, *ApJ*, **376**, 404.
Brainerd, T. G., Specian, M. A. 2003, *ApJ*, **593**, L7.
Brito, W., Barai, P., Martel, H. 2009, in preparation.
Carlberg, R. G. *et al.* 1997, *ApJ*, **485**, L13.
Castro-Rodriguez, N., Aguerri, J. A. L., Arnaboldi, M., Gerhard, O., Freeman, K. C., Napolitano, N. R., Capaccioli, M. 2003, *A&A*, **405**, 803.
Cavaliere, A., Fusco-Femiano, R. 1976, *A&A*, **49**, 137.

Cellone, S. A., Buzzoni, A. 2005, *MNRAS*, **356**, 41.
Côté, S., Freeman, K. C., Carignan, C., Quinn, P. J. 1997, *AJ*, **114**, 1313.
De Propris, R. *et al.* 2003, *MNRAS*, **342**, 725.
Drinkwater, M. J. *et al.* 2003, *Nature*, **423**, 519.
Ettori, S. 2003, *MNRAS*, **344**, L13.
Feldmeier, J. J., Mihos, J. C., Morrison, H. L., Harding, P., Kaib, N., Dubinski, J. 2004a, *ApJ*, **609**, 617.
Feldmeier, J. J., Ciardullo, R., Jacoby, G. H., Durrell, P. R. 2004b, *ApJ*, **615**, 196.
Gal-Yam, A. *et al.* 2003, *AJ*, **125**, 1087.
Gerhard, O. *et al.* 2005, *ApJ*, **621**, L93.
Girardi, M., Giuricin, G., Mardirossian, F., Mezzetti, M., Boschin, W. 1998, *ApJ*, **505**, 74.
Gonzalez, A. H., Zabludoff, A. I., Zaritsky, D., Dalcanton, J. J. 2000, *ApJ*, **536**, 561.
Gonzalez, A. H., Zabludoff, A. I., Zaritsky, D. 2005, *ApJ*, **618**, 195.
Gonzalez, A. H., Zaritsky, D., Zabludoff, A. I. 2007, preprint (arXiv0705.1726).
Grebel, E. K. 2001, *ASPC*, **239**, 280.
Gregg, M. D., West, M. J. 1998, *Nature*, **396**, 549.
Jordan, A., Côté, P., West, M. J., Marzke, R. O., Minniti, D., Rejkuba, M. 2004, *AJ*, **127**, 24.
Karachentseva, V. E., Karachentsev, I. D., Boerngen, F. 1985, *A&AS*, **60**, 213.
King, I. 1962, *AJ*, **67**, 471.
Krick, J. E., Bernstein, R. A., Pimbblet, K. A. 2006, *AJ*, **131**, 168.
Krick, J. E., Bernstein, R. A. 2007, *AJ*, **134**, 466.
Lee, H. *et al.* 2003, *AJ*, **125**, 2975.
Lewis, I. *et al.* 2002, *MNRAS*, **334**, 673L.
Lin, Y.-T., Mohr, J. J. 2004, *ApJ*, **617**, 879.
Makino, N., Sasaki, S., Suto, Y. 1998, *ApJ*, **497**, 555.
Martel, H. 1991, *ApJ*, **377**, 7.
Mateo, M. L. 1998, *ARA&A*, **36**, 435.
Maughan, B. J., Jones, C., Jones, L. R., Van Speybroeck, L. 2007, *ApJ*, **659**, 1125.
Mieske, S., Hilker, M., Jordan, A., Infante, L., Kissler-Patig, M. 2007, preprint (arXiv:0706.2724).
Mihos, J. C., Harding, P., Feldmeier, J., Morrison, H. 2005, *ApJ*, **631**, L41.
Miller, G. E. 1983, *ApJ*, **268**, 495.
Moore, B., Katz, N., Lake, G., Dressler, A., Oemler, A. 1996, *Nature*, **379**, 613.
Murante, G. *et al.* 2004, *ApJ*, **607**, L83.
Napolitano, N. R. *et al.* 2003, *ApJ*, **594**, 172.
Navarro, J. F., Frenk, C. S., White, S. D. M. 1997, *ApJ*, **490**, 493.
Oegerle, W. R., Hill, J. M. 2001, *AJ*, **122**, 2858.
Piffaretti, R., Kaastra, J. S. 2006, *A&A*, **453**, 423.
Pratt, G. W., Arnaud, M. 2005, *A&A*, **429**, 791.
Quintana, H., Lawrie, D. G. 1982, *AJ*, **87**, 1.
Rudick, C. S., Mihos, J. C., McBride, C. 2006, *ApJ*, **648**, 936.
Ryan, R. E. Jr. *et al.* 2007, *ApJ*, **668**, 839.
Sandage, A., Binggeli, B., Tammann, G. A. 1985, *AJ*, **90**, 1759.
Schechter, P. 1976, *ApJ*, **203**, 297.
Schombert, J. M. 1988, *ApJ*, **328**, 475.
Sommer-Larsen, J. *et al.* 2005, *MNRAS*, **357**, 478.
Spergel, D. N. *et al.* 2007, *ApJS*, **170**, 377.
Thompson, L. A., Gregory, S. A. 1993, *AJ*, **106**, 2197.
Tyson, J. A., Fischer, P. 1995, *ApJ*, **446**, L55.
Wechsler, R. H., Bullock, J. S., Primack, J. R., Kravtsov, A. V., Dekel, A. 2002, *ApJ*, **568**, 52.
West, M. J. *et al.* 1995, *ApJ*, **453**, L77.
White, S. D. M., Navarro, J. F., Evrard, A. E., Frenk, C. S. 1993, *Nature*, **366**, 429.
White, P. M., Bothun, G., Guerrero, M. A., West, M. J., Barkhouse, W. A. 2003, *ApJ*, **585**, 739.
Willman, B., Governato, F., Wadsley, J., Quinn, T. 2004, *MNRAS*, **355**, 159.
Yang, X., Mo, H. J., van den Bosch, F. C. 2003, *MNRAS*, **339**, 1057.
Zibetti, S., White, S. D. M., Schneider, D. P., Brinkmann, J. 2005, *MNRAS*, **358**, 949.
Zwicky, F. 1951, *PASP*, **63**, 61.

J. Astrophys. Astr. (2009) **30,** 37–51

GMRT Detection of a New Wide-Angle Tail (WAT) Radio Source Associated with the Galaxy PGC 1519010

N. G. Kantharia[1,*], M. Das[2] & Gopal-Krishna[1]
[1]*National Centre for Radio Astrophysics, Tata Institute of Fundamental Research, Post Bag 3, Ganeshkhind, Pune University Campus, Pune 411 007, India.*
[2]*Raman Research Institute, Sadashivnagar, Bangalore 560 080, India.*
[*]*e-mail: ngk@ncra.tifr.res.in*

Received 2008 October 29; accepted 2009 March 13

Abstract. We report the serendipitous detection of a Wide-Angle Tail (WAT) radio galaxy at 240 and 610 MHz, using the Giant Metrewave Radio Telescope (GMRT). This WAT is hosted by a cD galaxy PGC 1519010 whose photometric redshift given in the SDSS DR6 catalogue is close to the spectroscopic redshifts (0.105, 0.106 and 0.107) of three galaxies found within 4′ of the cD. Using the SDSS DR6, we have identified a total of 37 galaxies within 15′ of the cD, whose photometric redshifts are between 0.08 and 0.14. This strongly suggests that the cD is associated with a group of galaxies whose conspicuous feature is a north–south chain of galaxies (filament) extending to at least 2.6 Mpc. The *ROSAT* all-sky survey shows a faint, diffuse X-ray source in this direction, which probably marks the hot intracluster gas in the potential well of this group.

We combine the radio structural information for this WAT with the galaxy clustering in that region to check its overall consistency with the models of WAT formation. The bending of the jet before and after its disruption forming the radio plume, are found to be correlated in this WAT, as seen from the contrasting morphological patterns on the two sides of the core. Probable constraints imposed by this on the models of WAT formation are pointed out. We also briefly report on the other interesting radio sources found in the proximity of the WAT. These include a highly asymmetric double radio source and an ultra-steep spectrum radio source for which no optical counterpart is detected in the SDSS.

Key words. Radio galaxies—cluster of galaxies—ram pressure—intracluster medium.

1. Introduction

Wide-Angle Tail (WAT) are a subset of radio galaxies near the Fanaroff–Riley (1974) luminosity transition, which have been extensively discussed because of their exclusive association with cluster dominant (cD) galaxies and also because of the abrupt flaring of their jets after maintaining a well collimated flow to distances ≥ 20 kpc from the core (e.g., Owen & Rudnick 1976; O'Donoghue *et al.* 1993). The jet disruption is

sudden unlike FR I jets and the resulting plumes are often sharply bent. On the other side, although the jets are collimated like FR II galaxies, they do not terminate in hot spots. Search for explanations of the WAT phenomenon began in the 1980s (e.g., Burns *et al.* 1981; Eilek *et al.* 1984; Leahy 1984; O'Dea & Owen 1985; O'Donoghue *et al.* 1990). Since neither the bending of the radio plumes occurs universally, nor is the bending of jet essential for its flaring and plume formation, jet bending is currently regarded as a phenomenon independent from jet flaring (Hardcastle & Sakelliou 2004; Hardcastle *et al.* 2005).

Since host galaxies of WATs are the dominant members of their group/cluster and hence located close to the bottom of the gravitational potential well, they are not expected to have a large motion relative to the intracluster medium (ICM). This situation is not conducive to large ram pressure that could bend the jet/plume leading to the WAT morphology. An alternative mechanism, based on numerical simulations has been investigated by Loken *et al.* (1995), Hooda & Wiita (1996) and Burns *et al.* (1994). In this picture, the sudden disruption of the jet and bending of its plume can arise, if upon crossing a sharp transition between the interstellar medium (ISM) of its host galaxy and the ICM, the jet encounters a transonic crosswind of the ICM resulting from cluster merger (an analytical treatment of the jet propagation through an ISM/ICM interface can be found in Gopal-Krishna & Wiita 1987). Another alternate mechanism proposed in Loken *et al.* (1995) invokes a jet crossing, an oblique shock formed due to colliding clumps in the cluster. Strong support for the merging cluster scenario comes from the detection of X-ray elongations which trace the merger axis and are found to be in the direction of WAT radio tails (Gomez *et al.* 1997) and perpendicular to the initial jet direction (Burns *et al.* 1994). Another mechanism, by Higgins *et al.* (1999), associates the jet flaring with its encounter with a discrete clump in the ICM. While all these mechanisms seem plausible, it is intriguing that the deep Chandra imaging, which is available for the best known WAT, namely 3C 465 (Hardcastle *et al.* 2005), has failed to reveal any discontinuity in the external medium at the locations where the jets flare. Moreover, for this same WAT, Jetha *et al.* (2006) and Hardcastle *et al.* (2005) have argued that, if the jet/plume is extremely light relative to the external medium, the speed of the host galaxy required for jet bending is only $\sim$100 km s^{-1}, which is not implausibly high even for the central galaxies of rich clusters (much higher speeds can occur for galaxies in merging clusters). Thus, the bending of the jet/plume in WATs can possibly be explained.

The circumstance of jet termination in WATs has been investigated in several studies. Hardcastle & Sakelliou (2004) have shown that the distance between the host galaxy and the base of the plume inversely correlate with the cluster richness as quantified in terms of the temperature of the ICM (also, Jetha *et al.* 2006). Since WATs reside at or close to gravitational centres of clusters and groups of galaxies, these can also be used as a signpost for the cluster or group of galaxies. Indeed, Blanton *et al.* (2000, 2001, 2003) have identified several clusters using the WAT sources detected in the FIRST survey (Becker *et al.* 1995).

In this paper, we report the GMRT detection of a WAT associated with the galaxy PGC 1519010 (SDSS J113920.37+165206). The radio source was noticed by us while imaging the radio continuum of the low surface brightness galaxy UGC 6614. This was interesting, given that the galaxy PGC 1519010 has itself been catalogued as a low surface brightness galaxy (U1-3) by O'Neil *et al.* (1997). In this paper, we discuss

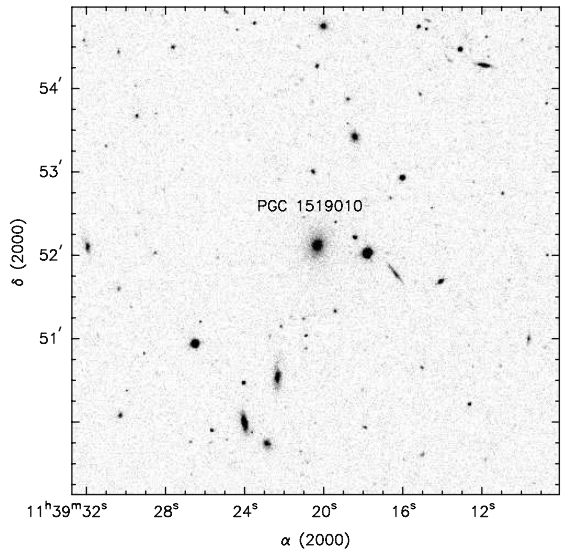

Figure 1. PGC 1519010 (U1-3) in optical – from the SDSS. Note the core-halo type of morphology indicating that it is a cD type elliptical with a large stellar halo extended north–south.

the nature of this radio source and its optical/X-ray environment. A Hubble constant of 70 km s^{-1} Mpc^{-1} is assumed.

2. PGC 1519010 – the host galaxy

PGC 1519010 is located ∼16′ to the south of UGC 6614, the giant low surface brightness (LSB) galaxy that was the principal target of our observations as part of our larger programme of observing the radio-band AGN activity in giant low surface brightness galaxies (see Das *et al.* 2007, 2008). We noticed that PGC 1519010 is catalogued by O'Neil *et al.* (1997) as the low surface brightness galaxy U1-3. The catalogue contains all those galaxies in the region of the Cancer and Pegasus clusters whose central surface brightness $\mu(0) \geq 22.0$ mag-arcsec^{-2} (O'Neil *et al.* 1997). Curiously, O'Neil *et al.* found that U1-3 has a central surface brightness of $\mu_b(0) = 22.39$ mag-arcsec^{-2} and that its radial brightness distribution is better fit by the King's model (1962, 1966), rather than the exponential profile characteristic of LSB (disk) galaxies. Since King's model is known to describe the surface brightness distribution of globular clusters in our galaxy, O'Neil *et al.* had in fact suggested that U1-3 (PGC 1519010) might be an LSB globular cluster. A closer inspection of the SDSS image, however, showed that it is an elliptical galaxy, most probably a cD with a large halo extending in the north–south (Fig. 1). Such a core-halo distribution of stars can be explained in terms of tidal distortion of an elliptical (with a typical de Vaucouleurs $r^{1/4}$ brightness profile) by its repeated gravitational encounters with other galaxies (e.g., Kormendy 1997), a highly plausible scenario for central regions of clusters and groups of galaxies.

Thus, we point out that the galaxy PGC 1519010 classified by O'Neil *et al.* (1997) as an LSB galaxy needs to be reclassified as an elliptical in view of its core-halo stellar distribution (see Fig. 1), akin to cD galaxies generally found near the centres of

Table 1. Optical properties of PGC 1519010 from literature.

Parameter	Value	Reference
Names	SDSS J113920.37+165206	1
	PGC 1519010	2
	2MASX J11392034+1652058	3
Photmetric z1	0.138	1
Photmetric zCC2	0.112	1
Photmetric zD1	0.104	1
Radial brightness	Kings's model	4
Morphological type code	2.1 ± 5	2
Total apparent corrected B-mag	16.69	2
Total apparent corrected I-mag	15.1	2
Inclination	35°	2
u-magnitude	18.72	1
g-magnitude	16.64	1
r-magnitude	15.62	1
i-magnitude	15.14	1
z-magnitude	14.83	1
$\mu_b(0)$ mag-arcsec^{-1}	22.39	4
Inclination angle	47.9°	4
Major axis upto $\mu_b = 25$ isophote	$17.9''$	4
Closeby cluster	NSC 113924+165506	5

1. SDSS DR6, 2. Hyperleda, Paturel *et al.* (2003), 3. NED, 4. O'Neil *et al.* (1997), 5. Gal *et al.* (2003).

clusters/groups of galaxies. The main properties of this galaxy obtained from literature are summarized in Table 1.

Figure 2(a, b) shows the radio continuum images of the WAT radio galaxy at 21 cm, reproduced from the FIRST survey (Becker *et al.* 1995) and the NVSS survey (Condon *et al.* 1998). The twin-lobed morphology consists of a diffuse radio lobe west of the core and a diffuse eastern lobe which suggests that the eastern jet has undergone bending prior to flaring. Such a morphology is indicative of WATs and we report here its structural details based on our GMRT observations. We also discuss the optical field around this galaxy, as well as the faint halo of soft X-rays picked up in the *ROSAT* all sky survey (Voges *et al.* 1999 and references therein).

3. GMRT observations and results

The field was observed on 30 December 2005 using GMRT (Swarup *et al.* 1991; Ananthakrishnan & Rao 2002), in the dual-frequency mode which allows simultaneous observations at 240 and 610 MHz (for details of the observations, see Das *et al.* 2009, in preparation). The data obtained in the native *lta* format were imported to and analysed using NRAO AIPS[1]. Data of single RFI-free channels were first gain-calibrated.

[1]The National Radio Astronomy Observatory is a facility of the National Science Foundation operated under co-operative agreement by Associated Universities, Inc.

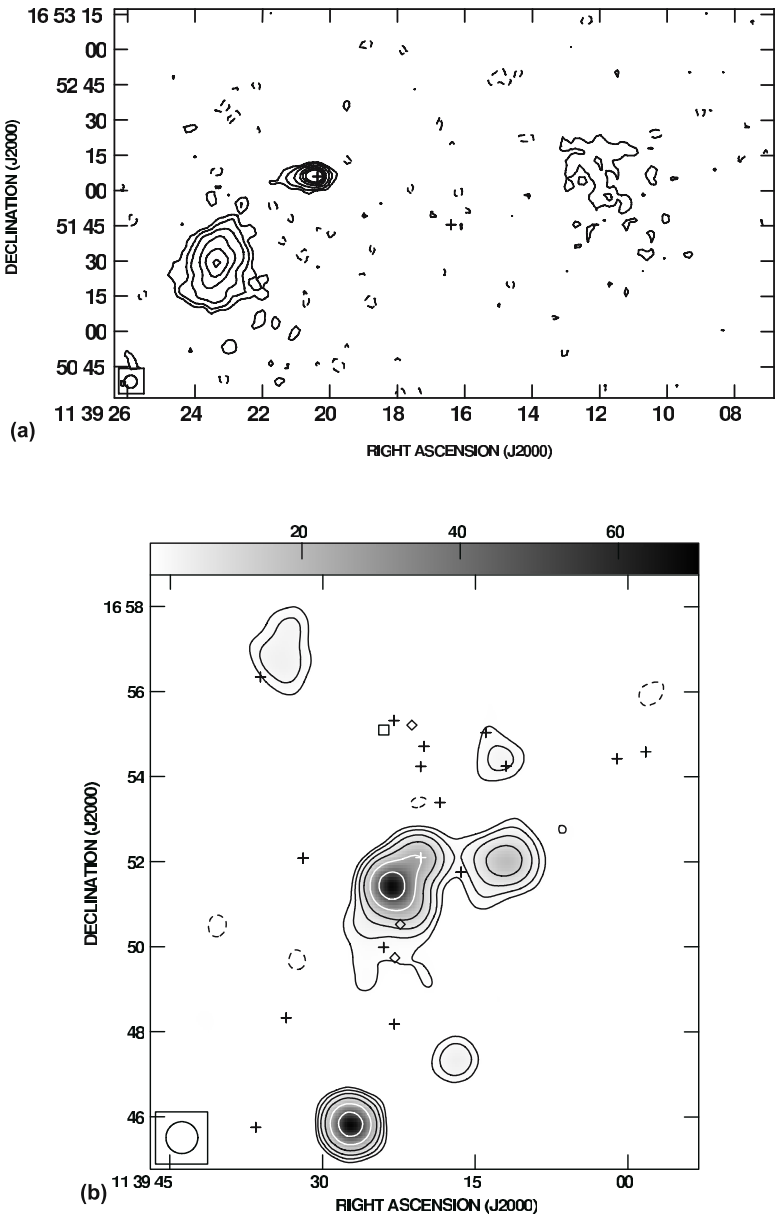

Figure 2. **(a)** PGC 1519010 in 21 cm radio continuum from the FIRST survey (resolution 5.7″). Note the double-lobed structure around the core of the galaxy and the jets emerging from the central galaxy in the FIRST map. The first contour is 0.36 mJy/beam and thereafter the contours are plotted in multiples of 2. Note the bent radio morphology on the eastern side of the core. **(b)** PGC 1519010 in 21 cm radio continuum from the NVSS (resolution 45″). Note the double-lobed structure around the core of the galaxy. The first contour in the map is 1.5 mJy/beam and thereafter the contours are plotted in multiples of 2. Note the bent morphology of the radio source. The plus (+) signs indicate the possible member galaxies of the group/cluster for which photometric redshifts are available, the diamonds indicate member galaxies for which spectroscopic redshifts are available and the square indicates the centre of the cluster given by Gal *et al.* (2003) which we discuss later in the paper.

Bandpass calibration was then applied, after which several frequency channels were collapsed to generate a continuum database. The 240 MHz data were severely affected by radio frequency interference with the net result that only 1.2 MHz of the total 6 MHz was usable and the rest of the data had to be discarded. The 610 MHz images were generated using a total bandwidth of 12.5 MHz. We made images employing the robust weighting scheme (Briggs 1995), setting robust = 0 (between uniform and natural weighting) and robust = 5 (natural weighting) at both frequencies. All the data were self-calibrated and primary beam corrected. The GMRT images are shown in Fig. 3(a and b). We note that the robust = 0 image at 240 MHz has a highly elliptical beam whereas the robust = 5 image at 610 MHz does not add any more information to the WAT structure and hence these are not presented here. Since the WAT is located about 16′ south of the phase centre of our observations, the sensitivity is compromised, especially at 610 MHz where half the power width of primary beam is about 50′.

A striking feature of this WAT, evident from all the maps is that the overall bending of the radio structure is conspicuous only on the eastern side of the core (see Figs. 2 and 3). More clarity about the morphology emerges from a joint inspection of the

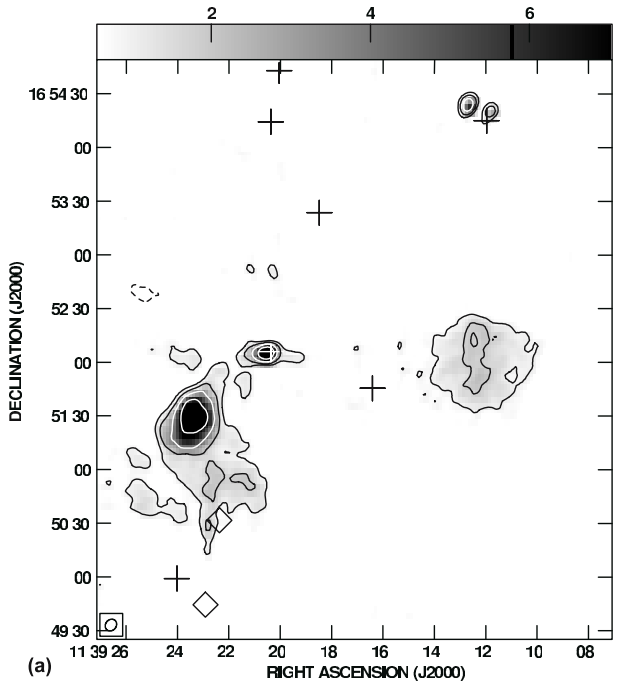

Figure 3. **(a)** The WAT associated with PGC 1519010 in 610 MHz radio continuum imaged using the GMRT. This image was made using Briggs robust = 0 and has an angular resolution of $7'' \times 6''$ at a position angle of -40.3°. The first contour is 0.9 mJy/beam and contours are subsequently plotted in multiples of 2. Note the C-shaped morphology of the radio structure and the clearly bent jet/plume in the east. **(b)** The WAT associated with PGC 1519010 in 240 MHz radio continuum imaged using the GMRT. Note the double-lobed structure around the core of the galaxy. The 240 MHz image was made using natural weighting with Briggs robust = 5 and has an angular resolution of about $43'' \times 34''$ at a position angle of -29.4°. The lowest plotted contour is 6 mJy/beam and the contours then increase in multiples of 2. The explanation of the symbols are as in Fig. 2.

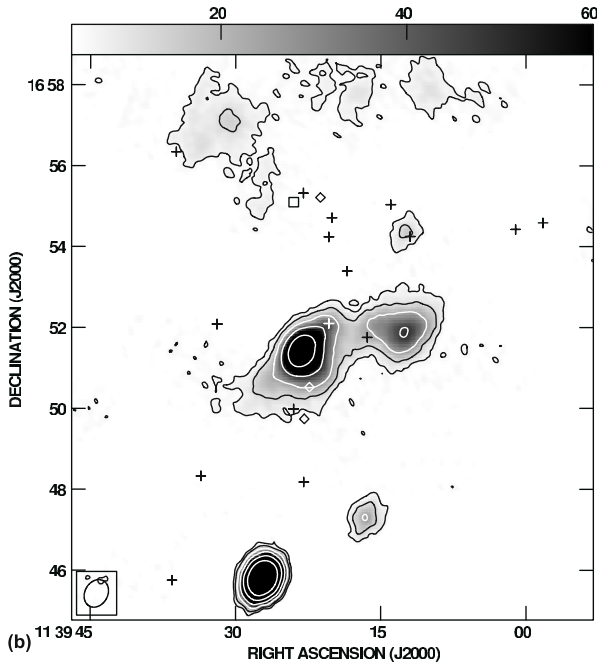

Figure 3. (*Continued*).

GMRT (610 MHz) and the FIRST (1.4 GHz) maps, both having a resolution of $\sim 6''$ (Figs. 2a and 3a). It is seen that the twin jets emerge from the core along the east–west direction and form their lobes. Evidently, only the brighter eastern jet undergoes bending. This occurs gradually along the jet and the plume followed by a sharp bending (towards a position angle of about 220°) of the tail (see Fig. 3a). In stark contrast, no sign of a bent morphology is evident on the western side, despite the sudden flaring of the jet after propagating for nearly 230 kpc from the core.

In Fig. 5, we show the spectral index distributions derived by combining the GMRT images with the NVSS and FIRST images at 1.4 GHz (Fig. 2). For this, the GMRT 240 MHz map was first smoothed to the $45''$ circular beam of the NVSS image. To examine the spectral index in the core region, the spectral index map was generated by combining the GMRT 610 MHz and the 1.4 GHz FIRST maps, after convolving the FIRST image to match the resolution of the 610 MHz GMRT image ($7'' \times 6''$). The spectral index distributions were generated using the $>3\sigma$ emission in the relevant maps. The spectrum is flat near the core ($\alpha = -0.4$) and starts steepening along the eastern jet. The spectrum further steepens to $\alpha \sim -1$ in the southernmost parts of the eastern plume (see Fig. 5). Near the peak of the eastern plume, we find $\alpha \sim -0.7$. Such a smooth variation in the spectral index away from the core is characteristic of WATs (see e.g., Hardcastle 1998).

3.1 *Interesting radio sources located near the WAT*

We also determined the spectral indices of the radio sources found within half a degree of the cD galaxy. The flux densities of the objects obtained from our 240 MHz map

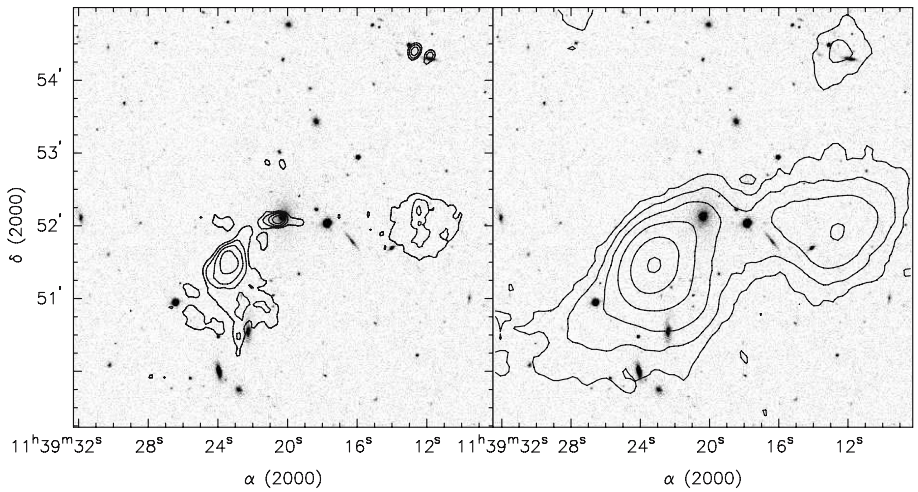

Figure 4. The WAT radio source associated with PGC 1519010 in the 610 MHz (left) and 240 MHz (right) radio continuum superposed on the SDSS R band image plotted on the same angular scale. The angular resolution of the 610 MHz image is $7'' \times 6''$ with a position angle of -40.3° whereas it is $43'' \times 34''$ at a position angle of -29.4° at 240 MHz. The bright optical object between the western jet and plume is classified as a star in the SDSS.

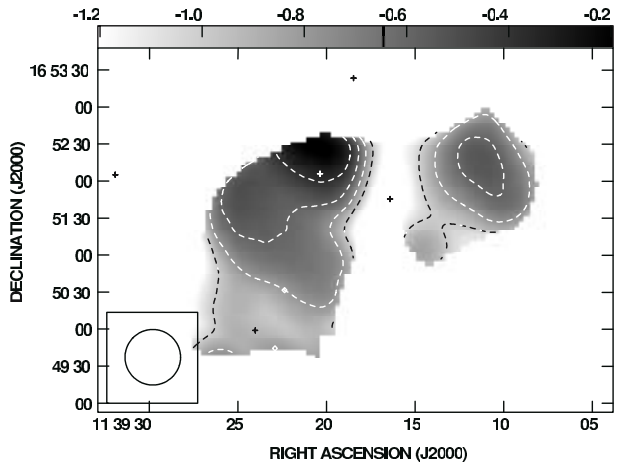

Figure 5. The low resolution ($45''$) spectral index distribution between 240 and 1.4 GHz. Note the gradual steepening of the spectrum along the jet and plume in the east with increasing separation from the core.

and from the FIRST (Becker *et al.* 1995) were used unless the object was extended (in which case NVSS data by Condon *et al.* 1998 were used). Two interesting objects were found and we list their flux densities and spectral indices in Table 2. The first object (GMRT1) has an ultra-steep spectrum with $\alpha = -1.2$ and no optical counterpart is seen in the SDSS. The source is not resolved in the highest resolution maps which translates to an upper limit on its angular extent of $1.8'' \times 0.6''$ at a position angle of 80° obtained from the FIRST. The nearest galaxy listed by SDSS is $15''$ away from

Table 2. Two interesting radio sources found within 15′ of the WAT radio galaxy. The 1.4 GHz flux density for GMRT1 is from FIRST and for GMRT2 is from NVSS data. Note that the radio position of GMRT1 and the position of the optical counterpart of GMRT2 are listed here. We use $S \propto \nu^{\alpha}$.

Object	α_{2000} hh mm ss.s	δ_{2000} dd mm ss.s	$S_{1420\,\mathrm{MHz}}$ mJy	$S_{610\,\mathrm{MHz}}$ mJy	$S_{240\,\mathrm{MHz}}$ mJy	α_{1400}^{240}
GMRT1	11 39 27.3	16 45 50.0	68.7	136	578	−1.2
GMRT2	11 38 23.1	16 51 50.1	24.8	34.5	107.3	−0.82

GMRT1. This strong ultra-steep spectrum object is located ∼3′ to the south of the eastern lobe of the WAT (Figs. 2b, 3b and 7).

The second object (GMRT2) listed in Table 2 lies to the west of the cD and is an extended source. SDSS lists five galaxies within 0.5′ of the radio source which are shown by crosses in Fig. 6. All are faint objects without reliable redshift estimates. Our 610 MHz image (Fig. 6) has picked up faint extended emission which shows that the source is, in fact, a highly asymmetric double of total angular size ∼80″. The likely counterpart is marked with a star in Fig. 6. If this source lies at the distance of the WAT, then its linear size would be about 180 kpc. However, since the host galaxy is faint, this object is likely to be more distant and therefore physically large.

4. Discussion

4.1 *A new WAT and its associated cluster*

The galaxy PGC 1519010, as inferred here from its optical morphology and the association with a powerful WAT, is a cD galaxy (Table 1).

As mentioned above, the most striking and peculiar morphological feature of this WAT is the contrast between the jet/plume bending on the opposite sides of the core, such that the bending is found exclusively on the eastern side. In order to investigate this further, we have inspected the SDSS database. Gal *et al.* (2003), using the SDSS have identified a cluster (NSC 113924+165506) centred ∼3′ north–east of PGC 1519010 (see Fig. 3, the square symbol) and having a photometric redshift of 0.1365, which is close to the value estimated for the WAT. To probe this further, we show in Fig. 7, the distribution of the galaxies listed in SDSS DR6. For the cD progenitor of the WAT, SDSS J113920.37+165206, the SDSS provides three estimates of $z_{\mathrm{phot}} = 0.138, 0.112$ and 0.104. These are in reasonable agreement with the afore-mentioned value for the cluster ($z_{\mathrm{phot}} = 0.1365$, Gal *et al.* 2003). In order to trace the optical field near this region we searched the SDSS for galaxies in the adjacent area and found three galaxies within ∼4′ of the cD galaxy PGC 1519010 (WAT), having spectroscopic redshifts between 0.105 and 0.107. These include U1-8 (U1-8, O'Neil *et al.* 1997), an LSB galaxy lying about 2′ south of the cD, for which Bergmann *et al.* (2003) have estimated a spectroscopic redshift of 0.10715 (photometric redshifts given in the SDSS catalogue are 0.141, 0.095 and 0.091). The second galaxy, SDSS J113921.25+165512.8 is close to U1-8 and SDSS database gives a spectroscopic redshift of 0.105 whereas the photometric redshifts listed there are 0.121, 0.118 and 0.108. The third galaxy lies about 3.5′ north of the cD and SDSS gives a spectroscopic redshift of 0.105 whereas

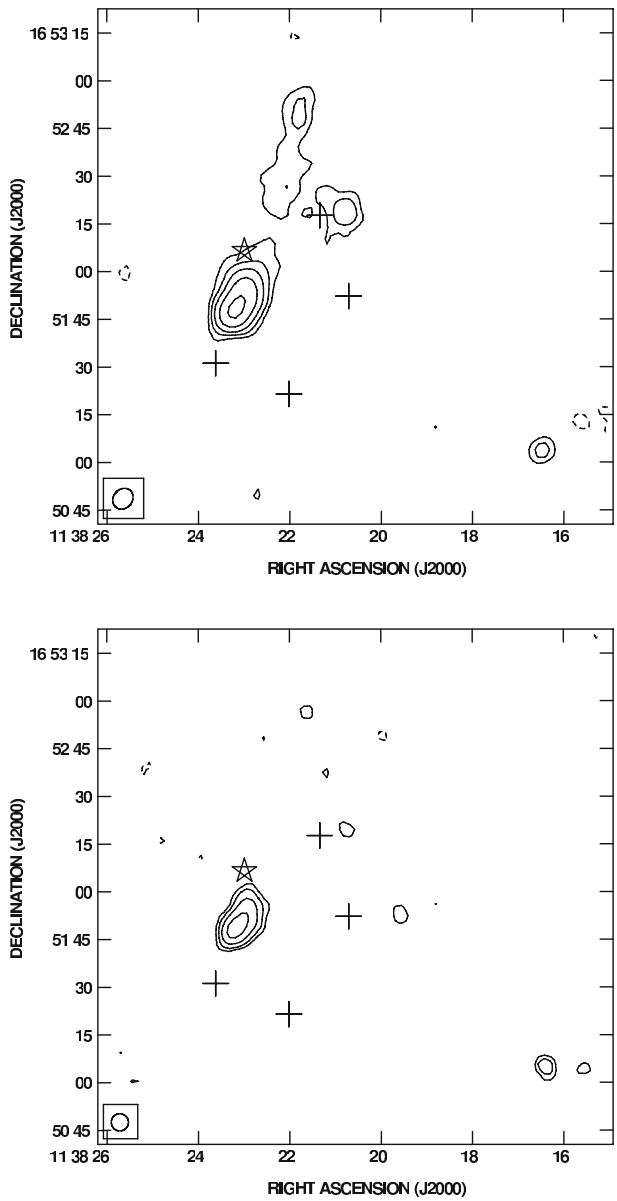

Figure 6. The radio source GMRT2 located to the west of the WAT (Table 2). The 610 MHz GMRT image is shown on the top and the 1.4 GHz image from FIRST is shown on the bottom. The lowest contour at 610 MHz is 0.6 mJy/beam and at 1.4 GHz is 0.45 mJy/beam and subsequently increases in multiples of 2. Note the extended faint emission detected at 610 MHz which is not seen in the FIRST map. Based on this detection, the star marks the position of the likely optical counterpart of the asymmetric double radio source whereas the plus signs (+) mark the positions of the remaining SDSS galaxies found within 30″ of the radio peak.

the photometric redshifts are quoted there to be 0.061, 0.094 and 0.0.095. All these spectroscopic redshifts strongly suggest that the true redshift of the cD (WAT) is close to 0.106, which would also be in reasonable accord with its photometric redshifts

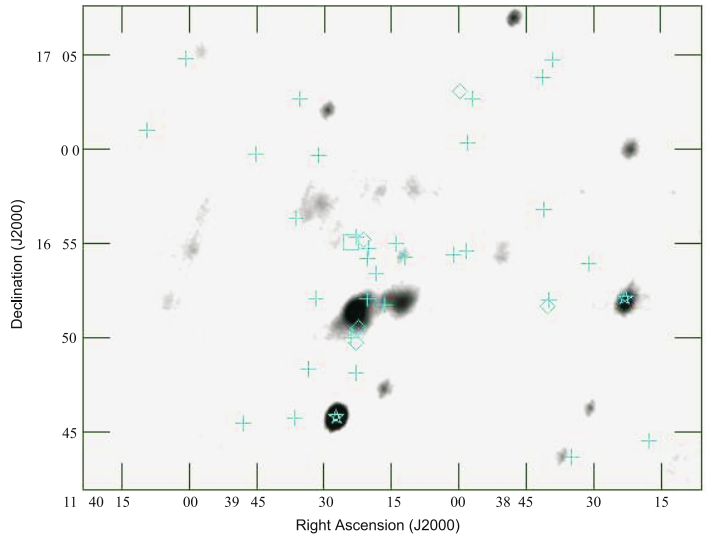

Figure 7. 240 MHz GMRT image of the WAT made with robust weighting = 5 is shown. The positions of 37 galaxies which are likely to be associated with the WAT are marked in the figure. Five of them with known spectroscopic redshift are marked with diamonds. The remaining 32 member galaxies are marked by plus (+) sign. The square marks the position of the cluster centre NSC 113924+165506 ($z = 0.1365$) as given by Gal *et al.* (2003). The cluster is about $20'$ (~ 2.5 Mpc) in size. Note the almost NS chain of galaxies extending southwards from the cluster centre towards the cD. The two interesting radio sources GMRT1 and GMRT2 (Table 2) are marked by stars.

mentioned above. Taking $z = 0.106$ for the cD, the radio luminosities of the WAT are 9.8×10^{23} Watt-Hz^{-1}-Sr^{-1} at 240 MHz and 3.2×10^{23} Watt-Hz^{-1}-Sr^{-1} at 1.4 GHz. These values lie in the region of the FR I/II transition and are thus characteristic of WATs. The distances from the core at which the jet flaring occurs are about 90 kpc and 230 kpc, for the eastern and western jets, respectively.

To probe the large scale environment around the cD, we examined the SDSS DR6 data over a 1° circular region centred at the cD. In particular, we searched for the galaxies for which a physical association with the cD is very probable. The criterion we employed was that the photometric redshifts of the optical objects should be between 0.08 and 0.41. A relatively wide range had to be admitted since the spectroscopic redshifts are available for only a few galaxies in the region. We found that the range roughly represents the typical scatter among the three SDSS estimates of the photometric redshifts for the objects in this region.

The 37 objects that we selected from the above criterion include only five galaxies with known spectroscopic redshifts. Nonetheless, they can be expected to manifest the gross features of the galaxy clustering associated with the cD (WAT) (see Fig. 7). Note also that in the soft X-ray band the *ROSAT* (Voges *et al.* 1999 and references therein) database shows a diffuse source of about 0.5° diameter, covering this region. The detection of hot gas is consistent with the proposed galaxy clustering scenario. As mentioned above, Gal *et al.* (2003) have reported a galaxy cluster with Abell richness zero which is close in both redshift and direction to the galaxy group we identify here to be associated with the WAT.

4.2 *Origin of the WAT*

Perhaps the most remarkable feature emerging from the galaxy distribution (Fig. 7) is a nearly 0.5 Mpc long chain of galaxies stretching from the cD roughly north–south towards the cluster centre defined by Gal *et al.* (2003) and possibly extending also to the south of the cD. It is along this filament that galaxies are likely to have approached the cD prior to merging with it. This galaxy merger scenario is further supported by the shape of the stellar halo of the cD which too is extended roughly north–south. Thus it appears plausible that a bulk motion of the intergalactic gas has been occuring along this galaxy filament. This circumstance may provide potentially interesting clues about the mechanism of the jet disruption and the jet/plume bending in this WAT.

Following upon the early attempts to understand the nature of WATs (e.g., Eilek *et al.* 1984; Leahy 1984; O'Dea & Owen 1985), a number of physical scenarios have been put forward to explain this rare type of phenomenon (section 1). In some of the models, the jet disruption occurs as the jet crosses the ISM of the host galaxy into the ICM, and is thereby subject to either a steep density gradient (Sakelliou & Merrifield 1999), or a side-way ram pressure ('crosswind' arising from bulk motion of the ICM, see Loken *et al.* 1995). In another scenario, the plumes form as the radio lobes of moderately powerful twin-jets are driven outwards due to buoyancy forces (Hardcastle 1999). The latter model is motivated by the observations that the jet in some WATs continue well into the plume (e.g., Hardcastle 1999; Hardcastle & Sakelliou 2004).

Despite the modest sensitivity of our radio maps, the present WAT offers some insight and a broad check on some of the proposed models. This is because of the morphological contrast observed between its two jet/plume structures, eventhough the kinetic powers of the two jets are expected to be similar. Firstly, in this WAT a correlation is clearly seen between the bending properties of the jet and the resulting plume. As seen from Figs. 2 and 4, the western jet must be propagating straight for about 230 kpc before flaring and the resulting radio plume likewise shows no sign of bending. A contrasting pattern is seen on the eastern side of the core, where the collimated jet undergoes a steady bending until its disruption and thereafter the resulting plume too exhibits a sharp bend consistent with the bent trajectory of the eastern jet. From this correlated behaviour it appears that a viable mechanism for jet disruption in WATs should be able to bend both the plume and the associated jet. This requirement casts some doubt on the mechanism which seeks to explain the jet disruption in terms of collision with a dense gas cloud (section 1). Indeed, the observed alignment of the bent eastern plume with the chain of galaxies (see Fig. 7) would seem to be basically consistent with the ram pressure scenario involving bulk relative motion between the ICM and the radio galaxy. The observed radio structure would also imply that the crosswind is in the NE–SW direction with the plume finally aligning with it (see Fig. 3a). However, were the ram pressure of the ICM crosswind effective only after the jet crosses the ISM/ICM interface, it would be hard to explain the steady bending of the preceding collimated portion of the jet. We may recall that a similar difficulty for the basic crosswind scenario (e.g., Loken *et al.* 1995) has been noticed in the case of the WAT 0647+693 where the 50 kpc long collimated western jet exhibits a steady bending before its disruption (Hardcastle & Sakelliou 2004). It appears, therefore, that the effect of the ICM crosswind moving along the galaxy filament which may eventually cause the sharp bending of the plume and its alignment along the filament also acts on the progenitor jet before its flaring. In fact, for the head-tail radio galaxy

NGC 1265, Jones & Owen (1979) have proposed that a pressure gradient set-up in the ISM due to the motion of the galaxy against ICM can bend its jet within the ISM, provided their Mach number is not too large. But, even if such a mechanism is viable for the present case, it will be required to explain the near absence of bending of the western jet and its radio plume (Figs. 3a and 4). It would seem *ad hoc* to explain the contrasting pattern on the two sides by postulating a much larger kinetic power for the western jet. A conceivable alternative would be to postulate the existence of inhomogeneities in the ICM on 100 kpc scale, but here too the inhomogeneity will have to be positioned, so as to operate on just one side of the nucleus. Nonetheless, this possibility needs to be investigated further. As a first step, it would be useful to make a deeper radio image of this WAT, in order to look for any bent faint extensions of the western plume and to trace the trajectories of the two jets more clearly. Secondly, this object is an excellent target for multi-object spectroscopy needed for a better delineation of the galaxy distribution around the cD. Finally, targeted X-ray imaging of this region is needed to establish the morphological details of the *ROSAT* detected diffuse X-ray source, so that the suspected filamentary gravitational potential well can be properly traced.

5. Summary

In this paper, we report the GMRT detection of a new wide-angle-tail radio source associated PGC 1519010 which we find to be a cD galaxy. These observations at 610 and 240 MHz were originally aimed at studying the low surface brightness galaxy located $16'$ to the north. The power of the radio source at 240 MHz is $\sim 10^{24}$ Watt-Hz^{-1}-Sr^{-1} which is close to the FR I/FR II break. Using the SDSS DR6 database, we have identified a cluster of 37 galaxies likely to be associated with the WAT. Further the *ROSAT* all sky survey shows faint diffuse extended X-ray emission in the same region which indicates the presence of a hot intracluster medium. Using the spectroscopic redshifts available for a few galaxies close to the cD, we suggest that the redshift of the group/cluster of galaxies associated with the WAT is 0.106. Moreover, we note that the clustering of member galaxies close to the WAT indicates a filament along which galaxies have been merging with the cD. This scenario also finds support in the observed NS extension of the stellar halo of the cD galaxy.

Our radio observations have highlighted the peculiar morphology of this WAT radio source. The source shows constrasting morphology on the two sides of the core: the eastern jet emerges from the core and undergoes a gradual bending before being disrupted to form the plume which itself continues to bend in the same direction. On the western side, the jet emerging from the core appears to continue straight for about 230 kpc, before being disrupted to form the faint plume which too shows no bent extension. The very different behaviour on the two sides suggests that the mechanism responsible for the plume bending is also causing the jet to bend. Several mechanisms for jet bending have been put forward and separate mechanisms have also been invoked to explain the jet and plume bending (section 1). However, from our present results for the WAT associated with PGC 1519010, the similar bending shown by the jet and the plume on the east of the core suggests that the same bending mechanism is operating on both components.

Several theories have tried to explain the WAT radio morphology. From our data, we favour the crosswind mechanism (Loken *et al.* 1995) wherein the jet runs into the

crosswind due to the merging of clusters and which, in turn, exerts ram pressure on the jet/plume, causing it to bend. We note that the eastern jet continues for about 90 kpc before being disrupted into a plume. Around this distance, the jet would have crossed the hot ISM of the host elliptical galaxy and would encounter the lower density ICM, causing it to flare. The direction of the bending of the jet/plume agrees with the filament of galaxies and the extension of the cD stellar halo. Diffuse X-ray emission too is extended roughly in the NS direction, lending further support to the crosswind mechanism. However, explaining the unaffected/unbent western jet/plume is difficult unless inhomogeneities in the ICM are invoked. More sensitive and high angular resolution observations are thus required to obtain a better understanding of this interesting system.

We also report the detection of an ultra-steep spectrum source ($\alpha = -1.2$) to the south of the eastern plume, which does not have an optical counterpart in SDSS. Another interesting source we have found is a highly asymmetric radio double source located to the west of WAT.

Acknowledgements

We thank the staff of GMRT who have made these observations possible. GMRT is run by the National Centre for Radio Astrophysics of the Tata Institute of Fundamental Research. This research has made use of the Sloan Digital Sky Survey (http://www.sdss.org) Data Release 6 (SDSS DR6), the Faint Images of Radio Sky at Twenty cms (FIRST) survey, the NRAO VLA Sky Survey (NVSS), NASA's Astrophysics Data System (ADS), ROSAT Data Archive (of the Max-Planck-Institut fr extraterrestrische Physik (MPE) at Garching, Germany), NASA/IPAC Extragalactic Database (NED) (which is operated by the Jet Propulsion Laboratory, California Institute of Technology, under contract with the National Aeronautics and Space Administration), and Hyperleda (http://leda.univ-lyon1.fr).

References

Ananthakrishnan, S., Rao, A. P. 2002, *Multicolour Universe* (eds) Manchanda, R., Paul, B., p. 233.
Becker, R. H., White, R. L., Helfand, D. J. 1995, *Astrophys. J.*, **450**, 559.
Bergmann, M. P., Jorgensen, I., Hill, G. J. 2003, *Astron. J.*, **125**, 116.
Blanton, E., Gregg, M. D., Helfand, D. J., Becker, R. H., White, R. L. 2000, *Astrophys. J.*, **531**, 118.
Blanton, E., Gregg, M. D., Helfand, D. J., Becker, R. H., Leighly, K. M. 2001, *Astron. J.*, **121**, 2915.
Blanton, E., Gregg, M. D., Helfand, D. J., Becker, R. H., White, R. L. 2003, *Astron. J.*, **125**, 1635.
Briggs, D. 1995, *High Fidelity Deconvolution of Moderately Resolved Sources*, PhD thesis.
Burns, J. O., White, R. A., Hough, D. H. 1981, *Astron. J.*, **86**, 1.
Burns, J. O., Rhee, G., Owen, F. N., Pinkney, J. 1994, *Astrophys. J.*, **423**, 94.
Condon, J. J., Cotton, W. D., Greisen, E. W., Yin, Q. F., Perley, R. A., Taylor, G. B., Broderick, J.J. 1998, *Astron. J.*, **115**, 1693.
Das, M., Kantharia, N. G., Ramya, S., Prabhu, T. P., McGaugh, S. S., Vogel, S. N. 2007, *Mon. Not. R. Astron. Soc.*, **379**, 11.
Das, M., McGaugh, S. S, Kantharia, N. G., Vogel, S. N. 2008, In: Dark Galaxies and Lost Baryons, *Proceedings of the IAU Symposium*, **244**, 352.
Das, M., Kantharia, N. G., Vogel, S. N., McGaugh, S. S. 2009, *Radio Emission from AGN in Giant LSB Galaxies*, In: Low Frequency Radio Universe (in press).

Doe, S. M., Ledlow, M. J., Burns J. O., White, R. A. 1995, *Astron. J.*, **110**, 46.
Eilek, J., Burns, J. O., O'Dea, C. P., Owen, F. N. 1984, *Astrophys. J.*, **278**, 37.
Fanaroff, B. L., Riley, J. M. 1974, *Mon. Not. R. Astron. Soc.*, **167**, 31.
Gal, R. R., De Carvalho, R. R., Lopes, P. A. A., Djorgovski, S. G., Brunner, R. J., Mahabal, A., Odewahn, S. C. 2003, *Astron. J.*, **125**, 2064.
Gopal-Krishna, Wiita, P. J. 1987, *Mon. Not. R. Astron. Soc.*, **226**, 531.
Gomez, P. L., Ledlow, M. J., Burns, J. O., Pinkey, J., Hill, J. M. 1997, *Astron. J.*, **114**, 1711.
Hardcastle, M. J. 1998, *Mon. Not. R. Astron. Soc.*, **298**, 569.
Hardcastle, M. J. 1999, *Astron. Astrophys.*, **349**, 341.
Hardcastle, M. J., Sakelliou, I. 2004, *Mon. Not. R. Astron. Soc.*, **349**, 560.
Hardcastle, M. J., Sakelliou, I., Worrall, D. M. 2005, *Mon. Not. R. Astron. Soc.*, **359**, 1007.
Higgins, S. W., O'Brien, T. J., Dunlop, J. S. 1999, *Mon. Not. R. Astron. Soc.*, **209**, 273.
Hooda, J. S., Wiita, P. J. 1996, *Astrophys. J*, **470**, 21.
Jetha, N., Hardcastle, M., Sakelliou, I. 2006, *Mon. Not. R. Astron. Soc.*, **368**, 609.
Jones, T. W., Owen, F. N. 1979, *Astrophys. J.*, **234**, 818.
King, I. 1962, *Astron. J.*, **67**, 471.
King, I. 1966, *Astron. J.*, **71**, 276.
Kormendy, J. 1977, *Astrophys. J.*, **218**, 333.
Leahy, J. P. 1984, *Mon. Not. R. Astron. Soc.*, **208**, 323.
Leahy, J. P. 1993, *Jets in Extragalactic Radio Sources*, Proceedings of a Workshop Held at Ringberg Castle, Tegernsee, FRG, September 22–28, 1991 (eds) Rser, H.-J., Meisenheimer, K., Springer-Verlag, Berlin-Heidelberg-New York. Also Lecture Notes in Physics, volume **421**, 1993, p. 1.
Loken, C., Roettiger, K., Burns, J. O., Normal, M. 1995, *Astrophys. J.*, **445**, 80.
O' Neil, K., Bothun, G. D., Cornell, M. E. 1997, *Astron. J.*, **113**, 1212.
O' Dea, C. P., Owen, F. N. 1985, *Astron. J.*, **90**, 927.
O'Donoghue, Aileen, A., Owen, F. N., Eilek, J. A. 1990 *Astrophys. J. Suppl. Ser.*, **72**, 75.
O'Donoghue, Aileen, A., Eilek, J. A., Owen, F. N. 1993 *Astrophys. J.*, **408**, 428.
Owen, F. N., Rudnick, L. 1976, *Astrophys. J.*, **205**, L1.
Paturel, G., Petit, C., Prugniel, P., Theureau, G., Rousseau, J., Brouty, M., Dubois, P., Cambrésy, L. 2003, *Astron. Astrophys.*, **412**, 45.
Sakelliou, I., Merrifield, M. R. 1999, *Mon. Not. R. Astron. Soc.*, **305**, 417.
Swarup, G., Ananthakrishnan, S., Kapahi, V. K. *et al.* 1991, *Curr. Sci.*, **60**, 95.
Voges, W. *et al.* 1999, *Astron. Astrophys.*, **349**, 389.

J. Astrophys. Astr. (2009) **30,** 53–69

A Self-similar Flow Behind a Shock Wave in a Gravitating or Non-gravitating Gas with Heat Conduction and Radiation Heat-flux

J. P. Vishwakarma* & Arvind K. Singh
Department of Mathematics and Statistics, D.D.U. Gorakhpur University, Gorakhpur 273 009, India.
**e-mail: jpv_univgkp@yahoo.com*

Received 2008 March 16; accepted 2009 March 16

Abstract. The propagation of a spherical shock wave in an ideal gas with heat conduction and radiation heat-flux, and with or without self-gravitational effects, is investigated. The initial density of the gas is assumed to obey a power law. The heat conduction is expressed in terms of Fourier's law and the radiation is considered to be of the diffusion type for an optically thick grey gas model. The thermal conductivity and the absorption coefficient are assumed to vary with temperature and density, and the total energy of the wave to vary with time. Similarity solutions are obtained and the effects of variation of the heat transfer parameters, the variation of initial density and the presence of self-gravitational field are investigated.

Key words. Shock wave—self-similar flow—self-gravitational effects—heat transfer effects—variable initial density—variable total energy.

1. Introduction

The explanation and analysis for the internal motion in stars is one of the basic problem in astrophysics. According to the observational data, the unsteady motion of large mass of the gas followed by sudden release of energy results flare-ups in novae and supernovae. A qualitative behaviour of the gaseous mass may be discussed with the help of the equations of motion and equilibrium taking gravitational forces into account. Numerical solutions for self-similar adiabatic flows in self-gravitating gas were obtained by Sedov (1959) and Carrus *et al.* (1951), independently. Purohit (1974) and Singh & Vishwakarma (1983) have discussed homothermal flows behind a spherical shock wave in a self-gravitating gas using similarity method. Nath *et al.* (1991) have studied the above problem assuming the flow to be adiabatic and self-similar and obtained the effects of the presence of a magnetic field. Shock wave through a variable density medium have been treated by Sedov (1959), Sakurai (1956), Rogers (1957), Rosenau & Frankenthal (1976a), Nath *et al.* (1991), Vishwakarma & Yadav (2003) and others. Their results are more applicable to the shock formed in the deep interior of stars.

Marshak (1958) studied the effects of radiation on the shock propagation by introducing the radiation diffusion approximation. Using the same mode of radiation,

Elliott (1960) discussed the conditions leading to self-similarity with a specified functional form of the mean free path of radiation and obtained a solution for self-similar spherical explosions. Wang (1964), Helliwell (1969) and Nicastro (1970) treated the problems of radiating walls, either stationary or moving, generating shocks at the head of self-similar flow-fields. The non-similar problem of a blast wave associated with diffusive radiation was analysed by Kim *et al.* (1975), using matched expansions upon the assumption that the radiation and conduction effects are significant only in a boundary-layer around the centre of explosion. Gretler & Wehle (1993) studied the propagation of blast waves with exponential heat release by taking internal heat conduction and thermal radiation in a detonating medium. Also, Abdel-Raouf & Gretler (1991) obtained the non-self-similar solution for the blast waves with internal heat transfer effects. Ghoniem *et al.* (1982) obtained a self-similar solution for spherical explosions taking into account the effects of both conduction and radiation in the two limits of Rosseland radiative diffusion and Plank radiative emission. In these works, where both the radiation and conduction effects are considered, the density of the medium ahead of the shock is taken to be uniform and effects of self-gravitation of the medium are not taken into consideration.

The purpose of this study is, therefore, to obtain self-similar solutions for the shock propagation in a non-uniform gas with or without self-gravitational effects, in the presence of heat conduction and radiation heat flux. The mediums ahead and behind the shock front are assumed to be inviscid and to behave as thermally perfect gases. The initial density of gas is assumed to vary as some power of distance. The heat transfer fluxes are expressed in terms of Fourier's law for heat-conduction and a diffusion radiation mode for an optically thick grey gas, which is typical of large-scale explosions. The thermal conductivity and absorption coefficient of the gas are assumed to be proportional to appropriate powers of temperature and density (Ghoniem *et al.* 1982). Also, it is assumed that the gas is grey and opaque, and the shock is isothermal. The assumption that the shock is isothermal is a result of the mathematical approximation in which the heat flux is taken to be proportional to the temperature gradient; this excludes the possibility of temperature jump (Zel'dovich & Raizer 1967; Rosenau & Frankenthal (1976b, 1978); Bhowmick 1981; Singh & Srivastava 1982). The counter pressure (the pressure ahead of the shock) is taken into account. The radiation pressure and radiation energy are neglected (Elliott 1960; Wang 1964; Ghoniem *et al.* 1982; Abdel-Raouf & Gretler 1991). The assumption of an optically thick grey gas is physically consistent with the neglect of radiation pressure and radiation energy (Nicastro 1970). The total energy of the flow-field behind the shock is assumed to be increasing with time due to pressure exerted by a piston or inner expanding surface. The gas ahead of the shock is assumed to be at rest. Effects of viscosity and magnetic field are not taken into account. The results of numerical calculations were shown in the form of graphs and tables. A comparative study was made between the results with and without self-gravitation. Also, the effects of variation of heat transfer parameters and the initial density exponent on the flow-field behind the shock and the shock velocity were investigated.

2. Equations of motion and boundary conditions

The fundamental equations governing the unsteady and spherically symmetric motion of an inviscid, ideal and self-gravitating gas, with heat conduction and radiation heat

flux taken into account, may be written as (Carrus *et al.* 1951; Ghoniem *et al.* 1982):

$$\frac{\partial \rho}{\partial t} + u\frac{\partial \rho}{\partial r} + \rho\frac{\partial u}{\partial r} + \frac{2\rho u}{r} = 0, \tag{1}$$

$$\frac{\partial u}{\partial t} + u\frac{\partial u}{\partial r} + \frac{1}{\rho}\frac{\partial p}{\partial r} + \frac{Gm}{r^2} = 0, \tag{2}$$

$$\frac{\partial m}{\partial r} - 4\pi\rho r^2 = 0, \tag{3}$$

$$\frac{\partial e}{\partial t} + u\frac{\partial e}{\partial r} - \frac{p}{\rho^2}\left(\frac{\partial \rho}{\partial t} + u\frac{\partial \rho}{\partial r}\right) + \frac{1}{\rho r^2}\frac{\partial}{\partial r}(r^2 q) = 0, \tag{4}$$

where r and t are independent space and time co-ordinates, ρ is the density, p the pressure, u the fluid velocity, m the mass of the gas contained in the sphere of radius r, G the gravitational constant, e the internal energy and q the heat flux. In the non-gravitating case, the equation (3) and the term Gm/r^2 in the equation (2) do not occur.

The total heat flux q, which appears in the energy equation may be decomposed as:

$$q = q_C + q_R, \tag{5}$$

where q_C is the conduction heat flux, and q_R the radiation heat flux.

According to Fourier's law of heat conduction

$$q_C = -K\frac{\partial T}{\partial r}, \tag{6}$$

where K is the coefficient of thermal conductivity of the gas and T is the absolute temperature.

Assuming local thermodynamic equilibrium and using the radiative diffusion model for an optically thick grey gas (Pomraning 1973), the term q_R, which represents radiative heat flux, may be obtained from the differential approximation of the radiation-transport equation in the diffusion limit as:

$$q_R = -\frac{4}{3}\left(\frac{\sigma}{\alpha_R}\right)\frac{\partial T^4}{\partial r}, \tag{7}$$

where σ is the Stefan–Boltzmann constant and α_R is the Rosseland mean absorption coefficient.

The above system of equations should be supplemented with an equation of state. A perfect gas behaviour of the medium is assumed, so that

$$p = \Gamma\rho T, \qquad e = \frac{p}{\rho(\gamma - 1)}, \tag{8a, b}$$

where Γ is the gas constant and γ is the ratio of specific heats.

The thermal conductivity K and the absorption coefficient α_R are assumed to vary with temperature and density. These can be written in the form of power laws, namely (Ghoniem *et al.* 1982)

$$K = K_0\left(\frac{T}{T_0}\right)^{\beta_C}\left(\frac{\rho}{\rho_0}\right)^{\delta_C}, \qquad \alpha_R = \alpha_{R_0}\left(\frac{T}{T_0}\right)^{\beta_R}\left(\frac{\rho}{\rho_0}\right)^{\delta_R}, \tag{9a, b}$$

where subscript '0' denotes a reference state. The exponents in the above equations should be compatible with the conditions of the problem and the form of the required solution.

We have also assumed that the total energy of the explosion is non-constant and increasing with time as (Rogers 1958; Freeman 1968; Director & Dabora 1977)

$$E = E_0 t^s, \tag{10}$$

where E_0 and s are constants. This increase of energy may be achieved by the pressure exerted on the gas by a piston. The piston may be, physically, the surface of the stellar corona or the condensed explosives or the diaphragm containing a very high pressure driver gas, at $t = 0$. By sudden expansion of the stellar corona or the detonation products or the driver gas into the ambient gas, a shock wave is produced in the ambient gas, in an infinitesimal time interval t_0 (say). The shocked gas is separated from the expanding surface which is a contact discontinuity. This contact surface acts as a 'piston' for the shock wave in the ambient medium.

A shock (spherical) is supposed to be propagating in the undisturbed ideal gas with variable density $\rho = Ar^{-w}$, where A and w are constants.

The flow variables immediately ahead of the shock front are:

$$u_1 = 0, \tag{11a}$$

$$\rho_1 = AR^{-w}, \tag{11b}$$

$$p_1 = \frac{2\pi G A^2}{(w-1)(3-w)} R^{2-2w}$$
in the case when the gas is self-gravitating, (11c)

$$p_1 = \text{constant in the non-gravitating case}, \tag{11d}$$

$$m_1 = \frac{4\pi A}{3-w} R^{3-w}, \tag{11e}$$

$$q_1 = 0 \text{ (Laumbach \& Probstein 1970)}, \tag{11f}$$

where R is the shock radius and the subscript '1' denotes the conditions immediately ahead of the shock.

The shock is assumed to be isothermal (the formation of the isothermal shock is a result of the mathematical approximation in which the flux is taken to be proportional to the temperature gradient. This excludes the possibility of a temperature jump, see for example, Zel'dovich & Raizer 1967; Rosenau & Frankenthal 1976b, 1978), and the conditions across it are:

$$\rho_1 V = \rho_2 (V - u_2), \tag{12a}$$

$$p_1 + \rho_1 V^2 = p_2 + \rho_2 (V - u_2)^2, \tag{12b}$$

$$e_1 + \frac{p_1}{\rho_1} + \frac{V^2}{2} + \frac{q_2}{\rho_1 V} = e_2 + \frac{p_2}{\rho_2} + \frac{1}{2}(V - u_2)^2, \tag{12c}$$

$$T_1 = T_2, \tag{12d}$$

$$m_1 = m_2, \tag{12e}$$

where subscript '2' denotes condition immediately behind the shock front, and $V = dR/dt$ denotes the velocity of the shock front. From equations (12), we get:

$$u_2 = \left(1 - \frac{1}{\gamma M^2}\right) V, \tag{13a}$$

$$\rho_2 = \gamma \rho_1 M^2, \tag{13b}$$

$$p_2 = \rho_1 V^2, \tag{13c}$$

$$m_2 = \frac{4\pi A}{3 - w} R^{3-w}, \tag{13d}$$

$$q_2 = \frac{1}{2}\left(\frac{1}{\gamma^2 M^4} - 1\right) \rho_1 V^3, \tag{13e}$$

where $M = (\rho_1 V^2/\gamma p_1)^{\frac{1}{2}}$ is the shock-Mach number.

3. Similarity solutions

Following the general similarity analysis we define the two characteristic parameters 'a' and 'b' with independent dimensions as:

$$[a] = [A], \tag{14a}$$

and

$$[b] = \left[\frac{E_0}{A}\right]. \tag{14b}$$

The single dimensionless independent variable in this case will be:

$$\eta = \left[\frac{\nu E_0}{A}\right]^{-1/(5-w)} r t^{-\delta}, \tag{15a}$$

where

$$\delta = \frac{2 + s}{5 - w}, \tag{15b}$$

and ν is a constant such that η assumes the value '1' at the shock front. This gives the shock propagation law in the explicit form as:

$$R = \left[\frac{\nu E_0}{A}\right]^{1/(5-w)} t^{\delta}. \tag{16}$$

This gives the shock propagation law as:

$$\frac{V}{V_0} = \left(\frac{R}{R_0}\right)^{(\delta-1)/\delta}, \tag{17}$$

where V_0 and R_0 are the velocity and radius of the shock at the instant of its generation.

We express the fluid velocity u, density ρ, pressure p, mass m and total heat flux q as:

$$u = VU(\eta), \qquad \rho = \rho_1 D(\eta), \qquad p = V^2 \rho_1 P(\eta), \tag{18a–c}$$

$$m = \rho_1 R^3 N(\eta), \qquad q = V^3 \rho_1 Q(\eta), \tag{18d–e}$$

where U, D, P, N and Q are functions of η only.

For the existence of similarity solutions the shock-Mach number M should be constant. Therefore, in the gravitating case

$$\delta = \frac{2}{w} \quad \text{and} \quad w = \frac{10}{s+4}, \tag{19a, b}$$

where $1 < s < 6$ $(1 < w < 2)$ or $0 \le s < 1$ $(2 < w \le 5/2)$.

In the non-gravitating case

$$\delta = \frac{2}{2-w} \quad \text{and} \quad s = \frac{6}{2-w}, \tag{20a, b}$$

where $0 < w < 2$ $(3 < s < \infty)$.

The conservation equations (1) to (4) can be transformed into a system of ordinary differential equations

$$(U-\eta)\frac{dD}{d\eta} + D\frac{dU}{d\eta} + \frac{2DU}{\eta} - wD = 0, \tag{21}$$

$$(U-\eta)\frac{dU}{d\eta} + \frac{1}{D}\frac{dP}{d\eta} + \left(\frac{\delta-1}{\delta}\right)U + \frac{G_0 N}{\eta^2} = 0, \tag{22}$$

$$\frac{dN}{d\eta} = 4\pi D\eta^2, \tag{23}$$

$$\begin{aligned}(U-\eta)D\frac{dP}{d\eta} - \gamma P(U-\eta)\frac{dD}{d\eta} + (\gamma-1)D\frac{dQ}{d\eta} \\ + 2\left(\frac{\delta-1}{\delta}\right)PD + D(\gamma-1)\left(\frac{2Q}{\eta} + wP\right) = 0,\end{aligned} \tag{24}$$

where

$$G_0 = \frac{(w-1)(3-w)}{2\pi\gamma M^2}. \tag{25}$$

By using equations (6), (7) and (9) in (5) we get:

$$q = -\left[\frac{K_0}{T_0^{\beta_C}\rho_0^{\delta_C}} T^{\beta_C}\rho^{\delta_C} + \frac{16}{3}\frac{\sigma T_0^{\beta_R}\rho_0^{\delta_R}}{\alpha_{R_0}} T^{3-\beta_R}\rho^{-\delta_R}\right]\frac{\partial T}{\partial r}. \tag{26}$$

Using the equations (8) and (18) in (26) we get:

$$Q = -\frac{d}{d\eta}\left(\frac{P}{D}\right)\left[\frac{K_0 A^{\delta_C-1} P^{\beta_C} \delta^{\frac{\delta}{\delta-1}\{w(\delta_C-1)+1\}} V^{2\beta_C-1-\frac{\delta}{\delta-1}\{w(\delta_C-1)+1\}}}{T_0^{\beta_C}\rho_0^{\delta_C}\Gamma^{\beta_C+1}D^{\beta_C-\delta_C}}\right.$$

$$\times\left\{\frac{\nu E_0}{A}\right\}^{\frac{w(\delta_C-1)+1}{(\delta-1)(5-w)}} + \frac{16\sigma T_0^{\beta_R}\rho_0^{\delta_R} P^{3-\beta_R} A^{-\delta_R-1}\delta^{\frac{\delta}{\delta-1}\{1-w(\delta_R+1)\}}}{3\alpha_{R_0}\Gamma^{4-\beta_R}D^{3-\beta_R+\delta_R}}$$

$$\left.\times\left\{\frac{\nu E_0}{A}\right\}^{\frac{1-w(\delta_R+1)}{(\delta-1)(5-w)}}\right]. \tag{27}$$

Equation (27) shows that the similarity solution of the present problem exists only when

$$\beta_C = 1 + \frac{1}{2\delta-2}\left[1 + w\delta(\delta_C - 1)\right], \tag{28a}$$

and

$$\beta_R = 2 - \frac{1}{2\delta-2}\left[1 - w\delta(\delta_R + 1)\right]. \tag{28b}$$

Therefore, equation (27) becomes:

$$Q = -X\left[\frac{1}{D}\frac{dP}{d\eta} - \frac{P}{D^2}\frac{dD}{d\eta}\right], \tag{29}$$

where

$$X = \left(\frac{P}{D}\right)^{(2\delta-1)/(2\delta-2)}\left[\Gamma_C\delta^{\frac{\delta}{\delta-1}\{1+w(\delta_C-1)\}}P^{\frac{w\delta(\delta_C-1)}{2\delta-2}}D^{\delta_C-\frac{w\delta(\delta_C-1)}{2\delta-2}}\right.$$

$$\left.+\Gamma_R\delta^{\frac{\delta}{\delta-1}\{1-w(\delta_R+1)\}}P^{\frac{-w\delta(\delta_R+1)}{2\delta-2}}D^{\frac{w\delta(\delta_R+1)}{2\delta-2}-\delta_R}\right]. \tag{30}$$

Here, Γ_C and Γ_R are the conductive and radiative non-dimensional heat transfer parameters, respectively. The parameters Γ_C and Γ_R depend on the thermal conductivity K and the mean free path of radiation $1/\alpha_R$, respectively, and also on the exponents δ and w, and they are given by:

$$\Gamma_C = \frac{K_0 A^{\delta_C-1}}{T_0\Gamma^2\rho_0^{\delta_C}}(T_0\Gamma)^{-\frac{1+w\delta(\delta_C-1)}{2\delta-2}}\left(\frac{\nu E_0}{A}\right)^{\frac{1+w(\delta_C-1)}{(\delta-1)(5-w)}}, \tag{31a}$$

and

$$\Gamma_R = \frac{16\sigma A^{-\delta_R-1}\rho_0^{\delta_R}T_0^2}{3\alpha_{R_0}\Gamma^2}(T_0\Gamma)^{\frac{w\delta(\delta_R+1)-1}{2\delta-2}}\left(\frac{\nu E_0}{A}\right)^{\frac{1-w(\delta_R+1)}{(\delta-1)(5-w)}}. \tag{31b}$$

Using the similarity transformations (18) and the equation (16), equations (13) can be written as:

$$U(1) = \left(1 - \frac{1}{\gamma M^2}\right), \tag{32a}$$

$$D(1) = \gamma M^2, \tag{32b}$$

$$P(1) = 1, \tag{32c}$$

$$N(1) = \frac{4\pi}{3-w}, \tag{32d}$$

$$Q(1) = \frac{1}{2}\left(\frac{1}{\gamma^2 M^4} - 1\right). \tag{32e}$$

By solving equations (21), (22), (24) and (29) for $dD/d\eta$, $dP/d\eta$, $dQ/d\eta$, $dU/d\eta$, we have:

$$\frac{dD}{d\eta} = -\frac{D}{U-\eta}\left[\frac{dU}{d\eta} + \frac{2U}{\eta} - w\right] \tag{33}$$

$$\frac{dP}{d\eta} = -D\left[(U-\eta)\frac{dU}{d\eta} + \left(\frac{\delta-1}{\delta}\right)U + \frac{G_0 N}{\eta^2}\right], \tag{34}$$

$$\begin{aligned}\frac{dQ}{d\eta} = {} & \frac{(U-\eta)^2 D - \gamma P}{\gamma - 1}\frac{dU}{d\eta} + \frac{D(U-\eta)}{\gamma-1}\left[\left(\frac{\delta-1}{\delta}\right)U + \frac{G_0 N}{\eta^2}\right] \\ & - \frac{\gamma P}{\gamma-1}\left(\frac{2U}{\eta} - w\right) - \frac{2Q}{\eta} - wP - \frac{2P}{\gamma-1}\left(\frac{\delta-1}{\delta}\right),\end{aligned} \tag{35}$$

$$\begin{aligned}\frac{dU}{d\eta} = {} & \frac{D(U-\eta)}{P - D(U-\eta)^2}\left[\left(\frac{\delta-1}{\delta}\right)U + \frac{G_0 N}{\eta^2}\right. \\ & \left. - \frac{2PU}{D\eta(U-\eta)} + \frac{wP}{D(U-\eta)} - \frac{Q}{X}\right].\end{aligned} \tag{36}$$

The condition to be satisfied at the inner expanding surface is that the velocity of the fluid is equal to the velocity of the surface itself. The kinematic condition, from equations (15) and (18), can be written as:

$$U(\overline{\eta}) = \overline{\eta}, \tag{37}$$

where $\overline{\eta}$ is the value of η at the inner expanding surface.

For exhibiting the numerical solutions it is convenient to write the flow variables in the non-dimensional form as:

$$\frac{u}{u_2} = \frac{U(\eta)}{U(1)}, \qquad \frac{\rho}{\rho_2} = \frac{D(\eta)}{D(1)}, \qquad \frac{p}{p_2} = \frac{P(\eta)}{P(1)}, \tag{38a–c}$$

$$\frac{m}{m_2} = \frac{N(\eta)}{N(1)}, \qquad \frac{q}{q_2} = \frac{Q(\eta)}{Q(1)}. \tag{38d–e}$$

Numerical integration of the differential equations (23), (33), (34), (35), (36) with the boundary conditions (32) give the solution in the gravitating case and of the differential equations (33), (34), (35), (36) with $G_0 = 0$ give the solution in the non-gravitating case.

4. Results and discussion

Distributions of the flow variables in the flow-field behind the shock front are obtained by numerical integration of the equations (23) and (33) to (36) with the boundary conditions (32) in the gravitating case and of the equations (33)–(36) in the non-gravitating case. The expressions for the gravitational parameter G_0 and the exponent in the shock propagation law δ are, in the gravitating case,

$$G_0 = \frac{(w-1)(3-w)}{2\pi\gamma M^2}, \qquad \delta = \frac{2}{w},$$

and in the non-gravitating case,

$$G_0 = 0, \qquad \delta = \frac{2}{2-w},$$

where w is the exponent in the law of variation (decrease) of the initial density. Also, the exponent in the law of variation of the total energy behind the shock 's' is related with w by $s = (10 - 4w)/w$ and $s = 6/(2 - w)$ in the two cases, respectively. For the purpose of numerical integration, values of the constant parameters are taken to be (Ghoniem *et al.* 1982) $\gamma = 1.4$; $M = 5; \delta_C = 1$, $\delta_R = 2$; $\Gamma_C = 1,\ 10,\ 100$; $\Gamma_R = 1,\ 100,\ 1000$; $w = 1.1, 1.2$.

Figures 1–10 show the variation of the flow variables $u/u_2,\ \rho/\rho_2,\ p/p_2,\ m/m_2,\ q/q_2$ with η at various values of the parameters $\Gamma_C,\ \Gamma_R, w$, and Fig. 11 shows the

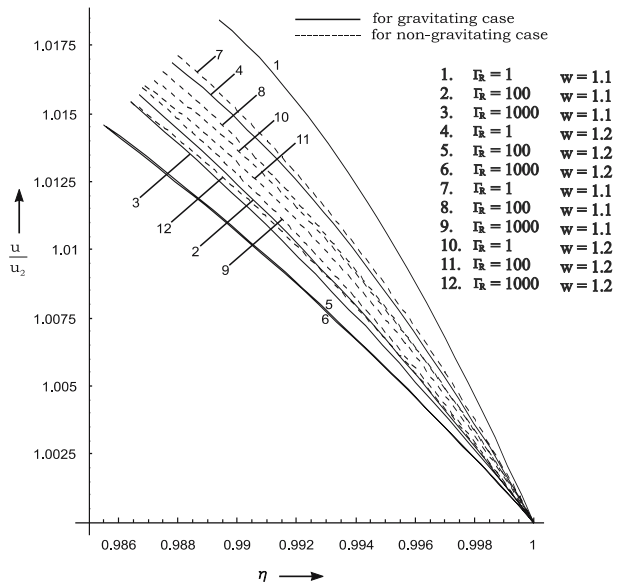

Figure 1. Variation of reduced velocity in the region behind the shock front with $\Gamma_C = 1$.

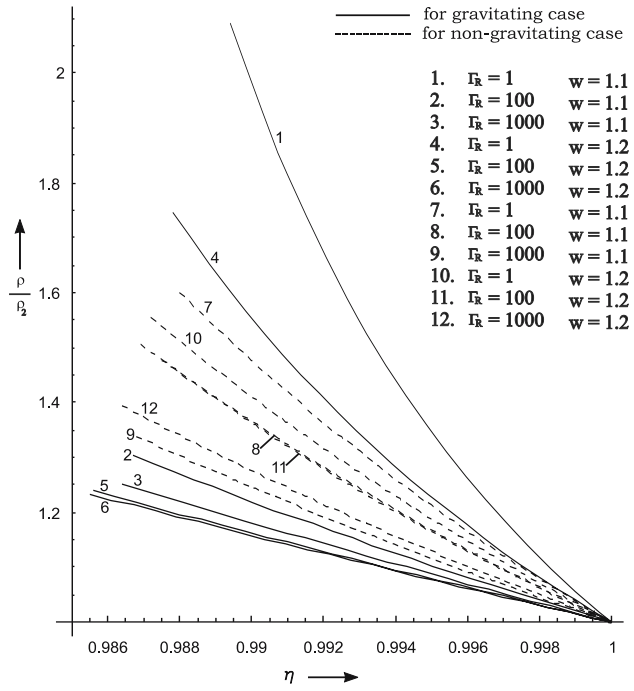

Figure 2. Variation of reduced density in the region behind the shock front with $\Gamma_C = 1$.

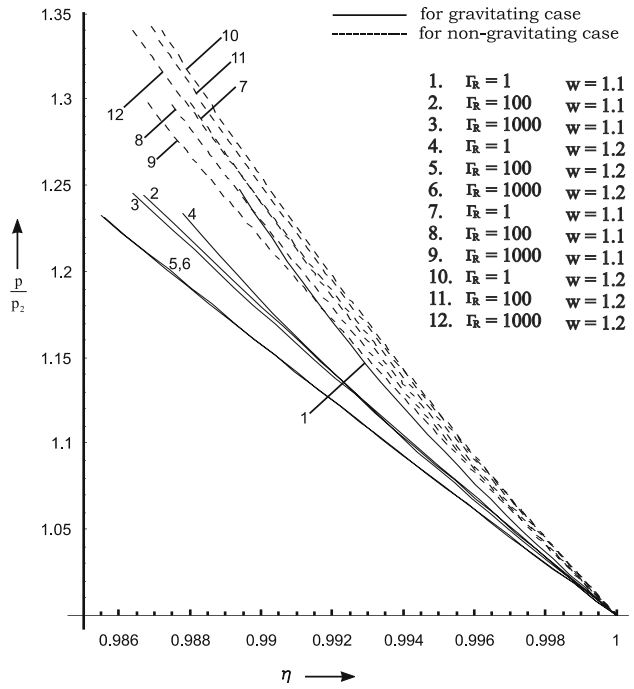

Figure 3. Variation of reduced pressure in the region behind the shock front with $\Gamma_C = 1$.

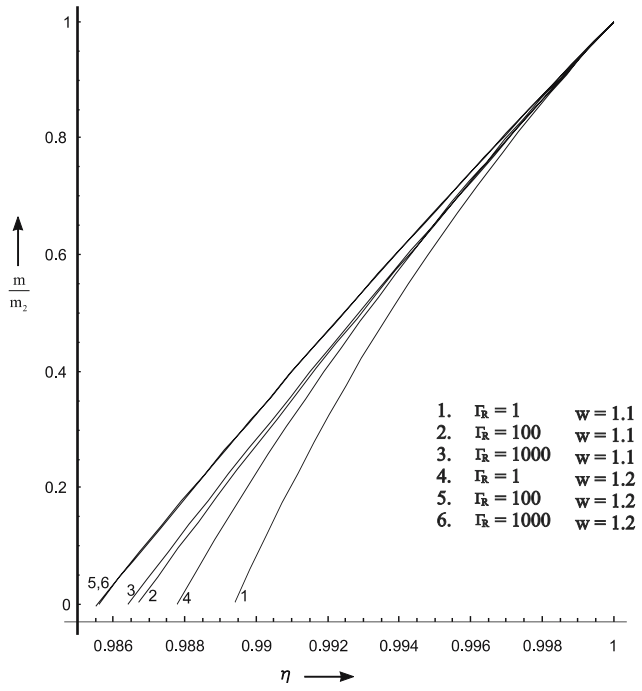

Figure 4. Variation of reduced mass in the region behind the shock front with $\Gamma_C = 1$.

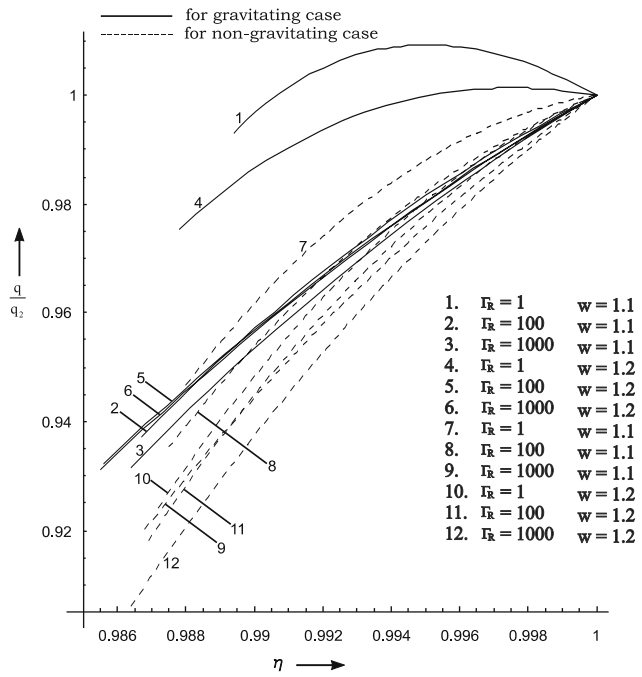

Figure 5. Variation of reduced total heat flux in the region behind the shock front with $\Gamma_C = 1$.

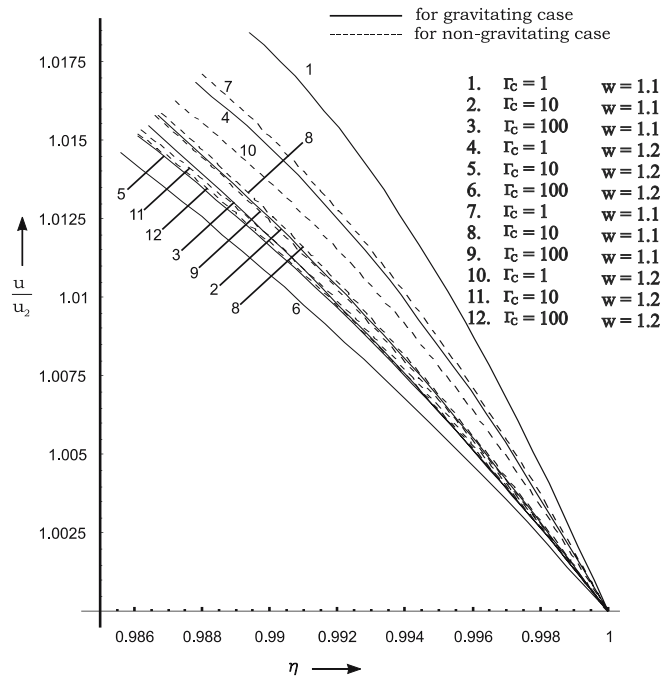

Figure 6. Variation of reduced velocity in the region behind the shock front with $\Gamma_R = 1$.

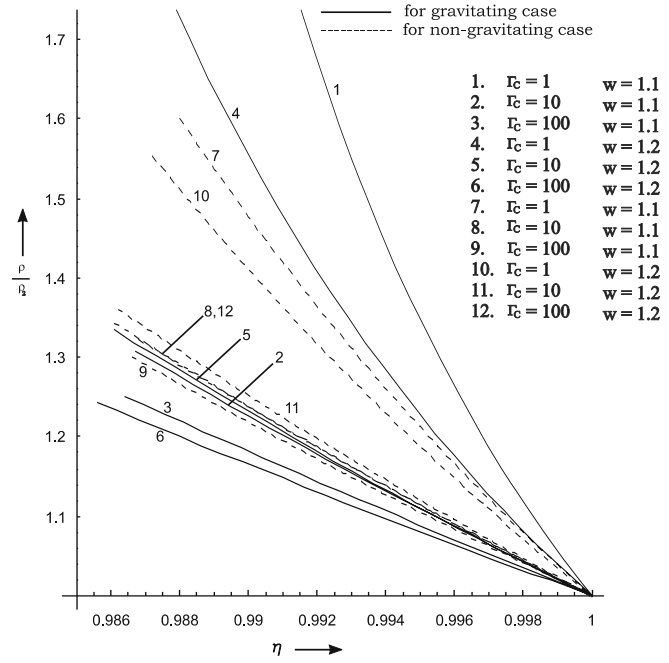

Figure 7. Variation of reduced density in the region behind the shock front with $\Gamma_R = 1$.

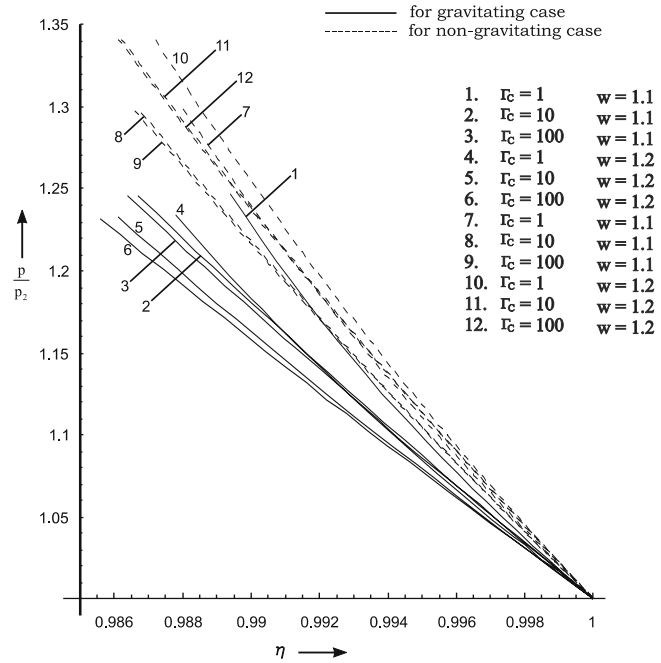

Figure 8. Variation of reduced pressure in the region behind the shock front with $\Gamma_R = 1$.

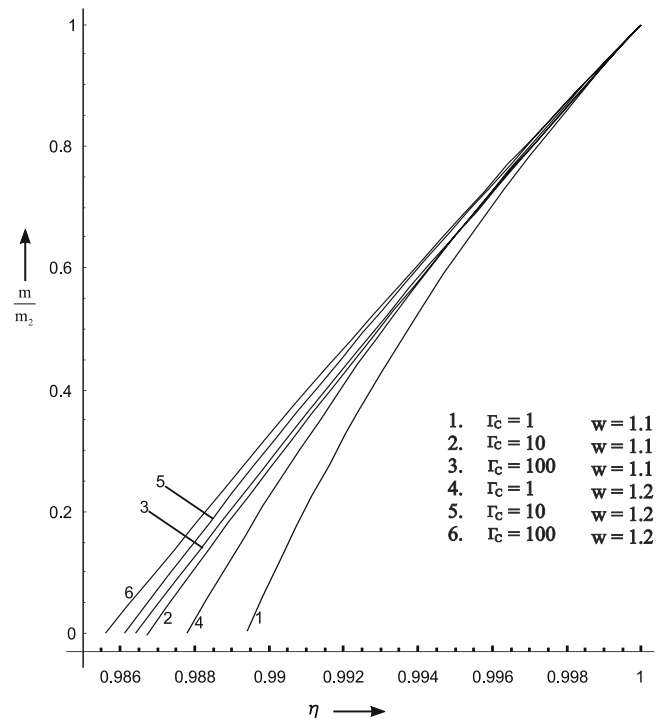

Figure 9. Variation of reduced mass in the region behind the shock front with $\Gamma_R = 1$.

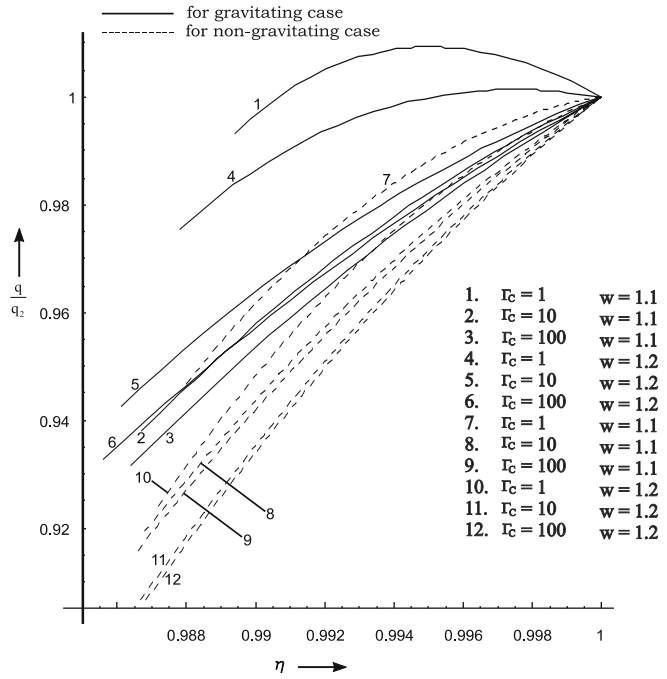

Figure 10. Variation of reduced total heat flux in the region behind the shock front with $\Gamma_R = 1$.

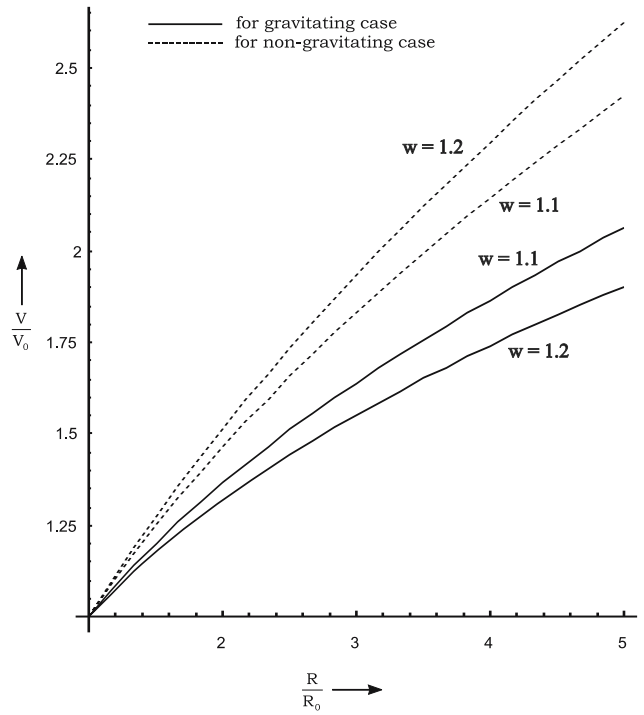

Figure 11. Variation of reduced shock velocity with reduced shock radius.

variation of the reduced shock velocity V/V_0 with reduced shock radius R/R_0 at various values of the parameter w. It is observed that, as we move inward from the shock front towards the inner expanding surface, the reduced fluid velocity u/u_2, reduced density ρ/ρ_2 and reduced pressure p/p_2 increase, and the reduced mass m/m_2 and reduced total heat flux q/q_2 decrease, in general. Also, the shock velocity V/V_0 increases with the shock radius R/R_0.

It is found that the effects of an increase in the value of radiation heat transfer parameter Γ_R are (from Figs. 1–5 and Table 1):

- to decrease the velocity u/u_2, density ρ/ρ_2, pressure p/p_2 and total heat flux q/q_2 at any point in the flow-field behind the shock;
- to increase the mass m/m_2;
- to increase the distance of the inner expanding surface from the shock front (see Table 1); and
- to decrease the slope of profiles of velocity, density, pressure and mass and to increase that of total heat flux.

The conduction heat transfer parameter Γ_C has similar effects on the flow-field behind the shock as the radiation heat transfer parameter Γ_R (see Figs. 6–10 and Table 2).

The effects of an increase in the density variation exponent w are (from Figs. 1–11 and Tables 1–2):

- to decrease the velocity u/u_2 and to increase the mass m/m_2 at any point in the flow-field behind the shock;
- to decrease the density ρ/ρ_2 in the gravitating case, in general; and in the non-gravitational case, to decrease ρ/ρ_2 for lower values of Γ_C and Γ_R and to increase that for higher values of Γ_C and Γ_R;
- to decrease the pressure p/p_2 in the gravitating case and to increase that in the non-gravitating case; and

Table 1. Position of the inner expanding surface $\overline{\eta}$ at different values of Γ_R for $\Gamma_C = 1$, $\gamma = 1.4$, $\delta_C = 1$, $\delta_R = 2$, $M = 5$ and $w = 1.1, 1.2$.

w	δ	s	G_0	Γ_R	$\overline{\eta}$
1.1	1.8181	5.0909	0.0008644	1	0.9894
				100	0.9867
				1000	0.9864
1.2	1.6666	4.3333	0.0016379	1	0.9878
				100	0.9856
				1000	0.9855
1.1	2.2222	6.6666	0	1	0.9880
				100	0.9875
				1000	0.9868
1.2	2.5	7.5	0	1	0.9872
				100	0.9869
				1000	0.9864

Table 2. Position of the inner expanding surface $\overline{\eta}$ at different values of Γ_C for $\Gamma_R = 1$, $\gamma = 1.4$, $\delta_C = 1$, $\delta_R = 2$, $M = 5$ and $w = 1.1, 1.2$.

w	δ	s	G_0	Γ_C	$\overline{\eta}$
1.1	1.8181	5.0909	0.0008644	1	0.9894
				10	0.9867
				100	0.9864
1.2	1.6666	4.3333	0.0016379	1	0.9878
				10	0.9861
				100	0.9856
1.1	2.2222	6.6666	0	1	0.9880
				10	0.9868
				100	0.9866
1.2	2.5	7.5	0	1	0.9872
				10	0.9862
				100	0.9861

- to decrease the total heat flux q/q_2 in the non-gravitating case; and in the gravitational case, to decrease q/q_2 for lower values of Γ_C and Γ_R ($\Gamma_C = 1$, $\Gamma_R = 1$) and to increase that for higher values of Γ_C and Γ_R;
- to increase the distance of the inner expanding surface from the shock front (see Tables 1 and 2);
- to decrease the shock velocity V/V_0 in the gravitating case, and to increase that in the non-gravitating case.

The effects of self-gravitational field (from Figs. 1, 2, 3, 5 and 6, 7, 8, 10, 11 and Tables 1–2) are:

- to increase the velocity u/u_2 and the density ρ/ρ_2 at lower value of Γ_R and Γ_C, and to decrease those at higher values of Γ_R and Γ_C, at any point in the flow-field behind the shock;
- to decrease the pressure p/p_2;
- to increase the total heat flux q/q_2; and
- to decrease the shock velocity V/V_0.

References

Abdel-Raouf, A. M., Gretler, W. 1991, Quasi-similar solutions for blast wave with internal heat transfer effects, *Fluid Dyn. Res.*, **8(5–6)**, 273–285.

Bhowmick, J. B. 1981, An exact analytical solution in radiation gas dynamics, *Astrophys. Space Sci.*, **74(2)**, 481–485.

Carrus, P., Fox, P., Haas, F., Kopal, Z. 1951, The propagation of shock waves in a stellar model with continuous density distribution, *Ap. J.*, **113(3)**, 496–518.

Director, M. N., Dabora, E. K. 1977, An experimental investigation of variable energy blast waves, *Acta Astronautica*, **4(3)**, 391–407.

Elliott, L. A. 1960, Similarity methods in radiation hydrodynamics, *Proc. R. Soc. Lond. A*, **258(3)**, 287–301.

Freeman, R. A. 1968, Variable-energy blast waves, *Brit. J. Appl. Phys. (J. Phys. D)*, **1(2)**, 1697–1710.

Ghoniem, A. F., Kamel, M. M., Berger, S. A., Oppenheim, A. K. 1982, Effects of internal heat transfer on the structure of self-similar blast waves, *J. Fluid Mech.*, **117**, 473–491.
Gretler, W., Wehle, P. 1993, Propagation of blast waves with exponential heat release and internal heat conduction and thermal radiation, *Shock Waves*, **3(2)**, 95–104.
Helliwell, J. B. 1969, Self-similar piston problem with radiative heat transfer, *J. Fluid Mech.*, **37(3)**, 497–512.
Kim, K. B., Berger, S. A., Kamel, M. M., Korobeinikov, V. P., Oppenheim, A. K. 1975, Boundary-layer theory of blast waves, *J. Fluid Mech.*, **71(1)**, 65–88.
Laumbach, D. D., Probstein, R. F. 1970, A point explosion in a cold exponential atmosphere-Part 2, Radiating flow, *J. Fluid Mech.*, **40(4)**, 833–858.
Marshak, R. E. 1958, Effect of radiation on shock wave behaviour, *Phys. Fluids*, **1(1)**, 24–29.
Nath, O., Ojha, S., Takhar, H. S. 1991, A study of stellar point explosion in a self-gravitating radiative magneto-hydrodynamic medium, *Astrophys. Space Sci.*, **183(1)**, 135–145.
Nicastro, J. R. 1970, Similarity analysis of radiative gas dynamics with spherical symmetry, *Phys. Fluids.*, **13(8)**, 2000–2006.
Pomraning, G. C. 1973, The Equations of Radiation Hydrodynamics, *Int. Ser. Monographs in Natural Philosophy*, Pergaman Press: Oxford.
Purohit, S. C. 1974, Self-similar homothermal flow of self-gravitating gas behind shock wave, *J. Phys. Soc. (Japan)*, **36(1)**, 288–292.
Rogers, M. H. 1957 Analytic solutions for the blast-waves problem with an atmosphere of varying density, *Astrophys. J.*, **125(2)**, 478–493.
Rogers, M. H. 1958, Similarity flows behind strong shock waves, *Quart. J. Mech. Appl. Math.*, **11(4)**, 411–422.
Rosenau, P., Frankenthal, S. 1976a, Equatorial propagation of axisymmetric magneto-hydrodynamic shocks, *Phys. Fluids*, **19(12)**, 1889–1899.
Rosenau, P., Frankenthal, S. 1976b, Shock disturbances in a thermally conducting solar wind, *Astrophys. J.*, **208(2)**, 633–637.
Rosenau, P., Frankenthal, S. 1978, Propagation of magnetohydrodynamic shocks in a thermally conducting medium, *Phys. Fluids*, **21(4)**, 559–566.
Sakurai, A. 1956, Propagation of spherical shock waves in stars, *J. Fluid Mech.*, **1(4)**, 436–453.
Sedov, L. I. 1959, *Similarity and Dimensional Methods in Mechanics*, Academic Press: New York.
Singh, J. B., Srivastava, S. K. 1982, Propagation of spherical shock waves in an exponential medium with radiation heat flux, *Astrophys. Space Sci.*, **88(2)**, 277–282.
Singh, J. B., Vishwakarma, P. R. 1983, Self-similar solutions in the theory of flare-ups in novae I, *Astrophys. Space Sci.*, **95(1)**, 99–104.
Vishwakarma, J. P., Yadav, A. K. 2003, Self-similar analytical solutions for blast waves in inhomogeneous atmospheres with frozen-in-magnetic field, *Eur. Phys. J. B*, **34(2)**, 247–253.
Wang, K. C. 1964, The "piston problem" with thermal radiation, *J. Fluid Mech.*, **20(3)**, 447–455.
Zel'dovich, Ya. B., Raizer, Yu. P. 1967, *Physics of Shock Waves and High Temperature Hydrodynamic Phenomena*, Vol. II (Translated from 2nd Russian edn.), Academic Press: New York.

J. Astrophys. Astr. (2009) **30,** 71–77

Predicting Maximum Sunspot Number in Solar Cycle 24

Nipa J Bhatt[1,*], Rajmal Jain[2] & Malini Aggarwal[2]
[1]*C. U. Shah Science College, Ashram Road, Ahmedabad 380 014, India.*
[2]*Physical Research Laboratory, Navrangpura, Ahmedabad 380 009, India.*
[*]*e-mail: nijibhatt@hotmail.com*

Received 2008 November 22; accepted 2008 December 23

Abstract. A few prediction methods have been developed based on the precursor technique which is found to be successful for forecasting the solar activity. Considering the geomagnetic activity *aa* indices during the descending phase of the preceding solar cycle as the precursor, we predict the maximum amplitude of annual mean sunspot number in cycle 24 to be 111 ± 21. This suggests that the maximum amplitude of the upcoming cycle 24 will be less than cycles 21–22. Further, we have estimated the annual mean geomagnetic activity *aa* index for the solar maximum year in cycle 24 to be 20.6 ± 4.7 and the average of the annual mean sunspot number during the descending phase of cycle 24 is estimated to be 48 ± 16.8.

Key words. Sunspot number—precursor prediction technique—geomagnetic activity index *aa*.

1. Introduction

Predictions of solar and geomagnetic activities are important for various purposes, including the operation of low-earth orbiting satellites, operation of power grids on Earth, and satellite communication systems. Various techniques, namely, even/odd behaviour, precursor, spectral, climatology, recent climatology, neural networks have been used in the past for the prediction of solar activity. Many investigators (Ohl 1966; Kane 1978, 2007; Thompson 1993; Jain 1997; Hathaway & Wilson 2006) have used the 'precursor' technique to forecast the solar activity. Ohl (1966) noted that the geomagnetic activity in the declining phase of a sunspot cycle is found to be well correlated with the sunspot maximum of the next cycle. Using the geomagnetic activity *aa* index as the precursor, Jain (1997) predicted the maximum annual mean sunspot number for cycle 23 to be 166.2 which is found to be higher than the observed value of 120. In fact, he did not propose the error estimate in the predicted number otherwise it could have been within error limits.

In this view, we predict the maximum amplitude of solar cycle 24 using the precursor technique described by Jain (1997) in this paper. Section 2 describes about the acquisition of data of annual mean sunspot number and the geomagnetic activity *aa* index used in the current investigation. In section 3, we explain the analysis and results obtained. We briefly discuss and conclude our results in section 4 in the light of other investigations.

2. Data

There are several indices that are used as indicators of geomagnetic activity: Kp, Dst, *aa*, ap, Ap, and AE. The geomagnetic activity indices, *viz.*, Ap and *aa* are used as precursors to estimate the solar activity in future. In the present analysis, we exploit *aa* indices as geomagnetic precursor to estimate the maximum amplitude of upcoming solar cycle 24. These *aa* indices are derived using data from two nearly antipodal observatories, where magnetograms were available since 1868. The *aa* index represents the activity level at an invariant magnetic latitude of about 50°. The two observatories were Greenwich (1868–1925) in Northern Hemisphere and Melbourne (1868–1919) in Southern Hemisphere. Greenwich was replaced by Abinger in 1926 and by Hartland in 1957. Melbourne was substituted by Toolangui in 1920 and by Canberra in1980. The data is normalized by cross-correlation over the instruments distributed over the globe and over the time, and therefore may be considered homogeneous over the period under current study. The daily mean of the geomagnetic *aa* index has been obtained from http://isgi.cetp.ipsl.fr/ for the period 1868–2008.

The relative sunspot number (International Sunspot Number), Ri, is an index of the activity of the entire visible disc of the Sun. It is determined each day from an observing station without reference to preceding days using the form $Ri = K(10g + s)$, where g is the number of sunspot groups and s is the total number of distinct spots. The scale factor K (usually less than unity) depends on the observer and is intended to affect the conversion to the scale originated by Wolf. Therefore, the relative sunspot number Ri (international) is derived from the statistical treatment of data originating from more than twenty-five observing stations. The observed daily sunspot number for the period 1868–2008 was acquired from the following website http://www.ngdc.noaa.gov/stp/SOLAR/ftpsunspotnumber.html.

3. Analysis and results

3.1 *Prediction of the maximum annual mean sunspot number*

Considering the geomagnetic activity *aa* index as the precursor, the maximum amplitude of the solar cycle 24 is predicted using the method employed by Jain (1997). The temporal behaviour of observed annual mean sunspot number (red) and annual mean *aa* index (blue) for solar cycles 11 to 23 considered in our investigation is shown in Fig. 1. We observed from the figure that the annual mean *aa* index ranges from 5.7 (in 1901) to 36.6 (in 2003) which is an indicator of minimum and maximum geomagnetic activity respectively, during the period of 1868–2008. Whereas, the annual mean sunspot number varies between 1.4 (in 1913) and 190.2 (in 1957). Sunspot numbers rise steadily to maximum and then fall steadily to a low level during each sunspot cycle, whereas geomagnetic indices (Ap or aa) show two or more maxima per cycle, one near or before the sunspot maximum and others in the declining phase, and the gap between the two primary maxima (the Gnevyshev gap) results in the quasi-biennial and quasi-triennial periodicities observed in the geomagnetic indices (Kane 1997).

As the annual mean sunspot number for the year 2008 (until October) is 2.86, which is within the range of sunspot minimum value, we have considered the sunspot minimum year for solar cycle 23 to be 2008 in the present study. The annual mean *aa* index and annual mean sunspot number are obtained by averaging the monthly mean

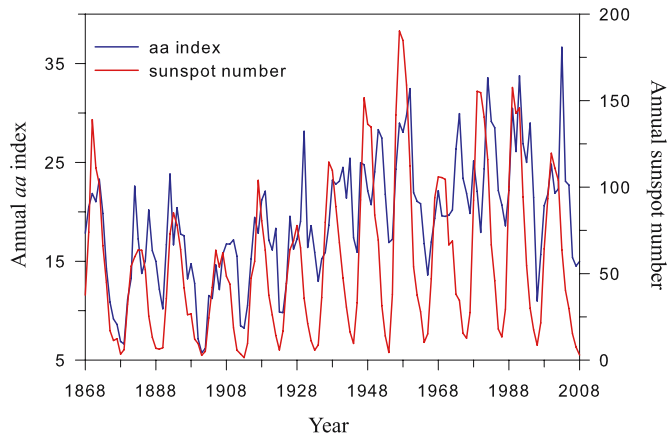

Figure 1. The observed annual mean *aa* index (blue) and annual mean sunspot number (red) for the period of 1868–2008. Note that the annual mean sunspot number for 2008 is 2.86.

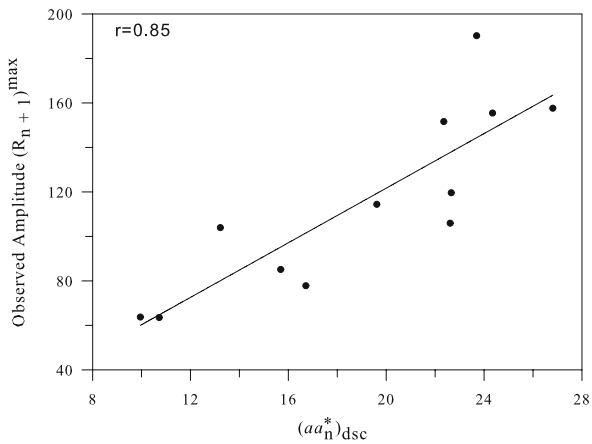

Figure 2. Observed amplitude $(R_{n+1})^{\max}$ is plotted against $(aa_n^*)_{\rm dsc}$. Correlation coefficient is found to be $r = 0.85$.

of geomagnetic activity index *aa* and monthly mean of sunspot number respectively for the period 1868–2008.

For nth cycle, we determined $(aa_n^*)_{\rm dsc}$, an average of the geomagnetic *aa* index, of the year in which observed sunspot is minimum and four years preceding to it (i.e., total 5 years). Then we compared $(aa_n^*)_{\rm dsc}$ of the nth cycle with the observed maximum annual mean sunspot number $(R_{n+1})^{\max}$ of $(n+1)$th cycle and obtained a relationship between $(aa_n^*)_{\rm dsc}$ and $(R_{n+1})^{\max}$ which is shown in Fig. 2. The best linear fit to the data with the correlation coefficient of 0.85 led us to derive an asymptotic relation as follows:

$$(R_{n+1})^{\max} = 6.138(aa_n^*)_{\rm dsc} - 1.1. \tag{1}$$

Using relation (1), we have obtained the maximum annual mean sunspot number for cycles 12 to 23, which are almost in agreement with the observed values. The standard

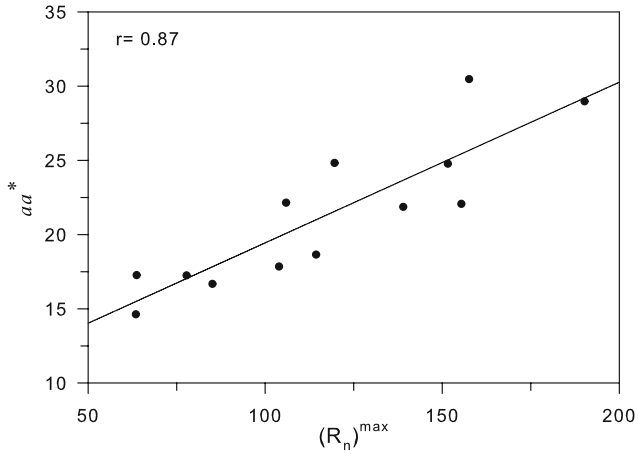

Figure 3. Representation of observed values of aa^* as a function of $(R_n)^{\max}$ of the same cycle. Correlation coefficient is 0.87.

deviation $\sigma = \pm 21$ is found from the difference between the calculated and observed values. The relation (1) enabled us to predict the maximum annual mean sunspot number for cycle 24 $(R_{23+1})^{\max}$ to be 111 ± 21. This suggests that the maximum amplitude will be less than that of cycles 21–22. Our prediction of the maximum amplitude is in good agreement with the predictions made by a few earlier investigators (Wang *et al.* 2002; Echer *et al.* 2004; Dabas *et al.* 2008; Hiramath 2008; Javaraiah 2008) while in contrast to Hathaway and Wilson (2006).

3.2 *Prediction of the annual mean geomagnetic activity index for the solar maximum year*

Next, in order to predict the level of geomagnetic activity for the sunspot maximum year in cycle 24, we obtained aa^*, which is the annual mean of aa during the year when sunspot is maximum for each cycle 11–23. And then the relation between the observed $(R_n)^{\max}$, and aa^* is studied. Figure 3 represents the relationship between $(R_n)^{\max}$ and aa^* for a given cycle. A linear fit is obtained between the two with a correlation coefficient of ~ 0.87 which can be expressed as:

$$aa^* = 0.1082(R_n)^{\max} + 8.6158. \tag{2}$$

Using the above relation, we predicted aa^* for each cycle 11–23, which is in good agreement with the observations. Considering the predicted amplitude of cycle 24 to be 111 ± 21 (section 3.1), it enabled us to estimate the aa^* during the sunspot maximum year for the cycle 24 to be 20.6 ± 4.7. This predicted value of aa^* is lower compared to the observed 30.47 and 24.82 for cycle 22 and 23 respectively. This depicts the decreasing trend of geomagnetic activity during the sunspot maximum year of the upcoming cycle 24 as compared to previous two cycles.

Table 1. Period of descending phase and the corresponding average of observed annual mean sunspot number for solar cycles 11 to 23.

Sunspot cycle	Descending phase	$(\overline{R}_n)_{\rm dsc}$
11	1871–1878	46
12	1884–1889	28
13	1894–1901	33
14	1906–1913	30
15	1918–1923	38
16	1929–1933	28
17	1938–1944	53
18	1948–1954	68
19	1958–1964	84
20	1969–1976	56
21	1980–1986	79
22	1990–1996	70
23	2001–2008	47

3.3 *Prediction of average of the annual mean sunspot number during the descending phase*

Further, we have predicted $(\overline{R}_{24})_{\rm dsc}$, the average of annual mean sunspot number of the descending phase for solar cycle 24. The descending phase is defined as the period from the year following the sunspot maximum to the year of sunspot minimum for a solar cycle. We determined the average of annual mean sunspot number of the descending phase, $(\overline{R}_n)_{\rm dsc}$ for each cycle from 11 to 23 using the following relation:

$$(\overline{R}_n)_{\rm dsc} = \frac{1}{j}\sum_{i=1}^{j}, R_i$$

where $i = 1, 2, \ldots, j$, and j is the number of years in the descending phase, and R_i is the annual mean of sunspot number. The period of descending phase for solar cycles 11 to 23 and the corresponding $(\overline{R}_n)_{\rm dsc}$ are given in Table 1.

We found that the $(\overline{R}_n)_{\rm dsc}$ of a given solar cycle is well related to the maximum annual mean sunspot number $(R_n)^{\rm max}$ for that cycle as shown in Fig. 4. The linear fit with a statistically significant correlation coefficient of 0.93 is obtained which can be expressed in the form of an empirical relation:

$$(\overline{R}_n)_{\rm dsc} = 0.4651(R_n)^{\rm max} - 4.0141. \quad (3)$$

Using relation (3), the average of the annual mean sunspot number during the descending phase for cycles 11 to 23 is calculated and the standard deviation σ determined from the difference of the observed and predicted value is found as ± 7. The relation (3) enabled us to estimate $(\overline{R}_{24})_{\rm dsc}$ to be 48 ± 16.8 (considering error ± 21

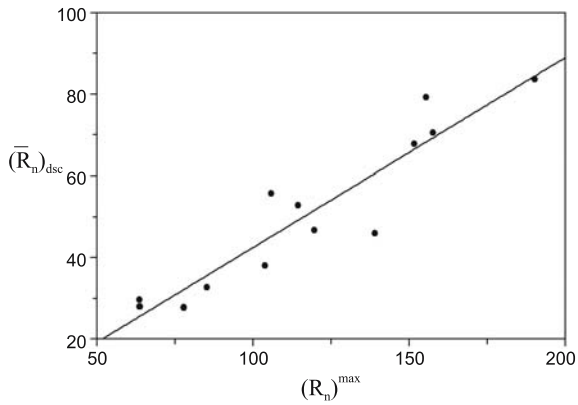

Figure 4. $(\overline{R}_n)_{\rm dsc}$ is plotted against $(R_n)^{\rm max}$ for solar cycles 11 to 23. Correlation coefficient is found to be remarkable and is 0.93.

in estimate of $(R_{24})^{\rm max}$) which is comparable to the observed annual mean sunspot number during the descending phase of cycle 23 (*cf.* Table 1). This also suggests that the sunspot activity during the descending phase of the upcoming solar cycle 24 will decline by about 30–40% as compared to the cycles 18, 19, 21 and 22 (*cf.* Table 1).

4. Discussion and conclusion

In the current investigation we have predicted maximum amplitude of annual mean sunspot number of upcoming solar cycle 24 to be 111 ± 21 by the 'precursor technique' using the long term data since 1868 to 2008. Further, we predicted annual mean *aa* index for the sunspot maximum year to be 20.6 ± 4.7. The average of annual mean sunspot number during the descending phase is estimated to be 48 ± 16.8, when the error of ± 21 in $(R_{24})^{\rm max}$ is considered.

The following investigators have used various techniques to determine the maximum amplitude of annual mean sunspot number for solar cycle 24 and are in agreement with our prediction. Javaraiah (2008) has predicted the amplitude of upcoming cycle 24 to be 103 ± 10 (or 87 ± 7) using the north–south asymmetry in the area sum of the previous cycle. Using a modified precursor method, Dabas *et al.* (2008) have predicted the maximum amplitude of about 124 ± 23. Hiramath (2008) predicted the amplitude of cycle 24 to be 110 ± 11 using the physical parameters (long-term amplitudes, frequencies, phases, decay factor) of the previous 22 solar cycles and by an autoregressive model. On the basis of extrapolation of sunspot number spectral components, Echer *et al.* (2004) have predicted the maximum to occur in 2012 (115 ± 13.2) or to occur in 2013 (117 ± 13.2). Wang *et al.* (2002) made a preliminary prediction of 83.2–119.4 for the maximum amplitude of cycle 24 using statistical characteristics of solar cycles which is in agreement with our prediction.

Based on Ohl's precursor method, Kane (2007) has given a preliminary prediction of Rz (max) to be 142 ± 24 (or 124 ± 26, if *aa* values are in error by 3 nT before 1957). Hathaway & Wilson (2006) based on the analysis of geomagnetic *aa* indices predicted the peak smoothed sunspot number to be 160 ± 25, which is higher than our prediction. The difference in prediction is due to the technique employed by Hathaway & Wilson

(2006) and ours. They considered the smoothed interplanetary component of the *aa* index which peaked in October 2003 whereas we have taken the annual mean of *aa* index from January 2004 to September 2008 from the descending phase of cycle 23, when the geomagnetic activity was low.

Many investigators have used different techniques to find the upcoming solar cycle 24. According to Dikpati *et al.* (2006), the upcoming cycle 24 will be about 30–50% stronger (R_z = 155–180) using modified flux transport solar dynamo model and the data of sunspot area. Choudhuri *et al.* (2007) modelled the last few solar cycles by 'feeding' observational data of the Sun's polar magnetic field into their solar dynamo model. They predict that cycle 24 will be about 35% weaker than cycle 23.

We conclude that our prediction of maximum amplitude, annual mean *aa* index for the sunspot maximum year and average of annual mean sunspot number during the descending phase of solar cycle 24 will hold good.

Acknowledgements

We acknowledge the sunspot data from SIDC, RWC Belgium, World Data Center for the Sunspot Index, Royal Observatory of Belgium (years 1868–2008). The daily mean of the geomagnetic *aa* index has been obtained from the website: http://isgi.cetp.ipsl.fr/ for the period January 1868–September 2008. We thank the anonymous referees for their suggestions in improving the paper.

References

Choudhuri, Arnab Rai, Chatterjee, Piyali, Jiang, Jie 2007, *Phys. Rev. Lett.*, **98**, 13, id. 131103.
Dabas, R. S., Sharma, Kavita, Das, Rupesh M., Pillai, K. G. M., Chopra, Parvati, Sethi, N. K. 2008, *Solar Phys.*, **250(1)**, 171–181.
Dikpati, M., de Toma, G., Gilman, P. A. 2006, *Geophys. Res. Lett.*, **33**, L05102.
Echer, E., Rigozo, N. R., Nordemann, D. J. R., Vieira, L. E. A. 2004, *Ann. Geophys.*, **22**, 2239–2243.
Hathaway, D. H., Wilson, R. M. 2006, *Geophys. Res. Lett.*, **33**, L18101.
Hiramath, K. M. 2008, *Astrophys. Space Sci.,* **314(1–3)**, 45–49.
Jain, R. 1997, *Solar Phys.*, **176**, 431–437.
Javaraiah, J. 2008, *Solar Phys.*, **252**, 419–439.
Kane, R. P. 1978, *Nature*, **274,** 139.
Kane, R. P. 1997, *Geophys. Res. Lett.*, **25**, 3121.
Kane, R. P. 2007, *Solar Phys.*, **243,** 205–217.
Ohl, A. I. 1966, *Soln. Dann.,* **12**, 84.
Thompson, R. J. 1993, *Solar Phys.*, **148**, 383.
Wang, J. L., Gong, J. C., Liu, S. Q., Le, G. M., Sun, J. L. 2002, *Chinese J. Astron. Astrophys.*, **2(6)**, 557–562.

J. Astrophys. Astr. (2009) **30,** 79–85

Reconnection in Solar Flares: Outstanding Questions

Hiroaki Isobe[1,*] & Kazunari Shibata[2]
[1]*Department of Earth and Planetary Science, University of Tokyo, Hongo, Bunkyo-ku, Tokyo 113-0033, Japan. e-mail: isobe@eps.s.u-tokyo.ac.jp*
[2]*Kwasan and Hida Observatories, Kyoto University, Yamashina, Kyoto 607-8471, Japan. e-mail: shibata@kwasan.kyoto-u.ac.jp*

Received 2007 April 9; accepted 2009 April 10

Abstract. Space observations of solar flares such as those from Yohkoh, SOHO, TRACE, and RHESSI have revealed a lot of observational evidence of magnetic reconnection in solar flares: cusp-shaped arcades, reconnection inflows, plasmoids, etc. Thus it has been established, at least phenomenologically, that magnetic reconnection does occur in solar flares. However, a number of fundamental questions and puzzles still remain in the physics of reconnection in solar flares. In this paper, we discuss the recent progresses and future prospects in the study of magnetic reconnection in solar flares from both theoretical and observational points of view.

Key words. Flares—magnetic reconnection—magnetohydrodynamics.

1. Introduction

Magnetic reconnection is believed to be a fundamental process in various energetic phenomena in space and astrophysical plasmas (Tajima & Shibata 1997; Priest & Forbes 2000). Although the idea of magnetic reconnection for explaining the energy release in solar flares had been proposed many decades ago (Parker 1957; Sweet 1958) it was after *Yohkoh* (Ogawara *et al.* 1991) observations that the reality of magnetic reconnection occurring during solar flares was established. Examples of evidence for reconnection include cusp-shaped post-flare loops (Tsuneta *et al.* 1992) a hard X-ray source above flaring loops (Masuda *et al.* 1994), plasmoid ejections in impulsive flares (Shibata *et al.* 1995), and supra-arcade downflows (McKenzie & Hudson 1999). Recent observations from SOHO, TRACE and RHESSI have been producing further evidence; an outstanding example is the discovery of reconnection inflows (Yokoyama *et al.* 2001; Lin *et al.* 2005; Narukage & Shibata 2006). See Shibata (1999) and Martens (2003) for reviews of observational evidence of reconnection.

The idea of magnetic reconnection has been applied, not only to solar flares, but to various explosive phenomena in the solar atmosphere (e.g., Shibata *et al.* 1992;

*Present address: Unit of Synergetic Studies for Space, Kyoto University, Japan. e-mail: isobe@kwasan.kyoto-u.ac.jp

Innes *et al.* 1997; Pariat *et al.* 2004). However, the theories of magnetic reconnection itself still have fundamental difficulties. The authors' list of the remaining outstanding problems in the physics of reconnection is as following:

- How is fast reconnection realized in a highly conducting plasma?
- What is and what determines the rate of reconnection?
- Is reconnection in the solar corona Petschek type, generalized Sweet–Parker type, or other type? Can we find slow and fast shocks?
- What is the nature of coupling between micro and macro scales?
- What is the origin of anomalous resistivity?
- What is the acceleration mechanism of non-thermal particles?
- What is the energy build-up process and the triggering mechanism of reconnection in solar flares ?
- What are the differences of reconnection in different plasma environment?
- What are the three-dimensional topology and dynamics?

We are aware that this is a biased list, perhaps biased towards macroscopic aspects. Also, many of the listed items are not independent but closely related to each other. In the rest of the paper we will review the previous achievements and future prospects on the selected issues from the list.

2. How and why reconnection is fast?

The time scale of energy release in a solar flare is typically 10–100 τ_A (100 $\sim$1000 s), where $\tau_A = L/v_A$ is Alfvén transit time, L is the characteristic size of the system and $v_A = B/\sqrt{4\pi\rho}$ is the Alfvén velocity. Since the resistivity η is extremely small in the solar corona, the diffusion time $\tau_\eta = L^2/\eta$ is huge (say, 100 years). Therefore, we need a mechanism that can drastically increase the rate of energy release, i.e., magnetic reconnection.

It is well known that Sweet–Parker reconnection is too slow to explain solar flares. In Sweet–Parker reconnection, the non-dimensional reconnection rate is given by $v_{\rm in}/v_A = w/L = \sqrt{S}$, where $v_{\rm in}$ is the inflow velocity, w and L are the thickness and the length of the current sheet, and $S = Lv_A/\eta$ is the Lundquist number (magnetic Reynolds number defined with v_A). If one uses classical Spitzer resistivity in the corona, S is as large as 10^{14}, and thus the reconnection rate is as small as 10^{-7}.

Sweet–Parker reconnection is slow because the aspect ratio w/L of the diffusion region (current sheet) is small and therefore plasma exhausting by reconnection outflow is insufficient. In order to overcome this problem, Petschek (1964) considered that the diffusion region is localized in a small region. Then the plasma is heated and accelerated through two pairs of MHD slow mode shocks that extend from the diffusion region. Petschek showed that for large S the reconnection rate is given by $v_{\rm in}/v_A = \pi/8 \log S \approx 0.01$–$0.1$. This is fast enough to energize solar flares. MHD simulations have demonstrated that such Petschek-type (i.e., with slow shocks) fast reconnection is realized when resistivity is spatially localized (e.g., Ugai & Tsuda 1977; Yokoyama & Shibata 1994), though reconnection is usually highly intermittent in non-steady simulations (e.g., Kliem *et al.* 2000; Tanuma *et al.* 2001).

How fast is reconnection in real solar flares? Attempts to measure the reconnection rate in flares have been made by many authors (Dere 1996; Tsuneta 1996; Ohyama & Shibata 1997; Isobe *et al.* 2002, 2005; Saba *et al.* 2006; Nagashima & Yokoyama

2006). It is not straight forward to measure the reconnection rate because measurement of coronal magnetic field $B_{\rm corona}$, and inflow velocity $v_{\rm in}$ are difficult. However, separation of chromospheric flare ribbons provides a good measure of reconnection rate (Forbes & Lin 2000). Assuming that reconnection is steady and two-dimensional, the reconnected magnetic flux per unit time is given by:

$$B_{\rm corona} v_{\rm in} = B_{\rm foot} v_{\rm foot}, \tag{1}$$

where $B_{\rm foot}$ and $v_{\rm foot}$ are the magnetic field strength and separation velocity of chromospheric flare ribbons. Isobe *et al.* (2002, 2005) considered this equation and the energy release rate H given by the Poynting flux of reconnection inflow,

$$H = 2\frac{B_{\rm corona}^2}{4\pi} v_{\rm in} A_r, \tag{2}$$

where A_r is the area of reconnection inflow. Using these two equations, they calculated the non-dimensional reconnection rate $v_{\rm in}/v_A$ for several flares from available observations. The calculated values fell in the range of 0.001–0.1. Other studies cited above found similar values, as summarized in Table 4 of Narukage & Shibata (2006).

Direct evidence of reconnection inflows was first found in EUV images of a limb flare observed by SOHO/EIT (Yokoyama *et al.* 2001). Narukage & Shibata (2006) found further such examples. The estimated reconnection rate was 0.001–0.07. In these studies, the inflow velocity $v_{\rm in}$ was measured from the apparent motion in the images and hence may not be the real plasma velocity (Chen *et al.* 2004). Spectroscopic detection of reconnection inflow is therefore important, but such observations are still rare (Lin *et al.* 2005; Hara *et al.* 2006). It is obviously an important target of EUV imaging spectrometer (EIS) onboard *Hinode* (Solar-B).

In summary, the previous quantitative analyses of reconnection rate have indicated that the reconnection rate is in the range of 0.001–0.1. This is fast enough to explain the energy release rate of flares and roughly consistent with Petschek-type reconnection. The lower values in some cases ($\sim$0.001) are probably the spatial and temporal averages. As discussed further in the next section, the reconnection process is likely to be quite intermittent, both in time and in space. Temporal and spatial variation of reconnection rate should be studied in future using high resolution data (Saba *et al.* 2006).

Another important observational challenge is detection of slow shocks. The cusp-shaped loops and Y-shaped structure found by Soft X-ray Telescope aboard *Yohkoh* may be the reconnection slow shocks (Tsuneta *et al.* 1992; Shiota *et al.* 2003), but further evidence, e.g., jump in plasma density, pressure, and velocity, is obviously needed. *Hinode*/EIS will be a strong tool for this purpose (Brooks *et al.* 2004; Shiota *et al.* 2004).

3. Macro–micro coupling

One of the most fundamental problems of Petschek-type MHD reconnection is the nature and origin of localized diffusion region. A localized resistivity may be realized by an anomalous resistivity caused by wave-particle interactions or kinetic instabilities. Although the microscopic origin of such an anomalous resistivity has not been clarified, magnetospheric observations (e.g., Sergeev *et al.* 1993), particle simulations

(e.g., Horiuchi & Sato 1999), and laboratory experiments (e.g., Ono *et al.* 1997) indicate that fast magnetic reconnection is initiated when the thickness of the current sheet becomes as thin as the ion inertia length or the ion Larmour radius, where kinetic effects of the plasma becomes significant.

However, both the ion inertia length and ion Larmour radius are of the order of 10^2 cm, while the characteristic size of solar flares is about 10^9 cm. This is a big difference from the magnetospheric case, where the ratio of global scale to ion scales is of the order of 10–100. See Terasawa *et al.* (2000) for a comparison of solar flares and magnetospheric substorms. How to link this huge gap between different scales is the most challenging and fundamental problem in reconnection physics. Perhaps there are some meso-scale structures that connect the global and microscopic scales?

Observations give us some hints to tackle this problem. As mentioned already, reconnection in solar flares is quite intermittent. This is inferred from fine structures in flare ribbons (e.g., Kitahara & Kurokawa 1990; Fletcher *et al.* 2004) and fast temporal variation of hard X-ray and radio lightcurves (e.g., Aschwanden *et al.* 1996; Karlický *et al.* 2005). Such spatial and temporal fine structures suggest the existence of fine structures in the reconnecting current sheet.

Another significant observational fact is the correlation of reconnection and plasmoid ejection. Almost all the explosive events in the solar corona is accompanied by ejection of plasma, from coronal mass ejections to microflares (e.g., Shibata *et al.* 1995; Innes *et al.* 1997; Zhang *et al.* 2001; Sakajiri *et al.* 2004; Asai *et al.* 2004). Careful examination of plasmoid motion and flare lightcurve have revealed that the plasmoid had started to move slowly well before the impulsive phase of the flare, and then suddenly accelerated and ejected during the impulsive phase (Ohyama & Shibata 1997; Chifor *et al.* 2006). From such observations, Shibata & Tanuma (2001) suggested 'plasmoid-induced' reconnection model, in which fast reconnection and plasmoid ejection are dynamically coupled.

Karlický *et al.* (2005) examined the Fourier power spectra of pulsating structure observed in 500–1500 MHz, which is interpreted as the result of plasmoid ejection from reconnection site. They found power law spectra in the short period (0.06–0.2 s) range. This indicates that there is no characteristic scale in reconnection and hence the reconnecting current may have a turbulent, possibly fractal structure as suggested by Tajima & Shibata (1997). Similar picture of a reconnecting current sheet, i.e., full of many small plasmoid, has been given by Aschwanden (2002). Such turbulent structure may give a way to link the microscopic and macroscopic scales in reconnection.

What can be the origin of such turbulent structures in a current sheet? Shibata & Taunua (2001) suggested multiple tearing instability. This is a 'top-down' process, approaching from macro-scale to micro-scale by an MHD instability. For magnetospheric reconnection, Hoshino *et al.* (1994) proposed an opposite approach, i.e., formation of large-scale plasmoid by bottom-up process from microscopic scales. Presumably both happen at the same time in the solar case.

A three-dimensional MHD simulation carried out by the authors provides an interesting result that may be related to this problem (Isobe *et al.* 2005, 2006). Figure 1 shows three-dimensional visualizations of the MHD simulation of magnetic reconnection between an emerging flux and pre-existing coronal field. It was shown that the top of the emerging flux becomes unstable to the magnetic Rayleigh–Taylor instability in the corona. As the Rayleigh–Taylor instability grows, an interchanging, filamentary structure is created in the emerging flux, which is similar to an arch filament

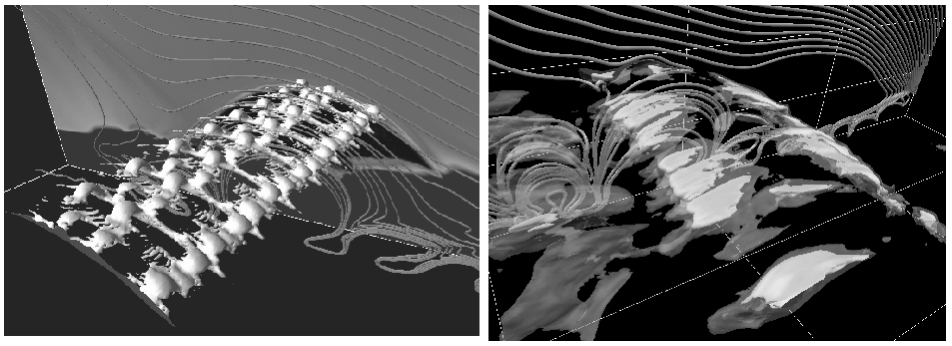

Figure 1. Three-dimensional visualization of the result of MHD simulation of magnetic reconnection between an emerging flux and a pre-existing coronal field. Left: Isosurface of plasma pressure and a selected magnetic field lines. Right: Isosurfaces of the magnitude of velocity, corresponding 60 km s^{-1} (transparent) and 120 km s^{-1}.

system observed in Hα. See Isobe *et al.* (2006) for details of the simulation. Consequently, the current sheet between the emerging flux and coronal field also undergoes interchanging. Tearing instability locally occurs in the current sheet, creating many small plasmoid as shown in the left panel of Fig. 1. This is remarkably similar to the cartoon by Aschwanden (2002, Fig. 47) in which many plasmoids exist in a reconnecting current sheet. After the ejection of these plasmoids, fast reconnection occurs in temporally and spatially intermittent way. The right panel shows the structure of the reconnection outflows. Many narrow jets are ejected from the localized diffusion regions.

Thus, the MHD simulation has demonstrated the turbulence excitation and associated reconnection in a self-consistent way. In this case, the origin of turbulence is an ideal MHD instability, namely the magnetic Rayleigh–Taylor instability. From this simulation result, we conjecture that a possible scenario to link the micro and macro scales is as follows. First, small scale structure is created by ideal MHD instabilities such as Rayleigh–Taylor instability or Kelvin–Helmholtz instability (top-down process). When the turbulence cascades down to the ion scale, tearing and reconnection are initiated at such small scale. Then the small scale islands become bigger by coalescence (bottom-up process).

Of course, this is still a rough conjecture. Direct numerical simulation of such processes requires multi-scales and multi-physics. It is a big challenge of the theoretical and numerical studies in the next decades.

4. Reconnection in the lower atmosphere

In this section we briefly mention the magnetic reconnection in the lower atmosphere of the Sun. Reconnection is likely to be occurring in the photosphere and chromosphere. Canceling magnetic features (Litvinenko & Martin 1999) and Ellerman bombs (Pariat *et al.* 2004; Isobe *et al.* 2007) are believed to be the manifestations of such lower level reconnection. Chromospheric reconnection may play a significant role in the coronal heating (Sturrock 1999).

Although the photosphere and the chromosphere are weakly ionized regions and therefore the resistivity is relatively large, the Lundquist number is still larger than 10^4.

Reconnection in such plasma environment is also of interest in some astrophysical systems such as protoplanetary disks (Inutsuka & Sano 2005), but it is still poorly understood (Litvinenko 1999; Chen *et al.* 2001; Chae *et al.* 2002). Theoretical and observational studies on this subject are therefore desired. The Solar Optical Telescope on *Hinode* will provide further detailed observations of the lower atmospheric reconnection.

5. Conclusion

In this paper we have discussed a selected issue on the outstanding questions of the physics of magnetic reconnection. Due to the space restriction we did not discuss some very important issues such as particle acceleration (Aschwanden 2002) and three-dimensionality (Priest & Forbes 1992; Isobe *et al.* 2002; Tripathi *et al.* 2006).

The solar atmosphere provides an excellent laboratory to study the basic plasma physics. Since magnetic reconnection is of great interest not only for solar physics but also for much larger fields of plasma physics and astrophysics, it is desirable to utilize the solar observation to study reconnection, not only to utilize reconnection to interpret the solar phenomena. Recently launched *Hinode* satellite and other upcoming projects will provide us further advanced data, from which we may get deeper insight of the basic physics of reconnection.

References

Asai, A., Yokoyama, T., Shimojo, M. *et al.* 2004, *Astrophys. J.*, **611**, 557.
Aschwanden, M. J. 2002, *Space Sci. Rev.*, **101**, 1.
Aschwanden, M. J., Wills, M. J., Hudson, H. S. *et al.* 1996, *Astrophys. J.*, **468**, 398.
Brooks, D. H., Isobe, H., Shibata, K., Chen, P. F., Lanzafame, A. C. 2004, In: *The Solar-B Mission and the Forefront of Solar Physics, ASP Conference Series* (eds) Sakurai, T., Sekii, T. **325**, 367.
Chae, J., Choi, B.-K., Park, M. 2002, *J. Korean Astron. Soc.*, **35**, 59.
Chen, P. F., Fang, C., Ding, M. D. 2001, *Chinese J. Astron. Astrophys.*, **1**, 176.
Chen, P. F., Shibata, K., Brooks, D. H., Isobe, H. 2004, *Astrophys. J.*, **602**, L61.
Chifor, C., Mason, H. E., Tripathi, D., Isobe, H., Asai, A., 2006, *Astron. Astrophys.*, **458**, 965.
Dere, K. P. 1996, *Astrophys. J.*, **472**, 864.
Fletcher, L., Pollock, J., Potts, H. E. 2004, *Solar Phys.*, **222**, 279.
Forbes, T. G., Lin, J. 2000, *Atmos. Sol.-Terr. Phys.*, **62**, 1499.
Hara, H., Nishino, Y., Ichimoto, K., Delaboudinière, J.-P. 2006, *Astrophys. J.*, **648**, 712.
Horiuchi, R., Sato, T. 1999, *Phys. Plasmas*, **6**, 4565.
Hoshino, M., Nishida, A., Yamamoto, T., Kokubun, S. 1994, *Geophys. Res. Lett.*, **21**, 2935.
Innes, D. E., Inhester, B., Axford, W. I., Willhelm, K. 1997, *Nature*, **386**, 811.
Inutsuka, S., Sano, T. 2005, *Astrophys. J.*, **628**, L155.
Isobe, H., Miyagoshi, T., Shibata, K., Yokoyama, T. 2005, *Nature*, **434**, 478.
Isobe, H., Miyagoshi, T., Shibata, K., Yokoyama, T. 2006, *Publ. Astron. Soc. Japan*, **58**, 423.
Isobe, H., Shibata, K., Machida, S. 2002, *Geophys. Res. Lett.*, **29**(**21**), 2014.
Isobe, H., Takasaki, H., Shibata, K. 2005, *Astrophys. J.*, **632**, 1184.
Isobe, H., Tripathi, D., Archontis, V. 2007, *Astrophys. J.*, **657**, L53.
Isobe, H., Yokoyama, T., Shimojo, M. *et al.* 2002, *Astrophys. J.*, **566**, 528.
Karlický, M., Bárta, M., Mészárosová, H., Zlobec, P. 2005, *Astron. Astrophys.*, **432**, 705.
Kitahara, T., Kurokawa, H. 1990, *Solar Phys.*, **125**, 321.
Kliem, B., Karlický, M., Benz, A. O. 2000, *Astron. Astrophys.*, **360**, 715.
Lin, J., Ko, Y.-K., Sui, L. *et al.* 2005, *Astrophys. J.*, **622**, 1251.
Litvinenko, Y. E. 1999, *Astrophys. J.*, **515**, 435.

Litvinenko, Y. E., Martin, S. F. 1999, *Solar Phys.*, **190**, 45.
Martens, P. C. H. 2003, *Adv. Space Res.*, **32**, 905.
Masuda, S., Kosugi, T., Hara, H., Tsuneta, S., Ogawara, Y. 1994, *Nature*, **371**, 495.
Nagashima, K., Yokoyama, T. 2006, *Astrophys. J.*, **647**, 654.
Narukage, N., Shibata, K. 2006, *Astrophys. J.*, **637**, 1122.
Ogawara, Y. *et al.* 1991, *Solar Phys.*, **136**, 17.
Ohyama, M., Shibata, K. 1997, *Publ. Astron. Soc. Japan*, **49**, 249.
Ono, Y., Inomoto, M., Okazaki, T. *et al.* 1997, *Phys. Plasmas*, **4**, 1953.
Pariat, E., Aulanier, G., Schmieder, B. *et al.* 2004, *Astrophys. J.*, **614**, 1099.
Parker, E. N. 1957, *J. Geophys. Res.*, **62**, 509.
Petschek, H. E. 1964, In: *AAS-NASA Symp. on Solar Flares* (ed.) Hess, W. N. (NASA SP-50), 425.
Priest, E. R., Forbes, T. G. 2000, *Magnetic reconnection: MHD theory and applications*, Cambridge University Press, New York.
Priest, E. R., Forbes, T. G. 1992, *J. Geophys. Res.*, **97**, 1521.
Saba, J. L. R., Gaeng, T., Tarbell, T. D. 2006, *Astrophys. J.*, **641**, 1197.
Sakajiri, T., Brooks, D. H., Yamamoto, T. *et al.* 2004, *Astrophys. J.*, **616**, 578.
Sergeev, V. A., Mitchell, D. G., Russell, C. T. *et al.* 1993, *J. Geophys. Res.*, **98**, 17,345.
Shibata, K. 1999, *Astrophys. Space Sci.*, **264**, 129.
Shibata, K. *et al.* 1992, *Publ. Astron. Soc. Japan*, **44**, L173.
Shibata, K., Masuda, S., Shimojo, M. *et al.* 1995, *Astrophys. J.*, **451**, L83.
Shibata, K., Tanuma, S. 2001, *Earth, Planets Sci.*, **53**, 473.
Shiota, D., Isobe, H., Brooks, D. H., Shibata, K., Chen, P. F. 2004, In: *The Solar-B Mission and the Forefront of Solar Physics*, (eds) Sakurai, T., Sekii, T., *ASP Conference Series* **325**, 373.
Shiota, D., Yamamoto, T. T., Sakajiri, T. *et al.* 2003, *Publ. Astron. Soc. Japan*, **55**, L35.
Sturrock, P. A. 1999, *Astrophys. J.*, **521**, 451.
Sweet, P. A. 1958, In: *IAU Symp. No.6, Electromagnetic Phenomena in Cosmical Physics* (ed.) Lehnert, B., 123.
Tajima, T., Shibata, K. 1997, *Plasma Astrophysics* (Massachusetts: Addison-Wesley).
Tanuma, S., Yokoyama, T., Kudoh, T., Shibata, K. 2001, *Astrophys. J.*, **551**, 312.
Terasawa, T., Shibata, K., Scholer, M. 2000, *Adv. Space Res.*, **26**, 573.
Tripathi, D., Isobe, H., Mason, H. E. 2006, *Astron. Astrophys.*, **453**, 1111.
Tsuneta, S. 1996, *Astrophys. J.*, **456**, 840.
Tsuneta, S. *et al.* 1992, *Publ. Astron. Soc. Japan*, **44**, L63.
Ugai, M., Tsuda, T. 1977, *J. Plasma Phys.*, **17**, 337.
Yokoyama, T., Akita, K., Morimoto, T., Inoue, K., Newmark, J. 2001, *Astrophys. J.*, **546**, L69.
Yokoyama, T., Shibata, K. 1994, *Astrophys. J.*, **436**, L197.
Zhang, J., Dere, K. P., Howard, R. A., Kundu, M. R., White, S. M. 2001, *Astrophys. J.*, **559**, 452.

J. Astrophys. Astr. (2009) **30,** 87–91

Spectroscopic Binaries near the North Galactic Pole Paper 12A: 6 Boötis

R. F. Griffin
The Observatories, Madingley Road, Cambridge CB3 0HA, England.
e-mail: rfg@ast.cam.ac.uk

Received 2009 June 17; accepted 2009 July 8

Abstract. About 25 years ago, in Paper 12 of this series, the author presented a spectroscopic orbit for 6 Boo. The velocity amplitude of little more than 1 km s^{-1} was much smaller than for any star whose orbit had been determined up till that time. Although it was objectively demonstrated that the orbit was very secure, a few years ago subjective misgivings prompted the author to restore the star to his observing programme. New observations of much higher precision confirm not only the spectroscopic-binary nature of 6 Boo but also, with almost astonishing fidelity, the elements already given for it.

Key words. Radial velocities—spectroscopic binaries—orbits—stars: individual—6 Boo.

1. Introduction

This series of papers, which has been in abeyance for the past few years, has given spectroscopic orbits for 34 of the stars discovered (or, in one or two cases, confirmed) to be binaries in the course of the comprehensive survey by Yoss & Griffin (1997) of all the late-type stars that are listed in the *Henry Draper Catalogue* and are within 15° of the North Galactic Pole (NGP). Paper 12 of the series (Griffin 1985) presented the orbit of 6 Boo (HR 5201, HD 120539; also sometimes known as e Boo (Baily 1845; Goldin & Makarov 2007)), a fifth-magnitude K4 III star near the following margin of the NGP field and the ninth-brightest of the stars qualifying for inclusion in the NGP survey.

The observations underlying the orbit in Paper 12 were all made at the Cambridge 36-inch reflector with the original radial-velocity spectrometer (Griffin 1967)—the instrument with which the writer developed the cross-correlation method of measuring radial velocities, which has of course subsequently been universally adopted and has been responsible for most of the evidence for such disparate objects as black holes and extra-solar planets. Although it had been developed as an experimental instrument, it remained in actual research use for 25 years, during which time, of course, it became substantially outmoded. The radial-velocity traces were drawn in real time by a pen on a continuous paper chart, and the reductions were done by measurements made on the chart by hand and eye. Even so, it gave velocities with characteristic errors a

little under 1 km s^{-1}, which was regarded as a handsome accuracy at the time that the spectrometer was developed.

The orbit so determined for 6 Boo was the most ambitious one that was ever attempted with the original instrument—it had a velocity amplitude not much more than 1 km s^{-1}, which was about twice the r.m.s. residuals from the orbit. The smallest amplitude found for any plausible spectroscopic orbit previously was 2.39 km s^{-1} (ϕ Her, Aikman 1976). The 6 Boo paper demonstrated how the orbital period, of a little under 1000 days, seemed to be visible in the velocities when they were simply plotted directly against time. Moreover, a statistical argument (kindly vetted by a professional statistician who had been good enough to correct me (Bassett 1978) after I made serious mistakes in the early papers in another series) showed that the orbit was altogether unassailable: a variance-ratio test gave an F ratio of 17.2 in a situation where even the 0.1%-significance level was only 4.9.

All the same, from time to time the writer found himself hoping that the star really does have an orbit much like the one that he asserted for it, and despite the objective evidence that it *does* there came a time when he decided to put it back on his observing programme, which was then being carried out at the same telescope as before but with a spectrometer analogous to the *Coravel* of Baranne *et al.* (1979), which gives velocities of a substantially higher quality than those of the original instrument.

2. Radial-velocity measurements and orbit

There are 35 new *Coravel* observations, made in the years 2004–2009; they are set out in Table 1. An improved scheduling scheme has ensured that they are distributed tolerably uniformly in phase. The earlier paper (Griffin 1985) listed the 54 measurements made with the original radial-velocity instrument and one each with the Palomar (Griffin & Gunn 1974) and Dominion Astrophysical Observatory (DAO; Fletcher 1982) spectrometers. It also listed a few velocities made at Lick (Campbell & Moore 1928) and Mount Wilson (Adams *et al.* 1929; Abt 1973) which were zero-weighted in the solution of the orbit. Since that time one velocity has been published from Ames by Beavers & Eitter (1986), and a listing referred to by de Medeiros & Mayor (1999) has given two more. None of the mentioned measurements has been included in Table 1 other than the 35 new ones obtained at Cambridge; the new orbit presented below utilizes the writer's own earlier data given in Paper 12, but none of the others, which could be considered to be too sparse and too heterogeneous to contribute usefully. It should be explained that the cycle numbers in Table 1 (the numbers before the decimal point in the 'Phase' column) start at the periastron passage preceding the first observation made with the original spectrometer in 1966; although the table gives only the recent *Coravel* measurements, the earlier ones were also used in the computation of the orbit, albeit with low weight.

In the new solution, the Cambridge *Coravel* velocities have been given unit weight, while those made with the original spectrometer have been weighted 1/20, as is needed to bring their weighted variance approximately into line with that of the new observations. The single Palomar and DAO measures have been attributed half-weight. Thus fully 90% of the total weight of the data going into the new orbit is accounted for by the fresh observations, so the result could be considered to all intents and purposes to be an independent orbit. It does, however, benefit by

Table 1. New *Coravel* radial-velocity observations of 6 Boötis.

Date (UT)			MJD	Velocity (km s^{-1})	Phase	$(O-C)$ (km s^{-1})
2004	May	23.00	53148.00	−1.3	14.935	+0.1
	June	25.90	181.90	−1.0	0.970	+0.2
	Aug.	7.86	224.86	−1.2	15.016	+0.1
2005	Jan.	9.25	53379.25	−2.9	15.180	+0.1
	Mar.	25.14	454.14	−3.5	0.259	−0.2
	Apr.	22.06	482.06	−3.3	0.289	+0.1
	May	27.97	517.97	−3.3	0.327	+0.1
	July	9.90	560.90	−3.8	0.372	−0.3
	Aug.	15.87	597.87	−3.7	0.411	−0.2
	Dec.	17.27	721.27	−3.5	0.542	−0.1
2006	Jan.	29.25	53764.25	−3.3	15.588	0.0
	Mar.	1.17	795.17	−3.2	0.620	0.0
	Apr.	4.09	829.09	−3.2	0.656	−0.1
	May	9.97	864.97	−2.9	0.694	+0.1
	June	3.98	889.98	−3.0	0.721	−0.1
	July	2.95	918.95	−2.9	0.752	−0.1
	Aug.	7.87	954.87	−2.6	0.790	−0.1
	Nov.	26.27	54065.27	−1.6	0.907	0.0
2007	Jan.	14.28	54114.28	−1.3	15.958	−0.1
	Feb.	4.21	135.21	−1.5	0.981	−0.3
	Mar.	2.20	161.20	−1.4	16.008	−0.1
	Apr.	1.08	191.08	−1.4	0.040	+0.1
	May	1.04	221.04	−1.9	0.072	0.0
	June	1.03	252.03	−2.4	0.104	−0.1
	July	7.95	288.95	−2.7	0.144	0.0
	Sept.	6.81	349.81	−3.3	0.208	−0.2
2008	Feb.	2.22	54498.22	−3.4	16.365	+0.1
		25.19	521.19	−3.5	0.390	0.0
	Mar.	31.12	556.12	−3.5	0.427	0.0
	Apr.	24.06	580.06	−3.4	0.452	+0.1
		19.02	605.02	−3.4	0.479	+0.1
	June	25.92	642.92	−3.3	0.519	+0.1
2009	Apr.	2.08	54923.08	−2.3	16.816	+0.1
	May	4.03	955.03	−2.1	0.849	0.0
		29.97	980.97	−1.9	0.877	0.0

having its period much improved by the increase of the time base from 5 to 43 years by the inclusion at some level of the writer's older observations; the period obtained from the new data in isolation is 941 ± 7 days. The new solution is plotted in Fig. 1; its elements are given in Table 2, with those determined previously for comparison.

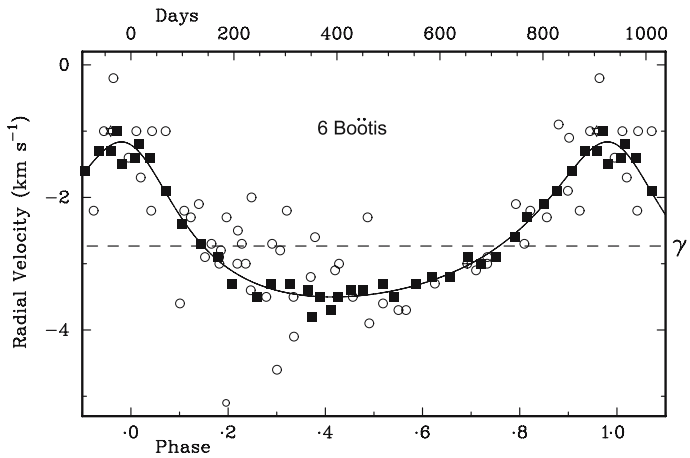

Figure 1. Velocity curve computed from the new orbit for 6 Boötis, with the measured radial velocities plotted. The measurements made with the Cambridge *Coravel* are plotted as filled squares, whereas those made with the original spectrometer (weighted 1/20 in the solution of the orbit) appear as open circles. Single observations from Palomar and the DAO, both weighted 1/2, are shown as a circle with a plus in it, and an open star, respectively.

Table 2. Orbital elements for 6 Boötis.

Element	Griffin (1985)	This paper
P (days)	944 ± 8	943.7 ± 1.1
T (MJD)	44739 ± 31	53210 ± 10
γ (km s^{-1})	-2.63 ± 0.09	-2.734 ± 0.022
K (km s^{-1})	1.19 ± 0.15	1.170 ± 0.031
e	0.41 ± 0.09	0.357 ± 0.025
ω (degrees)	359 ± 15	16 ± 5
$a_1 \sin i$ (Gm)	14.1 ± 1.9	14.2 ± 0.4
$f(m)$ ($M_\odot$)	0.00013 ± 0.00005	0.000128 ± 0.000011
r.m.s. residual (wt. 1) (km s^{-1})	0.6	0.13

3. Discussion

Table 2 and Fig. 1 both demonstrate how very well the old orbit is vindicated by the new one. Arguably the most important elements, P and K, are almost identical in the two solutions. Only two of the seven quantities for which a direct comparison can be made in Table 2, the γ-velocity and ω, differ by more than their joint standard deviation, and then only barely; that is in any case altogether right and proper, since almost one-third of a normal distribution lies outside $\pm 1\sigma$.

References

Abt, H. A. 1973, *ApJS*, **26**, 365.
Adams, W. S., Sanford, R. F., Strömberg, G. 1929, *ApJ*, **70**, 207.

Aikman, G. C. L. 1976, *PDAO*, **14**, 379.
Baily, F. 1845, *Catalogue of Stars of the British Association* ... (London: R. & J. E. Taylor), 206.
Baranne, A., Mayor, M., Poncet, J. L. 1979, *Vistas Astr.*, **23**, 279.
Bassett, E. E. 1978, *The Observatory*, **98**, 122.
Beavers, W. I., Eitter, J. J. 1986, *ApJS*, **62**, 147.
Campbell, W. W., Moore, J. H. 1928, *Pub. Lick Obs.*, **16**, 202.
de Medeiros, J. R., Mayor, M. 1999, *A&AS*, **139**, 433.
Fletcher, J. M., Harris, H. C., McClure, R. D., Scarfe, C. D. 1982, *PASP*, **94**, 1017.
Goldin, A., Makarov, V. V. 2007, *ApJS*, **173**, 137.
Griffin, R. F. 1967, *ApJ*, **148**, 465.
Griffn, R. F. 1985, *JA&A*, **6**, 77.
Griffn, R. F., Gunn, J. E. 1974, *ApJ*, **191**, 545.
Yoss, K. M., Griffin, R. F. 1997, *JA&A*, **18**, 161.

J. Astrophys. Astr. (2009) **30,** 93–118

The Ks-band Tully–Fisher Relation – A Determination of the Hubble Parameter from 218 ScI Galaxies and 16 Galaxy Clusters

David G. Russell
Owego Free Academy, Owego, NY 13827, USA.
e-mail: Russeld1@oacsd.org

Received 2007 April 27; accepted 2009 June 10

Abstract. The value of Hubble parameter (H_0) is determined using the morphologically type dependent Ks-band Tully–Fisher Relation (K-TFR). The slope and zero point are determined using 36 calibrator galaxies with ScI morphology. Calibration distances are adopted from direct Cepheid distances, and group or companion distances derived with the Surface Brightness Fluctuation Method or Type Ia Supernova. It is found that a small morphological type effect is present in the K-TFR such that ScI galaxies are more luminous at a given rotational velocity than Sa/Sb galaxies and Sbc/Sc galaxies of later luminosity classes. Distances are determined to 16 galaxy clusters and 218 ScI galaxies with minimum distances of 40.0 Mpc. From the 16 galaxy clusters a weighted mean Hubble parameter of $H_0 = 84.2 \pm 6\,\mathrm{km\ s^{-1}\ Mpc^{-1}}$ is found. From the 218 ScI galaxies a Hubble parameter of $H_0 = 83.4 \pm 8\,\mathrm{km\ s^{-1}\ Mpc^{-1}}$ is found. When the zero point of K-TFR is corrected to account for recent results that find a Large Magellanic Cloud distance modulus of 18.39 ± 0.05, a Hubble parameter of $88.0 \pm 6\,\mathrm{km\ s^{-1}\ Mpc^{-1}}$ is found. Effects from Malmquist bias are shown to be negligible in this sample as galaxies are restricted to a minimum rotational velocity of $150\,\mathrm{km\ s^{-1}}$. It is also shown that the results of this study are negligibly affected by the adopted slope for the K-TFR, inclination binning, and distance binning. A comparison with the results of the Hubble Key Project (Freedman *et al.* 2001) is made. Discrepancies between the K-TFR distances and the HKP I-TFR distances are discussed. Implications for Λ-CDM cosmology are considered with $H_0 = 84\,\mathrm{km\ s^{-1}\ Mpc^{-1}}$. It is concluded that it is very difficult to reconcile the value of H_0 found in this study with ages of the oldest globular clusters and matter density of the universe derived from galaxy clusters in the context of Λ-CDM cosmology.

Key words. Distance scale—galaxies: distances and redshifts.

1. Introduction

Hubble (1929) discovered the existence of a linear relationship between the radial velocity (cz) of a galaxy and the distance to the galaxy estimated from absolute magnitude criteria. The Hubble Law is a key component of cosmological theory and

the current value of the Hubble parameter (H_0) provides an important constraint on cosmological models (e.g., Spergel *et al.* 2003, 2006; Hinshaw *et al.* 2009; Dunkley *et al.* 2009; Komatsu *et al.* 2009).

Determination of the Hubble parameter requires accurate redshift independent distances to a large number of galaxies or clusters of galaxies. The Hubble Key Project (Freedman *et al.* 2001 and references therein – hereafter HKP) utilized several dozen galaxies with Cepheid distances to calibrate five secondary distance indicators – Type Ia SN, Type II SN, the Fundamental Plane (FP), the Surface Brightness Fluctuation Method (SBF), and the Tully–Fisher Relation (TFR). From these five methods the HKP found $H_0 = 72\,\mathrm{km\ s^{-1}\ Mpc^{-1}}$. This value is supported by the recent WMAP results (Spergel *et al.* 2003, 2006; Hinshaw *et al.* 2009; Dunkley *et al.* 2009; Komatsu *et al.* 2009).

While there is general agreement that $H_0 = \sim 70$ to $74 \pm 8\,\mathrm{km\ s^{-1}\ Mpc^{-1}}$, there have been several recent studies that suggest higher or lower values for the Hubble parameter. Sandage *et al.* (2006) find $H_0 = 62 \pm 5\,\mathrm{km\ s^{-1}\ Mpc^{-1}}$. Tully & Pierce (2000) found $H_0 = 77 \pm 8\,\mathrm{km\ s^{-1}\ Mpc^{-1}}$ from 12 galaxy clusters with the I-band TFR. The Tully & Pierce (TP00) study predates the final HKP Cepheid distances (Freedman *et al.* 2001). Utilizing the HKP Cepheid distances with the 24 zero point calibrators in the TP00 study results in a downward revision of their I-band zero point from 21.56 to 21.50 with a resulting increase in H_0 to $79\,\mathrm{km\ s^{-1}\ Mpc^{-1}}$. This value is closer to the value the HKP found with the FP ($H_0 = 82 \pm 9\,\mathrm{km\ s^{-1}\ Mpc^{-1}}$) than the final adopted value of $H_0 = 72\,\mathrm{km\ s^{-1}\ Mpc^{-1}}$.

Recent work also argues for a shorter distance to the Large Magellanic Cloud (LMC) than the value adopted by the HKP (Macri *et al.* 2006; An *et al.* 2007; Benedict *et al.* 2007; Grocholski *et al.* 2007; van Leeuwen *et al.* 2007; Catelan & Cortes 2008; Feast *et al.* 2008). These studies suggest an LMC distance modulus of 18.39 ± 0.05 whereas the HKP adopted an LMC distance modulus of 18.50 ± 0.10. The newer LMC distance modulus results in an increase of H_0 of $\sim 5\%$.

In this work, the value of H_0 is re-evaluated using the Ks-band TFR and taking advantage of recent improvements in data available for Tully–Fisher studies. The Two Micron All Sky Survey (2MASS – Strutskie *et al.* 2006) has provided near infrared Ks-band photometry for a much larger sample of galaxies than was available for the study of TP00. The use of K-band TFR is advantageous because extinction corrections are significantly smaller in the K-band than in the B-band or I-band. Recently, Springob *et al.* (2007) have corrected for systematic differences between rotational velocities measured from 21 cm emission and rotational velocities measured from optical rotation curves (Mathewson & Ford 1996) and provided a large database of uniformly corrected spiral galaxy rotational velocities for Tully–Fisher studies.

Utilizing these data sources and the morphologically type dependent TFR (Russell 2004) strict selection criteria are applied to provide a highly accurate set of distances to 16 galaxy clusters and over 200 ScI galaxies with distances greater than 40 Mpc. From the galaxy clusters, the Hubble parameter is found to be $H_0 = 84.2 \pm 6\,\mathrm{km\ s^{-1}\ Mpc^{-1}}$. The ScI galaxy sample gives $H_0 = 83.4 \pm 8\,\mathrm{km\ s^{-1}\ Mpc^{-1}}$.

This paper is organized as follows: section 2 describes the calibration of the morphologically type dependent K-band TFR. Section 3 describes the sample selection for the determination of Hubble parameter. Section 4 discusses the value of the Hubble parameter found in this study and considers possible influences on the value of H_0. Section 5 compares the results of this study with those of the HKP. Section 6 is a discussion

of implications for cosmology if $H_0 = 84\,\mathrm{km\,s^{-1}\,Mpc^{-1}}$ and a brief conclusion is provided in section 7.

2. Calibration, sample selection, and scatter of the K-band TFR for ScI galaxies

2.1 *Calibration of Ks-band TFR*

The accuracy of results derived from TFR distance estimates depends critically upon a large calibration sample for the determination of slope and zero point and strict selection criteria that eliminate galaxies from the sample which are most likely to have large TFR errors. The following sections describe the selection criteria utilized in the calibration of the Ks-TFR for this analysis.

2.1.1 *Morphological type effect in the TFR*

Russell (2004, 2005a) found evidence that the B-band TFR may be split into two morphological groups with identical slope but a zero-point offset of 0.57 mag. The first morphological group (ScI group) includes galaxies classified as ScI, ScI-II, ScII, SbcI, SbcI-II, SbcII and Seyfert galaxies with spiral morphology. The second morphological group (Sb/ScIII group) includes Sab/Sb/Sbc/Sc galaxies that do not have ScI group morphology. ScI group galaxies are more luminous at a given rotational velocity than Sb/ScIII group galaxies (Russell 2004). Failure to account for this type effect results in overestimated B-band TFR distances for Sb/ScIII group galaxies, underestimated B-band TFR distances for ScI group galaxies, and a TFR slope that is too steep. While the morphological type effect is largest in the B-band, it persists in the I-band and Ks-band (Giovanelli *et al.* 1997b; Masters *et al.* 2008).

For the calibration of Ks-band TFR (hereafter K-TFR) in this analysis, the ScI group calibrators were restricted to galaxies with Hubble T-types ranging from 3.1 to 6.0 and with luminosity classes ranging from 1.0 to 3.9 as classified in HyperLeda (Paturel *et al.* 2003). The ScI group was calibrated, and then cluster samples were used to determine the zero point offset for the Sb/ScIII group as discussed in section 2.2. The ScI group calibrator sample includes 10 galaxies with direct distance determinations from Cepheid variables (Freedman *et al.* 2001); 1 galaxy (NGC 2903) with a direct distance determined from photometry of bright stars (Drozdovsky & Karachentsev 2000); 18 galaxies that are members of groups or companions of galaxies from the SBF survey of Tonry *et al.* (2001); and seven galaxies that are companions of galaxies with Type Ia SN distances from Freedman *et al.* (2001). As found by Ajhar *et al.* (2001), the SBF distance moduli from Tonry *et al.* (2001) are reduced by 0.06 mag in order to align them with the final HKP Cepheid distance scale. The calibrator sample is listed in Tables 1 and 2.

2.1.2 *Rotational velocities*

The greatest source of uncertainty in TFR distances is found in the measurement and correction of rotational velocities derived from HI linewidths and optical rotation curves (Haynes *et al.* 1999). In addition to uncertainty in raw 21 cm linewidths, corrections must be made for inclination and turbulence. Inclination corrections are larger

Table 1. Calibrators with direct distance measurements.

Galaxy	log Vrot	±	Inclination (°)	Ktc	m-M	zp Ks
N1365	2.459	0.088	39	6.33	31.27	22.81
N1425	2.254	0.021	62	8.24	31.70	23.02
N2903	2.319	0.012	60	5.96	29.75	22.81
N3198	2.190	0.009	71	7.64	30.70	23.14
N3351	2.267	0.036	44	6.61	30.01	22.85
N4321	2.357	0.079	32	6.56	30.91	23.06
N4414	2.340	0.038	51	6.88	31.24	23.21
N4535	2.285	0.037	45	7.36	30.99	22.93
N4548	2.333	0.040	35	7.08	31.05	22.87
N4725	2.324	0.030	63	6.11	30.46	23.33
N7331	2.431	0.006	65	5.91	30.84	23.03

Table 2. Calibrators with companion SBF or SN Ia distance measurements.

Galaxy	log Vrot	±	Inclination (°)	Ktc	m-M	zp Ks	Companion
N3089	2.246	0.019	52	9.24	32.60	22.98	Antlia
N3095	2.313	0.043	55	8.58	32.60	23.09	Antlia
N3223	2.438	0.021	47	7.49	32.60	23.15	Antlia
N3318	2.310	0.034	58	8.86	32.60	22.84	Antlia
N3347	2.338	0.048	69	8.34	32.60	23.13	Antlia
I2560	2.311	0.016	64	8.57	32.60	23.12	Antlia
I2522	2.276	0.043	48	9.22	32.60	22.76	Antlia
N4575	2.224	0.027	51	9.24	32.58	23.14	Cen30
N4603	2.345	0.007	51	8.25	32.58	23.14	Cen30
N1255	2.204	0.038	45	8.33	31.47	23.11	N1201
N3054	2.366	0.017	54	8.25	32.67	23.06	N3078
N5011a	2.192	0.037	57	10.02	33.05	23.10	N5011
N5033	2.365	0.019	63	6.87	31.03	22.80	N5273
N7610	2.176	0.039	52	10.94	33.56	22.82	N7619
I4538	2.208	0.016	39	9.41	32.59	23.11	N5903
E582-12	2.211	0.020	56	9.10	32.26	23.07	N5898
E377-31	2.230	0.015	60	10.17	33.24	22.82	N3557
E287-13	2.249	0.017	78	9.17	32.49	22.92	N7097
E471-49	2.521	0.013	60	9.80	35.39	22.95	E471-27
E471-51	2.322	0.036	53	11.40	35.39	22.99	E471-27
E471-2	2.355	0.012	71	11.13	35.39	22.99	E471-27
E577-1	2.294	0.024	71	11.28	35.05	23.00	E508-67
N4541	2.421	0.019	64	10.01	34.93	23.10	N4493
E444-31	2.338	0.020	50	11.11	35.34	23.10	I4232
A530465	2.207	0.021	67	12.27	35.34	23.01	I4232

and subject to greater uncertainty as galaxies approach face on orientation. For this reason, calibrator galaxies selected for this analysis were restricted to inclinations $> 30^\circ$ and $\leq 80^\circ$. An inclination limit of 80° was chosen because luminosity class cannot be assigned for edge on galaxies and therefore edge on galaxies cannot be accurately classified as ScI or Sb/ScIII group.

The influence of turbulence corrections is greater at smaller linewidths (Giovanlli *et al.* 1997b). It is also now well established that slower rotating galaxies have larger TFR scatter than faster rotators (Federspiel *et al.* 1994; Giovanelli 1996; Giovanelli *et al.* 1997b; Masters *et al.* 2006, 2008). For example, Federspiel *et al.* (1994) found that TFR scatter decreases from ± 0.90 mag for the slowest rotators to only ± 0.43 mag for the fastest rotators. Giovanelli (1996) also found that the fastest rotators had a scatter about a factor of 2 smaller than the slowest rotators.

In order to avoid the problems associated with the large TFR scatter of the slowest rotators, calibrators were also restricted to galaxies with rotational velocities $\geq 150\,\mathrm{km\ s^{-1}}$ in the Springob *et al.* (2007) rotational velocity database.

2.1.3 *Ks-band magnitudes and corrections*

2MASS total Ks-band magnitudes (Strutskie *et al.* 2006) were extracted from NED and corrected for galactic and internal extinction following Tully *et al.* (1998) and a small cosmological k-correction was added following Poggianti (1997). The galactic and internal extinction corrections were made for each galaxy using the B-band extinction corrections provided in HyperLeda (Paturel *et al.* 2003). The corrections are as follows: the galactic B-band extinction (ag in HyperLeda) was multiplied by 0.086 to derive the extinction in the Ks-band and the internal absorption correction (ai in HyperLeda) was multiplied by 0.15 to derive the extinction in the Ks-band. Finally, the k-correction was approximated as -1.52z as per Poggianti (1997). Thus the total corrected Ks-band magnitudes (Ktc) in this study were derived from uncorrected 2MASS total Ks-band magnitudes according to the following:

$$\mathrm{Ktc} = \mathrm{Ktot} - 0.086\mathrm{ag} - 0.15\mathrm{ai} - 1.52\mathrm{z}. \quad (1)$$

2.1.4 *Slope and zero point of the ScI group Ks-band TFR*

Figure 1 is a plot of the absolute Ks-band magnitude ($\mathrm{M_K}$) *versus* the logarithm of the rotational velocity for the 36 ScI group calibrators listed in Tables 1 and 2. All rotational velocities used in this study are drawn from the sample of Springob *et al.* (2007). The solid line in Fig. 1 is a least squares fit and has a slope of -8.22 ± 0.37. The value of the slope does not significantly change when determined independently for the various subsamples from which the calibration distances were drawn. The 11 Table 1 calibrators with direct distance estimates, 18 Table 2 calibrators with SBF distance estimates, and seven Table 2 calibrators with Type Ia SN distance estimates give slopes of -7.78, -8.51, and -8.16 respectively.

Using the slope of -8.22 derived from the full sample of calibrators, a mean zero point of 23.01 ± 0.14 is found for the 36 calibrator galaxies. With the slope of -8.22, the value of zero point is not affected by the method from which the calibration distance was determined. The 11 galaxies with direct distance determinations in Table 1, 18 galaxies with SBF distance determinations in Table 2, and seven galaxies with Type

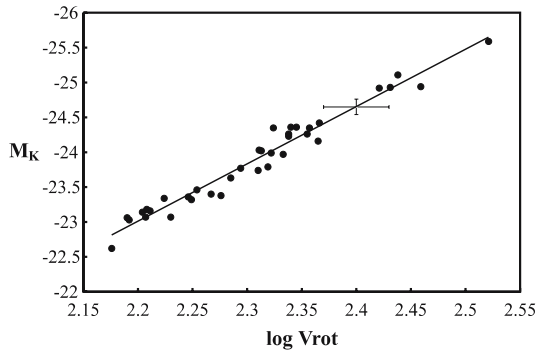

Figure 1. Calibration of the K-TFR with 36 calibrators from Tables 1 and 2. Solid line is a slope of −8.22 and error bars represent typical uncertainty in log Vrot and M_K.

Ia SN distance determinations in Table 2 give mean zero points of 23.01 ± 0.17, 23.01 ± 0.14, and 23.02 ± 0.06 respectively.

K-TFR distance moduli for ScI group galaxies in this analysis are calculated using the following equation:

$$m - M_K = Ktc + 8.22(\log Vrot - 2.2) + 23.01. \quad (2)$$

It is important to note that equation (2) should not be viewed as the global K-band TFR. The sample has a lower rotational velocity limit of 150 km s^{-1}, morphological restriction to Hubble T-types 3.1 to 6.0, and luminosity class restriction to luminosity classes I, I–II, II, and II–III. Caution should be used in applying the calibration developed here to galaxies that fall outside these ranges.

2.2 *Morphological type dependence in the K-band TFR*

Russell (2004) found that ScI group galaxies have a zero point 0.57 mag larger than Sb/ScIII galaxies. The effect of morphological type dependence is known to be smaller in the I-band where Giovanelli *et al.* (1997a) found a 0.32 mag smaller zero point for Sa/Sab galaxies and 0.10 mag smaller zero point for Sb galaxies relative to Sbc and later type spirals. It has generally been thought that any type effects should disappear in the near infrared bands. However, Masters *et al.* (2008) recently found evidence that there is a small type effect in the J, H, and K-band Tully–Fisher relations.

The Masters *et al.* (2008) sample includes a much broader range of morphological types (e.g., extreme late type and early type spirals) and slower rotators that have been excluded from this study. In order to test for a morphological type effect in the K-band we define the Sb group galaxies as all non-Seyfert galaxies of morphological T-types 1.0 to 3.0 and as found by Russell (2004) include in the Sb group later type spirals of Hubble T-types 3.1–6.0 and luminosity classes ≥ 4.0 as classified in HyperLeda.

If a type effect similar to that found in the B-band TFR (Russell 2004) exists in the K-TFR, then Sb galaxies within clusters should have larger mean distances than ScI group galaxies when Sb group distances are calculated using the ScI group zero point. To test for this effect, clusters were selected from the template sample of Springob *et al.* (2007). The selection criteria adopted for the galaxies within the clusters was consistent with that utilized for the ScI group calibrator sample. Specifically, galaxies were

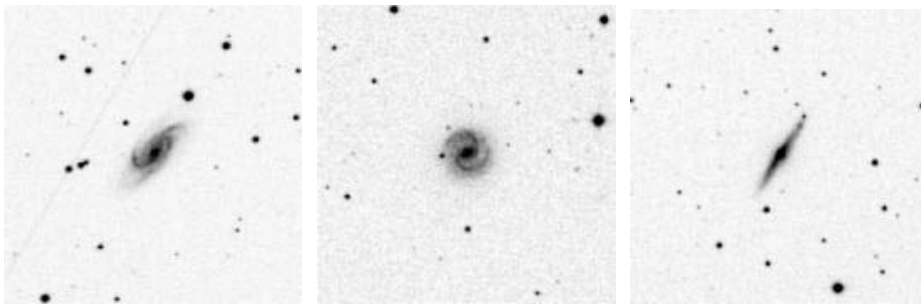

(a) ScI NGC 551 (b) NGC 2582 (c) UGC 1695

Figure 2. Visual inspection of images helps confirm galaxy morphology and inclinations derived from photometry.

required to have inclinations between 35° and 80°, rotational velocities $\geq 150\,\mathrm{km\ s^{-1}}$, and Hubble T-types from 1.0 to 6.0. Clusters used for estimating the size of the type effect in the K-band all had at least 12 member galaxies from the Springob *et al.* (2007) sample meeting the above criteria and a minimum of four galaxies in both the ScI and the Sb morphological groups. For the Abell 400 cluster, the sample was also restricted to galaxies with redshifts ranging from $6500\,\mathrm{km\ s^{-1}}$ to $8000\,\mathrm{km\ s^{-1}}$.

At larger distances, fewer galaxies in the HyperLeda database are assigned luminosity classes. For this reason, before calculating distances the HyperLeda image of each candidate galaxy meeting all other criteria was visually inspected in order to determine if the morphology of the galaxy is ScI group morphology or Sb group morphology. For example, NGC 551 (Fig. 2a) in the Pisces supercluster is classified as SBbc in HyperLeda, but no luminosity class is provided. Visual inspection of the DSS image in HyperLeda confirms NGC 551 has arm structure of ScI group morphology and thus is included in the ScI group sample.

Visual inspection also serves as an independent check on the inclination estimates provided by Springob *et al.* (2007). For example, Springob *et al.* (2007) report an inclination of 51° for NGC 2582 in the Cancer cluster. However, visual inspection of the NGC 2582 image (Fig. 2b) clearly indicates an inclination much closer to face on orientation than 51°. UGC 1695 in the Pisces supercluster has an inclination of 76° in the Springob *et al.* (2007) database and thus would meet the selection criteria of this study. However, visual inspection of the UGC 1695 image (Fig. 2c) reveals an inclination very close to 90° and it is therefore impossible to determine the luminosity class of this galaxy. Galaxies for which visual inspection of the image indicated an unambiguous problem with the reported inclination were rejected from the sample.

The Pisces supercluster (Abell 262, NGC 507, and NGC 383 clusters), Abell 400, Coma, Cancer, Abell 1367, and Hydra clusters had enough galaxies meeting the selection criteria above to estimate the size of the morphological type effect in the K-band. Distances to all galaxies not removed from the sample by the selection criteria described above were calculated for these six clusters using equation (2). The resulting mean distances to the Sb group and ScI group galaxies in each cluster are provided in Table 3. It can be seen that for each cluster the mean Sb group distance to the cluster is greater than the mean ScI group distance to the cluster by +0.06 to +0.40 mag. The mean difference for the 56 Sb group galaxies in Table 3 is $+0.19 \pm 0.10$ mag. This indicates

Table 3. Type effect in the K-band TFR.

Cluster	N Sb	m-M Sb	N ScI	m-M ScI	Sb-ScI
Pisces	13	34.02	17	33.87	+0.15
A400	10	34.84	6	34.58	+0.26
Coma	9	34.65	6	34.59	+0.06
Cancer	9	34.21	6	33.81	+0.40
A1367	11	34.72	4	34.60	+0.12
Hydra	4	33.84	8	33.49	+0.35

that a smaller but still detectable type effect remains in the K-band TFR. All distances to Sb group galaxies will therefore be calculated using equation (2), but with a zero point of 22.82 rather than the zero point of 23.01 found for ScI group galaxies.

2.3 *Comparison with other K-band TFR studies*

One of the largest potential sources of a systematic bias in TFR distances arises when an incorrect TFR slope is applied to the TFR sample. For this reason it is important that the TFR derived in this study is only applied to galaxies meeting the selection criteria utilized to calibrate the type dependent K-band TFR.

Karachentsev *et al.* (2002), Noordermeer and Verheijen (2007), and Masters *et al.* (2008) developed K-band Tully–Fisher relations from 2MASS photometry that are suitable for comparison with this study. Karachentsev *et al.* (2002) found a K-TFR slope of -9.02 ± 0.25 using Hubble distances for 436 galaxies. No corrections for morphological type dependence are applied and the sample includes galaxies with rotational velocities as small as 75 km s^{-1}. Noordmeer & Verheijen (2007) found a K-TFR slope of -8.65 ± 0.19 from a sample of 48 spirals with rotational velocities as small as 83 km s^{-1}. No corrections for morphological type dependence were applied. Masters *et al.* (2008) used a 'basket of clusters' technique to create a K-TFR template with 888 spiral galaxies including galaxies with rotational velocities smaller than 75 km s^{-1}. The Masters *et al.* (2008) sample provides a global K-TFR corrected for several types of bias (see section 3 of Masters *et al.* 2008) with a direct slope of -8.85 for the full sample.

It is interesting to note that these studies utilize different samples and calibration techniques and yet find consistent slopes in the small range of -8.65 to -9.02 for the direct K-band TFR. These slopes are slightly steeper than the slope of -8.22 found in this study for a sample restricted to galaxies with ScI group morphology and with rotational velocities $\geq$150 km s^{-1}. Masters *et al.* (2008) also applied all bias corrections and the direct TFR to 374 'High mass' galaxies in their template sample with rotational velocities in excess of 160 km s^{-1} and found a shallower slope of -8.06 which is consistent with the slope found with the 36 calibrators in Tables 1 and 2. This suggests that the shallower slope found in this study results from the exclusion of slower rotators from the sample.

The slope for the ScI calibrator sample was also determined using only the 33 ScI galaxies with rotational velocities $\geq$160 km s^{-1} and was found to remain unchanged. It is reassuring to note that the slope derived from 36 ScI group calibrators is only slightly steeper than the slope Masters *et al.* (2008) found from 374 comparable

galaxies after applying their complete set of bias corrections. The slope found in this study is unbiased as long as it is applied to galaxies meeting the selection criteria utilized in compiling the calibrator sample. Inclusion of slower rotating galaxies would require a steeper slope.

Masters *et al.* (2008) also calibrated the K-TFR using a bivariate fit and found an even steeper slope of -10.02 for their complete sample of 888 galaxies. In order to test for the possible influence of the slope on the results of this study the zero point was calculated for the 36 ScI group calibrators using a slope of -10.02. The resulting zero point is reduced from 23.01 ± 0.14 to 22.84 ± 0.20 with the steeper slope. Keeping a 0.19 mag type effect, Sb group galaxy distances will be calculated using a zero point of 22.65 when the slope of -10.02 is utilized.

In this analysis, the Hubble parameter will be derived from the slope and zero points found in sections 2.1.4 and 2.2. However, as a test of the effect of the K-TFR slope on the Hubble parameter, the distances to galaxies in the cluster sample (section 3.1) will also be calculated using the slope of -10.02 and the zero points of 22.84 and 22.65 for the ScI and Sb group respectively (section 4.2).

2.4 *Scatter in the type dependent K-band TFR*

The subject of scatter in the TFR has been widely studied (Bernstein *et al.* 1994; Willick 1996; Raychaudhury *et al.* 1997; Giovanelli *et al.* 1997b; Tully & Pierce 2000; Sakai *et al.* 2000; Kannappan *et al.* 2002; Russell 2005b; Masters *et al.* 2008). For the purpose of this study, it is important to note that the scatter observed with this sample is only applicable to the selection criteria utilized in creating the Tully–Fisher relations discussed in sections 2.1 and 2.2. Larger intrinsic scatter will occur with a less restrictive set of sample selection criteria. The RMS scatter for the 36 ScI group calibrators in Tables 1 and 2 is ± 0.14 mag relative to the calibration distance moduli.

Most 2MASS Ks-band magnitudes for galaxies in the sample have an uncertainty of only ± 0.03 to ± 0.10 mag. However, Noordermeer & Verheijen (2007) point to reasons for suspecting that the 2MASS uncertainty estimates are overly optimistic and suggest a more realistic estimate of ± 0.11 mag for the typical K-band uncertainty – which is adopted for this study. The mean uncertainty of logarithm of the rotational velocities (Springob *et al.* 2007) used for the 36 calibrators is ± 0.030. Thus the greatest source of uncertainty in the K-band TFR distances should be expected to arise from the effect of inclination uncertainty on the correction of the rotational velocity to edge on orientation. Since visual inspection of images eliminated galaxies with grossly inaccurate or uncertain inclinations (section 2.2), the galaxies in the final sample have inclinations that should be accurate to 5° or better.

With a slope of -8.22 the typical distance modulus uncertainty is ± 0.247 mag from the uncertainty in the rotational velocities as reported by Springob *et al.* (2007). This may be added in quadrature with a Ks-band magnitude uncertainty of ± 0.11 mag to yield a total expected distance modulus uncertainty of ± 0.27 mag. The RMS scatter of the ScI group calibrator zero point is only ± 0.14 mag which is significantly smaller than the scatter expected from the rotational velocities. This may be an indication that the uncertainty in the rotational velocities is overestimated by Springob *et al.* (2007) The mean uncertainty Springob *et al.* (2007) reported for the rotational velocities is of the magnitude expected for a $\pm 6^\circ$ inclination uncertainty. The small observed scatter suggests that inclinations are actually accurate to $\sim \pm 3^\circ$ in most cases. In any case, the

small observed scatter in the K-TFR zero point indicates that there is negligible intrinsic scatter in the K-TFR for galaxies meeting the selection criteria adopted in this study.

3. Samples for determination of the Hubble parameter

3.1 *Springob et al. (2007) galaxy cluster sample*

Table 4 lists the 10 clusters from the template sample of Springob *et al.* (2007) that had at least five galaxies meeting the selection criteria utilized to define the calibration samples as discussed in sections 2.1 and 2.2. Column 1 is the cluster. Column 2 is the number of cluster members in the full Springob *et al.* (2007) sample. Columns 3, 4, and 5 are the number of galaxies within each cluster rejected for not meeting the rotational velocity, inclination, and Hubble T-type criteria respectively. Column 6 is the number of galaxies rejected for having K-TFR distances that fall outside the primary distribution of K-TFR distances for the cluster. Column 7 provides notes on several rejections specific to individual clusters or galaxies. Column 8 is the final sample of accepted galaxies for each cluster. In order to reduce the effect of motions within the local velocity field and cluster depth effects, the cluster sample was also restricted to those clusters with a minimum distance of 40.0 Mpc.

In addition to the criteria discussed in section 2, galaxies were restricted to the redshift range of 6500–8000 km s^{-1} for the Abell 400 cluster and 8000–10000 km s^{-1} for the Abell 2197/99 cluster. Six of the 10 clusters had member galaxies meeting all other criteria rejected based upon the distance distribution of the cluster members (column 6 of Table 4). With the exception of UGC 8229 in the Coma cluster which has a K-TFR distance modulus 2.3σ less than the Coma cluster mean, all galaxies rejected as being outside the primary cluster distance distribution were at least $\pm 2.5\sigma$ from the mean of the accepted galaxies.

The largest sample of galaxies from the Springob *et al.* (2007) template sample is found in the Pisces supercluster which is comprised of galaxies in the Abell 262, NGC 507, and NGC 383 clusters. The selection criteria utilized in this study are illustrated using this sample of 95 galaxies (Table 4). As indicated in Table 4, 23 galaxies from the

Table 4. Cluster template sample rejection reasons.

Cluster	N	log Vrot	*i*	*t*	Distance distribution	Other	Final sample
Pisces	95	39	19	7	7		23
A400	50	13	7	2	4	3 declination rejected 9 redshift range rejected	12
Cancer	49	20	13	1	5		10
Coma	43	14	9	5	4		11
A1367	33	6	6	6	3		12
Hydra	31	9	9	0	2	1 uncertain 2MASS Ks	10
A3574	29	12	8	0	0	1 no Ks; 1 R.A. rejected	7
A2197/99	22	1	8	0	0	4 redshift range rejected	9
A2634	22	9	3	2	0		8
A779	17	7	2	4	0		5

Table 5. Pisces supercluster galaxies rejected for distance distribution.

Galaxy	m-M K-TFR	Vcmb	Δm-M	Mpc
NGC 688	34.36	3894	+0.59	74.5
UGC 1744	34.67	4578	+0.90	85.9
U1416	35.08	5222	+1.31	103.8
U1257	34.59	4404	+0.82	82.8
U724	34.63	4880	+0.86	84.3
U1493	33.05	3895	−0.72	40.8
U1672	32.96	4367	−0.81	39.1

Pisces supercluster met all selection criteria applied. These 23 galaxies have a mean distance modulus of 33.77 ± 0.21 and all have distance moduli within the range 33.35 to 34.19.

Note that 39 of the 95 galaxies in the Pisces supercluster template sample had rotational velocities less than 150 km s^{-1}. For 27 of these galaxies it was possible to calculate K-TFR distances. The 27 slow rotators had a mean distance modulus of 34.06 with a substantially larger RMS scatter of ±0.87 mag when compared with the 23 accepted galaxies. In fact only eight of the 27 slow rotators have K-TFR distance moduli that fall within the distance modulus range of the 23 accepted galaxies. This situation does not improve if the slope of −10.02 is adopted as the mean distance for the slow rotators is then decreased to 33.57 ± 0.90. The significantly larger scatter found for the slow rotators justifies the exclusion of slower rotators from the sample and is consistent with the findings of Federspiel *et al.* (1994) who found a scatter of ±0.90 mag for slow rotators but only ±0.40 mag for faster rotators. It was also suggested by Giovanelli (1996) that the safest means of obtaining the tightest possible TFR is to exclude lower luminosity galaxies.

The Pisces supercluster sample had seven galaxies (listed in Table 5) rejected for a distance modulus that deviated from the mean of the accepted galaxies by $\pm 2.5\sigma$ or greater. Accepting these seven galaxies would slightly increase the mean distance modulus to 33.86 but significantly increase the observed RMS scatter about the mean to ±0.45 mag. The accepted galaxies have K-TFR distances ranging from 47 to 69 Mpc. It seems prudent then to reject from the Pisces supercluster sample a galaxy such as UGC 1416 which has a K-TFR distance of 104 Mpc and therefore potentially a large error in the K-TFR distance. In fact, UGC 1416 may be a genuine background galaxy as the 2MASS total K-band angular diameter of UGC 1416 (rotational velocity = 209 km s^{-1}) is only 1.00′ whereas the accepted Pisces supercluster galaxy UGC 1676 (Vrot = 214 km s^{-1}) has a K-band angular diameter of 2.19′. However, whether UGC 1416 is a genuine background galaxy or a galaxy with an extremely large K-TFR distance error, it would be inappropriate to use UGC 1416 in calculating the mean distance to the Pisces supercluster as it is clearly not representative of the normal distance distribution of cluster members.

The 10 Springob *et al.* (2007) template clusters were supplemented with six additional clusters or groups from the non-template sample of Springob *et al.* (2007) which had at least five galaxies meeting the selection criteria of this study. The value of the Hubble parameter derived from these 16 clusters is discussed in section 4.

3.2 *ScI galaxies from the Mathewson & Ford sample*

Mathewson & Ford (1996 – MF96) provided a catalog of 2447 galaxies – most with rotational velocities derived from optical rotation curves. Springob *et al.* (2007) corrected the rotational velocities from MF96 to standardize them with rotational velocities derived from hydrogen linewidths and have included the MF96 sample in their non-template catalog. The MF96 catalog was searched for all ScI group galaxies meeting the rotational velocity, inclination, and morphology selection criteria of this study. This yielded 140 galaxies with ScI group morphology as classified in HyperLeda and distances of at least 40.0 Mpc but not greater than 140.0 Mpc.

The image of each galaxy from the MF96 sample with Hubble T-types from 3.1–6.0, but for which the luminosity class was not provided was visually inspected. An additional 78 ScI group galaxies were identified by examining arm structure in the images bringing the total sample to 218 ScI group galaxies with distances in the 40.0 Mpc to 140.0 Mpc range. Note that these 78 galaxies were identified visually before determining the K-TFR distance and therefore the decision of whether or not to include these galaxies in the sample was not influenced by prior knowledge of the distance to each galaxy.

In the process of identifying the 218 ScI group galaxies, 12 galaxies were identified for which there was a 15° or greater discrepancy between the HyperLeda and the MF96 inclination, or for which the inclination provided in MF96 was highly uncertain. In some cases the inclination uncertainty results from unusual elongated arm structure that produces an inclination closer to edge on orientation than visual inspection of the image indicates. For example, ESO 384-9 has a 59° inclination in Springob *et al.* (2007) but the visual appearance suggests an inclination closer to 40° with arms that are significantly elongated. Visual inspection of the 218 accepted ScI group galaxies confirmed that the Springob *et al.* (2007) inclinations for the accepted galaxies are reasonable.

For these 218 ScI galaxies, rotational velocities were taken from Springob *et al.* (2007) and 2MASS Ks-band magnitudes were corrected as discussed in section 2.1.3. The value of the Hubble parameter derived from the 218 ScI galaxies is discussed in the next section.

4. The Hubble parameter

4.1 *The value of the Hubble parameter from 16 galaxy clusters and 218 ScI galaxies*

Table 6 lists the mean distances, redshifts and the value of the Hubble parameter indicated for each of the 16 galaxy clusters discussed in section 3.1. The mean RMS scatter of the distance moduli of cluster members around the cluster mean is ±0.26 mag. Note that the intrinsic K-TFR scatter must be smaller than this because of an expected contribution to the observed scatter from cluster depth effects. The 10 template clusters give an unweighted mean for the Hubble parameter of $85.1 \pm 5\,\mathrm{km\ s^{-1}\ Mpc^{-1}}$. The weighted mean is $85.0 \pm 5\,\mathrm{km\ s^{-1}\ Mpc^{-1}}$. The individual template clusters give values of the Hubble parameter within the remarkably small range from $H_0 = 82.9\,\mathrm{km\ s^{-1}\ Mpc^{-1}}$ to $H_0 = 86.9\,\mathrm{km\ s^{-1}\ Mpc^{-1}}$. The six non-template clusters generally have smaller numbers of accepted cluster members and have a larger range in H_0 values

Table 6. Cluster Hubble parameter.

Cluster	N	m-M	±	Mpc	Vcmb	H_0	±
Template							
Pisces	23	33.77	0.21	56.8	4794	84.4	7.7
A1367	12	34.49	0.22	79.1	6559	82.9	7.9
A400	12	34.60	0.18	83.2	7227	86.9	7.0
Coma	11	34.70	0.26	87.1	7563	86.8	9.8
Cancer	10	33.61	0.34	52.7	4523	85.8	12.5
Hydra	10	33.43	0.19	48.4	4080	84.3	7.0
A2197/99	9	35.26	0.21	112.7	9479	84.1	7.8
A2634	8	35.00	0.22	100.0	8689	86.9	8.4
A3574	7	33.80	0.29	57.6	4903	85.1	10.6
A779	5	34.76	0.43	89.5	7532	84.2	15.2
Non-Template							
A548	8	35.64	0.43	134.3	12062	89.8	16.1
A114	7	36.52	0.26	201.4	17810	88.4	9.9
A1736	7	35.57	0.22	130.0	11585	89.1	8.6
A3716	7	35.94	0.28	154.2	14382	93.3	11.3
ESO 596	6	34.85	0.23	93.3	7043	75.5	7.6
ESO 471	5	35.40	0.21	120.2	8429	70.1	6.4

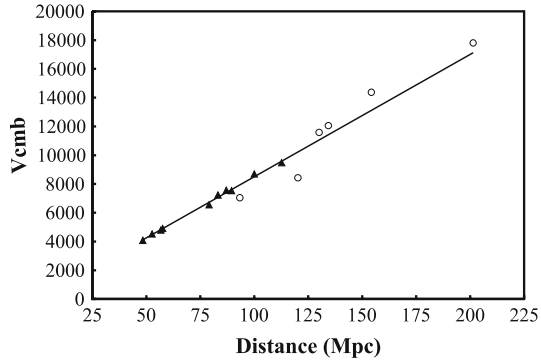

Figure 3. Hubble plot for 16 galaxy clusters in Table 6. Filled triangles are template clusters and open circles are non-template clusters. Solid line represents $H_0 = 84$.

($H_0 = 70.1$ to 93.3). The unweighted mean for the full sample of 16 clusters is $H_0 = 84.9 \pm 5\,\mathrm{km\ s^{-1}\ Mpc^{-1}}$ and the weighted mean is $H_0 = 84.2 \pm 5\,\mathrm{km\ s^{-1}\ Mpc^{-1}}$. The redshift velocity–distance relation for the 16 clusters is shown in Fig. 3.

Table 7 lists the mean values of H_0 grouped into five distance bins for the 218 ScI galaxies discussed in section 3.2. The mean value of H_0 for the 218 ScI galaxies is $83.4 \pm 8\,\mathrm{km\ s^{-1}\ Mpc^{-1}}$ which is very close to the weighted mean value found for the 16 clusters in Table 6. The two samples therefore indicate a Hubble parameter of $84 \pm 6\,\mathrm{km\ s^{-1}\ Mpc^{-1}}$ using the morphologically type dependent K-TFR.

It is important to note that if Malmquist bias significantly affects the sample, then the value of the Hubble parameter is expected to increase significantly with distance

Table 7. MF96 ScI Hubble parameter.

Distance range	N	log Vrot	H_0
40–59.9	52	2.306	82.9
60.0–79.9	63	2.298	83.3
80.0–99.9	52	2.326	86.5
100.0–119.9	28	2.336	82.1
120.0–139.9	23	2.368	79.5
Total	218		83.4

(Bottinelli *et al.* 1986, 1988; Federspiel *et al.* 1994). The effects of Malmquist bias are not observed in Table 7 as there is very little variation in H_0 from one distance bin to the next. It is also worth noting that the two most distant distance bins have the lowest mean H_0 values and thus run counter to what is expected when there is a significant Malmquist bias. Lack of a signature from Malmquist bias is not surprising given that the observed scatter of the K-TFR in this study is very small and that Masters *et al.* (2008) concluded that the effects of Malmquist bias are negligible in a sample that included many, much slower rotators theoretically more susceptible to introducing Malmquist bias effects than the fast rotators used in this study.

4.2 *Effect of the slope of K-TFR*

It is worth investigating whether or not the results would change if a steeper slope is adopted for the K-TFR. As discussed in section 2.3, while Masters *et al.* (2008) find a slope for fast rotators consistent with that found from the 36 calibrators in Tables 1 and 2, they found a slope of -10.02 for the K-TFR from a bivariate fit that includes slower rotators. Using this global K-TFR slope of -10.02 and the mean zero points for ScI group and Sb group galaxies calculated in section 2.3, distances to all 16 clusters were recalculated (Table 8). The unweighted mean values for the Hubble parameter are 83.9 ± 7 km s^{-1} Mpc^{-1} for the 10 template clusters and 83.7 ± 7 km s^{-1} Mpc^{-1} for the full sample of 16 clusters. Therefore the value of the Hubble parameter derived in this study is not significantly affected by the adopted K-TFR slope.

It is important to note that the steeper slope produces mean distances to individual cluster members that are rotational velocity dependent. For example in the A400 cluster the six fastest and six slowest rotators have mean distance moduli of 34.84 ± 0.16 and 34.55 ± 0.27, respectively, with a slope of -10.02. With the slope of -8.22 the mean distance moduli of the fastest and slowest rotators are 34.65 ± 0.15 and 34.55 ± 0.21, respectively, suggesting that the shallower slope used in this study is more appropriate for a sample restricted to faster rotators. The discrepancy between fast and slow rotators is smaller than A400 for the Pisces supercluster ($+0.12$ mag) but even larger than A400 for the Coma cluster ($+0.45$ mag).

4.3 *Effect of inclinations*

In order to test the possible effects of galaxy inclinations on the derived value of H_0, the 218 ScI galaxies were grouped into four inclination bins (Table 9). It can be seen in Table 9 that the inclination bins from 50°–69° give a mean Hubble parameter of

Table 8. Cluster Hubble parameter with K-TFR slope of −10.02.

Cluster	m-M K-TFR	H_0
Pisces	33.81	82.9
A1367	34.47	83.8
A400	34.69	83.4
Coma	34.77	84.0
Cancer	33.61	85.8
Hydra	33.35	87.2
A2197/99	35.33	81.4
A2634	35.08	83.7
A3574	33.80	85.1
A779	34.82	81.8
A548	35.65	89.4
A114	36.53	88.1
A1736	35.47	93.3
A3716	36.05	88.7
ESO 596	34.82	76.5
ESO 471	35.59	64.2

Table 9. Hubble parameter for 218 ScI galaxies group by inclination bins.

Inclination range (°)	N	H_0
35–49	38	79.7
50–59	75	84.3
60–69	70	84.3
70–80	35	83.1
Total	218	83.4

84.3 km s^{-1} Mpc^{-1}, consistent with the weighted mean value found for the 16 galaxy clusters. The galaxies with inclinations from 50°–69° are especially important because they comprise two-third of the ScI sample and are least susceptible to the problems associated with low or high inclinations. The galaxies with inclinations from 35°–49° give $H_0 = 79.7$ km s^{-1} Mpc^{-1} which is mildly discrepant when compared with the other inclination bins. This discrepancy is not unexpected as uncertainty in corrected rotational velocities increases for galaxies closer to face on orientation.

4.4 *Effect of visual inspection of images*

As described in section 2, images of candidate galaxies for this sample were visually inspected to verify inclination estimates from axial ratios and morphological luminosity classification. For the cluster sample, galaxies not assigned a luminosity class

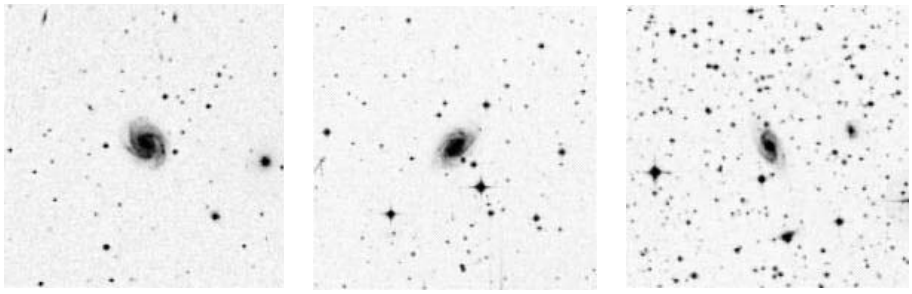

(a) ESO 578-16 (b) ESO 385-26 (c) ESO 328-16

Figure 4. Examples of galaxies from the Mathewson & Ford (1996) sample that were identified as ScI galaxies from visual inspection of images for this study.

in HyperLeda were in some cases found to have ScI group morphology (Fig. 2a) and therefore had distances calculated with the ScI group zero point rather than the Sb group zero point. Thus within the clusters, the effect of visual inspection of images leads to a slight increase in clusters distances if galaxies were incorrectly judged to have ScI group morphology.

For the ScI sample 140 of the 218 galaxies were classified as ScI group galaxies in HyperLeda. The remaining 78 galaxies were classified as ScI group galaxies from visual inspection of images. A sample of these galaxies is provided in Fig. 4 to illustrate the identification of ScI morphology. Not surprisingly, 61 of these 78 additions were at distances beyond 80.0 Mpc. The 78 added galaxies seem to have the effect of slightly increasing the overall value of H_0. The value of H_0 for the 140 galaxies classified as ScI group in HyperLeda is $82.2 \pm 8\,\mathrm{km\,s^{-1}\,Mpc^{-1}}$ whereas the 78 galaxies added from visual inspection give $H_0 = 85.7 \pm 8\,\mathrm{km\,s^{-1}\,Mpc^{-1}}$.

However, both subsets are very close to the weighted mean H_0 value found from the 16 clusters ($H_0 = 84.2\,\mathrm{km\,s^{-1}\,Mpc^{-1}}$) and therefore support the higher value of H_0 found in this study. It is also important to recognize that the galaxies added to the ScI sample from visual inspection of images would have even closer distances if the Sb zero point was utilized and therefore would give an even larger value for H_0.

4.5 *Effect of distance distribution rejection for clusters*

Table 10 lists the distances to the 16 clusters when the galaxies rejected as having anomalous K-TFR distances relative to the cluster mean are included. The unweighted mean H_0 value then is $84.5 \pm 5\,\mathrm{km\,s^{-1}\,Mpc^{-1}}$ which may be compared with an unweighted mean H_0 value of $84.9 \pm 5\,\mathrm{km\,s^{-1}\,Mpc^{-1}}$ found when 25 galaxies are rejected from the clusters due to large discrepancies in their distances relative to the accepted galaxies. The rejection of individual galaxies within the clusters based upon the distance distribution of the cluster members therefore has a negligible effect on the value of H_0.

4.6 *The large Magellanic cloud distance modulus*

In section 4.1, a Hubble parameter of $84\,\mathrm{km\,s^{-1}\,Mpc^{-1}}$ was found. The zero point calibration for the K-TFR assumes a distance modulus to the LMC of 18.50 ± 0.10 as

Table 10. Clusters with distance distribution rejected galaxies included.

Cluster	N	m-M	Mpc	Vcmb	H_0
Template					
Pisces	30	33.86	59.1	4716	79.8
A1367	15	34.55	81.3	6618	81.4
A400	16	34.62	83.9	7291	87.3
Coma	15	34.51	79.8	7402	92.8
Cancer	12	33.79	57.3	4534	79.1
Hydra	12	33.54	51.1	4144	81.1
A2197/99	9	35.26	112.7	9479	84.1
A2634	8	35.00	100.0	8689	86.9
A3574	7	33.80	57.6	4903	85.1
A779	5	34.76	89.5	7532	84.2
Non-template					
A548	8	35.64	134.3	12062	89.8
A114	7	36.52	201.4	17810	88.4
A1736	7	35.57	130.0	11585	89.1
A3716	7	35.94	154.2	14382	93.3
ESO 596	6	34.85	93.3	7043	75.5
ESO 471	5	35.40	120.2	8429	70.1

Table 11. LMC distance modulus.

Study	m-M LMC	±
Macri *et al.* (2006)	18.41	0.10
Benedict *et al.* (2007)	18.40	0.05
van Leeuwen *et al.* (2007)	18.39	0.05
Grocholski *et al.* (2007)	18.40	0.04
An *et al.* (2007)	18.34	0.06
Catelan & Cortes (2008)	18.44	0.11
Feast *et al.* (2008)	18.37	0.09

adopted by the HKP (Freedman *et al.* 2001). However, recent studies suggest the LMC distance modulus is closer to 18.39 ± 0.05 (Table 11). Macri *et al.* (2006) demonstrated an important metallicity effect in the Cepheid P–L relation and concluded that LMC distance modulus is 18.41 ± 0.10. A number of subsequent studies have adopted metallicity corrections for the Cepheid P–L relation. Benedict *et al.* (2007) provided new trigonometric parallaxes to Galactic Cepheids and found a distance modulus of 18.50 ± 0.03 without metallicity corrections but 18.40 ± 0.05 when applying the metallicity correction of Macri *et al.* (2006). van Leeuwen *et al.* (2007) used revised Hipparcos parallaxes and found the distance modulus to the LMC is 18.52 ± 0.03 without metallicity corrections or 18.39 ± 0.05 with metallicity corrections. An *et al.* (2007) constructed the Cepheid P–L relation from seven galactic clusters with Cepheids and found a distance to the LMC of 18.48 without metallicity

corrections and 18.34 ± 0.06 with metallicity corrections. Fouque *et al.* (2007) did not study the effects of metallicity on the P–L relation but concluded that the LMC distance modulus must be smaller than 18.50 after correcting for metallicity effects.

Using Type II Cepheid's and RR Lyrae variables, Feast *et al.* (2008) find an LMC distance modulus of 18.37 ± 0.09. Catelan and Cortes (2008) provide a revised trigonometric parallax to RR Lyrae and derive an LMC distance modulus of 18.44 ± 0.11. From the K-band luminosity of the red clump in 17 LMC clusters, Grocholski *et al.* (2007) find the LMC distance modulus to be 18.40 ± 0.04.

It is clearly seen from these results that the latest studies indicate that the best value for LMC distance modulus is ~ 0.10 mag smaller than the value adopted by the HKP when the required metallicity corrections are applied to the Cepheid P–L relation. The recent studies listed in Table 11 give an unweighted mean for the LMC distance modulus of 18.39 ± 0.05 and require a downward revision of -0.11 mag for the zero points of the K-TFR calibrators in Tables 1 and 2. Applying this correction to the K-TFR distances of this study increases the derived value of the Hubble parameter from the Type Dependent K-TFR to $88 \pm 6\,\mathrm{km\ s^{-1}\ Mpc^{-1}}$.

5. Comparison with the results of the Hubble key project

Since the value of the Hubble parameter found in this analysis is significantly higher than the value found by Freedman *et al.* (2001) from the I-TFR, SBF, FP, Type Ia SN, and Type II SN methods, the HKP results are reconsidered in the following sections. It is important to note that the HKP reported a Hubble parameter of 82 ± 9 from 11 clusters with fundamental plane distances – consistent with the result found in this study from 16 clusters and 218 ScI galaxies using the morphologically type dependent K-TFR. The remaining four methods used by the HKP give $H_0 = \sim 71$.

5.1 *The HKP I-TFR*

The HKP I-band TFR was calibrated by Sakai *et al.* (2000). Final adjustments to cluster distances were presented in Freedman *et al.* (2001) in order to account for the final Cepheid calibrator distances. From the I-TFR the HKP found $H_0 = 71 \pm 7\,\mathrm{km\ s^{-1}\ Mpc^{-1}}$, significantly smaller than the value found in this study. Table 12 compares the distances to the eight clusters in common with this study and Freedman *et al.* (2001).

Table 12. Comparison with HKP I-TFR distances.

Cluster	m-M K-TFR	m-M HKP I-TFR	I-TFR – K-TFR
Pisces	33.77	34.01	+0.24
A1367	34.49	34.75	+0.26
A400	34.60	34.73	+0.13
Coma	34.70	34.66	−0.04
Cancer	33.61	34.35	+0.74
Hydra	33.43	33.83	+0.40
A3574	33.80	33.97	+0.17
A2634	35.00	35.30	+0.30

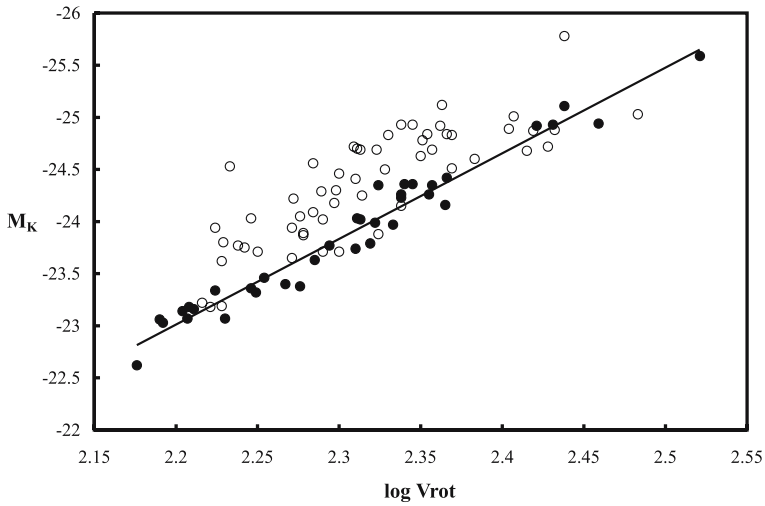

Figure 5. K-TFR plot for ScI galaxies in the cluster sample at the I-TFR distances reported by Freedman *et al.* (2001). Filled circles are the 36 calibrators from Tables 1 and 2 and solid line is a slope of −8.22. Open circles are the ScI's in the cluster sample at the I-TFR distances of the HKP.

In every cluster except Coma, the HKP cluster distances are larger than the K-TFR distances found in this study with a mean distance modulus difference of +0.28 mag.

Figure 5 is a plot of the absolute magnitude (M_K) *versus* the logarithm of the rotational velocity (log Vrot) for the ScI group galaxies in the cluster sample (open circles) of this study at the I-TFR cluster distances determined by the HKP. Also plotted in Fig. 5 are the 36 ScI group calibrators from this study (filled circles). It is clearly seen in Fig. 5 that the cluster galaxies would be systematically over-luminous relative to the calibrators if they were at the I-TFR distances found by the HKP.

There is independent evidence that the problem is not the K-TFR distances to the clusters found in this study, but rather the I-TFR distances found by the HKP. For example, the HKP found an I-TFR distance to Cen30 of 43.2 Mpc. However, a Cepheid distance to the Cen30 galaxy NGC 4603 was determined by Newman *et al.* (1999) and the galaxy was found to be at 33.3 Mpc–10 Mpc closer than the HKP I-TFR. Tonry *et al.* (2001) found a distance to the Centaurus cluster of 32.8 Mpc from nine early type galaxies with SBF distances – a value in excellent agreement with the NGC 4603 Cepheid distance.

The HKP I-TFR distance to the Antlia cluster is 45.1 Mpc. Four galaxies in the Antlia cluster with SBF distances in Tonry *et al.* (2001) give a distance of 33.1 Mpc. Recently Bassino *et al.* (2008) determined the distances to the giant ellipticals NGC 3258 and 3268 in Antlia from the globular cluster luminosity function (GCLF). The mean distance of the two giant ellipticals is 33.4 Mpc – in excellent agreement with the SBF distances. It should also be noted that seven galaxies from the Antlia cluster were included in the calibration sample for the K-TFR of ScI galaxies using the Tonry *et al.* (2001) SBF distances to Antlia (Table 2). The mean zero point of these seven galaxies is in exact agreement (23.01 ± 0.16) with the overall mean found from the full sample of 36 ScI calibrators. In order for the HKP I-TFR distance to Antlia to be correct, the K-TFR zero point would need to be increased by 0.67 mag, which is 4.8σ larger than the observed scatter in the K-TFR zero point.

The explanation for the discrepancy in the HKP project I-TFR distances is beyond the scope of this paper. However, the above evidence strongly argues for a problem with the HKP I-TFR distances rather than the K-TFR distances found in this study.

5.2 *HKP SBF distances*

The HKP found $H_0 = 70 \pm 6$ km s^{-1} Mpc^{-1} from six galaxies with surface brightness fluctuation distances. For each of these galaxies it is possible to compare the HKP SBF distance with cluster or group FP, SBF, or K-TFR distance estimates from this or other studies.

NGC 4881 is a member of the Coma cluster and for this galaxy the HKP finds an SBF distance of 102.3 Mpc. The HKP FP distance to Coma is 85.8 Mpc and the K-TFR distance is 87.1 Mpc. The SBF distance modulus to NGC 4881 is therefore +0.35 mag larger than that is found from other methods. Considering that the FP distance is derived from 81 galaxies and the K-TFR distance is derived from 11 galaxies, it would be reasonable to conclude that NGC 4881 is simply on the backside of the Coma cluster and not representative of the mean Coma cluster distance. In addition, Ferrarese *et al.* (2000) note that there is a large uncertainty in the NGC 4881 SBF distance because the galaxy was not observed in the V band.

NGC 4373 (ESO 322-6) is a member of the Cen30 cluster and the HKP found an SBF distance of 36.3 Mpc for this galaxy. This distance is in exact agreement with NGC 4373's nearby companion ESO 322-8 for which Tonry *et al.* (2001) find an SBF distance of 36.3 Mpc.

NGC 708 is a member of the Abell 262 cluster and the HKP reports an SBF distance of 68.2 Mpc. The K-TFR distance to A262 is 56.5 Mpc from 10 galaxies in A262 meeting the ScI or Sb/ScIII group selection criteria of this study. The NGC 708 SBF distance modulus is 0.41 mag larger than the K-TFR distance modulus.

NGC 5193 is listed as a member of the Abell 3560 cluster in Ferrarese *et al.* (2000). However, Abell 3560 is actually a background cluster with $cz = \sim$15,000 km s^{-1}. NGC 5193 is coincident with coordinate distribution of the Abell 3574 cluster sample of Springob *et al.* (2007). The HKP reports an SBF distance of 51.5 Mpc for NGC 5193 in excellent agreement with the HKP FP distance to A3574 of 51.6 Mpc. The K-TFR distance to Abell 3574 is 57.6 Mpc – somewhat larger than the SBF and FP distance. Corrected to the cosmic microwave background reference frame the redshift of NGC 5193 is 3991 km s^{-1} which is consistent with the lower redshift members of Abell 3574.

IC4296 is also coincident with the Abell 3574 cluster and has an SBF distance of 55.5 Mpc – very close to the value found with the K-TFR and consistent with the HKP FP distance.

NGC 7014 has an SBF distance of 67.3 Mpc. The ScI galaxy ESO 286-79 is the closest neighbor to NGC 7014 for which a K-TFR distance can be calculated. Using the rotational velocity provided by MF96 ($\log \mathrm{Vrot} = 2.468$) and a corrected 2MASS K-band magnitude of 8.71, the K-TFR distance to ESO 286-79 is 60.8 Mpc. The NGC 7014 SBF distance modulus is larger by +0.22 mag.

The HKP SBF estimate for H_0 is based upon only six galaxies in six clusters. There is a certain amount of risk in determining the distance to a cluster from a single galaxy as the selected galaxy may be on the front or backside of the cluster. It is therefore reasonable to conclude that the value of H_0 found in this study with the K-TFR using

a sample of 16 galaxy clusters with a minimum of five cluster members and a sample of 218 ScI galaxies provides a more reliable sampling of the Hubble flow than a value derived from six SBF distances.

However, it is interesting to note that the three nearest galaxies in the HKP SBF sample (NGC 4373, IC 4296 and NGC 5193) have distances in excellent agreement with Tonry *et al.* (2001) SBF, HKP FP, and K-TFR distances from this study. The three most distant SBF galaxies have distance moduli, a mean +0.33 mag larger than the distance moduli, found from the other methods. This may indicate a systematic problem with the application of the SBF method at distances beyond ~ 60 Mpc, but a larger number of SBF distances will be needed in order to test that possibility in any meaningful way.

5.3 *Type II and Type Ia SN*

The HKP found $H_0 = 72 \pm 9\,\mathrm{km\ s^{-1}\ Mpc^{-1}}$ from four Type II SN. Four galaxies is too small a sample to draw meaningful conclusions about the value of H_0. In addition, only three galaxies with Cepheid distances were available for fixing the zero point of the Type II SN distance scale (Table 11 of Freedman *et al.* 2001). Given these problems with sample size, the HKP Type II SN result is not considered here.

The HKP found $H_0 = 71 \pm 6\,\mathrm{km\ s^{-1}\ Mpc^{-1}}$ from 36 Type Ia SN. In compiling the K-TFR calibrator sample for this study seven ScI galaxies were identified as nearby companions to four of the Type Ia SN. For the remaining 32 Type Ia SN, companion ScI galaxies for which K-TFR distances could be calculated were not found. The seven ScI's with calibration distances defined by the Type Ia SN are shown as open diamonds against the remaining 29 calibrators (filled circles) in Fig. 6. Note that the seven galaxies with Type Ia SN distances fall tightly on the mean relation defined by the other 29 galaxies (solid line).

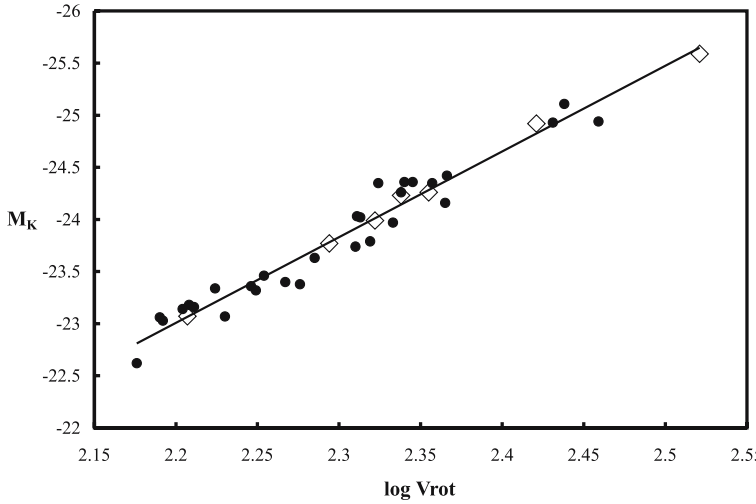

Figure 6. Comparison of seven ScI calibrators (open diamonds) that are companions of galaxies with Type Ia SN distances compared with the remaining 29 ScI calibrators (filled circles). Solid line has a slope of −8.22.

It should also be recalled from section 2.1 that the slope defined by the seven ScI's with SN calibration distances is −8.16 which is in excellent agreement with the slope defined by the full sample of 36 calibrators. In addition, the mean zero point of these seven galaxies is 23.01 ± 0.06 – in exact agreement with the overall mean.

While the comparison sample is an uncomfortably small sample of only four Type Ia SN distances, the comparison suggests that there is excellent agreement between the Type Ia SN distances and the K-TFR distances of this study. The comparison can only be improved when greater numbers of Type Ia SN distances become available in the local universe.

5.4 *Can the Hubble parameter be* $70\,km\,s^{-1}\,Mpc^{-1}$?

Supported by the results of the HKP (Freedman *et al.* 2001) and WMAP (Spergel *et al.* 2003, 2006; Hinshaw *et al.* 2009; Dunkley *et al.* 2009) it is generally accepted that the value of H_0 is $\sim 70\,km\,s^{-1}\,Mpc^{-1}$. Sandage *et al.* (2006) find an even smaller value for H_0 of $62 \pm 5\,km\,s^{-1}\,Mpc^{-1}$. In this study, the value of H_0 was found to be $H_0 = 84 \pm 6\,km\,s^{-1}\,Mpc^{-1}$ when adopting the HKP zero point for the LMC. Adopting an LMC distance modulus of 18.39 indicated from recent studies (section 4.6) increases H_0 to $88 \pm 6\,km\,s^{-1}\,Mpc^{-1}$. The values found in this study are significantly larger than those found in other studies.

Figure 7 is a plot of the K-band absolute magnitudes *versus* the logarithm of the rotational velocity for the 36 calibrators in Tables 1 and 2 and the ScI galaxies in the 16 clusters. The K-band absolute magnitudes for the calibrators are calculated for an LMC distance modulus of 18.39 whereas absolute magnitudes of the cluster galaxies are derived assuming the mean cluster distances for $H_0 = 70\,km\,s^{-1}\,Mpc^{-1}$. A Hubble parameter of $70\,km\,s^{-1}\,Mpc^{-1}$ is adopted as a reasonable average of the H_0 values the

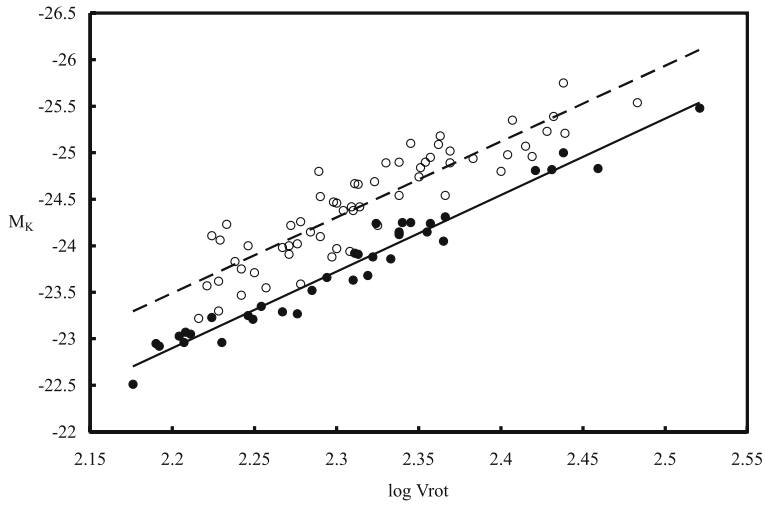

Figure 7. K-TFR plot for ScI galaxies in the 16 clusters (Table 6) at redshift distances using $H_0 = 70\,km\,s^{-1}\,Mpc^{-1}$. Open circles are cluster ScI's at Hubble distances and dashed line is a least squares fit. Filled circles are the 36 calibrators from Tables 1 and 2 with an LMC distance modulus of 18.39 and solid line is a least squares fit. The ScI's are systematically more luminous than the calibrators at the $H_0 = 70$ distances.

HKP and Sandage *et al.* (2006) teams would find using an LMC distance modulus of 18.39.

It is evident in Fig. 7 that the K-TFR defined by the calibrators is inconsistent with $H_0 = 70\,\mathrm{km\,s^{-1}\ Mpc^{-1}}$. There are reasons for suspecting the discrepancy between the HKP results and this study could arise from problems with the HKP distances and samples. First, it is important to note again that the HKP value of H_0 from the fundamental plane was $H_0 = 82 \pm 9\,\mathrm{km\,s^{-1}\ Mpc^{-1}}$ which is in excellent agreement with the results of this study.

It was shown in section 5.1 that the HKP I-TFR distances are significantly at odds with SBF, Cepheid, and GCLF distance estimates for the Antlia and Cen30 clusters whereas the K-TFR calibration of this study is an excellent fit to the other distance estimates. In addition, the K-TFR selection criteria used in this sample eliminates galaxies likely to contribute to Malmquist bias and large distance errors; whereas a more generous sample selection criteria is employed by Sakai *et al.* (2000).

The HKP SBF H_0 value was determined from only six individual SBF distance estimates and the HKP Type II SN H_0 estimate was determined from only four distance estimates with three zero point calibrators. These sample sizes used to determine H_0 are 6–9 times smaller than the zero point calibrator sample used in this study and do not compare favorably with the K-TFR sample sizes used to calculate H_0 in this study. In addition, the SBF distances agree well with FP and K-TFR distance estimates for the closest galaxies, but are systematically too large for the more distant galaxies in the HKP sample suggesting a possible problem with the SBF at larger distances.

Finally, the HKP used 36 Type Ia SN for which a small comparison sample suggests excellent agreement between the SN distances and the K-TFR calibration of this study. However, the HKP again finds a much smaller value of H_0 than found in this study. The reason for this discrepancy will only be resolved with a larger sample of galaxies with both Type Ia SN and K-TFR distances. However, the discrepancy suggests that either the HKP Type Ia SN sample or the K-TFR sample of this study inadequately samples the Hubble flow. Given that the HKP Type Ia SN sample is significantly smaller, and spread over a much larger distance range (58.0 to 467.0 Mpc) than the ScI and cluster samples of this study (40.0 to 140.0 Mpc range for all but 2 clusters), it is possible that the Type Ia SN distances have not uniformly sampled the Hubble flow.

6. Implications for cosmology

The value of the Hubble constant provides an important constraint upon cosmological models. The HKP value for H_0 has been argued to support the Λ-CDM concordance cosmology model (hereafter Λ-CDM – e.g., Spergel *et al.* 2003, 2006; Hinshaw *et al.* 2009; Dunkley *et al.* 2009; Komatsu *et al.* 2009). In this section we briefly consider implications for cosmology if $H_0 = 84\,\mathrm{km\,s^{-1}\ Mpc^{-1}}$.

A basic requirement of any cosmological model is that the universe must be older than the oldest objects contained within it. Currently, the oldest dated objects in the Milky Way are globular clusters which have ages as large as ~ 13 Gyr (e.g., Salaris & Weiss 2002; Rakos & Schombert 2005). If it is assumed that the Milky Way is nearly as old as the universe, then any internally consistent set of cosmological parameters must be able to account for a universe that is at least 13.5 Gyr.

Retaining the prevailing Λ-CDM parameters with a flat universe, $\Omega m = 0.27$ and $\Omega\Lambda = 0.73$ a Hubble constant of $84\,\mathrm{km\,s^{-1}\ Mpc^{-1}}$ results in a universe that is

11.55 Gyr (Wright 2006), younger than the oldest globular clusters. This discrepancy can be resolved at the cost of a lower matter density and higher dark energy density. A flat universe with $H_0 = 84$, $\Omega m = 0.14$ and $\Omega\Lambda = 0.86$ would have an age of 13.71 Gyr (Wright 2006) and would be consistent with the ages of the oldest globular clusters. However, a matter density of $\Omega m = 0.14$ is only at best marginally consistent with the matter density estimated from galaxy cluster studies. Carlberg *et al.* (1996) found $\Omega m = 0.24 \pm 0.05$ and more recently Muzzin *et al.* (2007) find $\Omega m = 0.22 \pm 0.02$.

This discrepancy is made more serious if other galaxies are older than the Milky Way thus requiring an even older age for the universe. For example, Lee *et al.* (2001) found that the globular clusters in NGC 1399 may be several billion years older than the galactic GC system. Bregman *et al.* (2006) determined the ages of 29 elliptical galaxies with IR spectral energy distributions and found eight galaxies (27.6% of their sample) had ages greater than 15.7 Gyr with the oldest galaxy being 20.6 Gyr. Based upon the obvious disagreement with Λ-CDM parameters, Bregman *et al.* (2006) argued that this discrepancy might indicate a problem for the absolute accuracy of their age dates and shifted the ages in their sample into a range that accommodates the standard Λ-CDM model. It is noted here that with $H_0 = 84$, the Bregman *et al.* (2006) ages would require a matter density of $\Omega m = 0.06$ to accommodate elliptical galaxies with ages of 16 Gyr. This matter density is clearly inconsistent with that found from galaxy clusters (Carlberg *et al.* 1996; Muzzin *et al.* 2007).

It is of concern to note that it is not possible to simultaneously reconcile the observed matter density of the universe ($\Omega m = 0.22 \pm 0.02$), estimated ages of the oldest globular clusters ($\sim$13 Gyr), and value of the Hubble parameter found in this study ($H_0 = 84 \pm 6$ km s^{-1} Mpc^{-1}) with Λ-CDM cosmology. Note that the discrepancy with Λ-CDM expectations becomes even more severe when the latest results for the LMC distance modulus are taken into account because the value of H_0 found in this study is then raised to 88 ± 6 km s^{-1} Mpc^{-1}. Whether or not this indicates a problem for the standard cosmological model will require further investigation.

7. Conclusion

The morphologically type dependent Tully–Fisher Relation (Russell 2004) was calibrated in the Ks-band for galaxies with a minimum rotational velocity of 150 km s^{-1}. Distances were derived for galaxies in 16 galaxy clusters and 218 ScI galaxies using rotational velocities from the Springob *et al.* (2007) database. Applying unweighted and weighted means as well as binning of sample galaxies by distance and inclination, the value of the Hubble parameter was consistently found to fall in the range of 82 to 85 km s^{-1} Mpc^{-1}with a preferred value of 84 ± 6 km s^{-1} Mpc^{-1}. If recent results for the value of the LMC distance modulus are adopted, the value of H_0 would increase to 88 ± 6 km s^{-1} Mpc^{-1}.

It is very difficult to fit the observed matter density of the universe derived from galaxy clusters ($\Omega m = 0.22 \pm 0.02$ – Muzzin *et al.* 2007); ages of the oldest globular clusters ($\sim$ 13 Gyr – Salaris & Weiss 2002); and the value of H_0 found in this study ($H_0 = 84 \pm 6$) with standard Λ-CDM cosmology. In order to reconcile the age of the universe for a flat universe with dominant dark energy component and $H_0 = 84$ requires a matter density of $\Omega m = 0.14$, which is 4.8σ below the value found by Muzzin *et al.* (2007).

While a Hubble parameter of 84 km s^{-1} Mpc^{-1} is significantly different from the value found by Freedman *et al.* (2001), it was shown that the Freedman *et al.* (2001) I-TFR distances to clusters result in a K-TFR for ScI galaxies in clusters that is systematically overluminous by $\sim$0.35 mag relative to the K-TFR defined by 36 calibrators in this study. Since the HKP I-TFR distances are also inconsistent with SBF, Cepheid, and GCLF distances to the Antlia and Cen30 clusters, it was concluded that the problem most likely lies with the HKP I-TFR distances rather than the K-TFR distances derived in this study. The discrepancy between the HKP I-TFR results and the K-TFR results of this study might seem puzzling in light of the fact that the 36 calibrators of this study are fixed to the same Cepheid distance scale utilized by the HKP. However, sample selection criteria play an important role, and evidence was presented that the strict selection criteria of this study provide more reliable distances as well as a slope more appropriate for the faster rotators used in this study.

A Hubble parameter of 84 km s^{-1} Mpc^{-1} is also inconsistent with the recent best estimate from WMAP (Dunkley *et al.* 2009; Hinshaw *et al.* 2009; Komatsu *et al.* 2009) which finds $H_0 = 71.9 \pm 2.7$ km s^{-1} Mpc^{-1} assuming a six parameter Λ-CDM cosmology with flat geometry. The implications of this discrepancy for cosmological modeling will require further study and it is concluded that the value of H_0 found in this study does not confirm the WMAP value of H_0.

Acknowledgements

I would like to thank the many researchers who have collected the data utilized in this research. This research has made use of the NASA/IPAC Extragalactic Database (NED) which is operated by the Jet Propulsion Laboratory, California Institute of Technology, under contract with the National Aeronautics and Space Administration. This research has made use of the HyperLeda database (http://leda.univ-lyon1.fr). Figures 2 and 4 are images extracted from the Digitized Sky Survey. The Digitized Sky Surveys were produced at the Space Telescope Science Institute under U.S. Government grant NAG W-2166. The images of these surveys are based on photographic data obtained using the Oschin Schmidt Telescope on Palomar Mountain and the UK Schmidt Telescope.This research also makes use of data from Two Micron All Sky Survey, which is a joint project of the University of Massachusetts and the Infrared Processing and Analysis Center, funded by NASA and the NSF. I would like to thank the anonymous referee for suggestions that led to significant improvements in the presentation of these results.

References

Ajhar, E., Tonry, J., Blakeslee, J., Riess, A., Schmidt, B. 2001, *ApJ*, **559**, 584.
An, D., Terndrup, D., Pinsonneault, M. 2007, *ApJ*, **671**, 1640.
Bassino, L., Richtler, T., Dirsch, B. 2008, *MNRAS*, **386**, 1145.
Benedict, F. *et al.* 2007, *AJ*, **133**, 1810.
Bernstein, G. M., Guhathakurta, P., Raychaudhury, S., Giovanelli, R., Haynes, M. P., Herter, T., Vogt, N. P. 1994, *AJ*, **107**, 1962.
Bregman, J. N., Temi, P., Bregman, J. D. 2006, *ApJ*, **647**, 265.
Bottinelli, L., Gouguenheim, L., Paturel, G., Teerikorpi, P. 1986, *A&A*, **166**, 393.
Bottinelli, L., Gouguenheim, L., Paturel, G., Teerikorpi, P. 1988, *ApJ*, **328**, 4.
Catelan, M., Cortes, C. 2008, *ApJ*, **676**, L135.

Carlberg, R., Yee, H. K., Ellingson, E., Abraham, R., Gravel, P., Morris, S., Pritchet, C. 1996, *ApJ*, **462**, 32.
Drozdovsky, I., Karachentsev, I. 2000, *A&AS*, **142**, 425.
Dunkley, J. *et al.* 2009, *ApJS*, **180**, 306.
Feast, M., Laney, C., Kinman, T., van Leeuwen, F., Whitelock, P. 2008, *MNRAS*, **386**, 2115.
Federspiel, M., Sandage, A., Tammann, G. A. 1994, *ApJ*, **430**, 29.
Ferrarese, L., Mould, J. R., Kennicutt, R. C., Huchra, J. *et al.* 2000, *ApJ*, **529**, 745.
Fouque, P. *et al.* 2007, *A&A*, **476**, 73.
Freedman, W. L. *et al.* 2001, *ApJ*, **553**, 47.
Giovanelli, R., 1996, preprint astro-ph/9610129.
Giovanelli, R., Haynes, M. P., da Costa, L. N., Freudling, W., Salzer, J. J., Wegner, G. 1997a, *ApJL*, **477**, 1.
Giovanelli, R., Haynes, M. P., Herter, T., Vogt, N. P., da Costa, L.N., Freudling, W., Salzer, J. J., Wegner, G. 1997b, *AJ*, **113**, 53.
Grocholski, A., Sarajedini, A., Olsen, K., Tiede, G., Mancone, C. 2007, *AJ*, **134**, 680.
Haynes, M., Giovanelli, R., Chamaraux, P. *et al.* 1999, *AJ*, **117**, 2039.
Hinshaw, G., Weiland, J., Hill, R. *et al.* 2009, *ApJS*, **180**, 225.
Hubble, E. 1929, *PNAS*, **15**, 168.
Kannappan, S. J., Fabricant, D. G., Franx, M. 2002, *PASP*, **114**, 577.
Karachensev, I., Mitronova, S., Karachentseva, V., Kudrya, Y., Jarrett, T. 2002, *A&A*, **396**, 431.
Komatsu, E. *et al.* 2009, *ApJS*, **180**, 330.
Lee, H., Yoon, S., Lee, Y. 2001, *ASPC*, **245**, 445.
Macri, L., Stanek, K., Bersier, D., Greenhill, L., Reid, M. 2006, *ApJ*, **652**, 1133.
Masters, K., Springob, C., Huchra, J. 2008, *AJ*, **135**, 1738.
Masters, K., Springob, C., Haynes, M., Giovanelli, R. 2006, *ApJ*, **653**, 861.
Mathewson, D. S., Ford, V. L. 1996, *ApJS*, **107**, 97 MF96.
Muzzin, A., Yee, H. K., Hall, P., Lin, H. 2007, *ApJ*, **663**, 150.
Newman, J., Zepf, S., Davis, M., Freeman, W., Madore, B., Stetson, P., Silbermann, N., Phelps, R. 1999, *ApJ*, **523**, 506.
Noordermeer, E., Verheijen, M. 2007, *MNRAS*, **381**, 1463.
Paturel, G., Petit, C., Prugniel, P., Theureau, G., Rousseau, J., Brouty, M., Dubois, P., Cambresy, L. 2003, *A&A*, **412**, 45.
Poggianti, B. M. 1997, *A&AS*, **122**, 399.
Rakos, K., Schombert, J. 2005, *PASP*, **117**, 245.
Raychaudhury, S., von Braun, K., Bernstein, G. M., Guhathakurta, P. 1997, *AJ*, **113**, 2046.
Russell, D. G. 2004, *ApJ*, **607**, 241.
Russell, D. G. 2005a, *Ap&SS*, **298**, 577.
Russell, D. G. 2005b, *Ap&SS*, **299**, 405.
Sakai, S. *et al.* 2000, *ApJ*, **529**, 698.
Salaris, M., Weiss, A. 2002, *A&A*, **388**, 492.
Sandage, A., Tammann, G., Saha, A., Reindl, B., Macchetto, F., Panagia, N. 2006, *ApJ*, **653**, 843.
Spergel, D. N. *et al.* 2003, *ApJS*, **148**, 175.
Spergel, D. N. *et al.* 2006, *ApJS*, **170**, 377.
Springob, C., Masters, K., Haynes, M., Giovanelli, R., Marinoni, C. 2007, *ApJS*, **172**, 599.
Strutskie, M. F. *et al.* 2006, *AJ*, **131**, 1163.
Tonry, J. L., Dressler, A., Blakeslee, J. P., Ajhar, E. A., Fletcher, A. B., Luppino, G. A., Metzger, M. R., Moore, C. B. 2001, *ApJ*, **546**, 641.
Tully, R. B., Pierce, M. J., Huang, J., Saunders, W., Verheijen, M., Witchalls, P. L. 1998, *AJ*, **115**, 2264.
Tully, R. B., Pierce, M. J. 2000, *ApJ*, **533**, 744.
van Leeuwen, F., Feast, M., Whitelock, P., Laney, C. 2007, *MNRAS*, **379**, 723.
Willick, J. A. 1996, preprint – astro-ph/9610200.
Wright, E. L. 2006, *PASP*, **118**, 1711.

J. Astrophys. Astr. (2009) **30,** 119–131

The Effect of Hypothetical Diproton Stability on the Universe

R. A. W. Bradford
Bennerley, 1 Merlin Haven, Wotton-under-Edge, Gloucestershire, England, GL12 7BA.
e-mail: RickatMerlinHaven@hotmail.com

MS received 2008 March 28; Accepted 2009 March 16

Abstract. By calculation of the proton–proton capture cross-section, it is shown that the existence of a bound diproton state would not lead to significant production of diprotons during big bang nucleosynthesis, contrary to popular belief. In typical stellar interiors, the stability of diprotons would lead to a reaction pathway for converting protons to deuterons perhaps $\sim 10^{10}$ times faster than the usual weak capture reaction. This would prevent stars of the familiar hot, dense type from occurring in the universe. However, if diproton stability is achieved by an increase in the low-energy strong coupling, g_s, then stars with temperatures and densities sufficiently reduced so as to offset the faster reaction pathway to deuterium will appear to meet elementary stability criteria. The claim that there is a fine-tuned, anthropic upper bound to the strong force which ensures diproton instability therefore appears to be unfounded.

Key words. Big bang nucleosynthesis—star formation—anthropic cosmology.

1. Introduction

The standard models of particle physics and cosmology involve as many as 31 dimensionless universal constants (Tegmark *et al.* 2006). It has long been the dream of physicists to derive the numerical values of these constants from underlying mathematical principles. The early hopes that string theory might achieve this goal have been dashed by the plethora of possible string theories which are now known to exist (Susskind 2003). Nevertheless, many of the universal constants cannot be varied greatly from their actual values without fatally compromising the production of a universe within which highly complex structures, including life, can evolve (Dyson 1971; Carter 1974; Carr & Rees 1979; Davies 1982; Barrow & Tipler 1986). This has led to a resurgence of interest in the anthropic constraint, expressed in recent years in terms of our location on the string landscape (Dine 2003; Susskind 2003; Davies 2004; Hogan 2006; Linde 2007a). The anthropic perspective fits well with the naturally occurring multiverse scenarios envisaged in eternal inflation cosmologies (Davies 2004; Linde 1994, 2007b; Guth 2007). Some success can be claimed in regard to specific applications of anthropic selection, including calculations of constraints on the magnitude of the cosmological constant, consistent with structure formation (Martel *et al.* 1998;

Weinberg 2007); and calculations of constraints on dark matter density, consistent with solar system stability (Tegmark *et al.* 2006).

The application of anthropic reasoning works by considering the implications of varying a chosen universal constant or constants, and determining what magnitude of variation can have catastrophic consequences for some key feature of the universe. An example is some change which would result in a universe without hydrogen. Whatever other elements may exist, the absence of hydrogen would be sufficient to radically alter the available chemistry. There would be no water, no hydrocarbons, no proteins, and no hydrogen bonds. There would be no life as we know it. Whether any form of life could exist without hydrogen is unknown. But, from the point of view of the multiverse, any such universes are de-selected as candidates for our universe by our own water-and-protein based existence.

The challenge implicit in such anthropic reasoning is that we must be confident in our ability to calculate reliably the consequences of specified changes in the magnitudes of the universal constants. By definition, we are required to assess the properties of a universe that is not our own. This is intrinsically hazardous. Unlike real-world physics, we no longer possess the advantage of having the answer at the end of the book (that is, at the end of an experiment or observation). Placing reliance purely upon theory which is unverifiable even in principle must be treated with the greatest circumspection. This paper addresses a salutary example, namely the much quoted implications of diproton stability.

Dyson (1971); Davies (1972, 1982, 2004); Carr & Rees (1979); Barrow & Tipler (1986), Rees (1999), and Tegmark *et al.* (2006) all state that diproton stability would lead to a universe devoid of hydrogen, since all the hydrogen would be burnt to helium, via diprotons, during big bang nucleosynthesis (BBN). We claim that this is untrue. This scenario would be realised only if the proton–proton capture reaction were sufficiently fast to ensure that virtually all the free protons were captured before the diminishing temperature and density in the minutes following the big bang led to the reaction being frozen-out. We shall show that, on the contrary, the pp capture reaction is not sufficiently fast.

This oft-quoted 'diproton disaster' appears to have been based on a false analogy with neutron–proton capture to form deuterium during BBN. In this paper we shall show that the proton–proton capture reaction rate is suppressed with respect to proton–neutron capture as a consequence of the former involving identical fermions. Such a universe therefore remains unaffected by diproton stability until the first stars form.

There are at least two ways in which diproton stability can be contrived. One is by an increase in the strength of the strong force (g_s), as envisaged in Dyson (1971); Davies (1972, 1982, 2004); Carr & Rees (1979); Barrow & Tipler (1986); and Rees (1999). The other is by a decrease in the Higgs vacuum expectation value (v), and consequently a reduction in the quark masses and a reduction in the pion mass, and thus an increase in strong binding as a result of the increased range of the nuclear force (Agrawal *et al.* 1998a, 1998b; Hogan 2000; Tegmark *et al.* 2006). In both cases, the percentage change required (in g_s or v) is quite modest. Either scenario is equivalent as regards what happens during BBN, provided they correspond to the same diproton binding energy (B). However, they differ as regards their implications for stars.

If a sufficiently large change in the Higgs vacuum expectation value, v, is considered, then there are profound effects on the cooling mechanisms for star formation and the heat transfer properties of the stellar medium, due to the changes in lepton masses.

This has been discussed in Agrawal *et al.* (1998a). Here we shall consider the alternative: that diproton stability has resulted from an increase in the low-energy effective strong coupling constant, g_s. This is a simpler scenario for understanding stars in that, only the nuclear heating is affected. The heat transfer properties, which depend upon the particle masses and electromagnetic interactions, are unchanged. We shall show that elementary stability criteria can be met by 'biophilic' stars in such a universe; that is, by stars with lifetimes of the order of billions of years, and with luminosities and surface temperatures appropriate for the nurturing of biological life based on conventional molecular chemistry.

There is a danger that this exercise might be regarded as falling into the same trap as the false claims of a 'diproton disaster'. The trap is one of hubris. One needs to bear in mind that the notional variation of a universal constant may be intrinsically nonsensical. This would be the case if, after all, the numerical magnitudes of the universal constants are fixed by pure mathematics. But even if different values of the universal constants do make sense, and perhaps are actually realised within some multiverse, we fall victim to the sin of Prometheus in imagining that our understanding is sufficient to embrace its full implications. But this exceeds our far more modest objective. We claim only to shift the burden of proof back to anyone claiming that diproton stability is anthropically de-selected.

2. The proton–proton capture cross-section

In what follows we assume g_s to have been increased sufficiently for the diproton to be bound. (Note that this g_s is the old-fashioned, low-energy effective strong coupling, as opposed from the running coupling of QCD determined perturbatively at higher energies). For definiteness we shall consider increases in g_s of 20%, 30% and 40%. The proton–proton capture cross-section ($\sigma_{\rm pp}^{\rm cap}$) is smaller than that for neutron–proton capture ($\sigma_{\rm np}^{\rm cap}$) for three reasons:

1) Most obviously, the Coulomb barrier reduces $\sigma_{\rm pp}^{\rm cap}$. This is a small effect at BBN temperatures ($\sim 10^9$K), but accounts for several orders of magnitude reduction in the corresponding reaction rate at, say, central solar temperatures ($\sim 14 \times 10^6$ K).
2) At the non-relativistic energies of interest (< 0.1 MeV), the neutron–proton capture cross-section can be estimated simply from Schrödinger matrix elements (see for example, Blatt & Weisskopf 1952; Evans 1955). The dominant contribution arises from the magnetic dipole term, i.e., the coupling between the nuclear spins and the magnetic component of the electromagnetic field. However, this matrix element is proportional to the difference between the magnetic dipole moments of the two incident particles, and is therefore zero for identical particles, e.g., for pp capture.
3) The second order term contributing to neutron–proton capture is the electric dipole interaction, i.e., the coupling between the charge and the electric component of the electromagnetic field. (The electric dipole cross-section is about an order of magnitude smaller than the dominant magnetic dipole cross-section at $\sim 10^9$K, and about three orders of magnitude smaller at $\sim 10^7$K). Because the deuteron is a spin triplet (^3S), and because the electric dipole interaction Hamiltonian (H_I^D) is proportional to $r \cdot \cos\theta$ and does not affect the spin, the only non-zero matrix element is for an initial spin-triplet P-wave state, i.e., $\langle {}^3S(\text{bound})|H_I^D|{}^3P(\text{free})\rangle$.

In contrast, the diproton is a spin singlet state (^1S), as required by the exclusion principle. The relative weakness of the singlet nuclear force is the reason why, in this universe, the diproton does not exist. The electric dipole matrix element for proton–proton capture would be $\langle {}^1S(\text{bound})|H_I^D|{}^1P(\text{free})\rangle$, but of course, the singlet P-state cannot exist for identical fermions. Hence, the second order term contributing to $\sigma_{\text{np}}^{\text{cap}}$ is also zero for $\sigma_{\text{pp}}^{\text{cap}}$.

We conclude that the lowest order non-zero term contributing to $\sigma_{\text{pp}}^{\text{cap}}$ must be the electric quadrupole term, i.e., $\langle {}^1S(\text{bound})|H_I^Q|{}^1D(\text{free})\rangle$, where, $H_I^Q \propto r^2 P_2(\cos\theta)$. Thus, it is clear that $\sigma_{\text{pp}}^{\text{cap}} \ll \sigma_{\text{np}}^{\text{cap}}$.

Standard methods, as in Blatt & Weisskopf (1952) and Evans (1955), may be used to derive an analytic expression for the cross-section if the Coulomb interaction is ignored, and in the zero-range approximation,

$$\sigma_{\text{pp}}^{\text{cap}} = \frac{64\pi\alpha(\hbar c)^2 B^{1/2} E^{3/2}}{15(M_p c^2)^3 (E+B)} \quad \text{(no Coulomb barrier)}, \tag{1}$$

where B is the postulated diproton binding energy and E is the sum of the two incident protons' kinetic energies in the centre-of-mass system. When the Coulomb barrier is included, the cross-section diminishes at sufficiently low energies proportionally to,

$$\sigma_{\text{pp}}^{\text{cap}} \propto \exp\left\{-\pi\alpha\sqrt{M_p c^2/E}\right\} \quad (E \sim 1\,\text{keV or smaller}), \tag{2}$$

in the usual way. We have chosen to evaluate numerically the Schrödinger wave-functions including the Coulomb potential, using a nominal singlet nuclear potential 'square well' with $a = 2.4$ fm and $V_0 = 16.1$ MeV (Blatt & Weisskopf 1952; Evans 1955) noting that great accuracy is not necessary. The potential well depth is increased proportionally as g_s^2, i.e., by factors of 1.2^2, 1.3^2 or 1.4^2, to derive the cross-section for diproton formation. (These correspond to diproton binding energies of 0.6, 2 and 4 MeV respectively). The numerical results have the low energy behaviour required by equation (2) and reproduce equation (1) when the Coulomb interaction is removed. The cross-section (in barns) is plotted against E in Fig. 1, and as a fraction of the neutron–proton capture cross-section in Fig. 2.

At $\sim$0.1 MeV, the proton–proton capture cross-section is about 5 orders of magnitude smaller than the neutron–proton capture cross-section. At $\sim$1 keV the difference is about 15 orders of magnitude. The latter is due largely to the Coulomb barrier. However, the smaller proton–proton capture cross-section compared to that of neutron–proton capture at $\sim$0.1 MeV, a typical BBN energy, is mostly due to the fact that the former involves identical particles, and hence a quadrupole interaction rather than a dipole interaction.

A reasonably good closed-form approximation to the numerical cross-section results (within an order of magnitude for 0.5 keV $< E <$ 5 MeV) is,

$$\sigma_{\text{pp}}^{\text{cap}} = \frac{64\pi\alpha(\hbar c)^2 B^{3/2} E^{1/2}}{15(M_p c^2)^3 (E+B)} \exp\left\{-\pi\alpha\sqrt{M_p c^2/E}\right\}. \tag{3}$$

Note that equation (3) differs from the simple product of equations (1) and (2) by an additional factor of B/E, motivated simply to improve agreement with the numerical

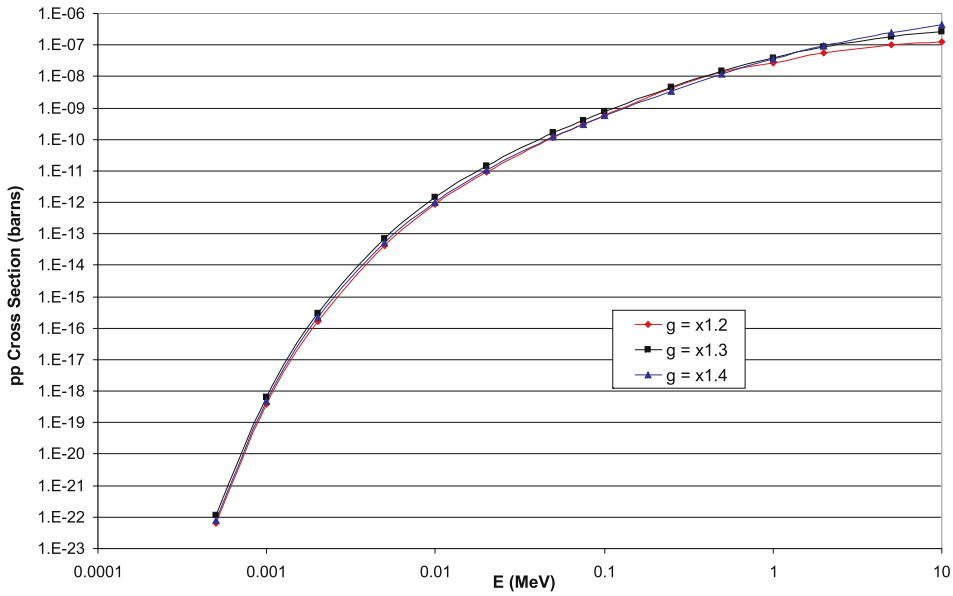

Figure 1. Numerical results for the pp capture cross-section (barns) *versus* energy.

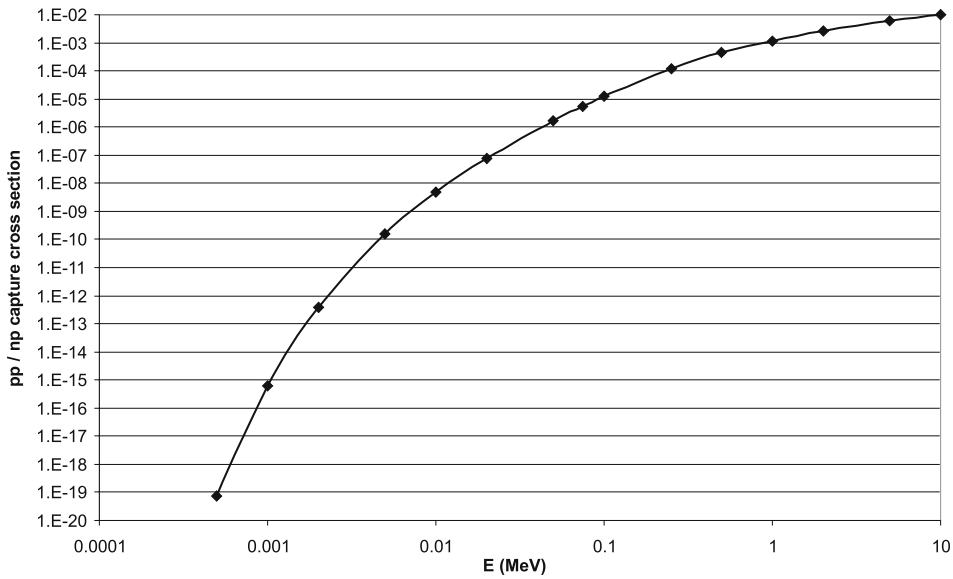

Figure 2. Numerical results for the pp capture cross-section as a fraction of the pn capture cross-section *versus* energy.

results shown in Fig. 1. Equation (3) tends to overestimate the cross-section in the energy range of interest, and hence any inaccuracy does not detract from the arguments which follow.

The overall reaction rate for a thermal distribution of proton energies is found by integrating the monochromatic rate, determined from equation (3), appropriately weighted by the Maxwell distribution. Using a first order approximation for the resulting 'Gamow peak' integral yields a reaction rate at temperature T given by,

$$R[T] \approx \frac{8 \cdot 2^{2/3}}{15} \pi b^{7/3} \alpha A \left(\frac{\hbar}{M_p c}\right)^2 \left(\frac{c}{M_p c^2}\right) \cdot \sqrt{\frac{B}{M_p c^2}} \cdot \frac{\exp\{-f_{\min}\}}{(kT)^{1/6}} \qquad (4)$$

where

$$f_{\min} = 3\left(\frac{b}{2\sqrt{kT}}\right)^{2/3} \quad \text{and} \quad b = \pi\alpha \cdot \sqrt{M_p c^2}, \qquad (5)$$

and where $E \ll B$ is assumed. A is the proton number density corresponding to one mole/cm^3 (i.e., 6×10^{29}/m^3). Equation (4) gives the reaction rate in s^{-1} (mole/cm^3)$^{-1}$ for kT in MeV. Using $B = 2$ MeV for illustration (i.e., for a 30% increase in g_s), we deduce an approximate reaction rate at temperature T,

$$R[T] = 3.5 \frac{\exp(-f_{\min})}{[\text{kT(MeV)}]^{1/6}} \text{ s}^{-1}(\text{mole/cm}^3)^{-1}. \qquad (6)$$

Again, any inaccuracies due to the approximations inherent in the derivations of equations (4) and (6) lead to an *over*-estimate of the reaction rate, and hence do not detract from the arguments which follow.

3. Are diprotons formed during BBN?

It is convenient to express results in terms of time (t), taken as correlated with temperature according to $T(K) = 10^{10}/\sqrt{t\,(\text{sec})}$. The photon–baryon ratio is taken to be 2×10^9. The diproton reaction times over the first hour following the big bang, derived from equation (6), are given in Table 1.

The condition for reaction freeze-out by cosmic expansion is that the reaction time exceeds $1/H \sim 2t$, i.e., that the last column in Table 1 should exceed ~ 2. Hence we see that the diproton formation reaction is frozen out at all times after ~ 1 second, and indeed somewhat before that. The situation contrasts with that for neutron–proton capture. Consistent with actual big bang nucleosynthesis, Fig. 2 implies that the reaction times for the latter are shorter than t during this period, as they must be.

To complete the argument that diprotons would not be a product of big bang nucleosynthesis we now demonstrate that diprotons would photodisintegrate prior to 1 second. All neutrons will be assumed to have combined as deuterons before the time at which diprotons become stable against photodisintegration. (The increased strength of the nuclear force will increase the binding energy of the deuteron, which will thus always be stable at higher temperatures than the diproton or the dineutron). The maximum possible diproton to photon ratio is thus $0.75/(2 \times 2 \times 10^9) = 2 \times 10^{-10}$, noting that the proportion of remnant protons ($\sim 75\%$) is not affected by the change in g_s.

The simplest estimate of the temperature at which diprotons will be stable against photodisintegration is obtained by equating the maximum possible diproton:photon

ratio to the fraction of photons with energies sufficient to cause photodisintegration, i.e., greater than B. This fraction is, from the blackbody photon spectrum,

$$0.416 \int_{x_1}^{\infty} \frac{x^2 dx}{e^x - 1} \approx 0.416[2 + 2x_1 + x_1^2]e^{-x_1}$$

where

$$x_1 = B/kT \gg 1. \tag{7}$$

Thus we find $x_1 = 28.22$ and the earliest times at which diprotons are stable are as given in Table 2.

Thus, diprotons do not become stable until well after ~ 1 second for increases in g_s of up to a factor of ~ 1.4. The proton–proton capture reaction is therefore frozen out before diprotons become stable. In other words, proton–proton capture freezes-out when the diproton density is still negligible. There would therefore be no large scale production of diprotons during BBN. The existence of a bound diproton state would not affect the chemical constitution of the primordial universe, which would remain about 75:25 hydrogen:helium.

In passing, we note that if g_s was increased by more than a factor of ~ 1.4, then deuterons would be stable before ~ 1 second. At this time the leptonic reactions which

Table 1. Diproton formation reaction times.

t (s)	kT (MeV)	Reaction rate $s^{-1}(mole/cm^3)^{-1}$	Proton density/m^3	Reaction time (s)	Reaction time/t
1	0.86	0.75	7.5E + 27	100	100
10	0.27	0.43	2.3E + 26	6,000	600
30	0.16	0.30	4.9E + 25	41,000	1,400
50	0.12	0.24	2.1E + 25	1.2E + 5	2,400
100	0.086	0.18	7.5E + 24	4E + 5	4,500
200	0.061	0.13	2.7E + 24	2E + 6	9,000
300	0.050	0.10	1.5E + 24	4E + 6	13,000
500	0.039	0.074	7.0E + 23	1E + 7	24,000
1000	0.027	0.044	2.3E + 23	6E + 7	60,000
2000	0.0193	0.026	8.5E + 22	3E + 8	140,000
3000	0.0157	0.018	4.6E + 22	7E + 8	240,000
5000	0.0122	0.011	2.2E + 22	2E + 9	500,000

Table 2. Times and temperatures for diproton stability for various g/g_{actual}.

g/g_{actual}	B (MeV)	T (K)	t (s)
1.2	0.6	2.5×10^8	1,600
1.3	2	8.2×10^8	150
1.4	4	1.65×10^9	37

interconvert neutrons and protons would still be active. The neutron:proton ratio is determined by thermodynamic equilibrium at such times. Hence, a substantial suppression in the hydrogen inventory of the universe would result if g_s was increased sufficiently to stabilise the deuteron at a small fraction of a second. For example, increasing g_s by a factor of ~ 4 would result in a universe with only $\sim 3\%$ hydrogen. However, the diproton is irrelevant in this scenario.

4. What effect does diproton stability have on stars?

It would appear that the stability of the diproton makes no difference to the primordial universe, which would retain its approximately 75:25 ${}^1_1H : {}^4_2\mathrm{He}$ constitution (by mass). However, the effect on star formation would obviously be dramatic. For example, at a solar central temperature of $\sim 15 \times 10^6$ K, the pp capture reaction rate would be about $10^{-5}\mathrm{s}^{-1}(\mathrm{mole/cm}^3)^{-1}$, and a solar central proton density of $4 \times 10^{31}\mathrm{m}^{-3}$ would lead to a pp reaction time of less than an hour. Thus, the rate of production of deuterons would be controlled by the rate of the weak decay of the diproton. Even if this were the order of a year, the overall deuteron production rate would be $\sim 10^{10}$ times faster than the usual weak capture reaction $p + p \rightarrow D + e^+ + \nu_e$ under the same conditions.

However, the diproton reaction is so rapid under solar temperature and density conditions that it would be explosive. Stars of this type could not form. It is clear, therefore, that the universe would be radically different from the actual universe once star formation started. What is not clear is whether stable, long-lived, stars would form with temperatures and densities suitably reduced so as to offset the faster reaction pathway to deuterium. We do not pretend to provide a definitive answer to this question here. However, the answer appears to be less clear cut than is often implied. In particular, the fact that the first, and rate controlling, nuclear reaction is intrinsically faster – even if it be 10^{10} times faster – does not preclude the possibility of stable, long-lived stars. The reason is that nuclear fusion reaction rates between charged reactants are exponentially sensitive to temperature. Consequently, even enormous intrinsic reaction rate differences can be tamed by relatively modest changes in core temperature. Thus, it is possible to have a strong-force mediated fusion reaction as the rate controlling step in stellar heat production, as was also envisaged by Harnik *et al.* (2006). To see this, consider a hypothetical star with a central temperature of 10^6 K in a universe with stable diprotons.

There are several elementary constraints which a stable star must respect. For example, dynamical stability requires that the radiation pressure within the star should not be too much larger than the gas pressure. This constraint leads to the familiar upper bound on stellar masses, in the order of ~ 100 solar masses, a limit which will also apply in our alternative universe. This constraint can also be written as a lower bound on the gas density required for stability, namely $\rho > 0.1 M_p (kT/\hbar c)^3$, which is $0.015\,\mathrm{kg/m}^3$ for our example (M_p is the proton mass).

The star must also be able to transport heat efficiently enough to balance the rate of nuclear heat generated. At the centre of the star there is a maximum power density consistent with purely radiative heat transfer, i.e., $\varepsilon_v < \varepsilon_v^{\max} = 4\pi cG\rho/\kappa$, where κ is the opacity (the subscript v denotes power per unit volume). Since the power density depends upon the square of the proton density, this limit on power density results in an upper limit on proton density. It evaluates to about $2.6\,\mathrm{kg/m}^3$ for our example.

This is based on the diproton reaction rate from equation (6) together with the reaction sequence given in the Appendix. Of significance is the fact that at 10^6 K, and a density of 2.6 kg/m^3, the opacity of pure hydrogen is only beginning to rise above the lower bound provided by Thompson scattering (namely ~ 0.3 m^2/kg, compared with the Thompson opacity of 0.034 m^2/kg).

Satisfying hydrostatic equilibrium and heat balance everywhere within the star would determine the unique central density for a given central temperature (if any stable solution exists). In the absence of a complete stellar model, however, we have instead derived the range within which the central density must lie, namely between 0.015 kg/m^3 and 2.6 kg/m^3.

An estimate for the star's lifetime is provided by the reaction time based on equation (6), noting that this is the slowest reaction in the subsequent sequence, as demonstrated in the Appendix. Using the above limiting densities suggests lives between 200 Myrs and 30 Byrs. This encompasses the biophilic range, permitting biological evolution the order of billions of years to carry out its work.

The mass of our star may be estimated from $kT_c \approx 0.24 G M_p M^{2/3} \rho_c^{1/3}$, which is an approximate rendering of the virial condition (i.e., being gravitationally bound), except that average quantities have been replaced by their central values. This implies masses of between ~ 3 and ~ 50 solar masses (the latter being, by construction, of the lower bound density). These fall within the usual stellar range and hence seem achievable, e.g., there is no obvious objection as regards the availability of cooling mechanisms during star formation.

Estimation of the surface temperature is more contentious. To do so we have assumed that one quarter of the star's mass is involved in nuclear reactions at the central rate. This results in luminosities of 300 to 8000 times solar luminosity. The radius is estimated using $R \approx 2.5(M/\rho_c)^{1/3}$, which suggests sizes 50 to 650 times solar size. Finally, the preceding results imply a surface temperature between 1400 K and 7600 K. Thus, the surface temperature is quite uncertain, but is not obviously inconsistent with planetary life based on conventional biochemistry. The point here is that biophilic stars require surface temperatures consistent with photons of an energy compatible with driving photosynthesis, or some comparable biochemistry.

Of course we have not definitively established that such stars could exist. To do so would require explicit demonstration that hydrostatic equilibrium and heat balance were respected at all points in the star, i.e., a complete stellar model. More problematical still, in our present state of knowledge, would be the requirement to demonstrate that such stars could actually form. Fortunately this is not where the burden of proof lies. We have seen that the elementary stability constraints can be consistent with a star which is sufficiently long-lived, sufficiently luminous, and has a suitable range of surface temperatures, to mimic the actual conditions of our universe to some approximation. In view of this, the burden of proof lies with any contention that diproton stability is anthropically catastrophic. It would appear not to be.

It is rather remarkable that a reaction which is so many orders of magnitude faster than the usual weak pp capture reaction, can result in a stable star simply by reducing the temperature and density. It is reasonable to ask whether this trick could be repeated for an even faster reaction. The limit may be that at still lower temperatures the opacity will start to climb steeply (Kramer's opacity $\propto 1/T^{7/2}$). This will severely restrict the power density which can be balanced by purely radiative heat transfer. It appears that our example is close to this limit.

It is amusing to speculate how physicists in an alternative universe, containing stars exclusively like that of our example, might view their situation. They might point to three remarkable 'coincidences'. The first would be that the Thompson lower bound opacity is attained at a temperature *just* low enough to support the required stellar heat transport. The second would be the good fortune that identical particles were involved in the first stellar reaction, thus suppressing the reaction rate due to the exclusion principle, and hence creating stars of sufficient longevity to support biological evolution. The third piece of luck, undeniable surely, would be that the strong nuclear force was *just* strong enough to bind the diproton – without which the first stellar nuclear reaction would not be possible, and hence there would be no stars and no chemical elements!

5. Conclusions

Increases in g_s sufficient to bind the diproton do not lead to significant production of diprotons during BBN. This has been demonstrated by direct evaluation of the pp capture rate for increases in g_s of up to 40%, corresponding to diprotons being roughly twice as stable as deuterons are in our universe (i.e., a binding energy of ~ 4 MeV).

Under solar conditions, the stability of diprotons would lead to a reaction pathway for converting protons to deuterons perhaps ~ 10 orders of magnitude faster than the usual weak capture reaction. This would prevent stars of the familiar hot, dense type from occurring in the universe. Nevertheless, elementary stellar stability requirements can be met by lower density stars, with lower central temperatures, when the diproton is stable. Such a universe therefore appears compatible with stars whose lifetimes are of the order of billions of years, and whose luminosities and surface temperatures are appropriate for the nurturing of biological life based on conventional molecular chemistry.

The above observations challenge the contention that the strong nuclear force has a fine-tuned anthropic upper bound requiring the diproton to be unbound.

However, this does not preclude there being other mechanisms which might impose an anthropic upper bound to the strong nuclear force. One possibility is the well-known 'Hoyle' resonance energies which promote the production of carbon and oxygen in stars. Even very small changes in g_s would presumably play havoc with these very delicate nuclear balances. We also note that increases in g_s rather greater than 40% would lead to deuterium being stable before 1 s. At such times the leptonic reactions which interconvert protons and neutrons were still active. The neutrons would thus escape into the sanctuary of helium-4 whilst the neutron:proton ratio was still determined by thermal equilibrium. If g_s was increased by a factor of ~ 4, so that deuterium was stable at about a millisecond, the primordial universe would contain only $\sim 3\%$ hydrogen. It is not clear if this is anthropically deselected, but if so it is a far weaker tuning of g_s than is usually envisaged.

Appendix – Stellar 'ppI' reaction sequence with a stable diproton

The possibilities for the reaction sequence, analogous to the usual ppI sequence, are listed in Table 3. Reactions involving nuclei with $Z > 2$, analogous to the ppII/ppIII sequences, have been ignored for simplicity, as have reactions involving neutrons as a

Table 3. Reactions and rates analogous to the 'ppI' sequence for a stable diproton.

Label	Reaction	Rate at 10^6K $s^{-1}(mole/cm^3)^{-1}$	Reference
[1a]	$p + p \rightarrow {}^{2}_{2}He + \gamma$	3.5×10^{-14}	Herein
[1b]	${}^{2}_{2}He \rightarrow {}^{2}_{1}D + e^{+} + \nu_e$	Assumed fast	–
[2]	$p + D \rightarrow {}^{3}_{2}He + \gamma$	1.64×10^{-11}	Smith (1988)
[3]	${}^{3}_{2}He + {}^{3}_{2}He \rightarrow {}^{4}_{2}He + 2{}^{1}_{1}p$	1.46×10^{-41}	Hoffman (2002)
[4]	${}^{2}_{1}D + {}^{2}_{1}D \rightarrow {}^{4}_{2}He + \gamma$	7.85×10^{-16}	Hoffman (2002)
[5]	${}^{2}_{1}D + {}^{2}_{1}D \rightarrow {}^{3}_{1}H + {}^{1}_{1}p$	6.72×10^{-9}	Hoffman (2002)
[6]	${}^{2}_{1}D + {}^{2}_{1}D \rightarrow {}^{3}_{2}He + {}^{1}_{0}n$	6.33×10^{-9}	Hoffman (2002)
[7]	${}^{3}_{1}H + {}^{2}_{1}D \rightarrow {}^{4}_{2}He + {}^{1}_{0}n$	1.88×10^{-7}	Hoffman (2002)
[8]	${}^{3}_{1}H + {}^{1}_{1}p \rightarrow {}^{4}_{2}He + \gamma$	3.56×10^{-11}	Smith (1988)
[9]	${}^{3}_{2}He + {}^{2}_{1}D \rightarrow {}^{4}_{2}He + {}^{1}_{1}p$	3.84×10^{-19}	Hoffman (2002)
[10]	${}^{3}_{2}He + {}^{3}_{1}H \rightarrow {}^{4}_{2}He + {}^{2}_{1}D$	1.42×10^{-22}	Hoffman (2002)
[11]	${}^{3}_{2}He + {}^{3}_{1}H \rightarrow {}^{4}_{2}He + {}^{1}_{0}n + {}^{1}_{1}p$	2.0×10^{-22}	Hoffman (2002)

reactant. The reaction rates given below have been taken from either Hoffman (2002) or Smith (1988), with the exception of [1a] which is derived above as equation (6). No correction has been made for the increased strength of the nuclear force as regards the rates of reactions after [1a]. For the electromagnetic reactions, this is reasonable. The justification for the other reactions is that reaction [1a] will be found to be the rate determining step. Hence, faster subsequent reactions will not cause a major change to the scenario outlined below.

The usual ppI sequence involves reactions [2] and [3]. At the low temperature considered, the reactions involving reactant nuclei with double charges are strongly suppressed by the Coulomb barrier. In particular, reaction [3] is not active and so the ppI sequence in our alternative universe must follow a different path. Reactions [4], [9], [10] and [11] are also too slow to contribute significantly. The dominant reaction sequences are thus,

$$[1a] \rightarrow [1b] \begin{cases} \nearrow [2] + [6]\ ({}^{3}\text{He production}) \\ \searrow [5] \rightarrow [7] + [8]\ ({}^{4}\text{He production}). \end{cases}$$

Note that helium-3 is not burnt at this temperature. The above rates are consistent with the timescale of the hydrogen burning phase being determined by reaction [1a]. Equilibrium deuteron and tritium densities are around 10^{-3} and 3×10^{-5} of the proton density respectively. The end product of the hydrogen burning phase is a mixture of roughly 75% helium-3 and 25% helium-4. Such a star would exhibit a distinct helium-3 burning phase after the hydrogen phase (following additional gravitational collapse to raise the temperature sufficiently to activate reaction [3]). Only after exhaustion of the helium-3 would the usual helium-4 burning phase occur, following further collapse of the core.

The power density suggested in the main text is an upper bound based on full conversion to helium-4 in the hydrogen burning phase. The heat released per helium nucleus equals, to a good enough approximation, the helium-4 binding energy less twice the neutron/proton mass difference. The binding energy is increased significantly in our hypothetical universe. Based on the energy levels of a square potential well, we estimate the binding energy to be,

$$\frac{B}{B_{\text{actual}}} = \left(\frac{g_s / g_s^{\text{actual}} - 0.85}{1.0 - 0.85} \right)^2 ,$$

because a reduction in g_s to $\sim 0.85 g_s^{\text{actual}}$ results in the deuteron being unbound (i.e., $B = 0$). This results in helium-4 binding energy estimates of 154, 255 and 380 MeV respectively, for g_s increased by $\times 1.2$, $\times 1.3$ and $\times 1.4$. The energy release is thus quite prodigious by normal standards. If the binding energy was estimated assuming scaling according to $(g_s / g_s^{\text{actual}})^4$ we would get 57, 81 and 109 MeV respectively. Hence, we have employed a rather generous upper bound power density since this strengthens the arguments of the main text.

References

Agrawal, V., Barr, S. M., Donoghue, J. F., Seckel, D. 1998a, Anthropic considerations in multiple-domain theories and the scale of electroweak symmetry breaking, *Phys. Rev. Lett.*, **80**, 1822.

Agrawal, V., Barr, S. M., Donoghue, J. F., Seckel, D. 1998b, The anthropic principle and the mass scale of the standard model, *Phys. Rev. D*, **57**, 5480.

Barrow, J. D., Tipler, F. J. 1986, The Anthropic Cosmological Principle, Oxford University Press.

Blatt, J. M., Weisskopf, V. F. 1952, Theoretical Nuclear Physics, John Wiley.

Carr, B. J., Rees, M. J. 1979, The anthropic principle and the structure of the physical world, *Nature*, **278**, 605.

Carter, B. 1974, Confrontation of cosmological theories with observation: Proc. IAU Symp. 63, 291, (ed.) Longair, M. S., Dordrecht, Reidel.

Davies, P. C. W. 1982, The Accidental Universe, Cambridge University Press.

Davies, P. C. W. 2004, Multiverse cosmological models, *Mod. Phys. Lett. A*, **19**, 727.

Davies, P. C. W. 1972, Time variation of the coupling constants, *J. Phys. A*, **5**, 1296.

Dine, M. 2003, Is there a string theory landscape: some cautionary remarks, Preprint hep-th/0402101.

Dyson, F. J. 1971, Energy in the universe, *Sci. Am.*, **225**, 51.

Evans, R. D. 1955, The Atomic Nucleus, McGraw-Hill.

Guth, A. H. 2007, Eternal inflation and its implications, *J. Phys. A: Math. Theor.*, **40**, 6811.

Harnik, R., Kribs, G. D., Perez, G. 2006, A universe without weak interactions, *Phys. Rev. D*, **74**, 035006.

Hoffman, R. 2002, Strong and Electromagnetic Reaction Rates 2002, Lawrence Livermore National Laboratory, Nuclear Theory & Modelling Group (http://www-phys.llnl.gov/Research/RRSN/semr/light_reacs.html).

Hogan, C. J. 2000, Why the universe is just so, *Rev. Mod. Phys.*, **72**, 1149.

Hogan, C. J. 2006, Nuclear astrophysics of worlds in the string landscape, *Phys. Rev. D*, **74**, 123,514.

Linde, A. 1994, *Sci. Am.*, **271**, 32.

Linde, A. 2007a, Sinks in the landscape, Boltzmann brains, and the cosmological constant problem, *J. Cosmol. Astropart. Phys., JCAP*, **0701**, 022.

Linde, A. 2007b, Inflationary cosmology, Preprint hep-th/0705.0164.

Martel, H., Shapiro, P. R., Weinberg, S. 1998, Likely values of the cosmological constant, *Astrophys. J.*, **492**, 29.

Rees, M. J. 1999, Just Six Numbers, Weidenfeld & Nicolson, London.
Smith, M. 1988, Caughlan & Fowler 1988 Thermonuclear Reaction Rates, Oak Ridge National Laboratory (http://www.phy.ornl.gov/astrophysics/data/cf88/directory.html).
Susskind, L. 2003, The anthropic landscape of string theory, Preprint hep-th/0302219.
Tegmark, M., Aguirre, A., Rees, M. J., Wilczek, F. 2006, Dimensionless constants, cosmology and other dark matters, *Phys. Rev. D*, **73**, 023505.
Weinberg, S. 2007, Living in the multiverse, In: *Universe or Multiverse* (ed.) Carr, B., Cambridge University Press, and Preprint hep-th/0511037.

J. Astrophys. Astr. (2009) **30,** 133–143

Close Separation Triple System QSO 1009-0252 with Discordant Redshifts: Is the Spectrum of One Component Blueshifted?

D. Basu
Department of Physics, Carleton University, Ottawa, ON K1S 5B6, Canada.
e-mail: basu@physics.carleton.ca

Received 2007 August 20; accepted 2009 July 27

Abstract. 1009-0252 is a Quasi Stellar Object (QSO) with three components A, B, C. A, B are thought to be the result of gravitational lensing of one object, and A, C constitute a close pair with redshifts 2.74 and 1.62 respectively. Close separation pairs of QSOs with discordant redshifts have received special attention in recent years, probably because of the possibility that they may be physically associated, implying non-cosmological redshifts. Attempts have been made to explain their occurrences due to the effect of gravitational lensing. However, gravitational lensing has not offered a completely satisfactory explanation for this triplet. Furthermore, examination revealed some inadequacies and inconsistencies in the redshift identification of the observed lines in the component A. Observational results of 1009-0252 therefore remain puzzling. We propose an alternative explanation by suggesting that A, B actually constitute a close pair and C is an unrelated object in the field. We show that the observed spectrum of A can be interpreted as blueshifted. This implies that A, B are two separate objects, one (A) approaching us and the other (B) receding from us, and are not the result of gravitational lensing of a single object. The oppositely directed pair A, B may have been ejected due to the merger of two galaxies.

Key words. Quasars: emission lines, absorption lines—individual: Q 1009-0252—cosmology: miscellaneous.

1. Introduction

Several close pairs of Quasi Stellar Objects (QSOs) have been observed in recent years, some with identical redshifts and others with discordant redshifts. The former includes 1429-008A, B (Hewett *et al.* 1989), 2153-2056A, B (Hewett *et al.* 1998) and the latter includes 1009-0252A, B (Hewett *et al.* 1994; Claeskens *et al.* 2001; Sluse *et al.* 2003), 1148+0055 (Claeskens *et al.* 2000; Sluse *et al.* 2003), 1548+114A, B (Wampler 1973; Claeskens *et al.* 2000; Sluse *et al.* 2003). Such pairs have attracted considerable extra interest and attention, one reason being the possibility that the pairs may be physically associated implying a non-cosmological origin of QSO redshifts, and attempts have been made to explain the occurrences of the close pairs in terms of gravitational lensing (see references later in this section).

1009-0252 is one such system with three components (Hewett *et al.* 1994, hereafter H94). The system was independently discovered by Surdej *et al.* (1994) with the ESO Key Project. Components A and B have identical redshifts 2.74 and are separated from one another by 1″.55. The third component C has a redshift 1.62 and is separated by 4″.6 from A and B. Further, both A and B exhibit absorption lines which have been identified for two redshift systems, viz., 0.869 and 1.622, the latter happens to be equal to the emission redshift of the component C, and is thought to be due to gas clouds associated with a cluster hosting C (Claeskens *et al.* 2001, hereafter C01). Objects A and B, resulting from the gravitational lensing of one QSO, are regarded as the same object, and the object C is regarded differently. As such, the triple system has been considered to form a close pair QSO between components A (which is same as B) and C with discordant redshifts (C01; Sluse *et al.* 2003).

However, extensive studies of gravitational lensing for the occurrences of close pairs of QSOs with discordant redshifts have been carried out for several pairs. These studies did not find any potential luminous deflector for 1120+019 (Maylan & Djorgovsky 1989), 1429-008 (Hewett *et al.* 1989), 1635+267 (Djorgovsky & Spinard 1984) or 2345+007 (Weedman *et al.* 1982), and any geometrical analysis between an observer, a deflector and the source was not considered worthwhile. Again, observational evidences in 1148+0055 and 2143-2056 did not support the gravitational lensing hypothesis, although the possibility that the pair in the latter may have resulted from gravitational lensing has not been ruled out (Hewett *et al.* 1998). Furthermore, no secondary lensed image, expected due to gravitational lensing effect, was detected in 1548+114 (Claeskens *et al.* 2000; Sluse *et al.* 2003).

Nonetheless, some of the observed properties of 1009-0252 can be explained by the gravitational lensing hypothesis for A and B. But, under this hypothesis, several factors must be responsible for the differences observed in the properties of the continuum and emission features of individual components, viz., differential flux or differential extinction by dust from the lens to each component, or variability of the QSO that has been lensed, or the effect of differential microlensing due to a compact object, all of which have been ruled out (H94). However, a lensing galaxy has recently been claimed to be detected at a redshift ≈ 0.8, which can be associated with the absorbing cloud at the redshift 0.869, and flux variability has also been claimed to be observed for both A and B (C01). But these authors would not make any definite conclusion with the present data, and have suggested further observations.

It appears that a completely satisfactory explanation with the gravitational lensing hypothesis may not have been established for 1009-0252. The remarks of H94 is noteworthy in this connection: "None [no explanation] provide an entirely satisfactory quantitative match to the observation" and also, "components A and B may be physically distinct quasars". Moreover, the redshift identification of the observed lines in A shows some inconsistencies and inadequacies (see section 3). Observational results of the triple system QSO 1009-0252 with discordant redshifts thus remain puzzling. We were therefore prompted to look for an alternative explanation. We suggest that the occurrence of A and B is *not* due to the gravitational lensing of a single object. Instead, in our opinion, A and B are separate objects forming a close pair and C is another *unrelated* object in the field.

The pair is probably produced on being ejected in opposite directions. This would imply that one component in the pair is approaching us and would exhibit a blueshifted spectrum, while the other component is receding from us, and would exhibit a

redshifted spectrum. As discussed in section 3, the rest frame equivalent widths of the major emission lines of the component A identified for the redshift determination are too small for these lines, and as such, this redshift may have been determined due to misidentification of the lines. The same lines in the component B are 1.2 to 1.3 times stronger, and their identifications appear correct. The purpose of this paper is to show that the spectrum of the component A can be better interpreted as blueshifted.

In what follows, we review observations of blueshifts in extragalactic objects in section 2. In section 3 we demonstrate some inadequacies and inconsistencies in the current interpretation of the spectrum of 1009-0252A involving redshifts. Section 4 deals with our interpretation of the spectrum in terms of blueshifts. Results are discussed in section 5. In section 6 we propose an ejection mechanism scenario to explain the close pair production involving the observed blueshift. Finally, some concluding remarks are presented in section 7.

2. Blueshifts

It is the usual practice of the astronomers to identify search lines with observed spectral lines located at the red side and determine redshifts in extragalactic objects. Identification programmes are, almost as a rule, prepared for determining redshifts *only*, and blueshifts are not considered at all.

On the other hand, the ejection process is a well recognized mechanism for the birth of QSOs. However, the ejection mechanism, applied by researchers so far, has *always* assumed ejection *away* from the observer and thus producing redshifts, although, the ejection should occur in all directions with *equal probability*. Gordon (1980) and Popowski & Weinzierl (2004) have shown that, under suitable conditions, an appreciable fraction of the vast number of currently known QSOs should exhibit blueshifted spectra if originated through ejection from parent galaxies, as conditions cannot *always* be satisfied for redshifts *only*. This basic notion appears to have been ignored in *all* models so far, and the ejection has *always* been considered *away* from us *only*, based on the assumption that blueshifted spectra do not exist. The latter, in its turn, is based on the fact that all line identification programmes are geared to the redshift determination *only*, as mentioned above.

Recent analyses have demonstrated that blueshifts can explain the observed spectra of extragalactic objects. Spectra of 15 high redshift galaxies were re-analysed and their spectra were shown to be blueshifted, redshifts assigned to them are probably misidentifications of observed lines (Basu 1998). The unusual spectrum of STIS123627+621755 (Chen *et al.* 1999) could not be explained when further observations were presented by Stern *et al.* (2000), leaving the redshift "undetermined" (Chen *et al.* 2000), and the spectra has subsequently been interpreted in terms of blueshifts (Basu 2001a). Re-examination of host galaxy spectra of four Supernovae Ia (Basu 2000) and those of four Gamma Ray Bursts (Basu 2001b) have led to the determination of their blueshifts. Furthermore, spectra of 25 QSOs were also reanalysed and search lines of longer wavelengths were identified with their observed lines to compute blueshifts (Basu & Haque-Copilah 2001), redshifts may have been assigned to these objects due to misidentification of the observed lines. Spectra of three additional QSOs, viz., SDSS 1533-00, PG 1407+265 and PKS 0637-752, which could not be explained in terms of redshifts, were interpreted successfully in terms of blueshifts (Basu 2004). Another QSO, viz., PKS 2149-306 and an AGN CXOCDFS J033225.3-274219, each exhibit

an emission feature in its X-ray spectrum which could not be explained in terms of the redshift determined from its optical spectrum (Yaqoob *et al.* 1999; Wang *et al.* 2003), and blueshift has succesfully interpreted the complete spectra (optical and X-ray) for each of these objects (Basu 2006a). Again, the X-ray source 1E 1207.4-5209 thought to be an isolated neutron star associated with the SNR G296.5+10.0, exhibits several absorption lines in the optical spectrum and also three confirmed variable absorption features in the X-ray spectrum at apparently harmonically related wavelengths, the latter being interpreted as due to cyclotron resonance. However, this interpretation has been found to show many inconsistencies, and both spectra have now been successfully interpreted as blueshifted (Basu 2006b). Further, several pairs of QSOs have been observed, with the two objects in each pair lying *across* an active galaxy, and the spectrum of each QSO in the pair has been interpreted as redshifted, apparently based on the assumption that both are moving away from the observer after being ejected from the parent galaxy. However, more logically, the two objects in the pair should be ejected in opposite directions and one spectrum should exhibit redshift moving *away* from the observer and the other should exhibit blueshift moving *toward* the observer. Spectra of four such pairs have been re-analyzed and one spectrum in each pair has been shown to exhibit blueshift (Basu 2006c). Objects like close pairs of QSOs with discordant redshifts, explanations of whose occurrence are inconclusive, should be particularly considered in this respect for the possibility of blueshifted spectra.

Moreover, GRB 011211 exhibits a redshift 2.14 computed from several absorption lines in its optical afterglow (Fruchter *et al.* 2001; Holland *et al.* 2002), while its X-ray afterglow shows several emission lines that yield a mean redshift 1.862 (Reeves *et al.* 2003). The energetics of the GRB has been explained by a supernova model on the basis of the mean redshift of the GRB as 2.141 (Reeves *et al.* 2003). However, some severe inconsistencies exist in the determination of the redshift of the spectra. It has been demonstrated that the observed spectra cannot be explained in terms of redshifts and, instead, the complete spectra comprising the optical and the X-ray, have been interpreted in terms of blueshifts (Basu 2009).

3. The current interpretation

The emission spectra of A and B demonstrate that these are 'reasonably similar', but certainly *not* identical. There are several discrepancies between the two components. The equivalent widths of the lines are significantly different for A and B, B is fainter than A, the continuum slope of B is redder than that of A. Moreover, the spectra exhibit an unexpected feature at 6550 Å, identified as 'the extremely rare' search line [NIII] 1750. The feature is prominent in the component B, 'while component A may contain a weak, somewhat broader feature at 6550 Å' (H94), and the feature 'is faintly visible in the spectrum of both components' (C01). Furthermore, examination of the spectrum of 1009-0252A revealed an additional emission line around 7723 Å which is not mentioned in C01, but appears real.

On the other hand, the redshift identification of observed lines in 1009-0252A shows several inconsistencies and inadequacies. It is known that Lyα + NV, CIV, CIII are three of the strongest lines in the search list for the redshift identification. Rest frame equivalent widths 28.4 Å, 24.6 Å, 6.4 Å obtained for these lines respectively (see Table 1), are too small for these lines.

Table 1. Redshifts and blueshifts observed in 1009-0252A.

EM/ABS(1)	λ_o(2)	W_o(3)	λ_r(4)	z_r(5)	W_{er}(6)	λ_b(7)	z_b(8)	W_{eb}(9)
EM	4539*	106	Lyα 1216	2.7327	28.4	Hα 6563	0.3084	153.3
	4585*	–	NV 1240	2.6976	–	[NII] 6584	0.3036	–
	5784	92	CIV 1549	2.7347	24.6	OI 8446	0.3154	134.4
	6523?	–	[NIII] 1750	2.7274	–	[SIII] 9532	0.3157	–
	7123	24	CIII] 1909	2.7313	6.4	HeII 10124	0.2964	34.1
	7723?	–	–	2.7247?	–	HeI 10830	0.2869	–
ABS I	4834.06	1.22	FeII 2586	0.8689	0.65	OI 8449	0.4279	2.13
	4859.63	2.33	FeII 2600	0.8689	1.25	CaII 8498	0.4281	4.07
	4868.61	1.22	FeII + MnII	–	–	CaII 8542	0.4300	2.14
	4890.04	0.45	FeII	–	–	CaII 8662	0.4355	0.80
ABS II	4962.77	0.32	–	–	–	H2 19570	0.7464	1.26
	5032.48	0.41	MgII 2796?	0.7992	0.23	H2 20338	0.7526	1.66
	5043.08	0.86	MgII 2803?	0.7992	0.48	H2 20587	0.7550	3.51
	5239.41	2.45	MgII 2803	0.8689	1.31	H2 20735	0.7432	9.51
	5255.93	3.16	MgII 2796	0.8798	1.69	H2 21218	0.7523	12.76
	5332.78	0.6	MgI 2853	0.8692	0.32	H2 21542	0.7525	2.42
	5505.50	0.37	CrI 2096	–	–	H2 22233	0.7524	1.49
ABS III	6793.63	1.91	FeII 2586	1.6264	0.73	Pδ 10049	0.3239	2.83
	6829.30	4.38	FeII 2600	1.6265	1.67	HeII 10124	0.3254	6.49
	7345.56	6.52	MgII 2796	1.6268	2.48	HeI 10830	0.3217	9.61
	7363.27	6.79	MgII 2803	1.6264	2.59	Pγ 10938	0.3268	10.09
	7494.70	1.33	MgI 2853	1.6270	0.51	OI 11210	0.3314	1.99

References: All emission lines are from Fig. 5 of C01, and all absorption lines are from Table 2 of H94.
$*$ Combined values for W_o, W_{er} and W_{eb}.

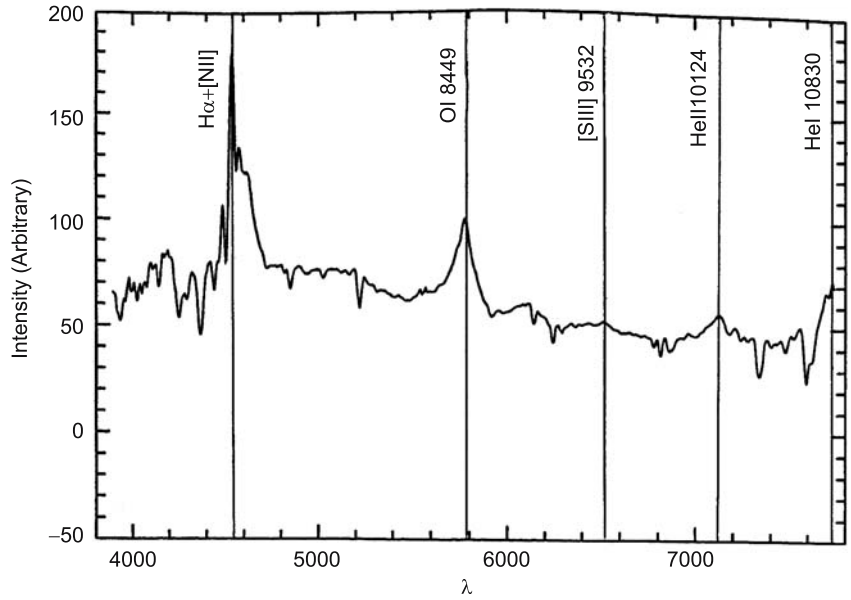

Figure 1. Spectrum of the component A of the triple system QSO 1009-0252A, B, C, adopted from Claeskens *et al.* (2001), with positions of identified lines, blueshifted as shown in Table 1, marked. The abscissa denotes the observed wavelengths. The spectrum has been extracted using the MEM method as presented in C01. Also, the data are smoothed slightly using five pixels filter box.

Additionally, three absorption lines, viz., those at 4962.77 Å, 5032.48 Å and 5043.08 Å, have either no or doubtful identifications. The lines at 5239.41 Å and 5255.93 Å have been identified with MgII doublet with wavelengths in the reverse order. The lower wavelength 5239.41 Å has been identified with the higher wavelength MgII 2803 and the line at 5255.93 Å has been identified with MgII 2796. Also, there is a serious error in the redshift computation of the line at 5255.93 Å which should be 0.8798 and not 0.8688.

4. The blueshift interpretation

We have interpreted the observed spectrum of 1009-252A, both emission and absorption, in terms of blueshifts, by identifying the observed lines with search lines of longer wavelengths as shown in Fig. 1 and Table 1.

In Table 1, column (1) gives the type of spectrum whether emission (EM) or absorption (ABS), column (2) is the observed wavelength (λ_o), column (3) is the observed equivalent width when available (W_o), column (4) is the search line used for identification for the redshift measurement (λ_r), column (5) is the redshift value (z_r), column (6) is the emitted equivalent width corresponding to the redshift (W_{er}), column (7) is the search line used for the identification of blueshift measurement (λ_b), column (8) is the blueshift value (z_b) and column (9) is the emitted equivalent width corresponding to the blueshift (W_{eb}).

It will be seen in Table 1 that we have identified *all* the observed lines, emission and absorption, exhibited by the spectra. The identified lines include usual Balmer, oxygen,

Table 2. Mean redshifts, blueshifts and spreads.

EM/ABS (1)	z_{rm} (2)	Δz_r (3)	z_{bm} (4)	Δz_b (5)
EM	2.7252	0.0371	0.3044	0.0288
ABS I	0.8689	0.0109	0.4304	0.0097
ABS II	1.6266	0.0006	0.7506	0.0086
ABS III	0.7992?	0.0000?	0.3258	0.0076

nitrogen, sulphur and helium lines in emission, of reasonable rest frame equivalent widths. Figure 1 shows the actual emission line spectrum of 1009-0252A with the blueshifted features identified. We have identified the feature at 4539 Å (Lyα1216 + NV1240 in the redshift scenario) as Hα6563 and [NII]6584. Absorption features have been identified, in three systems, viz., an oxygen line and the calcium triplet for the first system (ABS I), molecular lines of hydrogen including the strongest H2 21218 feature for the second system (ABS II), and Paschen series, helium and oxygen lines for the third system (ABS III). These are all well recognized search lines observed in the extragalactic literature.

The standard procedure has been followed in computing blueshift values in emission and absorption, viz., a 'shift' (red or blue) can be confirmed only when a minimum of two observed lines exhibit the same value after being identified with two separate search lines, and any third or more observed lines have also to obey this value when identified with other separate search lines (Basu 1973a, 1973b). In some cases, the stronger component of a doublet and/or the lower order line(s) of a series have been identified but the weaker component of the doublet and/or the higher order line(s) may be too weak to be seen, or the weaker component of a doublet and/or the higher order line(s) of the series have been identified but the stronger component of the doublet and/or the lower order line(s) are outside the observed region of the spectrum.

Additionally, we have also computed the quantity 'spread' for both redshift and blueshift systems, which is a measure of the goodness of fit for the identification process (see section 5).

Table 2 summarizes the result and shows emission (EM) or absorption (ABS) systems (column 1), mean redshifts z_{rm} (column 2), spreads in redshift systems Δz_r (column 3), mean blueshifts z_{bm} (column 4), spreads in blueshifts Δz_b (column 5). 1009-252A has the blueshift 0.3044, and exhibits three blueshift systems in absorption, viz., 0.3258, 0.4304 and 0.7506.

5. Discussion

The spread (Δz) is a measure of the range of values in each system, redshift (r) or blueshift (b), and is computed as the difference between the maximum and minimum values in the 'shift' (red or blue) in each system.

It should be noted that, in principle, the spread should be small – close to zero. However, the spread depends on the values of the 'shift' (red or blue) of individual lines, and the latter, in its turn, depends on the exact value of the observed wavelength (λ_o), which is the centroid of the line profile used for the determination of the 'shift'. λ_o is very difficult to be determined accurately in practice even in high s/n and high resolution records, as the profile may be double- or multi-peaked, broad, blended, of

complex nature due to various physical reasons. Hence, at least upto a certain extent, the spread may be due to some real physical effect rather than any error.

Table 2 demonstrates that the spread varies between 0.0006 and 0.0371 for redshift systems (without considering the third doubtful system), and between 0.0076 and 0.0288 for blueshift systems, the latter being somewhat smaller than the former. Furthermore, redshift literature would reveal that for absorption systems $\Delta z_{\rm r} < 0.01$. Table 2 shows that, for at least one system, $\Delta z_{\rm r} > 0.01$. The blueshift systems (ABS) have all $\Delta z_{\rm b} < 0.01$.

Furthermore, the spectrum of the component A also exhibits a series of absorption features, the so-called 'forest' blueward of the emission line at 4539 Å. In the blueshift interpretation, these features constitute the Hα forest which corresponds to the Lyα forest in the redshift interpretation. However, Hα forest implies that these absorptions originate from higher levels which, in turn, implies that these levels should be populated. This, again, in turn, necessitates that the particle density of the intergalactic medium (IGM) should be large. Unfortunately, this is not well known in the existing literature. Nevertheless, it is known that soft X-ray detection is an indicator of such particle density, and further investigation is suggested in this respect. It is interesting to note in this connection that Lyβ, OVI, and CIII forest (Danforth *et al.* 2006), and also X-ray forest (Nicastro *et al.* 2005) have been reported recently to suggest absorption in IGM.

Finally, it should be noted that the blueshift determined here for the spectrum of 1009-0252A is the shift in the wavelengths of the lines emitted by the component A to the wavelengths measured on earth by the earth-bound observer. The blueshift value is not the result of the Doppler effect alone, but is the result of superposition of the cosmological redshift produced by the general expansion of the universe and the Doppler shift due to the component A approaching the observer produced by the ejection mechanism as described in section 6 below. 1009-0252, A and B both components are therefore cosmological objects and not local ones.

Furthermore, it is known that Doppler shifting of the continuum is expected to give rise to an enhancement of the optical luminosity of the QSO for large blueshifts, since the infrared (IR) part of the continuum spectrum is shifted to the optical part and the IR continuum of QSOs exhibits a steep rise in the spectrum (Burbidge & Burbidge 1967). However, as seen in Table 1, the identified lines are located in the near-infrared (NIR) region and not in the IR region. The same is therefore true for the continuum involved. As such, the optical luminosity of A is expected to be somewhat large but certainly not very large for the blueshifted spectrum, as it is the less strong NIR part of the continuum and not the much stronger IR that is being blueshifted to the optical part. This is supported by the observational evidence (H94) which shows that the component A (blueshifted spectrum) is really somewhat more luminous than the component B (redshifted spectrum), the *B,V* magnitudes of A and B being 18.2, 17.9 and 20.3, 20.5, respectively.

6. The close pair production: a proposed scenario

The analysis presented here shows that the close separation pair QSO 1009-0252A, B comprises two separate objects – one approaching us and thus exhibiting blueshifts, the other moving away from us and thus exhibiting redshifts – and is not produced by the gravitational lensing of a single object. We propose a scenario in terms of the

ejection mechanism to explain the production of the close pair involving the observed blueshifts.

It is known that merger of black holes may lead to their ejections in oppositely directed pairs due to the inherent instability of the systems – the so called 'sling-shot' mechanism (Saslaw *et al.* 1974; Valtonen 1976a, 1976b). This situation may arise when two galaxies, each hosting a supermassive black hole at its centre, merge. Supermassive black holes are known to be seats of activities at the centres of galaxies (Basu *et al.* 1993; Capetti *et al.* 2005). A binary system is believed to be initially formed by the two central black holes (Valtaoja *et al.* 1989). Such systems have indeed been detected in NGC 6240 (Kommossa *et al.* 2003), probably in OJ 287 (Valtonen *et al.* 2006) and in SDSS J153636.22+044127.0 (Boronson and Lauer 2009). Further progress in the merger process would lead to the ejection of supermassive black holes (primaries) at relativistic or non-relativistic speeds (Mikkola & Valtonen 1990). It is noteworthy here that Haehnelt *et al.* (2006) have recently presented evidence of ejection of a supermassive black hole by the 'sling-shot' mechanism resulting from merger of galaxies. In addition, satellite black holes of intermediate masses are also believed to be usually accompanying the central supermassive black holes in galaxies (Carr 1978; Carr *et al.* 1984) and are ejected during the merger process, some of them assuming eccentric orbits around the primary ones (Valtonen & Basu 1991).

Again, a black hole at the centre of a galaxy is also known to possess a gaseous accretion disk around it, which survives the tidal disruption that accompanies the ejection process (Rees & Saslaw 1975; Lin & Saslaw 1977; De Young 1977). The interaction between the disk with the black hole and the surrounding may lead to the formation of a QSO (Rees 1984; Osterbrock & Mathews 1986; Valtonen & Basu 1991; Spriegel *et al.* 2005). It is reasonable to envisage that the satellite black holes, presumably also possessing gaseous disks, would undergo the same process of interaction with the gaseous disks around them and the surroundings, as their primary counterparts, albeit at reduced scales owing to their smaller masses, and would end up as faint or nascent galaxies.

The final result of the ejection process due to the merger of two galaxies is the birth of two QSOs ejected in opposite directions each accompanied by several galaxy-like objects, the latter acting as absorbing clouds if and when lying along the line of sight. To this respect, it was shown earlier (Basu 1982) that absorbing clouds are probably linked with the birth of a QSO itself. Also, faint or nascent galaxies associated with QSO-like objects have been observed (Dressler *et al.* 1993; Tripp *et al.* 1999; Teresse *et al.* 1999).

In principle, of course, it is possible for the ejection to occur in any direction. However, the probability of the occurrence toward the observer is non-zero. Hence, it is conceivable that 1009-0252A is the result of the ejection process and is approaching us exhibiting blueshifts in emission and absorption lines, the latter being produced by the accompanying three absorbing clouds. The other member of the pair, viz., 1009-0252B is also ejected by the same process, viz., the 'sling-shot' mechanism, and is receding from us exhibiting the redshifted spectra.

7. Concluding remarks

Possibility of blueshifts in extragalactic spectra has been ignored in modern line identification programmes. On the other hand, advances in modern observational

technology are making new discoveries, which, at least in some cases, cannot be explained and interpreted by the traditional redshift process. Occurrence of close pairs of QSOs is one such phenomenon, which appears to lack satisfactory explanations, although serious attempts have been made to explain it in terms of gravitational lensing of a single object. In this paper, we have studied one such pair, viz., 1009-0252A, B and have demonstrated that the spectrum of one of the objects in the pair can be interpreted in terms of blueshifts. Based on our analysis, we suggest that the pair consists of two separate objects originated by the ejection mechanism resulting from the merger of two galaxies. The third component, viz., C, of the triple system 1009-0252A, B, C is an unrelated object in the field.

Finally, it should be noted that the blueshift does not contradict the redshift but complements it, since only a fraction of extragalactic objects, not all, are probably exhibiting blueshifted spectra. We recommend that unusual cases, which appears difficult to be explained when spectra are interpreted in terms of redshifts, should be particularly looked for the alternative blueshift interpretation.

Acknowledgement

The author thanks the anonymous referee for helpul suggestions.

References

Basu, D. 1973a, *Nat. Phys. Sci.*, **241**, 159.
Basu, D. 1973b, *The Observatory*, **93**, 229.
Basu, D. 1982, *Ap. Letts.*, **22**, 139.
Basu, D. 1998, *A&SS*, **259**, 415.
Basu, D. 2000, *Mod. Phys. Letts. A*, **15**, 2357.
Basu, D. 2001a, *Ap. Letts. & Comm.*, **40**, 157.
Basu, D. 2001b, *Ap. Letts. & Comm.*, **40**, 225.
Basu, D. 2004, *Phys. Scr.*, **69**, 427.
Basu, D. 2006a, *Astron. J.*, **131**, 1231.
Basu, D. 2006b, *Astr. Nachr.*, **327**, 724.
Basu, D. 2006c, *J. Astrophys. Astron.*, **27**, 381.
Basu, D. 2009, *Can. J. Phys.*, **87**, 721.
Basu, D., Haque-Copilah, S. 2001, *Phys. Scr.*, **63**, 425.
Basu, D. *et al.* 1993, *Astron. Astrophys.*, **272**, 417.
Boronson, T., Lauer, T. 2009, *Nature*, **458**, 53.
Burbidge, G., Burbidge, E. 1967, *Quasi Stellar Objects*, W. H. Wheeler & Co., San Fransisco, p. 172.
Capetti, A. *et al.* 2005, *Astyron. Astrophys.*, **431**, 465.
Carr, B. 1978, *Comm. Ap.*, **7**, 161.
Carr, B. *et al.* 1984, *Astrophys. J.*, **277**, 445.
Chen, H.-W. *et al.* 1999, *Nature*, **398**, 586.
Chen, H.-W. *et al.* 2000, *Nature*, **408**, 562.
Claeskens, J.-F. *et al.* 2000, *Astron. Astrophys.*, **356**, 840.
Claeskens, J.-F. *et al.* 2001, *Astron. Astrophys.*, **367**, 748 (C01).
Danforth, C. *et al*. 2006, *Astrophys. J.*, **640**, 716.
De Young, D. 1977, *Astrophys. J.*, **211**, 329.
Djorgovsky, S., Spinard, H. 1984, *Astrophys. J.*, **282**, L1.
Dressler, A. *et al.* 1993, *Astrophys. J.*, **405**, L45.
Fruchter, A. *et al.* 2001, GCN GRB Obs. Rep. No. 1200.
Gordon, K. 1980, *Amer. J. Phys.*, **48**, 524.

Haehnelt, M. G. *et al.* 2006, *Mon. Not. Roy. Astron. Soc.*, **366**, L22.
Hewett, P. C. *et al.* 1989, *Astrophys. J.*, **346**, L61.
Hewett, P. C. *et al.* 1994, *Astron. J.*, **108**, 1534 (H94).
Hewett, P. C. *et al.* 1998, *Astron. J.*, **115**, 383.
Holland, S. *et al.* 2002, *Astron. J.*, **126**, 639.
Kommossa, S. *et al.* 2003, *Astrophys. J.*, **582**, L15.
Lin, D., Saslaw, W. 1977, *Astrophys. J.*, **217**, 958.
Maylan, G., Djorgovsky, S. 1989, *Astrophys. J.*, **338**, L1.
Mikkola, S., Valtonen, M. 1990, *Astrophys. J.*, **348**, 412.
Nicastro, F. *et al.* 2005, *Astrophys. J.*, **629**, 700.
Osterbrock, P., Mathews, W. 1986, *Ann. Rev. Astron. Astrophys.*, **24**, 171.
Popowski, P., Weinzierl, W. 2004, *Mon. Not. Roy. Astron. Soc.*, **348**, 235.
Rees, M. 1984, *Ann. Rev. Astron. Astrophys.*, **22**, 471.
Rees, M., Saslaw, W. 1975, *Mon. Not. Roy. Astron. Soc.*, **171**, 53.
Reeves, J. *et al.* 2003, *Astron. Astrophys.*, **403**, 463.
Saslaw, W. C., Valtonen, M. J., Aarseth, S. J. 1974, *Astrophys. J.*, **190**, 253.
Sluse, D. *et al.* 2003, *Astron. Astrophys.*, **397**, 539.
Spriegal, V. *et al.* 2005, *Astrophys. J.*, **620**, L79.
Stern, D. *et al.* 2000, *Nature*, **408**, 560.
Surdej, J. *et al.* 1994, In: *Gravitational Lenses in the Universe*, 31st Liege Int. Astroph. Coll., 1993, (ed.) Surdej, J. *et al.* (Universite de Liege, Liege), p. 153.
Teresse, L. *et al.* 1999, *Astron. Astrophys.*, **346**, L21.
Trip, T. *et al.* 1998, *Astrophys. J.*, **508**, 200.
Valtaoja, L. *et al.* 1989, *Astrophys. J.*, **343**, 47.
Valtonen, M. 1976a, *Astron. Astrophys.*, **46**, 429.
Valtonen, M. 1976b, *Astron. Astrophys.*, **46**, 435.
Valtonen, M., Basu, D. 1991, *J. Astrophys. Astron.*, **12**, 91.
Valtonen, M. *et al.* 2006, *Astrophys. J.*, **643**, L9.
Wampler, E. 1973, *Nature*, **246**, 203.
Wang, J. *et al.* 2003, *Astrophys. J.*, **590**, L87.
Weedman, D. W. *et al.* 1982, *Astrophys. J.*, **255**, L5.
Yaqoob, T. *et al.* 1999, *Astrophys. J.*, **525**, L9.

J. Astrophys. Astr. (2009) **30,** 145–151

A Method for Judging Decay or Growth of the Magnetic Field of Pulsar

Lin-Sen Li
Department of Physics, Northeast Normal University, Changchun 130 024, China.

Received 2008 June 9; accepted 2009 September 1

Abstract. This paper provides a method for judging growth or decay of the magnetic field of pulsar by using pulse period P, or frequency ν, and its first and second derivatives $\dot{P}$, $\ddot{P}$ or $\dot{\nu}$, $\ddot{\nu}$. The author uses this method to judge the growth or decay of the magnetic field of Crab pulsar. The judged result for Crab pulsar is that the magnetic field of Crab pulsar is growing now, but it is not decaying. The result corresponds with the actual case of Crab pulsar.

Key words. Pulsar—decay or growth of magnetic field—method of judgement.

1. Introduction

Usually the magnetic field of pulsars decay with time. Such is the case for a lot of pulsars, but the magnetic field for a distinct pulsar is growing. The young pulsar is possibly such a case when it is born. Afterward its magnetic field is decaying successively. When it arrive at old pulsar, its magnetic field is not decaying or nearly without variation or become a weak field. The magnetic field of Crab pulsar should be growing due to young pulsar. This point corresponds with the result for the research of some authors (Blandford & Romaru 1988; Lyne 2004). Lyne (2004) gave a formula for judging increase or decrease of the magnetic field of pulsar by using the braking index, and concluded that the magnetic field of Crab pulsar is increasing. The present paper provides a method for judging the decay or growth of the magnetic field of pulsar by using the observable data of the frequency or period and its first and second derivatives, and checked the result given by Lyne for the increase of the magnetic field of Crab pulsar.

2. The formulas for judging decay or growth of magnetic field of pulsar

We adopt the magnetic dipole model of pulsar to research this problem. We assume that the magnetic field can be decaying or growing as in the following exponential form:

$$B_p^2 = B_i^2 \exp(\pm \xi t). \tag{1}$$

where B_p is the magnetic field at magnetic pole of pulsar and B_i is the field strength at $t = 0$. ξ is the coefficient of the magnetic decay or growth. If ξ is positive, the magnetic field of pulsar is growing; if it is negative, the magnetic field is decaying.

The pulsar radiating energy at a rate can be written from the magnetic dipole model (Shapiro & Teukolsky 1983):

$$\dot{E} = -\frac{2|\ddot{m}|^2}{3c^3} = -\frac{B_p^2 R^6 \Omega^4 \sin^2\alpha}{6c^3}. \tag{2}$$

The energy carried away by the radiation from the rotational energy of pulsar is

$$E = \frac{1}{2} I \Omega^2, \qquad \dot{E} = I \Omega \dot{\Omega}. \tag{3}$$

2.1 *The situation for the inclination without variation*

The equation of the magnetic dipole radiation of pulsar can be derived from the formulas (2)–(3) assuming the magnetic inclination $\alpha = \text{const}$.

$$\dot{\Omega} = -\frac{B_p^2 R^6 \Omega^3 \sin^2\alpha}{6c^3 I}, \tag{4}$$

where R, I and Ω denote radius, moment inertia and angular velocity of pulsar respectively.

Let $\Omega = 2\pi/P$ (P: pulse period). Inserting it into the equation (4), we get

$$B_p^2 = \frac{3c^3 I}{2\pi^2 R^6 \sin^2\alpha} P\dot{P}. \tag{5}$$

Differentiating equation (5) with respect to time, we get

$$\frac{dB_p^2}{dt} = \frac{3c^3 I}{2\pi^2 R^6 \sin^2\alpha}(\dot{P}^2 + P\ddot{P}). \tag{6}$$

where $\dot{P} = (dP/dt)$, $\ddot{P} = (d^2P/dt^2)$.

Combining equation (6) with equation (5) or the two-hand sides of the equation (6) is divided by the two-hand sides of the equation (5), we get

$$\frac{1}{B_p^2}\frac{dB_p^2}{dt} = \frac{\dot{P}}{P} + \frac{\ddot{P}}{\dot{P}}. \tag{7}$$

Let ν be the pulsar frequency,

$$\dot{\nu} = \frac{d\nu}{dt}, \quad \ddot{\nu} = \frac{d^2\nu}{dt^2},$$
$$P = \frac{1}{\nu}, \quad \dot{P} = \frac{d}{dt}\left(\frac{1}{\nu}\right) = \frac{-\dot{\nu}}{\nu^2}, \quad \ddot{P} = \frac{d}{dt}\left(\frac{-\dot{\nu}}{\nu^2}\right) = \frac{2\dot{\nu}^2}{\nu^3} - \frac{\ddot{\nu}}{\nu^2}. \tag{8}$$

Substituting the expressions (8) into the equation (7), we obtain the formula (9)

$$\frac{1}{B_p^2}\frac{dB_p^2}{dt} = \frac{\ddot{\nu}}{\dot{\nu}} - 3\frac{\dot{\nu}}{\nu}. \tag{9}$$

We substitute the formula (1) into the formulas (7) and (9), we obtain

$$\pm\xi = \frac{\dot{P}}{P} + \frac{\ddot{P}}{\dot{P}} = \frac{\ddot{\nu}}{\dot{\nu}} - \frac{3\dot{\nu}}{\nu}. \tag{10}$$

The formula (10) is a formula for judging growth or decay of magnetic field of pulsar. If ξ is positive, the magnetic field of pulsar is growing; if it is negative, the magnetic field is decaying.

2.2 *The situation for the inclination with variation*

We research that the pulsar inclination α varies with time for the situation of the formula (10).

Differentiating the formula (5) with respect to time, we get

$$\frac{dB_P^2}{dt} = \frac{3c^3 I}{2\pi^2 R^6 \sin^2\alpha}(\dot{P}^2 + P\ddot{P}) - \frac{3c^3}{\pi^2 R^6}(IP\dot{P})\cot\alpha\csc^2\alpha\frac{d\alpha}{dt}. \tag{11}$$

For giving the expression for $d\alpha/dt$, we use the formula (Davis & Goldstein 1970)

$$I\frac{d(\Omega\cos\alpha)}{dt} = -\vec{N}\cdot\frac{\vec{M}}{M} = 0,$$

where M is the magnetic moment, N is the magnetic torque.

Let $\Omega = 2\pi/P$, and inserting it into the above formula, and then differentiating it, we get

$$\frac{d\alpha}{dt} = -\frac{\dot{P}}{P}\cot\alpha. \tag{12}$$

Substituting the expression (12) into the expression (11), then

$$\frac{dB_p^2}{dt} = \frac{3c^3 I}{2\pi^2 R^6 \sin^2\alpha}(\dot{P}^2 + P\ddot{P}) + \frac{3c^3 I}{\pi^2 R^6}\dot{P}^2\cot^2\alpha\csc^2\alpha. \tag{13}$$

when the two-hand sides of the equation (13) is divided by the two-hand sides of equation (5), we get

$$\frac{1}{B_p^2}\frac{dB_p^2}{dt} = \frac{\dot{P}}{P} + \frac{\ddot{P}}{\dot{P}} + 2\cot^2\alpha\left(\frac{\dot{P}}{P}\right) = (1 + 2\cot^2\alpha)\frac{\dot{P}}{P} + \frac{\ddot{P}}{\dot{P}}. \tag{14}$$

Substituting the expressions (8) into the above formula, we get

$$\frac{1}{B_p^2}\frac{dB_p^2}{dt} = \frac{\ddot{\nu}}{\dot{\nu}} - (3 + 2\cot^2\alpha)\frac{\dot{\nu}}{\nu}. \tag{15}$$

Substituting the formula (1) into the left side for the formulas (14) and (15), we get

$$\pm\xi = (1 + 2\cot^2\alpha)\frac{\dot{P}}{P} + \frac{\ddot{P}}{\dot{P}} = \frac{\ddot{\nu}}{\dot{\nu}} - (3 + 2\cot^2\alpha)\frac{\dot{\nu}}{\nu}. \tag{16}$$

The formulas (10) and (16) are the formulas for judging the growth or decay of the magnetic field of pulsar.

3. Application to crab pulsar

We use the formulas (10) and (16) to judge the growth or decay of the magnetic field of Crab pulsar. We use the following data to judge it.

The data for the first set (Bonazzola & Schneider 1974) are:

$$\left.\begin{aligned} \nu &= 30.2137051\,\mathrm{HZ} \\ \dot{\nu} &= -0.38594 \times 10^{-9}\,\mathrm{HZs}^{-1} \\ \ddot{\nu} &= 1.1 \times 10^{-20}\,\mathrm{HZs}^{-2} \end{aligned}\right\}. \tag{17}$$

The data for the second set (Wang *et al.* 2001) are:

$$\left.\begin{aligned} \nu &= 29.836059670\,\mathrm{HZ} \\ \dot{\nu} &= -3.743460(3) \times 10^{-10}\,\mathrm{HZs}^{-1} \\ \ddot{\nu} &= 1.17(2) \times 10^{-20}\,\mathrm{HZs}^{-2} \end{aligned}\right\}. \tag{18}$$

The data for the third set (ATNF pulsar catalogue) are:

$$\left.\begin{aligned} \nu &= 30.225\,\mathrm{HZ} \\ \dot{\nu} &= -3.86 \times 10^{-10}\,\mathrm{HZs}^{-1} \\ \ddot{\nu} &= 1.240 \times 10^{-20}\,\mathrm{HZs}^{-2} \end{aligned}\right\}. \tag{19}$$

Substituting the data for the first set into the formula (10), we get

$$\pm\xi = \frac{\ddot{\nu}}{\dot{\nu}} - \frac{3\dot{\nu}}{\nu} = +0.098191804 \times 10^{-10} > 0,$$

so ξ should be taken as positive.

Substituting the data for the second set into the formula (10), we get

$$\pm\xi = \frac{\ddot{\nu}}{\dot{\nu}} - \frac{3\dot{\nu}}{\nu} = +0.063323602 \times 10^{-10} > 0,$$

so ξ should be taken as positive.

Substituting the data for the third set into the formula (10), we get

$$\pm\xi = \frac{\ddot{\nu}}{\dot{\nu}} - \frac{3\dot{\nu}}{\nu} = +0.061883027 \times 10^{-10} > 0,$$

so ξ should be taken as positive.

If we consider the magnetic inclination, α, we need to use formula (16) for the calculation.

We consider: $0^\circ \leq \alpha \leq 90^\circ$, then $+\infty \leq \cot\alpha \leq 0$. So when $0^\circ \leq \alpha \leq 90^\circ$, and $\dot{\nu} < 0$ (negative), substituting the data of three sets into the formula (16), we still obtain $\xi > 0$ (positive). Hence the magnetic field of Crab pulsar is still growing.

If we consider: $90^\circ \leq \alpha \leq 180^\circ$, and then $0 \leq \cot\alpha \leq -\infty$, we get

$$(3 + 2\cot^2\alpha)\frac{\dot{\nu}}{\nu} \leq 3\frac{\dot{\nu}}{\nu}.$$

Substituting the data of three sets into the formula (16), because $\dot{\nu} < 0$, we get $\xi < 0$ (negative).

So the magnetic field of Crab pulsar is decaying, only when its inclination is that of $90^\circ \leq \alpha \leq 180^\circ$. But for Crab pulsar its magnetic inclination α is (Davis & Goldstein 1970)

$$\alpha = 59^\circ.2.$$

So $0^\circ \leq \alpha \leq 90^\circ$, and $\xi > 0$ (positive). It is not negative. Hence when we consider magnetic inclination, α, the magnetic field of Crab pulsar is still growing with time.

Next we calculate the increase of magnetic field with time for the Crab pulsar. We take the average value of three sets for ξ in the expressions (17)–(19), we get

$$\xi = 0.0744682 \times 10^{-10}(c,\ g,\ s). \tag{20}$$

We use the present strength of the magnetic field of Crab pulsar $B_0 = 5.2 \times 10^{12} G$ ($\sin\alpha = 1$) (Shapiro & Teukolsky 1983). Substituting the values for ξ and B_0 into the formula (1) and taking ξ as the positive symbol, we get

$$\begin{aligned} B_p(t) &= 5.2006 \times 10^{12} G, \\ \therefore\ \Delta B_p(t) &= B_p(t) - B_p(0) = (5.2006 - 5.2000) \times 10^{12} \\ &= +0.0006 \times 10^{12}\, G/\text{yr}. \end{aligned} \tag{21}$$

i.e., the magnetic filed is increasing (growing). The increment is $6 \times 10^8\, G$ per year for Crab pulsar.

4. Discussion

(1) The formula given by Lyne and the correction for the formula,
Lyne (2004) derived a formula for judging the increase or decrease of the magnetic field of pulsar. He uses the magnetic dipole model

$$B = -\sqrt{\frac{3c^3 I}{8\pi^2 R^6 \sin^2 a} P\dot{P}} = 3.2 \times 10^{19}\sqrt{P\dot{P}}\ \text{Gauss}, \tag{22}$$

$$P = \frac{1}{\nu}, \quad n = \nu\bar{\nu}/\dot{\nu}^2, \quad \tau = \frac{P}{2\dot{P}}. \tag{23}$$

And then, he obtained from the expressions (22) and (23)

$$\frac{dB}{dt} = \frac{B}{\tau}\{3 - n\}. \tag{24}$$

He infers from the above formula that the magnetic field is increasing, if $n < 3$ and the magnetic field is decreasing, if $n > 3$.

The formula (24) needs to be corrected.

Differentiating the equation (22), we obtain

$$\frac{dB}{dt} = \frac{B}{2}\left\{\frac{\dot{P}}{P} + \frac{\ddot{P}}{\dot{P}}\right\} \quad \text{or} \quad \frac{dB}{dt} = \left\{\frac{\ddot{\nu}}{\dot{\nu}} - 3\frac{\dot{\nu}}{\nu}\right\}. \tag{25}$$

We use

$$n = \frac{\nu\ddot{\nu}}{\dot{\nu}^2} = 2 - \frac{P\ddot{P}}{\dot{P}^2}. \tag{26}$$

In the above two equations, the equation (25) can be written as

$$\frac{dB}{dt} = \frac{B}{2}\frac{\dot{P}}{P}\{3 - n\} = \frac{B}{4\tau}\{3 - n\}. \tag{27}$$

This is the corrective formula for the formula (24) given by Lyne.

(2) This paper supports and has checked the result given by Lyne for the increase of the magnetic field of Crab pulsar.

It can be checked that the growth of the magnetic field of Crab pulsar can be used for the observable data of three sets $(\nu, \dot{\nu}, \ddot{\nu}\}$ provided by this paper.

Substitution of data of three sets (17)–(19) into the formula of the braking index (23) or (26), we get

$$n = 2.2313, \quad n = 2.4948, \quad n = 2.5154. \tag{28}$$

So, $n \prec 3$. Based on the formula (24) given by Lyne, the magnetic field of Crab pulsar is increasing by using the above three data of braking index. Hence this paper supports and has checked the result given by Lyne provided in this paper.

(3) The comparison of methods of this paper with Lyne's paper is given below:

Both papers start from and are based on the magnetic dipole model of pulsar, but the methods of derivation are different. The author uses the observational data for periods P, $\dot{P}$, $\ddot{P}$ or frequencies ν, $\dot{\nu}$, $\ddot{\nu}$ to judge the decay or growth of the magnetic field of pulsar. Lyne uses the braking index, n, to judge the increase or decrease of the magnetic field of pulsar. In addition, the results given by this paper consider the variation of the magnetic inclination with time. The results given by Lyne only consider the magnetic inclination as a constant.

5. Conclusion

(1) The magnetic field of a pulsar is denoted by

$$B^2 = B_i^2 \exp(\pm\xi t).$$

It is a decaying or a growing field, which is judged by the following formulas

$$\pm\xi = \frac{\dot{P}}{P} + \frac{\ddot{P}}{\dot{P}} = \frac{\ddot{\nu}}{\dot{\nu}} - \frac{3\dot{\nu}}{\nu}$$

or

$$\pm\xi = (1 + 2\cot^2\alpha)\frac{\dot{P}}{P} + \frac{\ddot{P}}{\dot{P}} = \frac{\ddot{\nu}}{\dot{\nu}} - (3 + 2\cot^2\alpha)\frac{\dot{\nu}}{\nu}.$$

If the value for $\xi > 0$, i.e., ξ is positive, then

$$B^2 = B_i^2 \exp(+\xi t).$$

The magnetic field is a growing field.

If the value for $\xi < 0$, i.e., ξ is negative, then

$$B^2 = B_i^2 \exp(-\xi t).$$

The magnetic field is a decaying field.

If the value $\xi = 0$ or $\xi \to 0$, the magnetic field

$$B^2 = B_i^2 \quad \text{or} \quad B^2 \to B_i^2,$$

i.e., the magnetic field is an invariable field or the field is a very weak field.

(2) The value of ξ suggests the evolutionary significance. When $\xi > 0$, the magnetic field is a growing field. This belongs to the situation for young pulsar. When $\xi < 0$, the magnetic field is a decaying field. This belongs to a pulsar between the young and old age. When $\xi = 0$ or $\xi \to 0$, the magnetic field is an invariable field or a weak field. This belongs to the situation for an old pulsar.

(3) We infer that the magnetic field of Crab pulsar is growing with time because the value of ξ is positive. The conclusion corresponds with the results of the research of the authors Blandford & Romaru (1988) and Lyne (2004).

References

ATNF Pulsar Catalogue (http://www.atnf.csiro.au/research/pulsar/psrcat/), 2007, Australia.
Blandford, R. D., Romaru, R. W. 1988, *MNRAS*, **234**, 57.
Bonazzola, S., Schneider, J. 1974, *ApJ*, **191**, 273.
Davis, L., Goldstein, M. 1970, *ApJ*, **159(2)**, pL 81.
Lyne, A. G. 2004, I Au Symposium no. 218, 2003 in Sydney, Australia (eds) Fernando Camilo and Pryann, Gaensler San Fraucisco (An Astronomical Society of Pacific, p 25).
Shapiro, S. L., Teukolsky, S. A. 1983, Black holes, White dwarfs, and Neutron stars, New York, Chichester, Brisbane, Toronto, Singapore, p 278.
Wang Na, Wu Xin-Ji, Manchester, R. N., Zhang Jin, Lyne, A. G., Yusup, A. 2001, *Chinese J. Astron. Astrophys.*, **1(3)**, 195.

J. Astrophys. Astr. (2009) **30,** 153–163

Velocity Curve Studies of Spectroscopic Binary Stars V380 Cygni, V401 Cyg, V523 Cas, V373 Cas and V2388 Oph

K. Karami[1,2,*] & R. Mohebi[1,**]
[1]*Department of Physics, University of Kurdistan, Pasdaran St., Sanandaj, Iran.*
[2]*Research Institute for Astronomy & Astrophysics of Maragha (RIAAM), Maragha, Iran.*
[*]*e-mail: KKarami@uok.ac.ir*
[**]*e-mail: rozitamohebi@yahoo.com*

Received 2008 May 11; accepted 2009 March 16

Abstract. Using measured radial velocity data of five double lined spectroscopic binary systems V380 Cygni, V401 Cyg, V523 Cas, V373 Cas and V2388 Oph, we find corresponding orbital and spectroscopic elements via the method introduced by Karami & Mohebi (2007) and Karami & Teimoorinia (2007). Our numerical results are in good agreement with those obtained by others using more traditional methods.

Key words. Stars: binaries: eclipsing—stars: binaries: spectroscopic.

Determining the orbital elements of binary stars helps us to obtain the necessary information such as the mass and the radius of stars which play important roles in the evolution of the stellar structures. Analyzing both the light and the radial velocity curves deducing from the photometric and the spectroscopic observations, respectively, leads to derivation of the orbital parameters. One of the usual methods to analyze the velocity curve is the method of Lehmann-Filhés, see Smart (1990). Here we use the method introduced by Karami & Mohebi (2007) and Karami & Teimoorinia (2007) (hereafter KM2007 and KT2007) for obtaining the orbits of five double-lined spectroscopic binary systems V380 Cygni, V401 Cyg, V523 Cas, V373 Cas and V2388 Oph.

V380 Cygni is a close detached binary with $P = 12.425612$ days. The spectral type is $B1.5II - III$, $B2V$ for the primary and secondary components, respectively. The polar temperature of primary is 24,500 K and for secondary is 23,600 K. The angle of inclination is $80.1 \pm 0.7^{\circ}$ (Hill & Batten 1984). The V401 Cyg appears to be a rather typical contact system and is a double-lined spectroscopic binary. The orbital period is 0.582714 days (Rucinski *et al.* 2002a, b). V523 Cas is one of the faintest known contact binaries. The spectral type is $K4V$ and the period is $P = 0.233693$ days (Rucinski *et al.* 2003a, b). V373 Cas is known to be a double-lined spectroscopic binary. The primary component is highly evolved and should be close to the Roche limiting surface of periastron. The spectral type of the primary and secondary components is $B0.5II$ and $B4III$, respectively. The mean effective temperature is $T_e = 22{,}000$ and 18,000 for the primary and secondary components. The angle of inclination is $\sim 60^{\circ}$ with a period of 13.4 days. See Hill & Fisher (1987). V2388 Oph is very close visual binary and has been the subject of many speckle interferometry investigations. The spectral type is W UMa-type with a relatively long period of 0.802 days. The system appears to be

one of the most luminous among currently known contact binaries. Orbital inclination angle is 90° (Rucinski *et al.* 2002a, b).

This paper is organized as follows. In section 2, we give a brief review of the method of KM2007 and KT2007. In section 3, the numerical results implemented for the five different binary systems are reported. Section 4 is devoted to conclusions.

1. A brief review of the method of KM2007 and KT2007

The radial velocity of star in a binary system is defined as follows:

$$\mathrm{RV} = V_{cm} + \dot{Z}, \tag{1}$$

where V_{cm} is the radial velocity of the center of mass of system with respect to the sun and

$$\dot{Z} = K[\cos(\theta + \omega) + e\cos\omega], \tag{2}$$

is the radial velocity of star with reference to the center of mass of the binary, see Smart (1990). In equation (2), the dot denotes the time derivative and θ, ω and e are the angular polar coordinate (true anomaly), the longitude of periastron and the eccentricity, respectively. Note that the quantities θ and ω are measured from the periastron point and the spectroscopic reference line (plane of sky), respectively. Also,

$$K = \frac{2\pi}{P}\frac{a\sin i}{\sqrt{1-e^2}}, \tag{3}$$

where P is the period of motion and inclination i is the angle between the line of sight and the normal of the orbital plane.

Following KM2007 and KT2007, one may show that the radial acceleration scaled by the period is obtained as:

$$P\ddot{Z} = \frac{-2\pi K}{(1-e^2)^{3/2}}\sin\left(\cos^{-1}\left(\frac{\dot{Z}}{K} - e\cos\omega\right)\right) \times \left\{1 + e\cos\left(-\omega + \cos^{-1}\left(\frac{\dot{Z}}{K} - e\cos\omega\right)\right)\right\}^2. \tag{4}$$

Equation (4) describes a nonlinear relation, $P\ddot{Z} = P\ddot{Z}(\dot{Z}, K, e, \omega)$, in terms of the orbital elements K, e and ω. Using the nonlinear regression of equation (4), one can estimate the parameters K, e and ω, simultaneously. Also one may show that the adopted spectroscopic elements, i.e., m_p/m_s, $m_p \sin^3 i$ and $m_s \sin^3 i$, are related to the orbital parameters. See KM2007 and KT2007.

2. Numerical results

Here we use the method of KM2007 and KT2007 to derive both the orbital and combined elements for the five different double lined spectroscopic systems V380 Cygni,

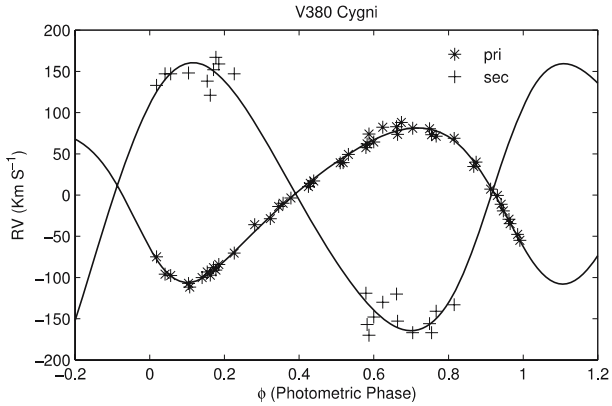

Figure 1. Radial velocities of the primary and secondary components of V380 Cygni plotted against the photometric phase. The observational data belong to Hill & Batten (1984).

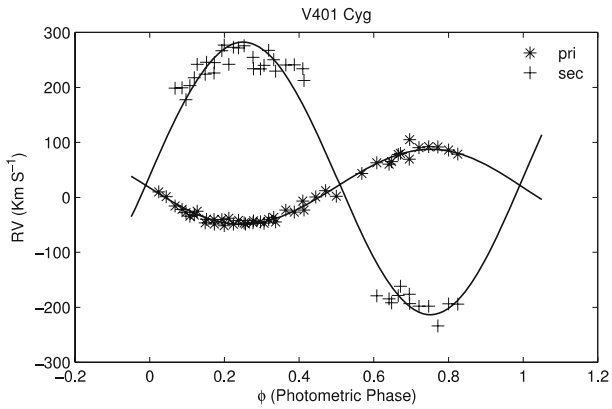

Figure 2. Same as Fig. 1, but for V401 Cyg. The observational data have been derived from Rucinski *et al.* (2002a, b).

V401 Cyg, V523 Cas, V373 Cas and V2388 Oph. Using the measured experimental data for radial velocities of the two components of these systems obtained by Hill & Batten (1984) for V380 Cygni, Rucinski *et al.* (2002a, b) for V401 Cyg and V2388 Oph, Hill & Fisher (1987) for V373 Cas and Rucinski *et al.* (2003a, b) for V523 Cas, the fitted velocity curves are plotted in terms of the photometric phase in Figs. 1–5.

Figures 6–15 show the radial acceleration scaled by the period versus the radial velocity for the primary and secondary components of V380 Cygni, V401 Cyg, V523 Cas, V373 Cas and V2388 Oph, respectively. The solid closed curves are the results of the nonlinear regression of equation (4), which their good coincidence with the measured data yields to derive the optimized parameters K, e and ω. Figures show that also for V401 Cyg, V523 Cas, and V2388 Oph due to having small eccentricities, their radial velocity-acceleration curves display an elliptical shape, while, in contrast for the eccentric systems V380 Cygni and V373 Cas, the acceleration-velocity curve shows some deviation from an ellipse (see Karami & Mohebi 2007).

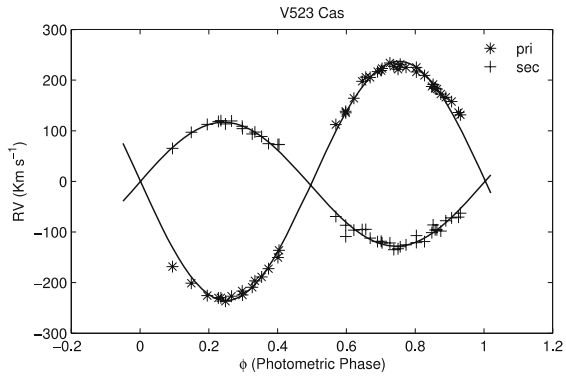

Figure 3. Same as Fig. 1, but for V523 Cas. The observational data belong to Rucinski *et al.* (2003a, b).

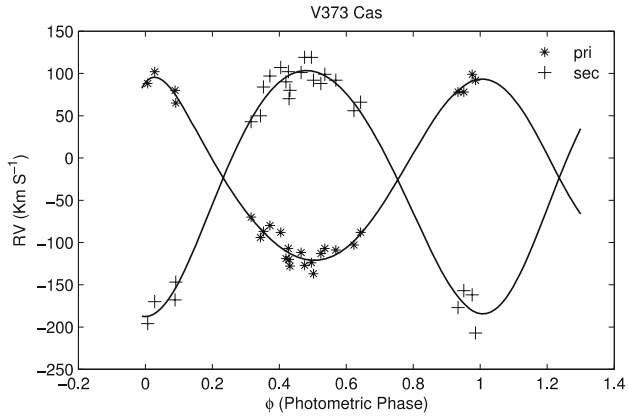

Figure 4. Same as Fig. 1, but for V373 Cas. The observational data belong to Hill & Fisher (1987).

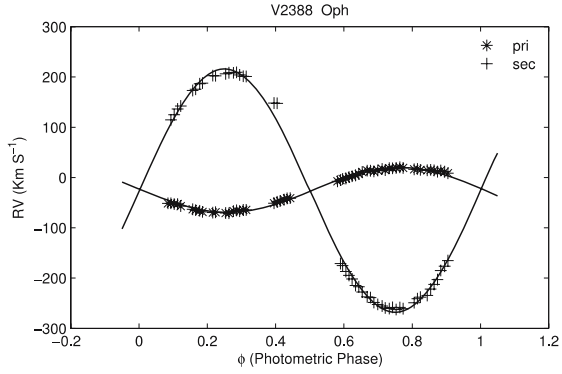

Figure 5. Same as Fig. 1, but for V2388 Oph. The observational data belong to Rucinski *et al.* (2002a, b).

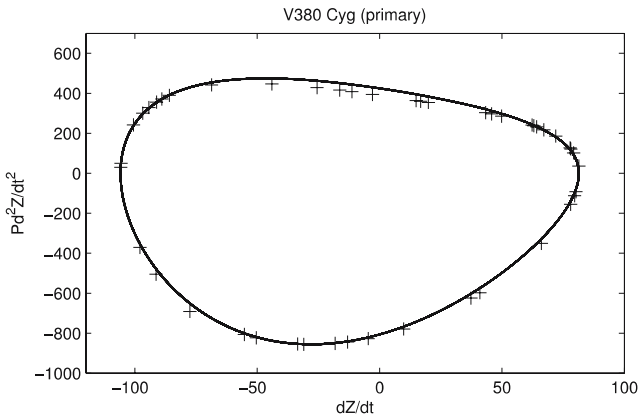

Figure 6. The radial acceleration scaled by the period *versus* the radial velocity of the primary component of V380 Cyg. The solid curve is obtained from the nonlinear regression of equation (14). The plus points are the experimental data.

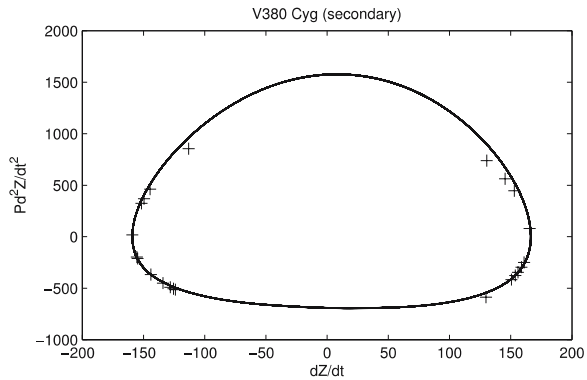

Figure 7. Same as Fig. 6, but for the secondary component of V380 Cyg.

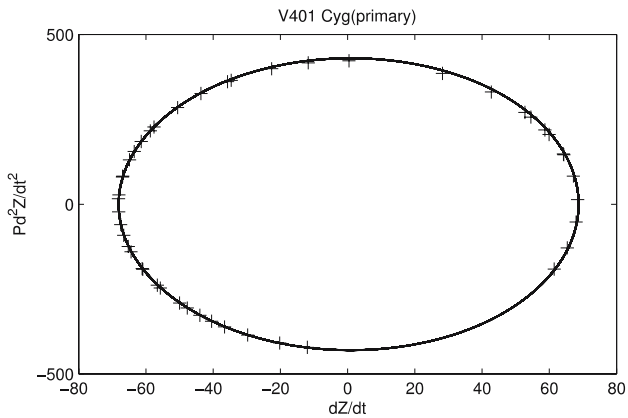

Figure 8. Same as Fig. 6, but for the primary component of V401 Cyg.

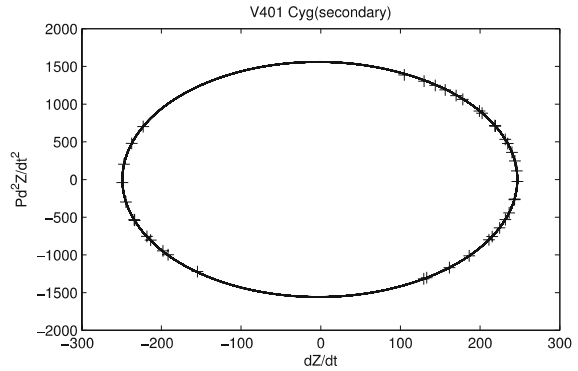

Figure 9. Same as Fig. 6, but for the secondary component of V401 Cyg.

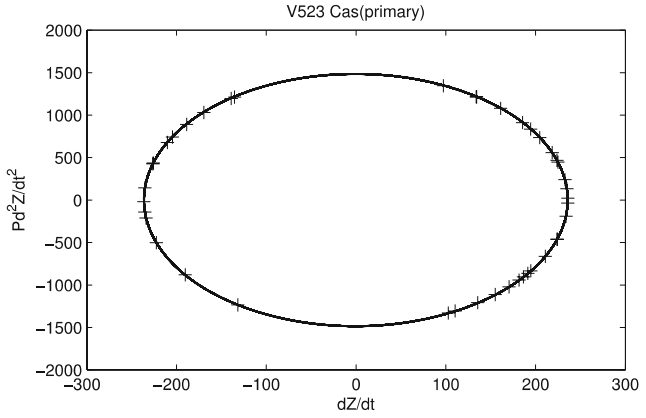

Figure 10. Same as Fig. 6, but for the primary component of V523 Cas.

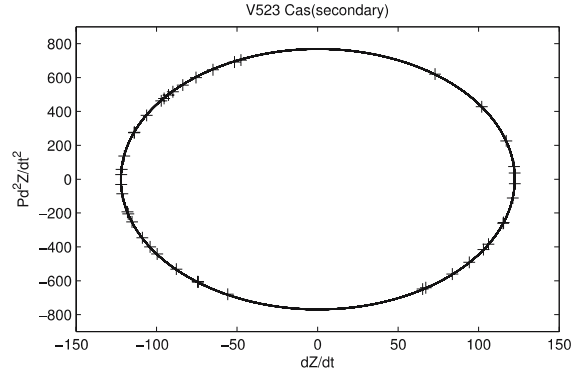

Figure 11. Same as Fig. 6, but for the secondary component of V523 Cas.

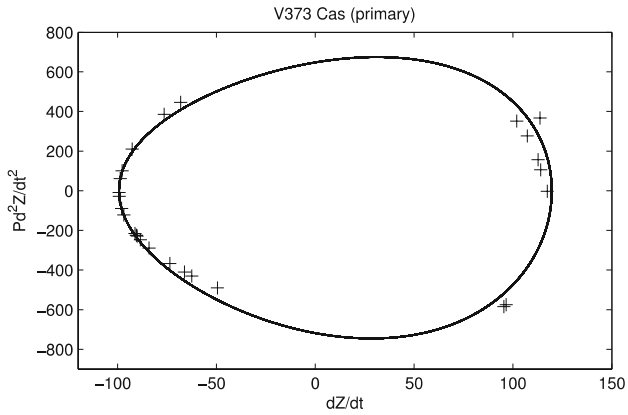

Figure 12. Same as Fig. 6, but for the primary component of V373 Cas.

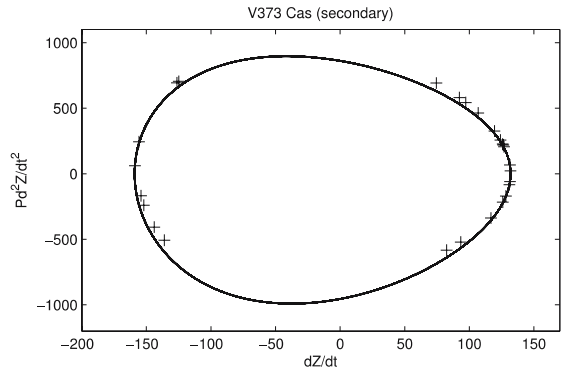

Figure 13. Same as Fig. 6, but for the secondary component of V373 Cas.

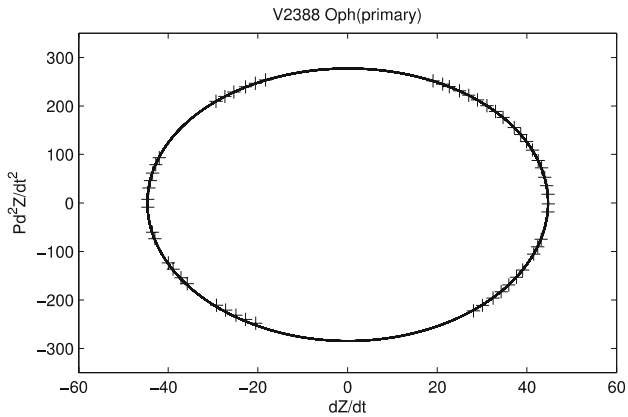

Figure 14. Same as Fig. 6, but for the primary component of V2388 Oph.

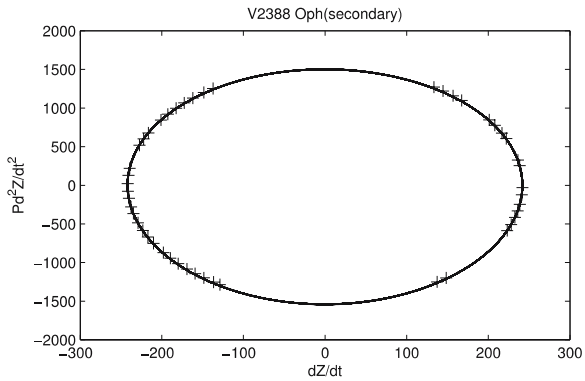

Figure 15. Same as Fig. 6, but for the secondary component of V2388 Oph.

Table 1. Spectroscopic and combined orbit of V380 Cygni.

	This paper	Batten (1960)	Hill & Batten (1984)
Primary			
$V_{cm}(\mathrm{km\,s^{-1}})$	-2.85 ± 0.23	-2.9 ± 0.8	-0.7 ± 0.7
$K_p(\mathrm{km\,s^{-1}})$	93.68 ± 0.12	93.4 ± 1.2	92.3 ± 1.1
e	0.204 ± 0.002	0.229 ± 0.013	0.22 ± 0.01
$\omega(^\circ)$	129.7 ± 0.7	128 ± 3.1	127.6 ± 2.8
Secondary			
$V_{cm}(\mathrm{km\,s^{-1}})$	-2.85 ± 0.23	2.5 ± 6.1	-18 ± 4.7
$K_s(\mathrm{km\,s^{-1}})$	162.82 ± 0.28	161.6 ± 7	168 ± 5.3
e	$e_s = e_p$	0.23	0.22
$\omega(^\circ)$	276.37 ± 0.33	128.0 (fixed)	127.6 (fixed)
$m_p \sin^3 i/M_\odot$	12.94 ± 0.08	12.4 ± 0.3	12.4 ± 0.3
$m_s \sin^3 i/M_\odot$	7.44 ± 0.04	7.2 ± 0.2	7.1 ± 0.2
$(a_p + a_s) \sin i/R_\odot$	61.64 ± 0.12	60.9 ± 1.7	60.7 ± 2
m_p/m_s	1.74 ± 0.01	1.72 ± 0.05	1.73 ± 0.06

The orbital parameters, K, e and ω, resulting from the nonlinear least squares of equation (4) for V380 Cygni, V401 Cyg, V523 Cas, V373 Cas and V2388 Oph, are tabulated in Tables 1, 2, 3, 4 and 5, respectively. The velocity of the center of mass, V_{cm}, is obtained by calculating the areas above and below the radial velocity curve. Where these areas become equal to each other, then the velocity of center of mass is obtained. Tables 1–5 show that the results are in good agreement with those obtained by Hill & Batten (1984) for V380 Cygni, Rucinski *et al.* (2002a, b) for V401 Cyg and V2388 Oph, Rucinski *et al.* (2003a, b) for V523 Cas and Hill & Fisher (1987) for V373 Cas. Note that in Table 1, the absolute value of V_{cm} of V380 Cygni in this paper is not in concord with the result obtained by Hill & Batten (1984) but it is in good agreement with the result of Batten (1960). In a binary

Table 2. Same as Table 1, but for V401 Cyg.

	This paper	Rucinski *et al.* (2002a, b)
Primary		
V_{cm}(km s^{-1})	27.24 ± 0.15	25.53(2.14)
K_p(km s^{-1})	68.46 ± 0.02	72.23(2.43)
e	$e_p = e_s$	–
$\omega(^\circ)$	$w_p = w_s + 180^\circ$	–
Secondary		
V_{cm}(km s^{-1})	27.24 ± 0.15	25.53(2.14)
K_s(km s^{-1})	247.99 ± 0.02	249.13(4.53)
e	0.0046 ± 0.0001	–
$\omega(^\circ)$	180.65 ± 5.21	–
$m_p \sin^3 i/M_\odot$	1.4993 ± 0.0005	–
$m_s \sin^3 i/M_\odot$	0.4139 ± 0.0002	–
$(a_p + a_s) \sin i/R_\odot$	3.643 ± 0.001	–
m_p/m_s	0.276 ± 0.001	0.290(11)
$(m_p + m_s) \sin^3 i/M_\odot$	1.9132 ± 0.0008	2.008(130)

Table 3. Same as Table 1, but for V523 Cas.

	This paper	Rucinski *et al.* (2003a, b)
Primary		
V_{cm}(km s^{-1})	-2.31 ± 0.71	-2.54(0.90)
K_p(km s^{-1})	236.22 ± 0.04	235.95(1.41)
e	0.0012 ± 0.0002	–
$\omega(^\circ)$	189.65 ± 10.61	–
Secondary		
V_{cm}(km s^{-1})	-2.31 ± 0.71	-2.54(0.90)
K_s(km s^{-1})	122.38 ± 0.02	121.64(1.14)
e	$e_s = e_p$	–
$\omega(^\circ)$	$w_s = w_p - 180^\circ$	–
$m_p \sin^3 i/M_\odot$	0.381 ± 0.002	–
$m_s \sin^3 i/M_\odot$	0.7355 ± 0.0004	–
$(a_p + a_s) \sin i/R_\odot$	1.6557 ± 0.0003	–
m_p/m_s	0.5181 ± 0.0002	0.516(7)
$(m_p + m_s) \sin^3 i/M_\odot$	1.117 ± 0.001	1.11(24)

system, the V_{cm} of the two components should be the same. In Table 1, there is another difference which is related to ω_s. Since we did not fix it, the method derives it freely.

Table 4. Same as Table 1, but for V373 Cas.

	This paper	Hill & Fisher (1987)
Primary		
$V_{cm}(\mathrm{km\,s^{-1}})$	-25.14 ± 0.76	-24.5 ± 2
$K_p(\mathrm{km\,s^{-1}})$	109.52 ± 0.22	106.7 ± 2.7
e	$e_p = e_s$	–
$\omega(^\circ)$	$w_p = w_s + 180^\circ$	–
Secondary		
$V_{cm}(\mathrm{km\,s^{-1}})$	-25.14 ± 0.76	–
$K_s(\mathrm{km\,s^{-1}})$	145.53 ± 0.02	–
e	0.0972 ± 0.0002	–
$\omega(^\circ)$	164.54 ± 0.27	–
$m_p \sin^3 i/M_\odot$	12.98 ± 0.03	12.6 ± 0.2
$m_s \sin^3 i/M_\odot$	9.77 ± 0.04	9.3 ± 0.2
$(a_p + a_s) \sin i/R_\odot$	67.305 ± 0.064	66.1 ± 0.9
m_p/m_s	1.33 ± 0.03	1.35 ± 0.04

Table 5. Same as Table 1, but for V2388 Oph.

	This paper	Rucinski *et al.* (2002a, b)
Primary		
$V_{cm}(\mathrm{km\,s^{-1}})$	-25.35 ± 0.88	$-25.88(0.52)$
$K_p(\mathrm{km\,s^{-1}})$	44.71 ± 0.01	$44.62(0.48)$
e	0.006 ± 0.001	–
$\omega(^\circ)$	275.62 ± 2.09	–
Secondary		
$V_{cm}(\mathrm{km\,s^{-1}})$	-25.35 ± 0.88	$-25.88(0.52)$
$K_s(\mathrm{km\,s^{-1}})$	241.99 ± 0.03	$240.22(0.98)$
e	$e_s = e_p$	–
$\omega(^\circ)$	$w_s = w_p - 180^\circ$	–
$m_p \sin^3 i/M_\odot$	1.653 ± 0.001	–
$m_s \sin^3 i/M_\odot$	0.3055 ± 0.0001	–
$(a_p + a_s) \sin i/R_\odot$	4.545 ± 0.001	–
m_p/m_s	0.184 ± 0.001	$0.186(2)$
$(m_p + m_s) \sin^3 i/M_\odot$	1.959 ± 0.001	$1.926(30)$

The combined spectroscopic elements including $m_p \sin^3 i$, $m_s \sin^3 i$, $(a_p + a_s) \sin i$ and m_p/m_s obtaining from the estimated parameters K, e and ω for the five systems are tabulated in Tables 1, 2, 3, 4 and 5 and show that our results are in good agreement with the those obtained by Hill & Batten (1984) for V380 Cygni, Rucinski *et al.* (2002a, b)

for V401 Cyg and V2388 Oph, Rucinski *et al.* (2003a, b) for V523 Cas and Hill & Fisher (1987) for V373 Cas, respectively.

3. Conclusions

Using the measured experimental data for radial velocities of V380 Cygni, V401 Cyg, V523 Cas, V373 Cas and V2388 Oph obtained by Hill & Batten (1984), Rucinski *et al.* (2002a, b), Rucinski *et al.* (2003a, b) and Hill & Fisher (1987) respectively, we find the orbital elements of these systems by the method of KM2007 and KT2007. Our numerical calculations show that the results obtained for both the orbital elements and the combined spectroscopic parameters are in good agreement with the those obtained by others using more traditional methods. In a subsequent paper we intend to study the other different systems.

Acknowledgements

This work was supported by the Research Institute for Astronomy & Astrophysics of Maragha (RIAAM), Maragha, Iran.

References

Hill, G., Batten, A. H. 1984, *A&A*, **141**, 39.
Hill, G., Fisher, W. A. 1987, *A&A*, **171**, 123.
Karami, K., Mohebi, R. 2007, *ChJAA*, **7**, 558.
Karami, K., Mohebi, R. 2007, *JAA*, **28**, 217.
Karami, K., Teimoorinia, H. 2007, *Ap&SS*, **311**, 435.
Rucinski, M. S., Capobianco, C. C., Lu, W. *et al.* 2002a, *AJ*, **124**, 1738.
Rucinski, M. S., Capobianco, C. C., Lu, W. *et al.* 2002b, preprint (astro-ph/0201213).
Rucinski, M. S., Capobianco, C. C., Lu, W. *et al.* 2003a, *AJ*, **125**, 3258.
Rucinski, M. S., Capobianco, C. C., Lu, W. *et al.* 2003b, preprint (astro-ph/0302399).
Smart, W. M. 1990, *Textbook on Spherical Astronomy*, 6th edn., Revised by Green, R. M. (Cambridge Univ. Press), 360.

J. Astrophys. Astr. (2009) **30,** 165–175

Rapid Neutron Capture Process in Supernovae and Chemical Element Formation

Rulee Baruah[1,*], Kalpana Duorah[2] & H. L. Duorah[2]
[1]*Department of Physics, HRH The Prince of Wales Institute of Engineering and Technology, Jorhat 785 001, India.*
[2]*Department of Physics, Gauhati University, Guwahati 781 014, India.*
[*]*e-mail: ruleebaruah@yahoo.co.in*

Received 2007 May 28; accepted 2009 September 29

Abstract. The rapid neutron capture process (r-process) is one of the major nucleosynthesis processes responsible for the synthesis of heavy nuclei beyond iron. Isotopes beyond Fe are most exclusively formed in neutron capture processes and more heavier ones are produced by the r-process. Approximately half of the heavy elements with mass number $A \succ 70$ and all of the actinides in the solar system are believed to have been produced in the r-process. We have studied the r-process in supernovae for the production of heavy elements beyond $A = 40$ with the newest mass values available. The supernova envelopes at a temperature $\succ 10^9$ K and neutron density of 10^{24} cm^{-3} are considered to be one of the most potential sites for the r-process. The primary goal of the r-process calculations is to fit the global abundance curve for solar system r-process isotopes by varying time dependent parameters such as temperature and neutron density. This method aims at comparing the calculated abundances of the stable isotopes with observation. We have studied the r-process path corresponding to temperatures ranging from 1.0×10^9 K to 3.0×10^9 K and neutron density ranging from 10^{20} cm^{-3} to 10^{30} cm^{-3}. With temperature and density conditions of 3.0×10^9 K and 10^{20} cm^{-3} a nucleus of mass 273 was theoretically found corresponding to atomic number 115. The elements obtained along the r-process path are compared with the observed data at all the above temperature and density range.

Key words. Supernova—nucleosynthesis—abundance—r-process.

1. Introduction

Burbidge *et al.* (1957), in their seminal paper, outlined the rapid neutron capture process in the supernova envelope at a high neutron density and a temperature of 10^9 degrees. According to them, this mode of synthesis is responsible for the production of a large number of isotopes in the range $70 \leq A \leq 209$, and also for synthesis of uranium and thorium. This would explain the abundances of the neutron rich nuclei in the periodic table. Major advances have been made in calculating r-process nucleosynthesis in supernovae (Woosley *et al.* 1992) and in using a wide range of

model parameters to obtain yields that approximate the solar r-process abundances (Kratz *et al.* 1993). Studies of galactic chemical evolution (Mathews & Cowan 1992) show that the enrichment of the r-process elements in the galaxy is consistent with low mass type II supernovae being the r-process sites. In the usual picture the r-process stops when the neutron supply ceases (freeze-out). The produced very neutron rich progenitor nuclei then undergo a series of β-decays until they reach a stable nucleus whose calculated abundance can then be compared with observation. It was recognised that the extremely high neutron densities and temperatures needed were probably attainable only in dynamical events, i.e., supernovae.

The essential feature of the r-process is that a large flux of neutrons becomes available in a short time interval for addition to elements of the iron group, or perhaps, in cases where the abundances in the iron group are abnormally small, for addition to light nuclei such as Ne^{22}. So we started our analysis with $A = 40$ and obtained the abundances beyond that. We have summarised our calculations within a site-independent, classical approach based on neutron number density n_n and temperature T_9, defining the neutron binding (separation) energy Q_n of the path, where the waiting point approximation, i.e., (n, γ) $\leftrightarrow$ (γ, n) equilibrium could be applied. The dependence on nuclear masses enters via Q_n.

We choose supernova as the site for r-process because the supernova light curves show the presence of ${}_{98}Cf^{254}$. We have considered the r-process in supernovae for the production of heavy elements, under extreme conditions of temperature and density. For our purpose, the most interesting evolution occurs as the temperature falls from 10^{10} K to 10^9 K. Beginning at about 10^{10} K, nuclear statistical equilibrium (NSE) favours the assemblage of nucleons into α-particles and heavy nuclei. As the temperature drops below about 5.0×10^9 K, the reactions responsible for converting α-particles back into heavy nuclei begin to fall out of equilibrium. By 3.0×10^9 K, the charged particle reactions freeze out. Below this temperature, the r-process occurs until the temperature reaches (1–2) $\times 10^9$ K, where the neutron reactions also cease as the neutrons are depleted (Woosley *et al.* 1994). Using new mass tables of Audi *et al.* (2003) we have calculated the average excess neutron binding energy to nuclei with neutron number which is then used in the calculation of neutron capture chain. We start with a temperature of 1.0×10^9 K and neutron number density of 10^{20} cm^{-3} as these are the conditions prevailing in supernova envelopes during the eventually expanding stages. In our present paper, we emphasize only on the r-process path to obtain the elements in our astrophysical conditions considered and consequent build-up to heavier nuclei. In our next paper, we propose to present the abundances of these elements along the path.

2. Source of neutron flux

For the r-process nucleosynthesis in supernovae, the existence of enormous neutron flux is necessitated. Normal stellar matter has a neutron/proton ratio near unity making it virtually impossible to free sufficient neutrons relative to seed nuclei. Reactions such as $^{13}C(\alpha, n)^{16}O$ can produce free neutrons in red giants, but the number of these free neutrons is also small. It is possible to circumvent this problem by having the only charged particles accompanying the neutrons be alphas. Single alpha particles do not capture neutrons. It is proposed that (Schramm 1973) at high temperatures associated with the collapse of massive iron core in type II supernovae, iron will photo-dissociate

into alphas and neutrons as:

$$^{56}\mathrm{Fe} \rightarrow 13\alpha + 4n.$$

As the material expands and cools from these photo-dissociation conditions, the alphas recombine again to produce heavy iron peak nuclei. However, these recombination is hampered by the fact that alphas only systhesize heavy elements via three-body interactions. Thus there will be a time during which a few iron peak seed nuclei have been produced in a sea of alphas and neutrons. The ratio of neutrons to seed will be large, so that an r-process can take place.

Another set of conditions where large number of free neutrons exist is when the temperature and density get sufficiently high that the reaction $\mathrm{p} + \mathrm{e}^- \rightarrow \mathrm{n} + \nu_e$ dominates over $\mathrm{n} + \mathrm{e}^+ \rightarrow \mathrm{p} + \bar{\nu}_e$ (Arnett 1979). Thus neutronisation refers to electron capture driven by high electron Fermi energy (i.e., high density). Subsequently, $\mathrm{p} + \mathrm{e}^- \rightarrow \mathrm{n} + \nu_e$ at high density. Moreover, nuclei resist electron capture because of the large threshold energies required as they become more neutron rich. Also electron capture on free protons is limited by the small abundance of free protons. These problems are eased by higher density and higher temperature, so neutronization speeds up as collapse continues. Once collapse begins, neutronization becomes the dominant mode of neutrino productions, overwhelming thermal processes.

According to Mukhopadhyay (2007), the neutrino–antinutrino oscillation under gravity explains the source of abnormally large neutron abundance to support the r-process nucleosynthesis in astrophysical site, e.g., supernova. He also proposed two related reactions

$$\mathrm{n} + \nu_e \rightarrow \mathrm{p} + \mathrm{e}^-; \quad \mathrm{p} + \bar{\nu}_e \rightarrow \mathrm{n} + \mathrm{e}^+$$

as given by Arnett (1979). If $\bar{\nu}_e$ is over-abundant than ν_e, then, from this expression, neutron production is expected to be more than proton production into the system. Therefore, the possible conversion of ν to $\bar{\nu}_e$ due to gravity induced oscillation explains the over-abundance of neutron.

In the build-up of nuclei by the r-process, the reactions which govern both the rate of flow and the track followed in the (A, Z) plane are the (n, γ) and (γ, n) reactions, beta decay and at the end of the track the neutron induced fission. The timescale τ_n for a heavy nucleus to capture an additional neutron is rapid on the competing timescale τ_β for it to undergo beta decay. Whereas τ_β depends only on nuclear species, τ_n depends critically on the ambient neutron flux.

$$\lambda_n > \lambda_\beta (\tau_n < \tau_\beta). \tag{1}$$

In rapid process, a sufficient flux of neutrons makes τ_n much shorter than τ_β. Then neutron capture will proceed into the very neutron rich and unstable regions far from the valley of beta stability. Once the neutron flux is exhausted, the unstable nuclei produced by the r-process will beta decay to the valley of stability to form the stable r-process elements.

3. Nuclear physics considerations and the r-process path

To illustrate the significant differences of the astrophysical conditions during the r-processing, we refer to the classical quantity, namely, the neutron binding

(separation S_n) energy Q_n, that represents the r-process path in the chart of nuclides once the specific values of neutron density n_n and the temperature T are assigned. The Q_n values vary in time as well as in space along with the dynamical evolution of our astrophysical environment.

3.1 *Dynamical evolution of the neutrino heating phase in type-II supernovae*

We first summarize the type-II supernova explosion scenario according to the current understanding. We emphasize some characteristic features on the hydrodynamical evolution of the neutrino wind phase. During the final stages of the evolution of a massive ($8 \sim 25\,M_\odot$) star, an 'iron' core forms in its central region and subsequently undergoes gravitational collapse. When the central density reaches nuclear matter density, the collapse stops abruptly to cause a 'core bounce'. A hydrodynamical shock wave is created and starts to propagate outward. According to calculations (Bruenn 1989a), this shock wave loses its entire kinetic energy within a few milliseconds to stall well inside the outer edge of the initial iron core, and no immediate disruption (the 'prompt' expolsion) of the star occurs. On a timescale from several tens of milliseconds to about half a second, the neutrinos streaming out from the new born neutron star can deposit energy behind the standing accretion shock at high enough a rate to revive its outward motion and initiate the final explosion of the star. This is the neutrino-driven 'delayed' explosion mechanism originally suggested by Wilson *et al.* (1986).

The neutron star releases its gravitational binding energy of several 10^{53} erg in the form of neutrino radiation. A region of net energy deposition by neutrinos ('neutrino heating') naturally emerges at the periphery of the neutron star because of the decrease of temperature with increasing radius. The energy is transferred to the stellar gas predominently by absorption of electron neutrinos (ν_e) on neutrons and electron anti-neutrinos ($\bar{\nu}_e$) on protons. About one percent of the neutron star's binding energy is sufficient to drive a powerful shock into the overlaying stellar mantle. Behind the shock, an extended and rapidly expanding region of low density and relatively high temperature develops and is further energized by neutrino heating.

Janka (1993) performed hydrodynamical simulations of the formation and evolution of the neutrino-wind phase of a type II supernova with a proper description of the neutrino physics and an adequate representation of the equation of state. The hydrodynamical investigations were carried on from an initial configuration made available by Wilson. From Wilson's post-collapse model the radial profiles of density, temperature, electron concentration, composition and velocity were taken to specify the initial conditions for the set of partial differential equations, which was integrated in time to follow the gas composition and the evolution of the fluid flow in spherical symmetry. The equation of state for the stellar gas contained the contributions from nucleus, α-particles, and a representative typical heavy nucleus in nuclear statistical equilibrium. The model evolved under the influence of the neutrino fluxes from the protoneutron star at the center. Since all hydrodynamical and thermodynamical quantities were determined from the numerically solved set of equations, the effects of the particular choice of the initial model configuration were not crucial and became even less relevant as time went on. The most important parameter of the input model to influence the simulated evolution was the mass of the central neutron star (Witti *et al.* 1994). However, the hydrodynamical evolution in the range of temperatures below $T_9 = 2$ is not very fast (Takahashi *et al.* 1994).

3.2 *The r-process network and the waiting-point approximation*

Supernova is a dynamical event. When a constant S_n (n_n and T) is assumed over a duration time τ, then the nuclei will still be existent in the form of highly unstable isotopes, which have to decay back to β-stability. In reality n_n and T will be time dependent. As long as these are high enough to ensure the waiting point approximation, the system will immediately adjust to the new equilibrium and only the new S_n (n_n and T) is important. The abundance flow from each isotopic chain to the next is governed by beta decays. The waiting point approximation is only valid for high temperatures and neutron number densities of the gas. If not, the flow of nuclei towards higher neutron number N for a given proton number Z is steadily depleted by beta decay. As a result only a small fraction of the flow can easily reach a waiting point. Cameron *et al.* (1983b) found that for temperatures of 2.0×10^9 K and higher, the waiting point approximation was valid for neutron number densities as low as 10^{20} cm^{-3}. For lower temperature ($T < 10^9$ K) even with high values of $n_n \approx 10^{25}$ cm^{-3}, the waiting point approximation is not valid. The r-process path requires a synthesis time of the order of seconds to form the heaviest elements such as thorium, plutonium and uranium.

The r-process network includes radiative neutron capture, i.e., (n, γ) reactions, the inverse photo-disintegration, i.e., (γ, n) reactions, β-decay, i.e., (β, γ) processes and β-delayed neutron emission, i.e., (β, n) processes. If the neutron density is very high, successive (n, γ) reactions may produce very neutron rich isotopes out of the limited α-process network in a 'mini r-process'. The (n, γ) and (γ, n) reactions are then much faster than β-decays. Therefore, as soon as the 'proper' r-process is started, the isotopic abundances, stuck at the most neutron-rich isotopes included in the α-process network, will quickly be redistributed according to the (n, γ) $\leftrightarrow$ (γ, n) equilibrium (Takahashi *et al.* 1994). In our model, the neutron number densities are so high that an equilibrium between the (n, γ) and (γ, n) reactions is quickly established.

In an (n, γ) $\leftrightarrow$ (γ, n) equilibrium (the waiting-point approximation), the maximum abundances in isotopic chains occur at the same neutron separation energy, which is determined by a combination of n_n and T_9 in an astrophysical environment. Connecting the abundance maxima in isotopic chains defines the so called r-process path. The build-up of heavy nuclei is governed by the abundance distribution in each isotopic chain from (n, γ) $\leftrightarrow$ (γ, n) equilibrium and by effective decay rates λ_β^Z of isotopic chains. After charged particle freeze-out, when only (n, γ) $\leftrightarrow$ (γ, n) equilibrium remain in place, matter can progress to heavier nuclei via β-decays between isotopic chains, which is modelled by the r-process network to follow further evolution (Freiburghaus *et al.* 1999).

4. Calculation of the r-process path

A nucleus of fixed Z cannot add neutrons infinitely even in the presence of an intense neutron flux. The binding energy of each successive neutron becomes progressively weaker as more and more neutrons are added until ultimately the binding falls to zero, which sets an upper limit to neutron addition at fixed Z. The nucleus then waits until β-decay allows it to move onto the next nucleus. Thus in a rapid process two inverse reactions $\mathrm{n} + (Z, A) \leftrightarrow (Z, A+1) + \gamma$ come to an equilibrium. This balance governs the equilibrium distribution of isotope abundances for a given Z. The maximum abundance along an isotope chain is determined by the temperature and neutron density.

Given that $A/(A+1) \approx 1$, the abundance maxima in each isotopic chain are determined by the neutron number density n_n and temperature T. The maximum value of the abundance occurs at neutron separation energy S_n which is same for all isotopic chains irrespective of Z. Approximating abundances $Y(Z, A+1)/Y(Z, A) \approx 1$ at the maximum and keeping all other quantities constant, the neutron separation energy S_n has to be the same for the abundance maxima in all isotopic chains.

The condition for the dynamical equilibrium between (n, γ) and (γ, n) reactions for nucleus $X(A, Z)$ is expressed as (Burbidge *et al.* 1957):

$$X(A, Z) + n \Longleftrightarrow X(A+1, Z) + \gamma + Q_n(A, Z), \tag{2}$$

where $Q_n(A, Z)$ is the neutron binding (separation energy S_n) to the nucleus $X(A, Z)$. Writing $n(A, Z)$ and n_n for the number densities of the nuclei (A, Z) and neutrons respectively, the statistical balance in this reaction is expressed by (Burbidge *et al.* 1957):

$$\log(n(A+1, Z)/n(A, Z)) = \log\ n_n - 34.07 - (3/2)\log\ T_9 + (5.04/T_9)Q_n \tag{3}$$

T_9 being temperature in units of 10^9 degrees.

Using the condition that in equilibrium, $n(A+1, Z) \approx n(A, Z)$ we obtain Q_n as:

$$Q_n = (T_9/5.04)(34.07 + (3/2)\log\ T_9 - \log\ n_n). \tag{4}$$

A rough estimate of Q_n values that are preferred for explaining the r-process abundance curve can be gained by taking into account the correlation between the r-process abundance peaks and the neutron magic numbers. The prominent peaks at $A \approx 130$ and $A \approx 195$ are correlated with the nuclear shell effects of their precursor nuclei near the neutron magic numbers 82 and 126 respectively. With the aid of nuclear mass formula, one finds from the abundance peaks that the Q_n value is most likely somewhere in between 2 and 4 MeV. To attain this, we take the temperature and density conditions considered here to range from

$$T = 1.0 \times 10^9\,\mathrm{K} \text{ to } 3.0 \times 10^9\,\mathrm{K} \quad \text{and} \quad n_n = 10^{20}\,\mathrm{cm}^{-3} \text{ to } 10^{30}\,\mathrm{cm}^{-3}.$$

The variation of Q_n values with temperature and neutron number densities is shown in Table 1.

We then tried to outline a method of calculation of r-process abundances which may eventually be capable of yielding a theoretical abundance curve on the basis of nuclear data alone. First, we consider the determination of $Q_n(A, Z)$ on the basis of smooth Weizsacker atomic mass formula given by equation (5) neglecting shell, pairing and quadrupole deformation effects:

$$\begin{aligned} M_w(A, Z) = (A-Z)M_n + ZM_p - (1/c^2)[\alpha A - \beta(A-2Z)^2/A \\ - \gamma A^{2/3} - \epsilon Z(Z-1)/A^{1/3}], \end{aligned} \tag{5}$$

where M_n and M_p are masses of the neutron and proton and α, β, γ and ϵ are constants in energy units, which represent volume, isotopic, surface and coulomb energy parameters respectively, the values being taken from Burbidge *et al.* (1957). With these we modify the expression for $M(A, Z)$ as:

$$M(A, Z) = M_w(A, Z) - (1/c^2)[f(N) + g(Z)], \tag{6}$$

Table 1. Variation of Q_n values with temperature and density.

T_9(K)	n_n(cm^{-3})	Q_n(Mev)	T_9(K)	n_n(cm^{-3})	Q_n(Mev)
1.0	10^{20}	2.79	1.0	10^{22}	2.39
1.2	10^{20}	3.37	1.2	10^{22}	2.90
1.4	10^{20}	3.96	1.4	10^{22}	3.41
1.6	10^{22}	4.56	1.6	10^{22}	3.93
1.0	10^{24}	1.99	1.8	10^{22}	4.45
1.2	10^{24}	2.41	1.2	10^{26}	1.95
1.4	10^{24}	2.85	1.4	10^{26}	2.30
1.6	10^{24}	3.29	1.6	10^{26}	2.65
1.8	10^{24}	3.73	1.8	10^{26}	3.01
2.0	10^{24}	4.17	2.0	10^{26}	3.38
1.6	10^{28}	2.02	2.2	10^{26}	3.74
1.8	10^{28}	2.30	2.4	10^{26}	4.11
2.0	10^{28}	2.58	2.2	10^{30}	1.98
2.2	10^{28}	2.87	2.4	10^{30}	2.19
2.4	10^{28}	3.16	2.6	10^{30}	2.42
2.6	10^{28}	3.45	2.8	10^{30}	2.63
2.8	10^{28}	3.74	3.0	10^{30}	2.84
3.0	10^{28}	4.03			

where $M_w(A, Z)$ represents the Weizsacker expression given by equation (5). With this we calculate the neutron binding energy as:

$$Q_n(A, Z) = B_n(A + 1, Z) = c^2[M(A, Z) + M_n - M(A + 1, Z)]. \tag{7}$$

We note that Q_n for nucleus (A, Z) is equal for the neutron binding energy B_n (taken positive) in nucleus $(A + 1, Z)$. These functions of N and Z separately takes into account the important effects on nuclear masses of:

- neutron and proton shell structure
- spheroidal quadrupole deformation of partially filled shells and
- pairing of neutrons and pairing of protons.

The quantities $f(N)$ and $g(Z)$ will be discontinuous functions at magic closed shell numbers for N and Z respectively. The sign is taken negative so that $f(N)$ and $g(Z)$ as positive quantities, decrease the mass and add to the stability of the nucleus.

We now obtain:

$$Q_n(A, Z) = f(A, Z) + f'(A - Z) \tag{8}$$

putting $M(A, Z)$ from equation (6) and using:

$$f'(A - Z) = f'(N) = df(N)/d(N) = f(A + 1 - Z) - f(A - Z). \tag{9}$$

On simplification and on putting $Z = A - N$, we rewrite equation (8) as:

$$Q_n(A, N) = f(A, N) + f'(N).$$

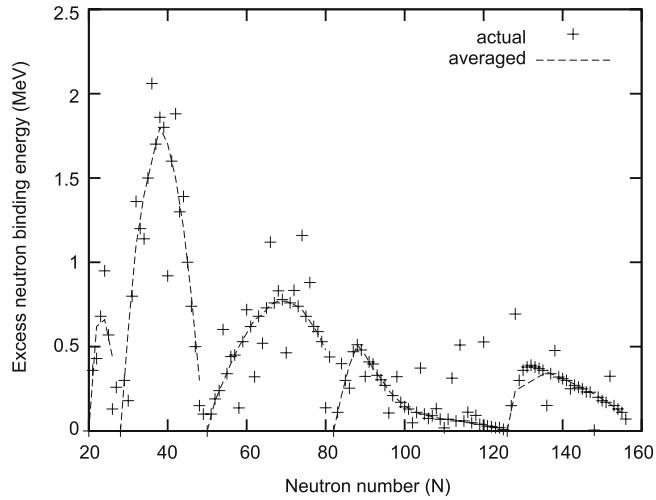

Figure 1. The average excess neutron binding energy *vs.* neutron number N, over that given by the smooth Weizsacker atomic mass formula.

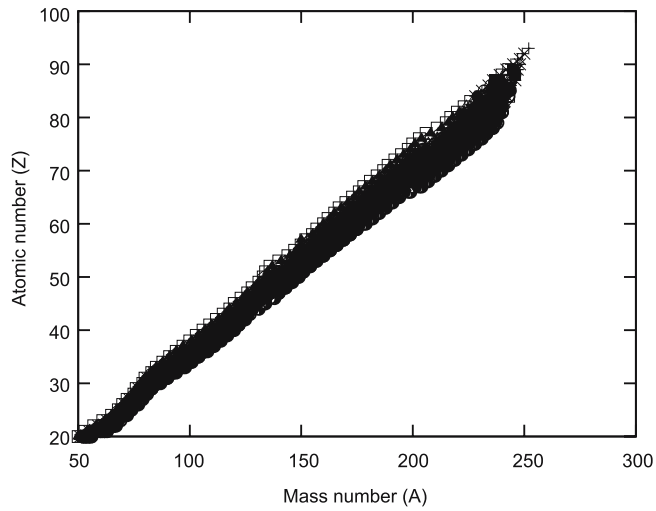

Figure 2. The average r-process path in the (A, Z) plane at all the temperature and density conditions considered, showing the schematic view of the isotopes produced.

Here $f'(N)$ is the excess neutron binding energy to nuclei with a specified N over that given by the smooth Weizsacker mass formula normalised to zero at the beginning of the shell in which N lies. We have used the mass tables of Audi *et al.* (2003) and for various N, the resulting average values have been plotted against N. Another form of averaging is then affected by drawing a smooth curve through the points obtained in this way and plotted in Fig. 1. These equations are then solved for fixed values of Z, to obtain the corresponding values of A by trial and error, at different temperature and density conditions which specify Q_n in equation (8). The neutron capture paths so obtained are then plotted in Fig. 2.

5. Existence of chemical elements along the r-process path

In our classical condition we notice an element of mass 273 corresponding to atomic number 115. Experimentally some new elements were synthesized at the Lawrence Berkley Laboratory, e.g., elements with $Z = 116$, 118, etc. (Swiatecki *et al.* 2005). Also theories have long predicted the island of stability for nuclei with approximately 114 protons and 184 neutrons. Thus we conclude that a nuclei with mass 273 is a possibility. The seed nuclei in the neutrino driven wind are produced early in the expansion by alpha-capture or by proton-capture processes. When the temperature and density become low in a short dynamic time scale and the charged particle reactions almost cease, the r-process starts from these seed nuclei. So we start our calculation at ${}_{20}\mathrm{Ca}^{40}$ and obtain the neutron capture path beyond that.

We notice that at densities $>10^{30}\,\mathrm{cm}^{-3}$, the r-process chain does not show the elements as seen in data of Audi *et al.* (2003). As we try to obtain the elements at lower densities in our analysis, we find them more prominently as we go from high to low density site. Most of our observed elements are seen in the range of neutron number density $10^{20}\,\mathrm{cm}^{-3}$ to $10^{24}\,\mathrm{cm}^{-3}$ and temperature from 2.0×10^9 K to 3.0×10^9 K. For example, at densities $10^{28}\,\mathrm{cm}^{-3}$, $10^{26}\,\mathrm{cm}^{-3}$, etc., the r-process chain does not give us all the observable elements. But at condition of density $10^{20}\,\mathrm{cm}^{-3}$ and temperature $T_9 = 2.0$, that path contains all the elements as was given in the experimental data of Audi *et al.* (2003).

We tabulate some of the elements (experimental) obtained along the r-process path as follows:

We note that the element ${}_{98}\mathrm{Cf}^{254}$ shown by the supernova light curves is found in our classical astrophysical condition of temperature $T_9 = 1.9$ and neutron number density $n_n = 10^{20}\,\mathrm{cm}^{-3}$. We also note that the double magic nucleus ${}_{28}\mathrm{Ni}^{78}_{50}$ is obtained at $T_9 = 1.0$ and $n_n = 10^{20}\,\mathrm{cm}^{-3}$; $T_9 = 1.1$ and $n_n = 10^{22}\,\mathrm{cm}^{-3}$; $T_9 = 1.2$ and $n_n = 10^{24}\,\mathrm{cm}^{-3}$; $T_9 = 1.4$ and $n_n = 10^{26}\,\mathrm{cm}^{-3}$; $T_9 = 2.0$ and $n_n = 10^{28}\,\mathrm{cm}^{-3}$; all of these conditions correspond to Q_n value ≈ 2.5 Mev. Another double magic

Table 2. Chemical elements at the r-process site.

Element	$T_9(10^9\,\mathrm{K})$	$n_n(\mathrm{cm}^{-3})$
${}_{56}\mathrm{Ba}^{137}$	2.5	10^{20}
${}_{82}\mathrm{Pb}^{207}$	2.5	10^{22}
${}_{92}\mathrm{U}^{236}$	3.0	10^{22}
${}_{98}\mathrm{Cf}^{254}$	1.9	10^{20}
For double magic nuclei		
${}_{28}\mathrm{Ni}^{78}_{50}$	1.0	10^{20}
	1.1	10^{22}
	1.2	10^{24}
	1.4	10^{26}
	2.0	10^{28}
${}_{50}\mathrm{Sn}^{132}_{82}$	1.7	10^{20}
	1.9	10^{22}

nucleus ${}_{50}\mathrm{Sn}_{82}^{132}$ is found in our analysis at $T_9 = 1.7$ and $n_n = 10^{20}\,\mathrm{cm}^{-3}$; $T_9 = 1.9$ and $n_n = 10^{22}\,\mathrm{cm}^{-3}$; these correspond to Q_n value ≈ 4.5 Mev.

6. Discussion and conclusion

Whenever and however the r-process operates, it appears to be very uniform and well confined in astrophysical parameter space. The temperature, density and neutron flux at r-process sites vary over a small range. This means that only a small minority of type II supernovae produces r-process elements. The beta decay lifetimes, separation energy, neutron flux, the temperature range, the equilibrium chain and collapse time, all are built in to the equations, which are, then numerically solved to determine the chain for various separation energies. The neutrino winds drive out the r-process elements which then decay to the lines nearer to the beta-stable valley, and, they are ready for comparison with observation.

We have studied the r-process path at various temperatures ranging from 1.0×10^9 K to 3.0×10^9 K and neutron number densities ranging from $10^{20}\,\mathrm{cm}^{-3}$ to $10^{30}\,\mathrm{cm}^{-3}$. We mostly concentrate our analysis at energies greater than 2 Mev as this is the condition prevailing in the supernova envelopes and neutron capture occurs during the later expanding stage. We have used the mass table of Audi *et al.* (2003) for the calculation of the average excess neutron binding energy which is obtained by the normalization at the magic neutron numbers 20, 50, 82, 126. It has been found that a nucleus is stable if the number of neutrons or protons in it is equal to the magic number, and it cannot capture further neutrons because the shells are closed and they cannot contain an extra neutron. With the subsequent addition of neutrons at fixed Z, correspondingly the binding falls and ultimately falls to zero. At this point, the nucleus undergoes a β-decay and gets converted to the next element. This r-process path is shown in Fig. 2 by corresponding relations between Z and A.

As the high density conditions do not show much of the experimentally observed elements, we propose that the heavy elements which must have been produced during the extreme condition of supernova explosion instantly undergo photo-disintegration at the high density and temperature situation. Only in the later expansion stages after the explosion, where the neutron density supposedly falls, the r-process nucleosynthesis produces the heavy elements which subsequently β-decays and the r-process path forms. We conclude that the heavy elements were created after supernova explosion and in the later expansion stages they were distributed all over the universe. In supernova during the expansion stage if the ejected matter flow reaches the waiting point nuclei associated with the magic neutron numbers at rather small radii above the neutron star, neutrino induced charged current reactions can compete with the β-decays of the longest lived waiting point nuclei and thus speed up the matter flow to heavier nuclei. We tried to get our abundances with respect to all the nuclei whose β-decay lifetimes are considerably higher. We conclude that our theoretical model will be successful in providing new light to solve some problems in the r-process and the corresponding build-up to heavier nuclei.

Acknowledgements

The authors are sincerely thankful to the Government of Assam for giving the permission to carry out the research work. Grateful thanks are due to B. K. Rajkhowa of

POWIET and Dr S. M. Hazarika of Tezpur University for their valuable help during the preparation of the manuscript.

References

Arnett, W. D. 1979, Proceedings of the workshop on Sources of Gravitational Radiation, Cambridge University Press, 311.
Audi, G., Wapstra, A. H., Thibault, C. 2003, *Nucl. Phys. A*, **729**, 337.
Borzov, I. N., Goriely, S. 2000, *Phys. Rev. C*, **62**, 03550.
Bruenn, S. W. 1989a, *ApJ*, **340**, 955.
Burbidge, E. M., Burbidge, G. R., Fowler, W. A., Hoyle, F. 1957, *Rev. Mod. Phys.*, **29**, 547.
Chetia, A., Duorah, H. L. 1986, *Il Nuovo Cimento*, **94B**, 93.
Fermi, E. 1950, University of Chicago, Chicago I11, 8.
Freiburghaus, C., Rembges, J. F., Rauscher, T., Kolbe, E., Thielemann, F. K., Kratz, K. L., Pfeiffer, B., Cowan, J. J. 1999, *ApJ*, **516**, 381.
Janka, H. T. 1993, Frontier Objects in Astrophysics and Particle Physics (eds) Giovannelli, F., Mannocchi, G., *Conf. Proc., SIF, Bologna*, **40**, p345.
Kratz, K. L., Pfeiffer, B., Thielemann, F. K., Bitouzet, J. P., Moller, P. 1993, *ApJ*, **402**, 216.
Mathews, G. J., Cowan, J. J. 1992, *ApJ*, **391**, 719.
Meyer, B. S., Mathews, G. J., Howard, W. M., Woosley, S. E., Hoffman, R. D. 1992, *ApJ*, **399**, 656.
Mukhopadhyay, B. 2007, *Class. Quant. Grav.*, **24**, 1433.
Qian, Y. Z., Vogel, P., Wasserburg, G. J. 1998, *ApJ*, **494**, 285.
Schramm, D. N. 1973, Proceedings of Conference on Explosive Nucleosynthesis, Austin, Texas.
Swiategki, W. J., Wilczynska, K. S., Wilczynski, J. 2005, *Phys. Rev. C.*, **71**, 014602.
Takahashi, K., Witti, J., Janka, H. T. 1994, *A&A*, **286**, 857.
Terasawa, M., Sumiyoshi, K., Kajino, T., Mathews, G. J., Tanihata, I. 2001, *ApJ*, **562**, 470.
Wanajo, S., Tamamura, M., Itoh, N., Nomoto, K., Ishimaru, Y., Beers, T. C., Nozawa, S. 2003, *ApJ*, **593**, 968.
Wilson, J. R., Mayle, R. W., Woosley, S. E., Weaver, T. 1986, *Ann. N. Y. Acad. Sci.*, **470**, 267.
Witti, J., Janka, H. T., Takahashi, K. 1994, *A&A*, **286**, 841.
Woosley, S. E., Hoffman, R. D., 1992, *ApJ*, **395**, 202.
Woosely, S. E., Wilson, J. R., Mathews, G. J., Hoffman, R. D., Meyer, B. S. 1994, *ApJ*, **433**, 229.

J. Astrophys. Astr. (2009) **30,** 177–185

On Out of Plane Equilibrium Points in Photo-Gravitational Restricted Three-Body Problem

M. K. Das[1], Pankaj Narang[2], S. Mahajan[3] & M. Yuasa[4]
[1]*Institute of Informatics and Communication, University of Delhi South Campus, Benitojuarez Road, New Delhi 110 021, India.*
[2]*Department of Physics, A.R.S.D. College, University of Delhi, New Delhi 110 021, India.*
[3]*Department of Physics & Astrophysics, University of Delhi, New Delhi 110 021, India.*
[4]*RIST, Kinki University , Higashi-Osaka 577-8502, Japan.*

Received 2008 August 17; accepted 2009 September 1

Abstract. We have investigated the out of plane equilibrium points of a passive micron size particle and their stability in the field of radiating binary stellar systems *Krüger*-60, *RW-Monocerotis* within the framework of photo-gravitational circular restricted three-body problem. We find that the out of plane equilibrium points (L_i, $i = 6, 7, 8, 9$) may exist for range of β_1 (ratio of radiation to gravitational force of the massive component) values for these binary systems in the presence of Poynting–Robertson drag (hereafter PR-drag). In the absence of PR-drag, we find that the motion of a particle near the equilibrium points $L_{6,7}$ is stable in both the binary systems for a specific range of β_1 values. The PR-drag is shown to cause instability of the various out of plane equilibrium points in these binary systems.

Key words. Radiation—Poynting–Robertson drag—binary stellar system—equilibrium points—stability.

1. Introduction

The photo-gravitational circular restricted three-body problem was first studied by Radzievskii (1950, 1953). In this work, besides the coplanar libration points L_i, $i = 1$ to 5, the effect of radiation was shown to result in the libration points $L_{6,7}$ that exist in a plane perpendicular to the orbital plane of the radiating primaries. Since then several authors (cf. Chernikov 1970; Perezhogin 1976; Scheurman 1980; Simmons *et al.* 1985; Ragos & Zagouras 1988; Murray 1994; Ragos & Zafiropoulos 1995; Ragos *et al.* 1995; Roman 2001; Kunitsyn & Chudayeva 2003; Kushvah & Ishwar 2004; Das *et al.* 2008a) extended the work to understand various issues related to the dynamics of a particle around radiating primaries. However, majority of these works involve the use of independent quantities $q_1 = 1 - \beta_1$ and $q_2 = 1 - \beta_2$, where β_i corresponds to the ratio of radiation pressure force to the gravitational force of i-th binary component. Since β_i does depend on the size, density of the particle and mass and luminosity of the respective binary component, we apply a realistic relation connecting the parameters β_1 and β_2 and study the location and stability of out of plane equilibrium points

of a micron size particle moving around a radiating binary stellar system. Incorporating the PR-drag effect, we observe that the libration points $L_{6,7}$ exist for certain range of values of β_1 for the binary systems *Krüger*-60 and *RW-Monocerotis*. Further, certain β_1 values exist for which it is also possible to have four libration points, i.e., L_i, $i = 6, 7, 8, 9$ in these binary stars. Using linear stability analysis, it is observed that the stability of motion around any of these points depends on the parameter β_1 and β_2 involving physical parameters, i.e., mass and luminosity of the given binary system. For the binary stellar systems considered here, we find that all such equilibrium points are unstable. However, in the absence of PR-drag we observe that it is possible to have linearly stable motion around $L_{6,7}$ for certain β_1 values in both the binary systems.

2. The location and stability of out of plane equilibrium points

Following Ragos & Zafiropoulos (1995) and Ragos *et al.* (1995) the equation of motion of an infinitesimal mass moving in the radiation and gravitational field of the binary system, in a rotating barycentric co-ordinate system (cf. Szebeheley 1967; Hénon 1983), could be written as:

$$\ddot{X} - 2\dot{Y} = \Omega_x, \quad \ddot{Y} + 2\dot{X} = \Omega_y, \quad \ddot{Z} = \Omega_z, \tag{1}$$

where

$$\begin{aligned}
\Omega_x = {} & X - \frac{Q_1(X+\mu)}{r_1^3} - \frac{Q_2(X+\mu-1)}{r_2^3} \\
& - \frac{W_1}{r_1^2}\left[\frac{X+\mu}{r_1^2}((X+\mu)\dot{X} + Y\dot{Y} + Z\dot{Z}) + \dot{X} - Y\right] \\
& - \frac{W_2}{r_2^2}\left[\frac{X+\mu-1}{r_2^2}((X+\mu-1)\dot{X} + Y\dot{Y} + Z\dot{Z}) + \dot{X} - Y\right] \qquad (2) \\
\Omega_y = {} & Y\left(1 - \frac{Q_1}{r_1^3} - \frac{Q_2}{r_2^3}\right) \\
& - \frac{W_1}{r_1^2}\left[\frac{Y}{r_1^2}((X+\mu)\dot{X} + Y\dot{Y} + Z\dot{Z}) + \dot{Y} + X + \mu\right] \\
& - \frac{W_2}{r_2^2}\left[\frac{Y}{r_2^2}((X+\mu-1)\dot{X} + Y\dot{Y} + Z\dot{Z}) + \dot{Y} + X + \mu - 1\right] \qquad (3) \\
\Omega_z = {} & \left[-\frac{Q_1}{r_1^3} - \frac{Q_2}{r_2^3}\right] Z \\
& - \frac{W_1}{r_1^2}\left[\frac{Z}{r_1^2}((X+\mu)\dot{X} + Y\dot{Y} + Z\dot{Z}) + \dot{Z}\right] \\
& - \frac{W_2}{r_2^2}\left[\frac{Z}{r_2^2}((X+\mu-1)\dot{X} + Y\dot{Y} + Z\dot{Z}) + \dot{Z}\right] \qquad (4)
\end{aligned}$$

$$\mu = \frac{M_2}{M_1 + M_2}, \quad Q_1 = q_1(1-\mu), \quad Q_2 = q_2\mu, \tag{5}$$

$$W_1 = \frac{(1-q_1)(1-\mu)}{C_d}, \quad W_2 = \frac{(1-q_2)\mu}{C_d}, \tag{6}$$

$$r_1^2 = (X+\mu)^2 + Y^2 + Z^2, \quad r_2^2 = (X+\mu-1)^2 + Y^2 + Z^2. \tag{7}$$

Here, M_1 and M_2 refer to masses of the respective binary component; $C_d = c/v_{\text{in}}$ corresponds to the dimensionless velocity of light and depends on the physical masses of primaries and distance between them; $q_{1,2} = 1 - \beta_{1,2}$ corresponds to radiation parameters from the respective primaries; r_1 and r_2 correspond to the distances between the third body and primaries. Further, β_i corresponds to the ratio of force due to radiation and the gravitational force of the i-th binary component (cf. Das *et al.* 2008b) from the i-th binary component. It is important to note that for solar dust particles less than a μm comprising spherical silicate BPCA, carbon BPCA, silicate compact, asteroidal dust, young and cometary dust grains, β may vary in the range $\sim 10^{-2}$–5.0 (cf. Wilck & Mann 1996; Krivov *et al.* 1998; Kimura *et al.* 2002). Therefore in a real situation, it is possible to have $\beta_i \geq 1$. However, there exists a relation:

$$\beta_2 = \beta_1 \frac{L_2}{L_1}\frac{M_1}{M_2}, \tag{8}$$

which connects the radiation parameters of respective binary components in terms of their luminosities and masses. We use the above relation to fix the value of the parameter β_2 in terms of the mass and luminosity of the binary components for a given $\beta_1 > 1$. Therefore, the quantities q_1 and q_2 are not independent. It may be noted that several authors (cf. Ragos & Zafiropoulos 1995; Ragos *et al.* 1995 and references quoted therein) have used the radiation parameters q_1 and q_2 as independent. It is in this sense their results are of limited applicability to the motion of a particle in stellar binary systems in general. Besides the classical coplanar equilibrium points (cf. Ragos & Zafiropoulos 1995; Das *et al.* 2008b), it is possible to have out of plane equilibrium points exclusively due to radiation from binary components. Such points do not have any classical analogue. In the following, we discuss the effect of radiation on the location and stability of possible equilibrium points in two steps. First only the major radial component of the pressure force is considered so that the problem is reduced to that of a central force only (cf. Radzievskii 1950, 1953). In fact this approach to the problem is already an approximate one: for particles with velocity $\mathbf{v}$, terms of order $\mathbf{v}/c$ and higher in the general radiation force term are neglected. In fact, due to radiation, the radiation force F on a particle may be written as $F = F_p + F_{PR}$ (cf. Robertson 1937) where F_{PR} is the Poynting–Robertson drag and corresponds to a first order term in $\mathbf{v}/c$. For a 1 μm dust particle at a distance of 1 AU from sun $F_{PR}/F_P \sim 10^{-4}$ and therefore significant changes in the location of various equilibrium points are unlikely by the inclusion of F_{PR} terms. However, the inclusion of F_{PR} drag term change the nature of problem from purely a central force to a dissipative one. Therefore, in the second step, we incorporate F_{PR} term as well and show that the various out-of plane equilibrium points of the binary system become unstable.

2.1 *Location and stability of equilibrium points in the absence of PR-drag*

In the absence of PR-drag, the stationary solutions of equation (1), for the case $Z \neq 0$, results in the following conditions:

$$X_0 - \frac{Q_1(X_0+\mu)}{r_{10}^3} - \frac{Q_2(X_0+\mu-1)}{r_{20}^3} = 0, \tag{9}$$

$$Y_0 = 0, \tag{10}$$

$$\left[\frac{Q_1}{r_{10}^3} + \frac{Q_2}{r_{20}^3}\right] = 0, \tag{11}$$

where

$$r_{10}^2 = (X_0+\mu)^2 + Z_0^2, \quad r_{20}^2 = (X_0+\mu-1)^2 + Z_0^2 \tag{12}$$

and the subscript '0' is used to denote the equilibrium values. Since $Z_0 \neq 0$, we observe that equations (9)–(11) are satisfied if:

$$X_0 = \frac{Q_1}{r_{10}^3} = -\frac{Q_2}{r_{20}^3}. \tag{13}$$

Obviously the last equation results in either $Q_1 < 0,\ Q_2 > 0$ or $Q_1 > 0,\ Q_2 < 0$, i.e., $Q_1 Q_2 < 0$. In view of the relation $q_{1,2} = 1 - \beta_{1,2}$, we observe that $Q_1 Q_2 < 0$ implies that either $\beta_1 > 1,\ \beta_2 < 1$ or $\beta_1 < 1,\ \beta_2 > 1$. Since for particles around $0.1\ \mu$m it is possible to have $\beta_1 > 1$, we find the possibilities of having $(1-\beta_1) < 0$ and $(1-\beta_2) > 0$ in some binary stellar system.

On elimination of Z_0, we may rewrite equation (13) as:

$$\Phi(X_0) = 8X_0^5 + 12(2\mu-1)X_0^4 + 6(2\mu-1)^2 X_0^3 + (2\mu-1)^3 X_0^2 - (Q_1^{2/3} - Q_2^{2/3})^3 = 0. \tag{14}$$

The solution of equation (14) for real X_0 along with real Z_0 obtained from:

$$Z_0 = \pm\left[\left(\frac{Q_1}{X_0}\right)^{2/3} - (X_0+\mu)^2\right]^{1/2}, \tag{15}$$

using equation (12), provides the equilibrium point in the X–Z plane.

It is readily observed that $X_0 = (1-2\mu)/2$ is a solution of equation (14) in case $|Q_1| = |Q_2|$. Further, from the plot of $\Phi(X_0)$ *vs.* X_0 (cf. Fig. 1), we observe that for certain β_1 value, if $|Q_1| < |Q_2|$ or $|Q_1| > |Q_2|$, only one real solution of equation (14) occurs in the region $X_0 < 0$ and $X_0 > 0$, respectively for *Krüger*-60 (curves 1 and 3 of Fig. 1). The equilibrium point $(X_0, 0, \pm Z_0)$ lying in the region $X_0 < 0$ and referred to as $L_{6,7}$ (cf. Radzievskii 1953) was shown to exist for a range of values of β_1 for binary system *RW-Monocerotis* and *Krüger*-60 (Das *et al.* 2008b). However, it is interesting to observe that for certain β_1 values three possible real root occurs (curve 2, Fig. 1). Of these three roots, one lies in the region $X_0 < 0$, and two roots in the region $X_0 > 0$. For such β_1 values, the root of equation (14) lying in the region $X_0 < 0$ results in

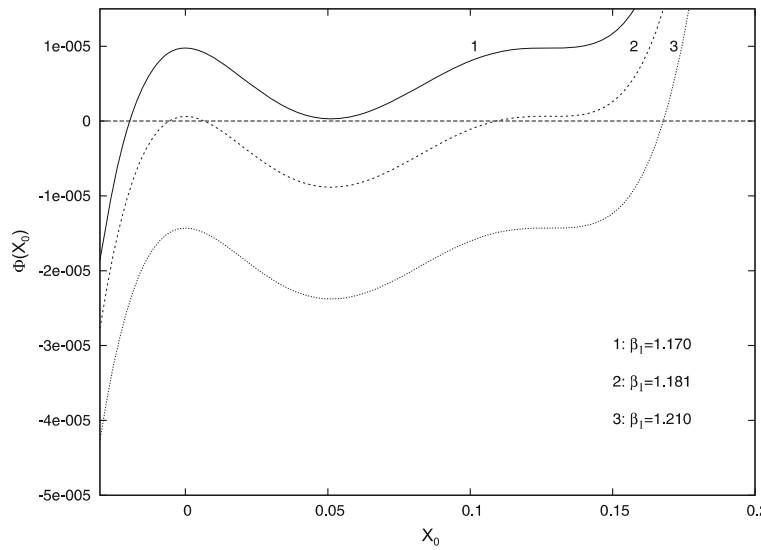

Figure 1. Variation of $\Phi(X_0)$ with X_0 in *Krüger*-60.

two equilibrium points $L_{6,7}$ while the two roots in the region $X_0 > 0$ provide four equilibrium points L_6, L_7, L_8 and L_9 for the two binary systems considered here. Earlier Lukyanov (1984) and Simmons *et al.* (1985) reported the possible existence of such equilibrium points in the general photo-gravitational restricted circular three-body problem in the absence of PR-drag. It may be noted that the application of equation (8) as a relation between β_i's ($i = 1, 2$) results in the location of various equilibrium points dependent on a single parameter β_1 rather than two independent parameters β_1 and β_2 considered earlier by Lukyanov (1984), Simmons *et al.* (1985) and Ragos & Zagouras (1988). Further since β_2 depends not only on β_1 but also on the physical parameters like mass and luminosity of the binary components, the present computational results of Fig. 2 showing the relationship between various components of L_6 and L_8 along with their variation with β_1 are expected to be more realistic for *Krüger*-60 and *RW-Monocerotis*.

In this work we have confined ourselves to linear stability analysis. The characteristic equation used for computing the eigenvalues for a given binary system is same as in Das *et al.* (2008b). Table 1 listing the real and imaginary components of the characteristic equation for various β_1 values for both the binary system clearly shows the possibility of having stable motion around $L_{6,7}$ in the domain $X_0 > 0$ (as all the eigen values are purely imaginary). However, the motion around $L_{6,7}$ in the domain $X_0 < 0$ is unstable. Further for all β_1 values considered, the motion around $L_{8,9}$ is also found to be unstable in these binary systems.

2.2 *Location and stability of the out of plane equilibrium points in the presence of PR-drag*

Following Ragos *et al.* (1995), we find the out of plane equilibrium points in the presence of PR-drag as solution of the following equations.

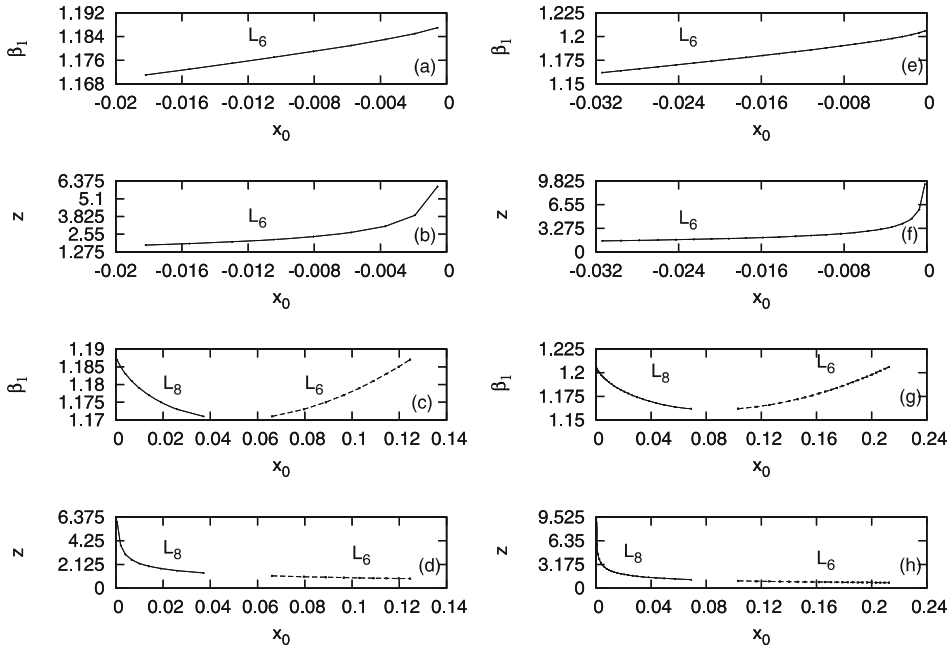

Figure 2. **(a), (e)** Variation of L_{6_x} with β_1 in the region $X_0 < 0$, **(b), (f)** variation of L_{6_z} with L_{6_x} in the region $X_0 < 0$, **(c), (g)** variation of L_{8_x} and L_{6_x} with β_1 in the region $X_0 > 0$, **(d)–(h)** variation of L_{8_z} and L_{6_z} with L_{6_x} in the region $X_0 > 0$ for *Krüger*-60 and *RW-Monocerotis*, respectively.

Table 1. Variation of eigenvalues of $L_{6,7}$ with β_1 for $X_0 > 0$.

Binary	β_1	λ_1	λ_2	λ_3
RW-Monocerotis	1.162	(0, 0.36217024)	(0, 0.84961841)	(0, 1.0709721)
	1.164	(0, 0.42888167)	(0, 0.76875324)	(0, 1.1068328)
	1.166	(0, 0.50137373)	(0, 0.68684667)	(0, 1.1299850)
Krüger-60	1.171	(0, 0.19666655)	(0, 0.92009171)	(0, 1.0558189)
	1.177	(0, 0.29345436)	(0, 0.79985195)	(0, 1.1287698)
	1.183	(0, 0.37515521)	(0, 0.70016981)	(0, 1.1700516)
	1.187	(0, 0.45360428)	(0, 0.61042658)	(0, 1.1923181)

$$X_0 - \frac{Q_1(X+\mu)}{r_1^3} - \frac{Q_2(X_0+\mu-1)}{r_2^3} + \left[\frac{W_1}{r_1^2} + \frac{W_2}{r_2^2}\right] Y_0 = 0, \tag{16}$$

$$\left[1 - \frac{Q_1}{r_1^3} - \frac{Q_2}{r_2^3}\right] Y_0 - \frac{W_1(X_0+\mu)}{r_1^2} - \frac{W_2(X_0+\mu-1)}{r_2^2} = 0, \tag{17}$$

$$\frac{Q_1}{r_1^3} + \frac{Q_2}{r_2^3} = 0. \tag{18}$$

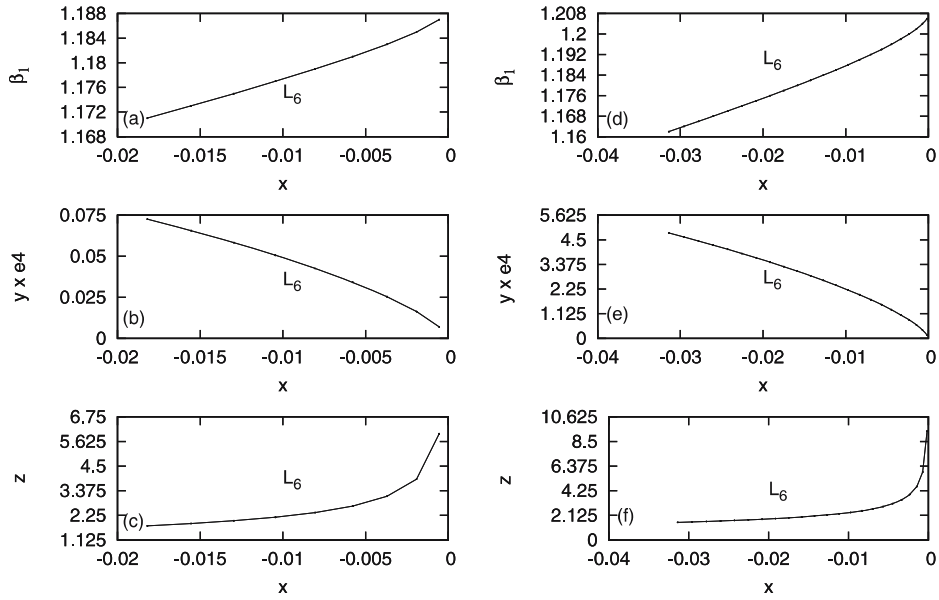

Figure 3. **(a), (d)** Variation of L_{6_x} with β_1; **(b), (e)** variation of L_{6_y} with L_{6_x}; **(c), (f)** variation of L_{6_z} with L_{6_x} in the region $X < 0$ for *Krüger*-60 and *RW-Monocerotis*, respectively.

The foregoing equations could be easily obtained by considering $\ddot{X} = \ddot{Y} = \ddot{Z} = 0$, $\dot{X} = \dot{Y} = \dot{Z} = 0$ in equation (1). Using the last equation, we note that $Q_1 Q_2 < 0$ or $q_1 q_2 < 0$ must be satisfied for the existence of the out of plane equilibrium points. Further, it may be observed that the presence of PR-drag results in the possibility of having $Y \neq 0$, unlike the situation discussed in section 2.2. From equations (17)–(19), we find that:

$$P(r_1) = a_6 r_1^6 + a_4 r_1^4 + a_2 r_1^2 + a_1 r_1 + a_0 = 0, \tag{19}$$

$$X_0 = \frac{1}{2}\left[1 - \left(\frac{Q_2}{Q_1}\right)^{2/3}\right] r_1^2 + \frac{1}{2} - \mu, \tag{20}$$

$$Y_0 = \frac{1}{2}\left[W_1 - W_2\left(\frac{Q_1}{Q_2}\right)^{2/3}\right] r_1^{-2}, \\ + \frac{1}{2}\left[W_1 - W_2 - \left(W_1\left(\frac{Q_2}{Q_1}\right)^{2/3} - W_2\left(\frac{Q_1}{Q_2}\right)^{2/3}\right)\right], \tag{21}$$

$$Z_0 = \pm\sqrt{r_1^2 - (X_0 + \mu)^2 - Y^2}. \tag{22}$$

Using equation (8) and the foregoing equations with coefficients $a_i, i = 0, 1, 2, 4, 6$ as defined in Ragos *et al.* (1995), we have computed the co-ordinates X_0, Y_0, and Z_0 for the out of plane equilibrium points of a binary system. In the presence of PR-drag also we observe that a critical β_1 exists for which it is possible to have two equilibrium

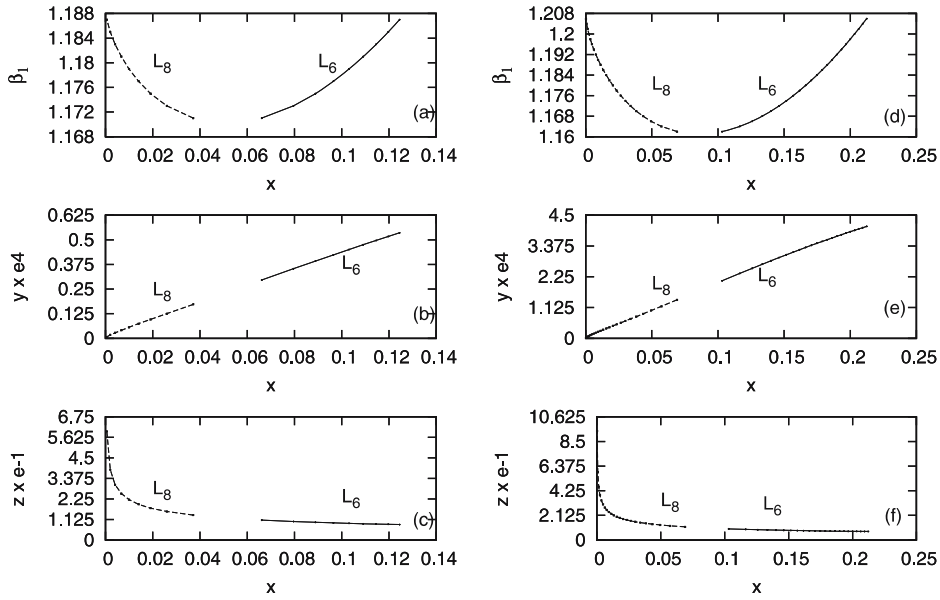

Figure 4. **(a), (d)** Variation of L_{6_x} and L_{8_x} with β_1; **(b), (e)** variation of L_{8_y} and L_{6_y} with L_{6_x}; **(c), (f)** variation of L_{8_z} and L_{6_z} with L_{6_x} in the region $X > 0$ for *Krüger*-60 and *RW-Monocerotis*, respectively.

points $L_{6,7}$ in the region $X_0 < 0$ and four equilibrium points, i.e., $L_{6,7,8,9}$ in the region $X > 0$. Figure 3(a) clearly shows that L_{6_x} increases with increase in β_1 in the region $X < 0$. In such a region, for *Krüger*-60, an increase in X_0 is accompanied by a decrease in Y while there is an increase in the Z values (Fig. 3b-c). Similar results are obtained for *RW-Monocerotis* (Fig. 3d–f). In the region $X > 0$, for *Krüger*-60 an increase in β_1 results in a decrease in the values of L_{8_x} while L_{6_x} increases (Fig. 4a). Further, it is observed that with increase in L_{6_x}, L_{8_y} and L_{6_y} increases while L_{8_z} and L_{6_z} decrease (Fig. 4b–c) in *Krüger*-60. For the binary system *RW-Monocerotis* we observe similar trends in variation of L_6 and L_8 co-ordinates (Fig. 4d–f).

The inclusion of PR-drag induces instability in motion. This is evident from the fact that all the roots of the characteristic equation for equilibrium points $L_{6,7,8,9}$ in entire domain considered here have finite (non-zero) real and imaginary components.

3. Results

The problem concerning the location of out of plane equilibrium points in the photo-gravitational restricted three-body problem has been investigated. We have incorporated the effect of PR-drag in our analysis. Unlike the work of Ragos *et al.* (1995) (and references quoted therein), we considered a realistic relation connecting the parameters β_1 and β_2 with the physical parameters such as mass and luminosity of the binary components and investigated the locations of equilibrium points and their stability using linear analysis for the binary systems *Krüger*-60 and *RW-Monocerotis*. In the absence of PR-drag unlike Roman (2001), we observe that the equilibrium points $L_{6,7}$ exist for several values of $\beta_1 > 1$ for $X_0 < 0$ in both the binary systems in the X–Z

plane. We also find that for $|Q_1| < |Q_2|$, there exists a range of β_1 for which it is also possible to have four equilibrium points L_6, L_7, L_8 and L_9 for $X_0 > 0$ in both the binaries. Increase in β_1 results in an increase in L_{6_x} while L_{8_x} tends to decrease in the region $X_0 > 0$ for both the binary systems in the absence of PR-drag. Further in the absence of PR-drag in both binary systems the components L_{8_z} and L_{6_z} show a decreasing trend with increase in L_{8_x} and L_{6_x} respectively. Similar trends are observed when PR-drag is incorporated in the analysis. However, inclusion of PR-drag in the analysis results in a small but finite y-component to the possible equilibrium points of the system. It is observed that both L_{8_y} and L_{6_y} increase with increase in L_{8_x} and L_{6_x}, respectively in both the binaries.

References

Chernikov, Yu. A. 1970, *Sov. Astronomy,* **14**, 176.
Das, M. K., Narang, P., Yuasa, M., Saha, L. M. 2008a, *Astrophys. Space Sci.*, **314**, 59.
Das, M. K., Narang, P., Mahajan, S., Yuasa, M. 2008b, *Astrophys. Space Sci.*, **314**, 261.
Hénon, M. 1983, Les Houches, Session XXXVI, p 54.
Kimura, H., Okamoto, H., Mukai, T. 2002, *Icarus*, **157**, 349.
Krivov, A., Kimura, H., Mann, I. 1998, *Icarus*, **134**, 311.
Kunitsyn, A. L., Chudayeva, A. M. 2003, *J. Appl. Maths. Mechs.*, **67**, 647.
Kushvah, B. S., Ishwar, B. 2004, *Bull. Cal. Math. Soc.*, **12**, 109.
Lukyanov, L. G. 1984, *Sov. Astron.*, **28**, 462.
Murray, C. D. 1994, *Icarus*, **112**, 465.
Perezhogin, A. A. 1976, *Sov. Astron. Lett.*, **2**, 174.
Radzievskii, V. V. 1950, *Astron. Zh*, **27**, 250.
Radzievskii, V. V. 1953, *Astron. Zh*, **30**, 265.
Ragos, O., Zafiropoulos, F. A. 1995, *Astron. Astrophys.*, **300**, 568.
Ragos, O., Zafiropoulos, F. A., Vrahatis, M. N. 1995, *Astron. Astrophys.*, **300**, 579.
Ragos, O., Zagourous, C. 1988, *CMeDA*, **44**, 135.
Robertson, H. P. 1937, *Mon. Not. Roy. Astron. Soc.*, **97**, 423.
Roman, R. 2001, *Astrophys. Space Sci.*, **275**, 425.
Schuerman, D. W. 1980, *ApJ*, **238**, 337.
Simmons, J. F. L., McDonald, A. J. C., Brown, J. C. 1985, *Cm*, **35**, 145.
Szebeheley, V. 1967, *Theory of Orbits*, Academic Press.
Wilck, M., Mann, I. 1996, *Planet. Space Sci.*, **44**, 493.
Zhou, H. N., Leung, K. C. 1988, *Astrophys. Space Sci.*, **141**, 257.

J. Astrophys. Astr. (2009) **30,** 187–205

Analytical Treatment of the Two-Body Problem with Slowly Varying Mass

W. A. Rahoma*, F. A. Abd El-Salam & M. K. Ahmed
Cairo University, Faculty of Science, Department of Astronomy, Cairo, Egypt.
**e-mail: walid_rahoma@yahoo.com*

Received 2008 March 6; accepted 2009 September 1

Abstract. The present work is concerned with the two-body problem with varying mass in case of isotropic mass loss from both components of the binary systems. The law of mass variation used gives rise to a perturbed Keplerian problem depending on two small parameters. The problem is treated analytically in the Hamiltonian frame-work and the equations of motion are integrated using the Lie series developed and applied, separately by Delva (1984) and Hanslmeier (1984). A second order theory of the two bodies eject mass is constructed, returning the terms of the rate of change of mass up to second order in the small parameters of the problem.

Key words. Mass loss—binary systems—two-body problem—perturbations.

1. Introduction

The two-body problem with variable mass is one of long-standing; its origin going back to the middle of 19th century. However, some confusion has persisted as to the dynamical equations which have to be used. Solutions of celestial mechanics problems for several variable mass bodies have been analytically tried and solved for two basic situations: the general two-body problem and the restricted three-body problem, with many modifications. The mathematical tool applied to these two basic problems usually relies upon the classical equations of motion in gravitational field with additional formal terms due to the variability of the gravitating masses. The motion is studied with the already classical procedure that interprets these terms as distinct fictitious perturbations applied to the unperturbed motion of stationary masses. There exists a related inverse procedure: interpretation of the actual perturbed motion as a formally unperturbed one, in the gravitational field generated by a variable effective mass. In this paper, we limit ourselves to the first basic problem (that of two variable-mass bodies).

2. History of the problem

The literature is full of research dealing with the problem of two-body with varying mass, and it will be beneficial to sketch some of these most important works.

Jeans (1924) was the first to pose this as an astrophysical problem basing his studies on the relationship between luminosity and star mass developed by Eddington (1924).

MacMillan (1925) introduced the detailed solution for the equation of the relative motion obtained by Mestscherskii.

Martin (1934) concluded that the eccentricity behaviour increases secularly if the mass loss of the binary star is inversely proportional to a distance power between its components.

Hadjidemetriou (1963) used Duboshin's idea of a formal comparison between the unperturbed equations in the Gylden–Meshcherskii problem and the perturbed Keplerian equations of motion in the gravitational field of a stationary mass with permanent tangential perturbation to calculate the perturbation arising from the isotropic variation of the mass of the system.

Mukhametkalieva (1987, 1988) investigated the behaviour of the eccentricity in this problem based on a representation of the eccentricity as a function of time and a periodic function of the true anomaly. Also, he obtained the Laplace integral for the Gylden problem.

Mioc *et al.* (1988a, 1988b, 1988c, 1988d), in a series of papers, covered the energy characteristics of motion in a two-body problem with variable mass.

Verhulst (1972, 1975), Hut & Verhulst (1976), Vinti (1977), Omarov & Omarkulov (1982), Omarov (1991), Minglibaev (1988), Demchenko & Omarov (1984), and Idlis & Omarov (1960) constructed analogous solutions to the Gylden problem for stationary masses in the presence of environmental resistance and quasi-elastic forces with various methods, including the Hamilton–Jacobi method. These works dealt with modeling various systems of osculating elements, discussing the structures of the intermediate motions, discussing the energy dissipation regimes combined with the influence of the elastic force, searching for the integrable cases, and discussing the feasibility of canonical transformation and Hamiltonian formalism including the case of nonconservative binary systems.

Dommangent (1963, 1964, 1981, 1982, 1997) published useful papers in which he stated that a correlation between eccentricities and orbital periods exists, such that on the average, a bigger eccentricity corresponds to a bigger period. Also, he suggested that this correlation is related to a substantial mass loss in the binary star components.

Prieto & Docobo (1997a, 1997b) and Docobo *et al.* (1999) published a series of papers in which they presented two approximate analytic solutions of the two-body problem with slowly decreasing mass, using Deprit's method of perturbations. They used Jeans law which give rise to a perturbed Keplerian problem dependent on one and two small parameters.

Andrade & Docobo (2002, 2003) analyzed the dynamics of binary systems with time-dependent mass loss and periastron effect, i.e., a supposed enhanced mass loss during periastron passage, by means of analytical and numerical techniques.

3. Different models of the mass loss

Since both the relative rate of mass change and the time intervals for this change must be included into the equations of motion, here below some interesting models of the rate of mass changes are addressed.

3.1 *Mestscherskii models*

Mestscherskii was the first to point out a specific case of the two-body problem with varying mass which is integrable by introducing special space–time variables in which

the problem is reduced to the classical problem of two bodies (Polyakhova 1994; Prieto & Docobo 1997a, 1997b).

These integrable cases correspond to three celebrated models by Mestscherskii for the change in the total mass of the system.

$$\mu_1(t) = \frac{1}{a + \alpha t} \tag{1}$$

$$\mu_2(t) = \frac{1}{\sqrt{a + \alpha t}} \tag{2}$$

$$\mu_3(t) = \frac{1}{\sqrt{a + \alpha t + \beta t^2}} \tag{3}$$

where a, α, β are certain constants and $\mu_i(t)(= m_1(t) + m_2(t))$, $i = 1, 2, 3$ are different models for the mass change.

3.2 *Martin model*

Martin (1934) from his work on double star systems with varying mass, reached to this statement,

$$\dot{m} = -\frac{\alpha m^n}{r^2} \tag{4}$$

where r is the value of radius vector between the two components of the system.

Hadjidemetriou (1966) addressed useful comments on the Martin model of varying mass. These are:

- The dependence of the rate of mass loss on the distance between the two components must be due to a tidal interaction, but since μ is the total mass of the system, this law states that the tidal interaction is independent of the ratio of the masses of the two components which does not seem realistic.
- The effect of one star on its mass-losing companion would most probably result in a non-isotropic loss of mass; and consequently, the treatment of the problem by usual methods is not valid.
- The tidal interaction is not likely to produce large velocities of ejection of mass, so that the ejected particles may not escape from the system instead, full on the other star.

For this reasons, such laws must be treated with great care and in close connection with the mechanism the mass loss takes place.

3.3 *Jeans models*

Jeans (1924) was the first to pose law of varying mass as an astrophysical problem. He based his studies on the theory developed by Eddington (mass-luminosity relation) by generalized law of mass loss:

$$\dot{m} = -\alpha m^n \tag{5}$$

where α, n are real numbers, the first one is $+ve$ approximate to zero and n varying between 1.4 and 4.4. This law is called Eddington–Jeans law.

Taking $n = 2$, we have Mestscherskii first integrable case, while taking $n = 3$, we have the last Mestscherskii case.

3.4 *Andrade and Docobo models*

Analyzing the dynamics of binary systems with time-dependent mass loss, the interaction between the two components must be taken into account. Andrade & Docobo (2003) could suppose that, close to periastron there is an appreciable enhancement of mass loss. This phenomenon will be called the periastron effect, and it will be more noticeable the greater the eccentricity and the smaller the minimum distance between the two stars.

Of the whole set of laws that take into account periastron effect by means of its dependence on distance, only some of them give rise to new behaviour in the evolution of the orbital elements, such as secular variations of eccentricity.

In these models they studied the following time- and distance-dependent mass-loss law:

$$\dot{\mu}(t; r; p_\theta) = \dot{\mu}(t) - \beta \frac{p_\theta}{r^2} \tag{6}$$

where the first term represent time-dependent mass loss, and the last one introduces the periastron effect, where r is the distance between the two components, p_θ is the total angular momentum and β is another small parameter close to zero.

4. Perturbation technique

In many cases in celestial mechanics, the series development of the disturbing function is not easily treated and is complicated. To avoid this difficulty we use an alternative approach (Delva 1984; Hanslmeier 1984) in which the procedure can be performed with an operator. A special linear differential operator, the Lie operator, produces a Lie series. The convergence of the series is the same as for Taylor series, since the series is only another analytical form of the Taylor series. In addition, we can change the step size easily (if necessary).

Let $\mathcal{H}(x, y, p_x, p_y, t)$ be the Hamiltonian function, x, y be the co-ordinates, p_x, p_y be the momenta, and t be the time. Then the equations of motion are:

$$\dot{x} = \frac{dx}{dt} = \frac{\partial \mathcal{H}}{\partial p_x} \qquad \dot{p}_x = \frac{dp_x}{dt} = -\frac{\partial \mathcal{H}}{\partial x},$$

$$\dot{y} = \frac{dy}{dt} = \frac{\partial \mathcal{H}}{\partial p_y} \qquad \dot{p}_y = \frac{dp_y}{dt} = -\frac{\partial \mathcal{H}}{\partial y}.$$

The linear Lie operator has the general form:

$$D = \frac{dx}{dt}\frac{\partial}{\partial x} + \frac{dy}{dt}\frac{\partial}{\partial y} + \frac{dp_x}{dt}\frac{\partial}{\partial p_x} + \frac{dp_y}{dt}\frac{\partial}{\partial p_y} + \frac{\partial}{\partial t} \tag{7}$$

and the solution $\vec{x}(x, y, p_x, p_y, t)$, $\vec{y}(x, y, p_x, p_y, t)$, $\overrightarrow{p_x}(x, y, p_x, p_y, t)$, and $\overrightarrow{p_y}(x, y, p_x, p_y, t)$ are then given by the Lie series:

$$\vec{x}(x, y, p_x, p_y, t) = [\{\exp(t - t_0)D\}x]_{\vec{x}=\overrightarrow{x_0}} = \sum_{j=0} [D^j \vec{x}]_{\overrightarrow{x_0}} \frac{(t - t_0)^j}{j!} \tag{8}$$

$$\vec{y}(x, y, p_x, p_y, t) = [\{\exp(t - t_0)D\}y]_{\vec{y}=\overrightarrow{y_0}} = \sum_{j=0} [D^j \vec{y}]_{\overrightarrow{y_0}} \frac{(t - t_0)^j}{j!} \tag{9}$$

$$\overrightarrow{p_x}(x, y, p_x, p_y,) = [\{\exp(t - t_0)D\}p_x]_{\overrightarrow{p_x}=\overrightarrow{p_{x_0}}} = \sum_{j=0} [D^j \overrightarrow{p_x}]_{\overrightarrow{p_{x_0}}} \frac{(t - t_0)^j}{j!} \tag{10}$$

$$\overrightarrow{p_y}(x, y, p_x, p_y, t) = [\{\exp(t - t_0)D\}p_y]_{\overrightarrow{p_y}=\overrightarrow{p_{y_0}}} = \sum_{j=0} [D^j \overrightarrow{p_y}]_{\overrightarrow{p_{y_0}}} \frac{(t - t_0)^j}{j!} \tag{11}$$

where $D^j \vec{x}$, $D^j \vec{y}$, $D^j \overrightarrow{p_x}$, and $D^j \overrightarrow{p_y}$ are to be evaluated for the initial conditions $\overrightarrow{x_0}(x_0, y_0, p_{x_0}, p_{y_0}, t_0)$, $\overrightarrow{y_0}(x_0, y_0, p_{x_0}, p_{y_0}, t_0)$, $\overrightarrow{p_{x_0}}(x_0, y_0, p_{x_0}, p_{y_0}, t_0)$, and $\overrightarrow{p_{y_0}}(x_0, y_0, p_{x_0}, p_{y_0}, t_0)$.

5. Hamiltonian

The Hamiltonian is constructed in terms of Delaunay's variables as:

$$\mathcal{K} \equiv \mathcal{K}(l, L, G; t) = -\frac{1}{2}\frac{\mu^2}{L^2} + \frac{\dot{\mu}}{\mu} Le \sin E \tag{12}$$

Equation (12) was already obtained by Deprit (1983), where $\mathcal{H}$ is the Hamiltonian of the two-body problem.

The equations of motion can be analytically integrated up to the second order of perturbation using the Deprit's method (1969) or Kamel method (1969).

We need first to expand the Hamiltonian function (12) in a small parameter ε using Jeans law of mass:

$$\dot{m}_k = -\alpha_k m_k^{n(k)}, \quad k = 1, 2 \tag{13}$$

For $\varepsilon = 0$, the Keplerian case would be obtained.

It seems that the parameter ε should be related to the coefficient α_k which appears in the Jeans law of mass variation. We will simply choose ε as nondimensional value of α_k. This choice also justifies the application of the method as far as the second order only, since α_k is very small and higher order would not contribute significantly. Let the total mass of the binary system be given by $\mu = m_1 + m_2$.

Expanding the function $\mu(t)$ in a Taylor series yields:

$$\mu = \mu_0 - (\alpha_1 m_{10}^{n(1)} + \alpha_2 m_{20}^{n(2)})(t - t_0) + \frac{1}{2}(\alpha_1^2 n(1) m_{10}^{2n(1)-1} + \alpha_2^2 n(2) m_{20}^{2n(2)-1})(t - t_0)^2 \tag{14}$$

where m_{10}, m_{20} are the values of mass for each component in certain initial instant t_0.

The Hamiltonian can now be rewritten in expandable form as:

$$\mathcal{K} = \mathcal{K}_0 + \sum_{n=1}^{2}\sum_{k=1}^{2}\frac{\alpha_k^n}{n!}\mathcal{K}_{nk} - \alpha_1\alpha_2 m_{10}^{n(1)} m_{20}^{n(2)}\left\{\frac{(t - t_0)^2}{L^2} + \frac{2}{\mu_0^2}(t - t_0)eL\sin E\right\} \tag{15}$$

with

$$\mathcal{K}_0 = -\frac{\mu_0^2}{2L^2}$$

$$\mathcal{K}_{11} = m_{10}^{n(1)}\left\{\frac{\mu_0}{L^2}(t - t_0) - \frac{1}{\mu_0}eL\sin E\right\}$$

$$\mathcal{K}_{12} = m_{20}^{n(2)}\left\{\frac{\mu_0}{L^2}(t - t_0) - \frac{1}{\mu_0}eL\sin E\right\}$$

$$\mathcal{K}_{21} = -m_{10}^{2n(1)-1}\left\{\frac{(n(1)\mu_0 + m_{10})}{L^2}(t - t_0)^2 + \frac{2m_{10}}{\mu_0^2}(t - t_0)eL\sin E\right\}$$

$$\mathcal{K}_{22} = -m_{20}^{2n(2)-1}\left\{\frac{(n(2)\mu_0 + m_{20})}{L^2}(t - t_0)^2 + \frac{2m_{20}}{\mu_0^2}(t - t_0)eL\sin E\right\}$$

where $\mathcal{K}_0$ represents the Keplerian part of the problem, $\mathcal{K}_{11}$, $\mathcal{K}_{12}$ represent the first order contributions that come from the first and second body mass loss, $\mathcal{K}_{21}$, $\mathcal{K}_{22}$ represent the second order contributions, while the term factored by $\alpha_1\alpha_2$ represents the coupling effect between the two bodies.

Introduce $\mathcal{X}_i = \alpha_i/\alpha$, $i = 1, 2$.

The Hamiltonian can now be rewritten as:

$$\mathcal{K} = -\frac{\mu_0^2}{2L^2} + \sum_{s=1}^{2}\frac{\alpha^s}{s!}\left\{\tilde{\zeta}_s(L, G)\tau^{s-1}\sin E + \tau^s\tilde{\eta}_s(L)\right\} \tag{16}$$

where

$$\tilde{\zeta}_s(L, G) = (\Phi_s + \Pi_{2(s-1)})eL$$

$$\tilde{\eta}_s(L) = \frac{(\Psi_s + \Pi_{s-1})}{L^2}$$

$$\tau = t - t_0$$

with

$$\Psi_1 = \mu_0(\mathcal{X}_1 m_{10}^{n(1)} + \mathcal{X}_2 m_{20}^{n(2)})$$

$$\Psi_2 = -\mu_0(n(1)\mathcal{X}_1^2 m_{10}^{2n(1)-1} + n(2)\mathcal{X}_2^2 m_{20}^{2n(2)-1}) + \mathcal{X}_1^2 m_{10}^{2n(1)} + \mathcal{X}_2^2 m_{20}^{2n(2)}$$

$$\Phi_1 = -\frac{1}{\mu_0}(\mathcal{X}_1 m_{10}^{n(1)} + \mathcal{X}_2 m_{20}^{n(2)})$$

$$\Phi_2 = -\frac{2}{\mu_0^2}(\mathcal{X}_1^2 m_{10}^{2n(1)} + \mathcal{X}_2^2 m_{20}^{2n(2)})$$

$$\Pi_1 = -2\mathcal{X}_1\mathcal{X}_2 m_{10}^{n(1)} m_{20}^{n(2)}$$

$$\Pi_2 = -\frac{4}{\mu_0^2}\mathcal{X}_1\mathcal{X}_2 m_{10}^{n(1)} m_{20}^{n(2)}$$

$$\Pi_0 = 0.$$

6. Solution of the problem

The non-vanishing final expressions of the variation in the orbital elements can be written as:

$$\dot{l} = \frac{m_0^2}{L^3} + \sum_{s=1}^{2} \frac{\alpha^s}{s!}\tau^{s-1}\left\{\tilde{\zeta}_{s,L}\sin E + \frac{a}{2r}\frac{G^2}{eL^3}\tilde{\zeta}_s \sin 2E + \tau\tilde{\eta}_{s,L}\right\} \tag{17}$$

$$\dot{g} = \sum_{s=1}^{2} \frac{\alpha^s}{s!}\tau^{s-1}\left\{\tilde{\zeta}_{s,G}\sin E - \frac{a}{2r}\frac{G}{eL^2}\tilde{\zeta}_s \sin 2E\right\} \tag{18}$$

$$\dot{L} = -\sum_{s=1}^{2} \frac{\alpha^s}{s!}\tau^{s-1}\left\{\frac{a}{r}\tilde{\zeta}_s \cos E\right\} \tag{19}$$

where

$$\tilde{\zeta}_{s,L} = \frac{\partial\tilde{\zeta}_s}{\partial L} = \frac{1}{e}(\Phi_s + \Pi_{2(s-1)})$$

$$\tilde{\zeta}_{s,G} = \frac{\partial\tilde{\zeta}_s}{\partial G} = -\frac{G}{eL}(\Phi_s + \Pi_{2(s-1)})$$

$$\tilde{\eta}_{s,L} = \frac{\partial\tilde{\eta}_s}{\partial L} = -\frac{2}{L^3}(\Psi_s + \Pi_{s-1}).$$

Since only the mutual gravitational attraction is considered and the mass lost by one body of the system is transferred to its companion, the total mass of the system is kept constant. This turns a constant mean motion $\tilde{n}$.

The linear Lie operator D, in terms of the Delaunay elements, has the general form:

$$D = \frac{dl}{dt}\frac{\partial}{\partial l} + \frac{dg}{dt}\frac{\partial}{\partial g} + \frac{dL}{dt}\frac{\partial}{\partial L} + \frac{dG}{dt}\frac{\partial}{\partial G} + \frac{\partial}{\partial t}.$$

Applying the operator D to l, g, L, G, and t yields:

$$Dl = \frac{dl}{dt} + \frac{\partial l}{\partial t} = \dot{l} + \tilde{n} \tag{20}$$

$$Dg = \frac{dg}{dt} = \dot{g} \tag{21}$$

$$DL = \frac{dL}{dt} = \dot{L} \tag{22}$$

$$DG = \frac{dG}{dt} = 0 \tag{23}$$

$$Dt = 1. \tag{24}$$

The solutions $\vec{l}(l,\ g,\ L,\ G,\ t)$, $\vec{g}(l, g, L, G, t)$, $\vec{L}(l, g, L, G, t)$, and $\vec{G}(l, g, L, G, t)$ are then given in terms of the Lie series as:

$$\vec{l}(l, g, L, G, t) = \sum_{j=0} [D^j \vec{l}]_{\overrightarrow{l_0}} \frac{(t - t_0)^j}{j!} \tag{25}$$

$$\vec{g}(l, g, L, G, t) = \sum_{j=0} [D^j \vec{g}]_{\overrightarrow{g_0}} \frac{(t - t_0)^j}{j!} \tag{26}$$

$$\vec{L}(l, g, L, G, t) = \sum_{j=0} [D^j \vec{L}]_{\overrightarrow{L_0}} \frac{(t - t_0)^j}{j!} \tag{27}$$

$$\vec{G}(l, g, L, G, t) = \sum_{j=0} [D^j \vec{G}]_{\overrightarrow{G_0}} \frac{(t - t_0)^j}{j!} \tag{28}$$

where $D^j\vec{l}$, $D^j\vec{g}$, $D^j\vec{L}$, and $D^j\vec{G}$ are to be evaluated for the initial condition $\overrightarrow{l_0}(l_0,\ g_0,\ L_0,\ G_0,\ t_0)$, $\overrightarrow{g_0}(l_0,\ g_0,\ L_0,\ G_0,\ t_0)$, $\overrightarrow{L_0}(l_0,\ g_0,\ L_0,\ G_0,\ t_0)$, and $\overrightarrow{G_0}(l_0,\ g_0,\ L_0,\ G_0,\ t_0)$. To find the terms of the series, it will be necessary to calculate the multiple action of D to the variables l, g, L, G, and t. The single action to l, g, L, and G produces:

$$Dx = x', \quad x = (l, g, L, G) \tag{29}$$

and hence, the multiple action gives:

$$D^j x = D^{j-1} x', \quad j \geq 1.$$

6.1 *The series for l*

The double action of the Lie operator, D on the mean anomaly l can be computed as:

$$D^2 l = \left(\frac{dl}{dt}\frac{\partial}{\partial l} + \frac{dg}{dt}\frac{\partial}{\partial g} + \frac{dL}{dt}\frac{\partial}{\partial L} + \frac{dG}{dt}\frac{\partial}{\partial G} + \frac{\partial}{\partial t}\right)[\dot{l} + \tilde{n}] \tag{30}$$

Setting

$$\tilde{\zeta}_{s,LL} = -(\Phi_s + \Pi_{2(s-1)})\frac{G^2}{e^3 L^3}$$

$$\tilde{\eta}_{s,LL} = \frac{6}{L^4}(\Psi_s + \Pi_{s-1})$$

equation (30) can be written as:

$$D^2 l = \sum_{n=0}^{5}\sum_{m=0}^{5}\left[\alpha\left(\frac{a}{r}\right)^m \mathcal{W}_{nm}^l \cos nE + \alpha^2\left\{\left[\left(\frac{a}{r}\right)^m \mathcal{Y}_{nm}^l + \mathcal{S}_n^l\right]\sin nE + \tau\left(\frac{a}{r}\right)^m \mathcal{Z}_{nm}^l \cos nE\right\}\right] \tag{31}$$

where the non-vanishing coefficients are:

$$\mathcal{W}_{11}^l = \left(\frac{m_0^2}{L^3}\right)\left[\tilde{\zeta}_{1,L} + \frac{3\tilde{\zeta}_1}{L}\right]$$

$$\mathcal{W}_{13}^l = -\frac{m_0^2 G^2}{4L^6}\tilde{\zeta}_1$$

$$\mathcal{W}_{22}^l = \frac{m_0^2 G^2}{eL^6}\tilde{\zeta}_1$$

$$\mathcal{W}_{33}^l = \frac{m_0^2 G^2}{4L^6}\tilde{\zeta}_1$$

$$\mathcal{S}_1^l = \frac{1}{2}\tilde{\zeta}_{2,L}$$

$$\mathcal{Y}_{12}^l = -\frac{3G^2}{4eL^3}\tilde{\zeta}_1\tilde{\zeta}_{1,L} + \frac{G^2}{4e^3L^4}(1+2e^2)\tilde{\zeta}_1^2$$

$$\mathcal{Y}_{13}^l = -\frac{G^2}{16L^3}\tilde{\zeta}_1\tilde{\zeta}_{1,L}$$

$$\mathcal{Y}_{15}^l = \frac{\mu G^4}{4eL^8}\tilde{\zeta}_1^2$$

$$\mathcal{Y}_{21}^l = \frac{1}{2}\tilde{\zeta}_{1,L}^2 - \frac{1}{2}\tilde{\zeta}_1\tilde{\zeta}_{1,LL} + \frac{G^2}{4eL^3}\tilde{\zeta}_2$$

$$\mathcal{Y}_{22}^l = \frac{1}{4}\left[\frac{G^2}{eL^3}\right]^2\tilde{\zeta}_1^2$$

$$\mathcal{Y}_{23}^{l} = -\frac{G^2}{4L^3}\tilde{\zeta}_1\tilde{\zeta}_{1,L} + \frac{1}{4}\left[\frac{G^2}{eL^3}\right]^2\tilde{\zeta}_1^2$$

$$\mathcal{Y}_{24}^{l} = \frac{\mu}{8L^2}\left[\frac{G^2}{eL^3}\right]^2\tilde{\zeta}_1^2$$

$$\mathcal{Y}_{25}^{l} = -\frac{\mu}{8L^2}\left[\frac{G^2}{eL^3}\right]^2\tilde{\zeta}_1^2$$

$$\mathcal{Y}_{32}^{l} = \frac{G^2}{eL^3}\tilde{\zeta}_1\tilde{\zeta}_{1,L}$$

$$\mathcal{Y}_{34}^{l} = \frac{G^4}{4eL^6}\left[\frac{1}{2e^2L}\left(1+2e^2\right)-1\right]\tilde{\zeta}_1^2$$

$$\mathcal{Y}_{35}^{l} = \frac{G^4}{4eL^6}\tilde{\zeta}_1^2$$

$$\mathcal{Y}_{43}^{l} = \frac{G^2}{16L^3}\tilde{\zeta}_1\tilde{\zeta}_{1,L}$$

$$\mathcal{Y}_{45}^{l} = -\frac{\mu G^4}{8e^2L^8}\tilde{\zeta}_1^2$$

$$\mathcal{B}_{54}^{l} = \frac{G^4}{8eL^6}\tilde{\zeta}_1^2$$

$$\mathcal{Z}_{00}^{l} = \tilde{\eta}_{2,L}$$

$$\mathcal{Z}_{11}^{l} = \tilde{\eta}_{1,L}\tilde{\zeta}_{1,L} - \tilde{\zeta}_1\tilde{\eta}_{1,LL} + \frac{m_0^2}{2L^3}\left(\tilde{\zeta}_{2,L} + \frac{3}{L}\tilde{\zeta}_2\right)$$

$$\mathcal{Z}_{13}^{l} = -\left(\frac{G_1^2}{4L^3}\tilde{\eta}_{1,L}\tilde{\zeta} - \frac{m_0^2}{8L^6}\tilde{\zeta}_2\right)$$

$$\mathcal{Z}_{22}^{l} = \frac{G^2}{eL^3}\left[\tilde{\zeta}_1\tilde{\eta}_{1,L} + \frac{m_0^2}{2L^3}\tilde{\zeta}_2\right]$$

$$\mathcal{Z}_{33}^{l} = \frac{G^2}{4L^3}\left[\tilde{\zeta}_1\tilde{\eta}_{1,L} + \frac{m_0^2}{2L^3}\tilde{\zeta}_2\right]$$

which can be rewritten as:

$$D^2 l = \sum_{n=0}^{5}\sum_{m=0}^{5}\left[-\frac{1}{\mu_0}(\alpha_1 m_{10}^{n(1)} + \alpha_2 m_{20}^{n(2)})\mathbb{W}_{nm}^{l}\cos nE + \frac{1}{\mu_0^2}(\alpha_1 m_{10}^{n(1)} + \alpha_2 m_{20}^{n(2)})^2\right.$$
$$\times\{(\mathbb{Y}_{nm}^{l} + \mathbb{S}_{n}^{l})\sin nE + \tau\mathbb{Z}_{nm}^{l}\cos nE\} + \frac{2}{L^3}\left\{\alpha_1^2[\mu_0 n(1)m_{10}^{2n(1)-1} - m_{10}^{2n(1)}]\right.$$
$$\left.\left.+\alpha_2^2[\mu_0 n(2)m_{20}^{2n(2)-1} - m_{20}^{2n(2)}] + \frac{4}{\mu_0^2}\alpha_1\alpha_2 m_{10}^{n(1)}m_{20}^{n(2)}\right\}\right] \tag{32}$$

where the non-vanishing coefficients are:

$$\mathbb{W}^l_{11} = \left(\frac{m_0^2}{L^3}\right)\left[\frac{1}{e} + 3e\right]$$

$$\mathbb{W}^l_{13} = -\frac{m_0^2 G^2 e}{4L^5}$$

$$\mathbb{W}^l_{22} = \frac{m_0^2 G^2}{L^5}$$

$$\mathbb{W}^l_{33} = \frac{m_0^2 G^2 e}{4L^5}$$

$$\mathbb{S}^l_1 = -\frac{1}{e}$$

$$\mathbb{Y}^l_{12} = -\frac{3G^2}{4eL^2} + \frac{G^2}{4eL^2}(1 + 2e^2)$$

$$\mathbb{Y}^l_{13} = -\frac{G^2}{16L^2}$$

$$\mathbb{Y}^l_{15} = \frac{\mu G^4 e}{4L^6}$$

$$\mathbb{Y}^l_{21} = \frac{1}{2e^2} + \frac{1}{2}\frac{G^2}{e^2 L^2} - \frac{G^2}{2L^2}$$

$$\mathbb{Y}^l_{22} = \frac{G^4}{4L^4}$$

$$\mathbb{Y}^l_{23} = -\frac{G^2 e^2}{4L^2}$$

$$\mathbb{Y}^l_{24} = \frac{\mu G^4}{8L^6}$$

$$\mathbb{Y}^l_{25} = -\frac{\mu G^4}{8L^6}$$

$$\mathbb{Y}^l_{32} = \frac{G^2}{eL^2}$$

$$\mathbb{Y}^l_{34} = \frac{G^4 e}{4L^4}\left[\frac{1}{2e^2 L}(1 + 2e^2) - 1\right]$$

$$\mathbb{Y}^l_{35} = \frac{G^4 e}{4L^4}$$

$$\mathbb{Y}^l_{43} = \frac{G^2}{16L^2}$$

$$\mathbb{Y}^l_{45} = -\frac{\mu G^4}{8L^6}$$

$$\mathbb{Y}^{l}_{54} = \frac{G^4 e}{8L^4}$$

$$\mathbb{Z}^{l}_{11} = \frac{1}{L^2}\left[\frac{2\mu_0^2}{eL} + 6e\mu_0^2 - \frac{m_0^2}{L}\left(\frac{1}{e} + 3e\right)\right]$$

$$\mathbb{Z}^{l}_{13} = -\frac{e}{2L^5}\left(\mu_0^2 G^2 + \frac{m_0^2}{2}\right)$$

$$\mathbb{Z}^{l}_{22} = \frac{G^2}{L^5}[2\mu_0^2 - m_0^2]$$

$$\mathbb{Z}^{l}_{33} = \frac{G^2 e}{4L^5}[2\mu_0^2 - m_0^2].$$

Then the solution

$$\begin{aligned} l(t) &= [l]_{\overrightarrow{l_0}} + [Dl]_{\overrightarrow{l_0}}(t - t_0) + [D^2 l]_{\overrightarrow{l_0}} \frac{(t - t_0)^2}{2} \\ &= [l]_{\overrightarrow{l_0}} + [\dot{l} + \tilde{n}]_{\overrightarrow{l_0}}(t - t_0) + [D^2 l]_{\overrightarrow{l_0}} \frac{(t - t_0)^2}{2}. \end{aligned} \tag{33}$$

6.2 *The series for g*

The double action of the Lie operator, D on argument of periapsis g can be computed as:

$$D^2 g = \left(\frac{dl}{dt}\frac{\partial}{\partial l} + \frac{dg}{dt}\frac{\partial}{\partial g} + \frac{dL}{dt}\frac{\partial}{\partial L} + \frac{dG}{dt}\frac{\partial}{\partial G} + \frac{\partial}{\partial t}\right)[\dot{g}] \tag{34}$$

setting

$$\tilde{\zeta}_{s,GL} = \frac{(\Phi_s + \Pi_{2(s-1)})G}{e^3 L^2}$$

equation (34) can be written as:

$$\begin{aligned} D^2 g = \sum_{n=0}^{5}\sum_{m=0}^{6}\Bigg[\alpha\left(\frac{a}{r}\right)^m \mathcal{W}^g_{nm}\cos nE + \alpha^2\Bigg\{\left[\left(\frac{a}{r}\right)^m \mathcal{Y}^g_{nm} + \mathcal{S}^g_n\right]\sin nE \\ + \tau\left(\frac{a}{r}\right)^m \mathcal{Z}^g_{nm}\cos nE\Bigg\}\Bigg] \end{aligned} \tag{35}$$

where the non-vanishing coefficients are:

$$\mathcal{W}^g_{11} = \frac{m_0^2}{L^3}\tilde{\zeta}_{1,G}$$

$$\mathcal{W}^g_{13} = \frac{m_0^2 G}{4L^5}\tilde{\zeta}_1$$

$$\mathcal{W}^g_{22} = -\frac{G m_0^2}{eL^5}\tilde{\zeta}_1$$

$$\mathcal{W}_{33}^{g} = -\frac{m_0^2 G}{4L^5}\tilde{\zeta}_1$$

$$\mathcal{Y}_{12}^{g} = \frac{G}{2eL^2}\left(\tilde{\zeta}_{1,L}\tilde{\zeta}_1 + \frac{G}{2L}\tilde{\zeta}_1\tilde{\zeta}_{1,G}\right)$$

$$\mathcal{Y}_{13}^{g} = \frac{G^3}{4e^2L^5}\tilde{\zeta}_1\tilde{\zeta}_{1,G}$$

$$\mathcal{Y}_{14}^{g} = \frac{G^3}{16eL^5}\tilde{\zeta}_1^2$$

$$\mathcal{Y}_{15}^{g} = \frac{G^3}{8e^3L^6}\left(\frac{1}{e^2L}(e^2+1)\tilde{\zeta}_1^2 - \tilde{\zeta}_1\tilde{\zeta}_{1,L}\right)$$

$$\mathcal{Y}_{16}^{g} = \frac{\mu G^4}{4e^2L^9}\tilde{\zeta}_1^2$$

$$\mathcal{S}_{1}^{g} = \frac{\tilde{\zeta}_{2,G}}{2}$$

$$\mathcal{Y}_{21}^{g} = \frac{1}{2}\left(\tilde{\zeta}_{1,L}\tilde{\zeta}_{1,G} - \tilde{\zeta}_{1,GL}\tilde{\zeta}_1 - \frac{G}{2eL^2}\tilde{\zeta}_2\right)$$

$$\mathcal{Y}_{23}^{g} = \frac{G}{16L^2}\tilde{\zeta}_{1,L}\tilde{\zeta}_1$$

$$\mathcal{Y}_{32}^{g} = -\frac{G}{4eL^2}\left(\tilde{\zeta}_1\tilde{\zeta}_{1,L} + \frac{1}{4e^2L}(e^2+1)\tilde{\zeta}_1^2\right)$$

$$\mathcal{Y}_{34}^{g} = \frac{G^3}{16eL^5}\tilde{\zeta}_1^2$$

$$\mathcal{Y}_{35}^{g} = -\frac{\mu G^3}{4eL^7}\tilde{\zeta}_1^2$$

$$\mathcal{Y}_{43}^{g} = -\frac{G}{2L^2}\left(\frac{1}{4}\tilde{\zeta}_1\tilde{\zeta}_{1,L} - \frac{G^2}{e^2L^3}\tilde{\zeta}_1^2\right)$$

$$\mathcal{Y}_{45}^{g} = -\frac{\mu G^3}{4e^2L^7}\tilde{\zeta}_1^2$$

$$\mathcal{Y}_{54}^{g} = -\frac{G^3}{16eL^5}\tilde{\zeta}_1^2$$

$$\mathcal{Z}_{11}^{g} = \left(\tilde{\eta}_{1,L}\tilde{\zeta}_{1,G} + \frac{m_0^2}{2L^3}\tilde{\zeta}_{2,G}\right)$$

$$\mathcal{Z}_{13}^{g} = -\left(\frac{G}{4L^2}\tilde{\zeta}_1\tilde{\eta}_{1,L} + \frac{m_0^2 G}{8L^5L^3}\tilde{\zeta}_2\right)$$

$$\mathcal{Z}_{22}^{g} = -\frac{G}{eL^2}\left[\frac{m_0^2}{2L^3}\tilde{\zeta}_2 + \tilde{\zeta}_1\tilde{\eta}_{1,L}\right]$$

$$\mathcal{Z}_{33}^{g} = -\frac{G}{4L^2}\left[\frac{m_0^2}{2L^3}\tilde{\zeta}_2 + \tilde{\zeta}_1\tilde{\eta}_{1,L}\right]$$

which can be rewritten as:

$$D^2 g = \sum_{n=0}^{5}\sum_{m=0}^{6}\left[-\frac{1}{\mu_0}(\alpha_1 m_{10}^{n(1)} + \alpha_2 m_{20}^{n(2)})\mathbb{W}_{nm}^{g}\cos nE + \frac{1}{\mu_0^2}(\alpha_1 m_{10}^{n(1)} + \alpha_2 m_{20}^{n(2)})^2 \times (\mathbb{Y}_{nm}^{g}\sin nE + \tau\mathbb{Z}_{nm}^{g}\cos nE)\right] \tag{36}$$

where the non-vanishing coefficients are:

$$\mathbb{W}_{11}^{g} = -\frac{m_0^2 G}{eL^4}$$

$$\mathbb{W}_{13}^{g} = \frac{m_0^2 Ge}{4L^4}$$

$$\mathbb{W}_{22}^{g} = -\frac{Gm_0^2}{L^4}$$

$$\mathbb{W}_{33}^{g} = -\frac{m_0^2 Ge}{4L^4}$$

$$\mathbb{Y}_{12}^{g} = \frac{G}{2eL^2}\left(L - \frac{G^2}{2L}\right)$$

$$\mathbb{Y}_{13}^{g} = -\frac{G^4}{4e^2L^5}$$

$$\mathbb{Y}_{14}^{g} = \frac{G^3 e}{16L^3}$$

$$\mathbb{Y}_{15}^{g} = \frac{G^3}{8eL^5}$$

$$\mathbb{Y}_{16}^{g} = \frac{\mu G^4}{4L^7}$$

$$\mathbb{S}_{1}^{g} = \frac{G}{eL}$$

$$\mathbb{Y}_{21}^{g} = \frac{1}{2}G\left(\frac{1}{L} - \frac{1}{e^2L} - 1\right)$$

$$\mathbb{Y}_{23}^{g} = \frac{G}{16L}$$

$$\mathbb{Y}_{32}^{g} = -\frac{G}{4eL}\left(1 + \frac{1}{4}(e^2+1)\right)$$

$$\mathbb{Y}_{34}^{g} = \frac{G^3 e}{16L^3}$$

$$\mathbb{Y}^g_{35} = -\frac{\mu G^3 e}{4L^5}$$

$$\mathbb{Y}^g_{43} = -\frac{G}{2L^2}\left(\frac{1}{4}L - \frac{G^2}{eL}\right)$$

$$\mathbb{Y}^g_{45} = -\frac{\mu G^3}{4L^5}$$

$$\mathbb{Y}^g_{54} = -\frac{G^3 e}{16L^3}$$

$$\mathbb{Z}^g_{11} = \left(-\frac{2\mu_0^2 G}{eL^4} + \frac{m_0^2 G}{eL^4}\right)$$

$$\mathbb{Z}^g_{13} = -\frac{eG}{2L^4}\left(\mu_0^2 - \frac{m_0^2}{2}\right)$$

$$\mathbb{Z}^g_{22} = -\frac{G}{eL^2}\left[-\frac{m_0^2}{L^2} + \frac{2\mu_0^2 e}{L^2}\right]$$

$$\mathbb{Z}^g_{33} = -\frac{Ge}{4L^4}[-m_0^2 + 2\mu_0^2].$$

Then the solution

$$g(t) = [g]_{\overrightarrow{g_0}} + [Dg]_{\overrightarrow{g_0}}(t - t_0) + [D^2 g]_{\overrightarrow{g_0}}\frac{(t-t_0)^2}{2}$$

$$= [g]_{\overrightarrow{g_0}} + [\dot{g}]_{\overrightarrow{l_0}}(t - t_0)_{\overrightarrow{l_0}}\frac{(t-t_0)^2}{2} + [D^2 g]_{\overrightarrow{g_0}}\frac{(t-t_0)^2}{2}. \tag{37}$$

6.3 *The series for L*

The double action of the Lie operator, D on momenta L can be computed as:

$$D^2 L = \left(\frac{dl}{dt}\frac{\partial}{\partial l} + \frac{dg}{dt}\frac{\partial}{\partial g} + \frac{dL}{dt}\frac{\partial}{\partial L} + \frac{dG}{dt}\frac{\partial}{\partial G} + \frac{\partial}{\partial t}\right)[\dot{L}] \tag{38}$$

which can be written as:

$$D^2 L = \sum_{n=0}^{5}\sum_{m=0}^{5}\left(\frac{a}{r}\right)^m [\alpha \mathcal{W}^L_{nm}\sin nE + \alpha^2\{\mathcal{Y}^L_{nm}\cos nE + \tau\mathcal{Z}^L_{nm}\sin nE\}] \tag{39}$$

where the non-vanishing coefficients are:

$$\mathcal{W}^L_{12} = \frac{m_0^2}{L^3}\tilde{\zeta}_1$$

$$\mathcal{W}^L_{23} = \frac{m_0^2 e}{2L^3}\tilde{\zeta}_1$$

$$\mathcal{Y}^L_{02} = \tilde{\zeta}_1\tilde{\zeta}_{1,L}$$

$$\mathcal{Y}_{04}^{L} = \frac{G^2}{8L^3}\tilde{\zeta}_1^2 - \left(\frac{a}{r}\right)^5 \frac{\tilde{\zeta}_1^2}{2}\frac{G^2}{L^3}\frac{\mu}{L^2}$$

$$\mathcal{Y}_{05}^{L} = -\frac{\mu G^2}{2L^5}\tilde{\zeta}_1^2$$

$$\mathcal{Y}_{11}^{L} = -\frac{\tilde{\zeta}_2}{2}$$

$$\mathcal{Y}_{13}^{L} = \frac{e}{4}\tilde{\zeta}_1\tilde{\zeta}_{1,L} - \frac{G^2}{4eL^3}\left(1 + \frac{1}{L^2}\right)\tilde{\zeta}_1^2$$

$$\mathcal{Y}_{15}^{L} = \frac{3\mu G^2}{4eL^5}\tilde{\zeta}_1^2$$

$$\mathcal{Y}_{22}^{L} = \tilde{\zeta}_1\tilde{\zeta}_{1,L}$$

$$\mathcal{Y}_{25}^{L} = -\frac{\mu G^2}{L^5}\tilde{\zeta}_1^2$$

$$\mathcal{Y}_{33}^{L} = \left[\frac{e}{4}\tilde{\zeta}_1\tilde{\zeta}_{1,L} + \frac{G^2}{4eL^5}(L^2 - 1)\tilde{\zeta}_1^2\right]$$

$$\mathcal{Y}_{35}^{L} = \frac{\mu G^2}{4eL^5}\tilde{\zeta}_1^2$$

$$\mathcal{Y}_{44}^{L} = -\frac{G^2}{8L^3}\tilde{\zeta}_1^2$$

$$\mathcal{Z}_{12}^{L} = \frac{m_0^2}{2L^3}\tilde{\zeta}_2 + \tilde{\zeta}_1\tilde{\eta}_{1,L}$$

$$\mathcal{Z}_{23}^{L} = \frac{e}{2}\left[\frac{m_0^2}{2L^3}\tilde{\zeta}_2 + \tilde{\zeta}_1\tilde{\eta}_{1,L}\right]$$

which can be rewritten as:

$$D^2L = \sum_{n=0}^{5}\sum_{m=0}^{5}\left[-\frac{1}{\mu_0}\left(\alpha_1 m_{10}^{n(1)} + \alpha_2 m_{20}^{n(2)}\right)\mathbb{W}_{nm}^{g}\sin nE + \frac{1}{\mu_0^2}(\alpha_1 m_{10}^{n(1)} + \alpha_2 m_{20}^{n(2)})^2 \times (\mathbb{Y}_{nm}^{g}\cos nE + \tau\mathbb{Z}_{nm}^{g}\sin nE)\right] \tag{40}$$

where the non-vanishing coefficients are:

$$\mathbb{W}_{12}^{L} = \frac{m_0^2 e}{L^2}$$

$$\mathbb{W}_{23}^{L} = \frac{m_0^2 e^2}{2L^2}$$

$$\mathbb{Y}_{02}^{L} = L$$

$$\mathbb{Y}_{04}^{L} = \frac{G^2 e^2}{8L}$$

$$\mathbb{Y}^L_{05} = -\frac{\mu G^2 e^2}{2L^3}$$

$$\mathbb{Y}^L_{11} = eL$$

$$\mathbb{Y}^L_{13} = \frac{eL}{4} - \frac{G^2 e}{4L}\left(1 + \frac{1}{L^2}\right)$$

$$\mathbb{Y}^L_{15} = \frac{3\mu G^2 e}{4L^3}$$

$$\mathbb{Y}^L_{22} = L$$

$$\mathbb{Y}^L_{25} = -\frac{\mu G^2 e^2}{L^3}$$

$$\mathbb{Y}^L_{33} = \frac{eL}{4} + \frac{G^2 e}{4L^3}(L^2 - 1)$$

$$\mathbb{Y}^L_{35} = \frac{\mu_0 G^2 e}{4L^3}$$

$$\mathbb{Y}^L_{44} = -\frac{G^2 e}{8L}$$

$$\mathbb{Z}^L_{12} = \frac{e}{L^2}(2\mu_0^2 - m_0^2)$$

$$\mathbb{Z}^L_{23} = \frac{m_0^2 e^2}{2L^2}(2\mu_0^2 - m_0^2).$$

Then the solution yields:

$$\begin{aligned} L(t) &= [L]_{\overrightarrow{L_0}} + [DL]_{\overrightarrow{L_0}}(t - t_0) + [D^2 L]_{\overrightarrow{L_0}} \frac{(t - t_0)^2}{2} \\ &= [L]_{\overrightarrow{L_0}} + [\dot{L}]_{\overrightarrow{L_0}}(t - t_0) + [D^2 L]_{\overrightarrow{L_0}} \frac{(t - t_0)^2}{2}. \end{aligned} \tag{41}$$

6.4 *The series for G*

The double action of the Lie operator, D on momenta G equal to zero

$$G(t) = [G]_{\overrightarrow{G_0}}. \tag{42}$$

7. Conclusion

The following concluding remarks and notes can be outlined:

- The ejection of mass from any body depends on many parameters, amongst the most important of which are the central condensation (which means, more or less, the degree of rigidity of the body) and the velocity of rotation which provides the

external layers with the angular momentum that activates the process of ejection of mass. But to simplify the model, we assumed that the rate of mass ejection depends explicitly, solely on the mass of the body.

- Since the different models of variable mass assume that the mass loss takes place isotropically, i.e., there is no preformed direction in the space, it is expected to find the Hamiltonian free from dependence on the inclination. This reflects the absence of H in the Hamiltonian of the problem. Therefore $\dot{h} = 0 \Rightarrow h = \text{const}$.
- Also, as the stars are assumed point masses, the Hamiltonian is free from orientation angles (g, h). This means that G and H are kept constants.
- The effect of one body ejects mass on the other body is declared through the appearance of the non-linear term factored by $\alpha_1\alpha_2$.

References

Andrade, M., Docobo, J. A. 2002, Classical Nova Explosions: International Conference on Classical Nova Explosions, (eds) Hernanz, M., José, J., American Institute of Physics, 82.

Andrade, M., Docobo, J. A. 2003, Winds, Bubbles, Explosions: A Conference to Honour John Dyson. Pàtzcuaro, Michoacàn. México, 9–13 September 2002 (eds) Arthur, S. J., Henney, W. J., Instituto de Astronomia, Universidad Nacional Autónoma de México, 223.

Delva, M. 1984, *Celest. Mech.*, **34**, 145.

Demchenko, B. I., Omarov, T. B. 1984, *Tr. Astrofiz. Inst. Akad. Nauk Kaz. SSR*, **29**, 11.

Deprit, A. 1969, *Celest. Mech.*, **1**, 12.

Deprit, A. 1983, *Celest. Mech.*, **31**, 1.

Docobo, J. A., Prieto, C., Ling, J. F. 1999, *Astrophys. Space Sci.*, **261**, 205.

Dommangent, J. 1963, Ann. Obs. Royal de Belguique, 3eme Ser. IX, Fas.c.5.

Dommangent, J. 1964, Comm. Obs. Royal de Belguique, no. 232.

Dommangent, J. 1981, "Effects of Mass Loss on Stellar Evolution" (eds) Chiosi, C., Stalio, R. 507.

Dommangent, J. 1982, "Binary and Multiple Stars as Tracers of Stellar Evolution" (eds) Kopal, Z., Rahe, J. 3eme Ser. IX, Fas.c.5.

Dommangent, J. 1997, "Visual Double Stars: Formation, Dynamics and Evolutionary Trachs" (eds) Docobo, J. A., Elipe, A., Hi, A., *McAlister ASSL*, **223**, 403.

Eddington, A. S. 1924, *Mont. Not. R. Astron. Soc.*, **84**, 308.

Hadjidemetriou, J. D. 1963, *Icarus*, **2**, 440.

Hadjidemetriou, J. D. 1966, *Zeitschrift fur Astophysik*, **63**, 116.

Halslmeier, A. 1984, *Celest. Mech.*, **34**, 135.

Hut, P., Verhulst, F. 1976, *Mon. Not. R. Astron. Soc.*, **177**, 545.

Idlis, G. M., Omarov, T. B. 1960, *Tr. Astrofiz. Inst. Akad. Nauk Kaz. SSR*, **10(13)**, 28.

Jeans, J. H. 1924, *Mon. Not. R. Astron. Soc.*, **85(1)**, 2.

Kamel, A. A. 1969, *Celest. Mech.*, **1**, 190.

MacMillan, W. D. 1925, *Mon. Not. R. Astron. Soc.*, **85(9)**, 904.

Martin, E. L. 1934, Reale Stazione Astron e Geof. di Carloforte (Cagliari), no. 30.

Minglibaev, M. D. 1988, *Tr. Astrofiz. Inst. Akad. Nauk Kaz. SSR*, **49**, 71.

Mioc, V., Pal, A., Giurgin, I. 1988a, Stud. Univ. Cluj, Romania, *Phys. Math.*, **33(4)**, 67.

Mioc, V., Pal, A., Giurgin, I. 1988b, Univ. Cluj, Romania, *Fac. Math. Res. Seminars*, no. 10, p. 3.

Mioc, V., Pal, A., Giurgin, I. 1988c, Univ. Cluj, Romania, *Fac. Math. Res. Seminars*, no. 10, p. 21.

Mioc, V., Pal, A., Giurgin, I. 1988d, Univ. Cluj, Romania, *Fac. Math. Res. Seminars*, no. 10, p. 91.

Mukhametkalieva, R. K. 1987, *Tr. Astrofiz. Inst. Akad. Nauk Kaz. SSR*, **47**, 60.

Mukhametkalieva, R. K. 1988, *Tr. Astrofiz. Inst. Akad. Nauk Kaz. SSR*, **49**, 74.

Omarov, T. B., Omarkulov, K. A. 1982, *Tr. Astrofiz. Inst. Akad. Nauk Kaz. SSR*, **39**, 108.

Omarov, T. B. 1991, *Izv. Akad. Naukkaz. SSR, Ser. Fiz. Mat.*, no. 4, p. 42.

Polyakhova, E. N. 1994, *Astron. Rep.*, **38(2)**, 283.

Prieto, C., Docobo, J. A. 1997a, *Astron. Astrophys.*, **318**, 657.
Prieto, C., Docobo, J. A. 1997b, *Celest. Mech. & Dyn. Astron.*, **68**, 53.
Verhulst, F. 1972, *Celest. Mech.*, **5(1)**, 27.
Verhulst, F. 1975, *Celest. Mech.*, **11(1)**, 95.
Vinti, J. P. 1977, *Celest. Mech.*, **16(3)**, 391.